



Design of flexible lead-free ceramic/biopolymer composite for energy storage and energy harvesting applications

Zouhair Hanani

► To cite this version:

Zouhair Hanani. Design of flexible lead-free ceramic/biopolymer composite for energy storage and energy harvesting applications. Material chemistry. Université de Bordeaux; Université Cadi Ayyad (Marrakech, Maroc), 2020. English. NNT : 2020BORD0288 . tel-03131916

HAL Id: tel-03131916

<https://theses.hal.science/tel-03131916>

Submitted on 4 Feb 2021

HAL is a multi-disciplinary open access archive for the deposit and dissemination of scientific research documents, whether they are published or not. The documents may come from teaching and research institutions in France or abroad, or from public or private research centers.

L'archive ouverte pluridisciplinaire **HAL**, est destinée au dépôt et à la diffusion de documents scientifiques de niveau recherche, publiés ou non, émanant des établissements d'enseignement et de recherche français ou étrangers, des laboratoires publics ou privés.

THÈSE EN COTUTELLE PRÉSENTÉE
POUR OBTENIR LE GRADE DE
DOCTEUR DE
L'UNIVERSITÉ DE BORDEAUX
ET DE L'UNIVERSITÉ CADI AYYAD DE MARRAKECH

ÉCOLE DOCTORALE SCIENCES CHIMIQUES
CENTRE DES ETUDES DOCTORALES SCIENCES ET TECHNIQUES
SPÉCIALITÉ : PHYSICO-CHIMIE DE LA MATIERE CONDENSEE

Par Zouhair HANANI

**CONCEPTION DE COMPOSITE FLEXIBLE CERAMIQUE SANS
PLOMB/BIOPOLYMER POUR DES APPLICATIONS DE
STOCKAGE ET DE RECUPERATION D'ENERGIE**

Sous la direction de Mohamed GOUNE
Co-directeur : M'barek AMJOUD
Co-directeur : Daoud MEZZANE

Soutenue le 14/12/2020

Membres du jury :

M. SAADOUNE Ismael	Université Cadi Ayyad de Marrakech	Président
M. CHAMPION Yannick	Institut polytechnique de Grenoble	Rapporteur
M. BENYOUSSEF Abdelilah	Académie Hassan II des Sciences et Technologies	Rapporteur
M. KUTNJAK Zdravko	Institut Jožef Stefan	Examinateur
M. EL MARSSI Mimoun	Université de Picardie Jules Verne	Examinateur
M. GOUNE Mohamed	Université de Bordeaux	Directeur de thèse
M. AMJOUD M'barek	Université Cadi Ayyad de Marrakech	Co-directeur de thèse
M. MEZZANE Daoud	Université Cadi Ayyad de Marrakech	Co-directeur de thèse
M. LAHCINI Mohammed	Université Cadi Ayyad de Marrakech	Invité

Design of flexible lead-free ceramic/biopolymer composite for energy storage and energy harvesting applications

Abstract

The existing energy storage and harvesting devices suffer from the moderate performances, low flexibility and the use of toxic compounds. This is how ceramic/polymer nanocomposite approach is highly promising for high-efficiency energy storage and harvesting applications, due to the high dielectric constant of the ceramic and the high breakdown strength, the flexibility and the ease of processing of the polymer. This thesis focuses on designing ceramic (BCZT)/polymer (PLA) nanocomposites for these applications. First, controlled syntheses of BCZT ceramics with different particle sizes, size distributions and shapes were performed and discussed. The effects of grain size and grain shape of BCZT ceramics on the dielectric properties were studied. It was found that the BCZT ceramic with near-spherical particles elaborated by low-temperature hydrothermal processing at 160 °C revealed enhanced dielectric and ferroelectric properties compared to the BCZT ceramics synthesized by other methods. Second, BCZT near-spherical particles BCZT nanorods and HZTO nanowires were embedded in the biodegradable PLA polymer matrix. The effects of the ceramic shape, arrangement, dielectric constant and aspect ratio on the dielectric constant of the nanocomposite were explored using the effective dielectric constant of the nanocomposite models. It was found that for improving the dielectric properties of the composite, it is important to control the ceramic fillers geometry rather the use of high-k ceramics. Afterwards, the energy storage properties of PLA-based nanocomposites were evaluated by D–E hysteresis loops, and high-energy storage performances were obtained in the nanocomposites based on rod-like fillers. The energy harvesting aspect was investigated by designing a bio-flexible piezoelectric nanogenerator (BF-PNG) based on BCZT/PLA nanocomposite film to convert the ambient mechanical energy to electrical energy. This BF-PNG could generate open-circuit voltage and short-circuit current of 14.4 V and 0.55 μ A, respectively, and large power density of 7.54 mW/cm³ at a low resistive load of 3.5 M Ω , under gentle finger tapping. The feasibility of the BF-PNG was tested by driving commercial electronics (charging capacitors and lighting an LED). Accordingly, this work demonstrates that BCZT lead-free ceramic in combination with PLA biopolymer can lead to flexible nanocomposite with enhanced energy storage and energy harvesting performances for application in self-powered devices.

Keywords: Lead-free ceramic; Hydrothermal; Biodegradable polymer; Composite; Energy storage; Energy Harvesting.

Conception de composite flexible céramique sans plomb/biopolymère pour des applications de stockage et de récupération d'énergie

Résumé

Les dispositifs de stockage et de récupération d'énergie existants souffrent des performances modérées, de la faible flexibilité et de l'utilisation de composés toxiques. Ainsi, l'approche nanocomposite céramique/polymère est très prometteuse pour les applications de stockage et de récupération d'énergie à haut rendement, en raison de la constante diélectrique élevée de la céramique et de la résistance à la rupture élevée, de la flexibilité et de la facilité de traitement du polymère. Cette thèse est articulée autour de la conception de nanocomposites céramique (BCZT)/polymère (PLA) pour répondre à ces exigences. Tout d'abord, des synthèses contrôlées de céramiques BCZT avec différentes tailles de particules, distributions de tailles et formes ont été réalisées et discutées. Les effets de la taille des particules et de la forme des grains des céramiques BCZT sur les propriétés diélectriques ont été étudiés. Il a été constaté que la céramique BCZT avec des particules presque sphériques élaborée par le procédé hydrothermal à basse température à 160 °C a révélé des propriétés diélectriques et ferroélectriques améliorées par rapport aux autres céramiques BCZT préparées par d'autres méthodes. Ensuite, des particules quasi sphériques BCZT, des nanorods BCZT et des nanofils HZTO ont été incorporés dans la matrice polymère PLA biodégradable. Les effets de la forme, de l'arrangement, de la constante diélectrique et du facteur de forme de la céramique sur la constante diélectrique du nanocomposite ont été étudiés en utilisant la constante diélectrique effective des modèles de nanocomposite. A l'issue de cette étude, il a été constaté que pour améliorer les propriétés diélectriques du composite, il n'est pas nécessaire d'utiliser des charges céramiques à haute permittivité mais plutôt, contrôler leurs géométries au sien du composite. Par la suite, les performances de stockage d'énergie des nanocomposites à base de PLA ont été évaluées par des boucles d'hystérésis D-E. Ainsi, une forte capacité de stockage énergie a été obtenue dans les nanocomposites à base de charges en forme de bâtonnets. L'aspect récupération d'énergie a été étudié en concevant un nanogénérateur piézoélectrique bio-flexible (BF-PNG) à base d'un film nanocomposite BCZT/PLA pour convertir l'énergie mécanique ambiante en énergie électrique. Ce BF-PNG pourrait générer une tension en circuit ouvert et un courant de court-circuit de 14,4 V et 0,55 μ A respectivement, et une grande densité de puissance de 7,54 mW/cm³ à une faible charge résistive de 3,5 M Ω , sous un léger tapotement du doigt. La faisabilité du BF-PNG a été testée en pilotant l'électronique commerciale (charge de condensateurs et allumage d'une LED). En conséquence, ce travail démontre que la céramique écologique sans plomb BCZT en combinaison avec le biopolymère PLA peut conduire à des nanocomposites flexibles avec des performances améliorées de stockage et de récupération d'énergie pour des applications dans des dispositifs auto-alimentés.

Mots clés : Céramique sans plomb ; Hydrothermal ; Polymère biodégradable ; Composite ; Stockage d'énergie ; Récupération d'énergie.

تصميم مركب مرن مكون من السيراميك لخلي من الرصاص وبوليمر ليج وتطبيقه لتخزين وحصاد الطاقة

ملخص

تعاني غالبية أجهزة تخزين وحصاد الطاقة من الأداء المعتدل والمرونة المنخفضة واستخدام المركبات السامة. ويعتبر نهج المركب النانوي السيراميك/البوليمر واعدًا للغاية لتطبيقات تخزين وحصاد الطاقة عالية الكفاءة، نظرًا لارتفاع ثابتة العزل الكهربائي للسيراميك، وقوة الانهيار العالية، والمرونة وسهولة معالجة البوليمر. تركز هذه الأطروحة على تصميم مركبات نانوية متعددة الوظائف من السيراميك/البوليمر لهذه التطبيقات. أولاً، تمت مناقشة توليفات متحكم فيها للسيراميك BCZT ذات جزيئات مختلفة القياسات، وتوزيعات القياسات والأشكال. تمت دراسة تأثير مقاس حبيبات سيراميك BCZT وشكلها على خصائص العزل الكهربائي. فلاحظنا أن سيراميك BCZT ذات جزيئات شبه كروية والتي تم تطويرها بواسطة معالجة حرارية منخفضة الحرارة عند 160 درجة مئوية، أسفرت عن خصائص عازلة وكهربائية حديدية محسنة مقارنة بالسيراميك BCZT الأخرى. ثانيًا، تم دمج جزيئات BCZT شبه الكروية، وعصيات BCZT وأسلاك HZTO النانوية في مصفوفة بوليمر PLA القابلة للتحلل الحيوي وتمت دراسة تأثيرات الشكل السيراميكي، والترتيب، وثابتة العزل الكهربائي، ونسبة أبعاد الجزيئات على ثابتة العزل الكهربائي للمركب النانوي باستخدام نماذج ثابتة العزل الفعال للمركبات النانوية. بعد الكشف عن نموذج ثابتة العزل الكهربائي مقابل نسبة الأبعاد، وجدنا أنه لتحسين الخواص العازلة للمركب، ليس من الضروري استخدام حشوات سيراميكية ذات ثابتة عزل كهربائي عالية، ويمكن التوصل لنفس النتيجة بتركيب أفضل في هندستها. بعد ذلك، تم تقييم أداء تخزين الطاقة للمركبات النانوية القائمة على PLA بواسطة حلقات التباطؤ D-E، وتم الحصول على أداء تخزين عالي الطاقة في المركبات النانوية المبنية على حشوات سيراميكية عضوية. كما تم فحص جانب حصاد الطاقة من خلال تصميم مولد نانوي كهربائي انضغاطي مرن حيويًا (BF-PNG) على أساس فيلم BCZT/PLA النانوي المركب لتحويل الطاقة الميكانيكية إلى طاقة كهربائية. وتحت ضغط لطيف بالإصبع، يمكن أن يولد هذا BF-PNG المتين جهدًا لدارة مفتوحة بقيمة 14.4 فولت، وتيار دائرة مقصورة بقيمة 0.55 ميكرو أمبير، وكثافة طاقة كبيرة تبلغ 7.54 ميكرو واط على سنتيمتر مكعب عند حمل مقاومة منخفض يبلغ 3.5 ميجا أوم. كما تم اختبار جدوى BF-PNG من خلال تشغيل الإلكترونيات التجارية كمشحن مكثفات وإضاءة مصباح LED. وفقًا لذلك، يوضح هذا العمل أن مزج سيراميك BCZT الخالي من الرصاص مع البوليمر القابل للتحلل PLA يمكن أن يؤدي إلى مركب نانوي مرن، وتخزين وحصاد للطاقة جيدين للتطبيق في الأجهزة ذاتية التشغيل.

الكلمات المفتاحية: سيراميك خال من الرصاص؛ معالجة حرارية؛ بوليمر قابل للتحلل؛ مركب؛ تخزين الطاقة؛ حصاد الطاقة.

Unités de Recherche:

ICMCB, UMR5026, 87 Avenue du docteur Albert Schweitzer, 33608, Pessac (France)
IMED-Lab, Université Cadi Ayyad, Avenue Abdelkrim Khattabi, 40000, Marrakech (Maroc)

Résumé long en Français de la Thèse

I.	Introduction et contexte généraux.....	v
II.	Élaboration et caractérisation des céramiques BCZT.....	vii
III.	Elaboration, caractérisation et propriétés des nanocomposites BCZT/PLA.....	xiii
IV.	Nanogénérateur piézoélectrique à base de film nanocomposite sans plomb pour la récupération d'énergie biomécanique	xviii
V.	Conclusions et perspectives.....	xxii
VI.	Bibliographie.....	xxv

I. Introduction et contexte généraux

De nos jours, la demande croissante d'appareils électroniques mobiles miniaturisés et qui peuvent être connectés les uns aux autres à tout moment suscite un engouement important. Ces nouvelles technologies prometteuses aux fonctions accrues nécessitent cependant une (ou plusieurs) alimentation(s) externe(s). Les batteries, qui sont une alternative possible, présentent cependant de nombreux inconvénients que constituent leur grand volume, leur poids relativement élevé, leur densité de puissance limitée et leur temps de charge et de décharge relativement long. L'une des voies prometteuses envisageable pour remédier à ces inconvénients est le développement de nouveaux systèmes auto-alimentés limités à la fois en taille et en poids qui peuvent convertir une source d'énergie telle que mécanique, thermique et photonique en énergie électrique. Les phénomènes physiques impliqués dans la récupération, le stockage et la conversion d'énergie peuvent être la piézoélectricité, la thermoélectricité et la photoélectricité.

Les matériaux ferroélectriques relaxeurs de structure pérovskite sont des candidats potentiels et crédibles pour le stockage et la conversion d'énergie. En effet, sur l'aspect « récupération », le courant électrique est généralement généré par polarisation interne. En conséquence, la puissance de sortie du récupérateur d'énergie sera améliorée en augmentant la densité de polarisation des ferroélectriques relaxeurs. Concernant l'aspect « stockage d'énergie », les matériaux de structure pérovskite peuvent également être considérés comme matériaux diélectriques prometteurs pouvant stocker et libérer de l'énergie électrique par polarisation et dépolarisation diélectriques. Il convient de noter que la densité de stockage d'énergie dans les matériaux diélectriques est déterminée à la fois par le déplacement électrique et le champ électrique. Elle est sensible à la variation de la rigidité diélectrique (résistance au claquage) et à la permittivité diélectrique [1]. De manière générale, les matériaux diélectriques de structure pérovskite possèdent une permittivité élevée mais une faible résistance à la rupture. Cette dernière limite leur capacité de stockage d'énergie et freine leur développement à plus grande échelle. L'engouement que suscitent actuellement les nanocomposites céramiques/polymères permet de relever ces défis [1–3]. En associant une céramique à forte permittivité et un polymère à forte rigidité diélectrique, l'effet composite résultant conduit généralement à l'obtention de composants qui possèdent de bon compromis entre des niveaux de permittivité et de rigidité diélectrique importants. Ceci est d'autant plus vrai si l'on arrive à contrôler la taille nanométrique et la forme du matériau diélectrique et l'architecture du nanocomposite obtenue [4–6]. A cet égard, il a été montré par modélisation en champ de phase que certaines configurations architecturales peuvent limiter la pénétration du claquage et repousse le champ de claquage vers des valeurs plus élevées [7].

Les céramiques à base de plomb tel que le titanate de zirconate de plomb (PZT) sont largement utilisées pour ces applications en raison de leurs excellentes propriétés ferroélectriques et piézoélectriques [8–11]. On les trouve dans les capteurs, les générateurs d'ultrasons, les résonateurs, les actionneurs, etc. [12,13]. Cependant, compte tenu des préoccupations liées à la pollution de l'environnement et à la santé humaine, les considérations environnementales mondiales exigent l'élimination des matériaux à base de plomb de tous les produits de consommation. En conséquence, leur remplacement par leurs homologues exempts de plomb avec des propriétés piézoélectriques comparables est une tâche émergente. En 2009, un coefficient piézoélectrique élevé ($d_{33} \sim 620$ pC/N) a été trouvé dans le matériau ferroélectrique exempt de plomb $0.5\text{Ba}(\text{Zr}_{0.2}\text{Ti}_{0.8})\text{O}_3-0.5(\text{Ba}_{0.7}\text{Ca}_{0.3})\text{TiO}_3$ (0,5BZT–0,5BCT, BCZT) sous forme de céramique grâce à sa composition située dans la limite de la phase morphotropique [12]. Une telle valeur élevée, comparable à celle des matériaux à base de plomb comme le PZT mou, montre que les céramiques ferroélectriques à base de BaTiO_3 sans plomb sont une alternative possible et non toxique. Pour fabriquer les céramiques BCZT pures et cristallines, la méthode de la réaction solide-solide qui nécessite une température élevée est souvent utilisée, en raison de sa simplicité et de sa capacité à obtenir des performances diélectriques, ferroélectriques et piézoélectriques améliorées. Récemment, des poudres BCZT ont été élaborées par des voies de chimie douce comme le sol-gel [13], la réaction au citrate [14], la solvothermale [15] et l'hydrothermale [16]. Cependant, un post-traitement thermique, exigeant une température relativement élevée, est nécessaire pour l'obtention d'une poudre BCZT pure et cristalline. Dans ce travail, nous avons développé de nouvelles voies de synthèse à basses températures, des poudres BCZT pures et cristallines de tailles et de formes géométriques différentes en vue d'améliorer leurs performances électriques.

Pour répondre à la problématique de stockage et de récupération d'énergie moyennant des matériaux respectueux de l'environnement à performances énergétiques améliorées, nous avons incorporé les différentes nanoparticules écologiques BCZT synthétisées dans une matrice de polymère d'acide polylactique (PLA) biodégradable en vue de concevoir des nanogénérateurs piézoélectriques flexibles à base de nanocomposites BCZT/PLA.

Pour ce faire, nous avons dans un premier temps synthétisé via quatre différentes voies de synthèse chimique des nanoparticules $0,5\text{Ba}(\text{Zr}_{0.2}\text{Ti}_{0.8})\text{O}_3-0,5(\text{Ba}_{0.7}\text{Ca}_{0.3})\text{TiO}_3$ (BCZT) sans plomb de tailles et de morphologies variables (quasi-sphériques, bâtonnets et multipodes) et examiné l'impact de ses caractéristiques sur les propriétés diélectriques et ferroélectriques des céramiques BCZT frittées afin de sélectionner la céramique présentant les propriétés les plus prometteuses en vue d'être incorporée dans la matrice polymérique.

Ensuite, les nanoparticules céramiques BCZT sélectionnées ainsi que les nanofils $H_2(Zr_{0.1}Ti_{0.9})_3O_7$ (HZTO) (oxyde non ferroélectrique) en tant que « référence », ont été dispersées dans la matrice biopolymère à base de PLA. L'évolution de la constante diélectrique effective en fonction de la forme, de la disposition (arrangement) et du facteur de forme ($\frac{c}{a}$ = longueur/largeur de la particule) et de la fonctionnalisation (core-shell) des nanoparticules quasi-sphériques BCZT par une couche de polydopamine (PDA) a été examinée et étudiée. Par la suite, les performances de stockage d'énergie (densité d'énergie totale, densité d'énergie récupérée et efficacité énergétique) des nanocomposites ont été étudiées à l'aide des boucles d'hystérésis du déplacement diélectrique–champ électrique (D–E).

Enfin, les performances en termes de récupération d'énergie par les nanocomposites BCZT/PLA ont été étudiées en utilisant le concept des nanogénérateurs piézoélectriques pour convertir l'énergie mécanique ambiante en une énergie électrique. À cet effet, les performances de sortie sous différents mouvements du corps humain ont été évaluées, et la faisabilité de piloter des composants électroniques commerciaux a été vérifiée en utilisant le nanogénérateur piézoélectrique bio-flexible basé sur le nanocomposite BCZT@PDA/PLA.

II. Élaboration et caractérisation des céramiques BCZT

Les céramiques BCZT de forme et de taille différentes ont été élaborées par traitement solvo/hydrothermal. Les nanoparticules sphériques de BCZT ont été synthétisées en utilisant deux stratégies : les voies (i) solvothermale (Figure 1a) et (ii) sol-gel-hydrothermale à basses températures (Figure 1b). La première approche implique l'utilisation de deux tensioactifs, l'un cationique : bromure de cetyltriméthylammonium, $C_{19}H_{42}BrN$, CTAB et l'autre anionique : sodium dodécyl sulfate, $NaC_{12}H_{25}SO_4$, SDS) et ce pour mieux contrôler la granulométrie des poudres BCZT (Figure 2a). Toutefois, une étape de calcination à 1000 °C/4 h a été nécessaire pour avoir des poudres BCZT pures et cristallines. Pour pallier cet inconvénient, une autre stratégie (ii) a été conçue en se basant sur le procédé sol-gel pour obtenir des nanoparticules de $Zr_{0.1}Ti_{0.9}O_3$ (ZTO) suivi une réaction hydrothermale entre le ZTO et les sels de baryum et de calcium. Il est important de noter que c'est la première fois que des poudres nanocristallines BCZT ont été élaborées à très basse température par cette méthode (Figure 2b), y compris à température ambiante. Pour fabriquer la céramique BCZT en forme de bâtonnet (B_NR), nous avons procédé au traitement solvothermal assisté par le surfactant CTAB en concentration plus élevée que dans le cas de la voie solvothermale (Figure 1c). Plus tard, des céramiques BCZT hiérarchiquement nanostructurées ont été conçues en utilisant un traitement hydrothermal en deux étapes (Figure 1d). Tout d'abord, des nanofils HZTO_NW, qui sert de modèle inorganique pour la préparation de BCZT, ont été élaborées par un traitement hydrothermal à 240 °C/48 h dans un

milieu très alcalin. Ensuite, une réaction entre HZTO_NW et les sels de baryum et de calcium a conduit à la formation des multipodes BCZT (Figure 1d). Le mécanisme de croissance en deux étapes des multipodes BCZT est décrit dans la Figure 3. Il consiste en la nucléation des cubes CZTO sur la surface de HZTO_NW puis en la nucléation perpendiculaire des multipodes BCZT sur les faces des cubes formés. Il a été constaté que les concentrations du précurseur du site A (baryum et calcium) jouent un rôle essentiel dans la formation des multipodes BCZT, et que la phase BCZT recherchée est favorisée en utilisant de faibles concentrations de baryum et de calcium.

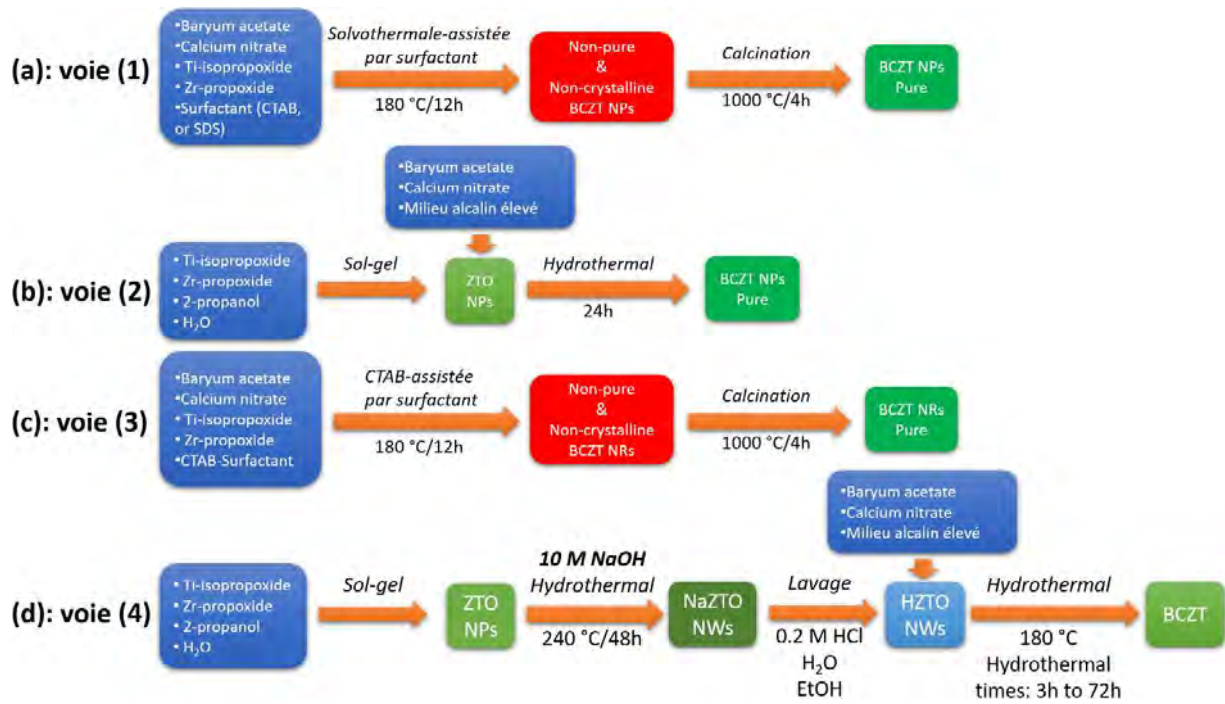


Figure 1. Voies de synthèse (a, b) des nanoparticules quasi-sphériques BCZT : (a) solvothermale-assistée par des surfactants et (b) hydrothermale à basses températures. (c) Synthèse des bâtonnets BCZT par voie solvothermale-assistée par le surfactant CTAB. (d) Elaboration de BCZT architecturé avec des morphologies complexes.

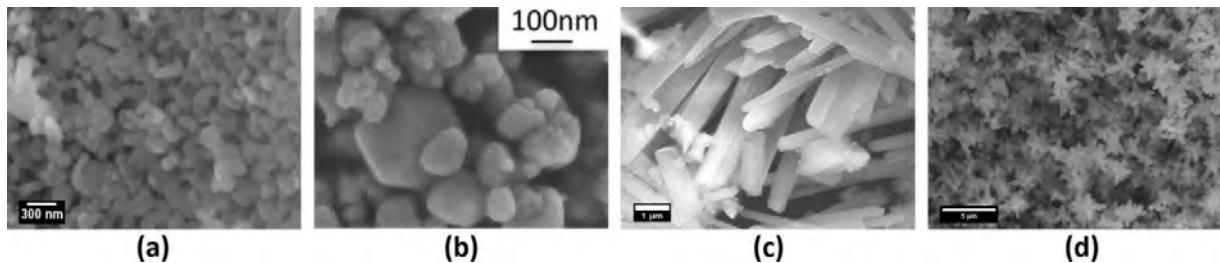


Figure 2. Micrographies MEB-FEG des poudres BCZT issues des voies de synthèse : (a) voie 1, (b) voie (2), (c) voie (3) and (d) voie (4).

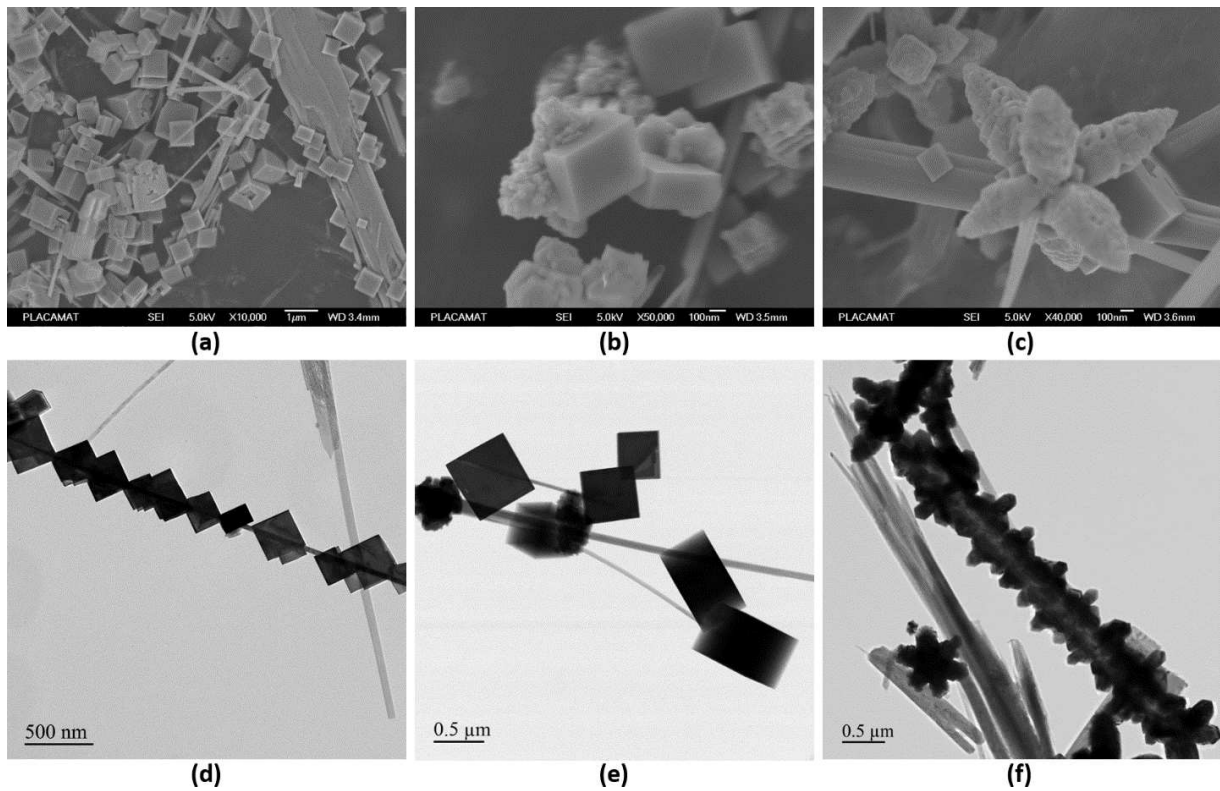


Figure 3. Micrographies (a-c) MEB-FEG et (d-f) MET-HR indiquant la morphogenèse des matériaux BCZT.

Par la suite, les propriétés diélectriques et ferroélectriques des céramiques BCZT frittées à 1250 °C/10 h ont été examinées pour chaque poudre (nanoparticules sphériques, nanorods et morphologies anisotropes) (Figure 4). Les effets de la taille et de la forme des grains des céramiques BCZT sur les propriétés diélectriques ont été discutés. Il est à noter que la présence du surfactant influence favorablement le processus de densification des céramiques et par conséquent, l'amélioration de leurs propriétés diélectriques. Ces propriétés diélectriques sont également améliorées avec l'augmentation de la température hydrothermale de 25 à 160 °C dans la voie 2. L'analyse des propriétés ferroélectriques des céramiques BCZT (Figure 4), étudiées en traçant les boucles d'hystérésis P-E a montré que la céramique BCZT (B-160), élaborée à 160 °C par le traitement sol-gel-hydrothermale et formée de nanoparticules sphériques (voie 2), présente des propriétés diélectriques et ferroélectriques améliorées par rapport aux autres types de BCZT. Sur la base de ces analyses, la céramique B-160 pourrait être un candidat prometteur pour être intégrée dans une matrice PLA afin préparer des films nanocomposites BCZT/PLA pour des applications de stockage et de récupération d'énergie.

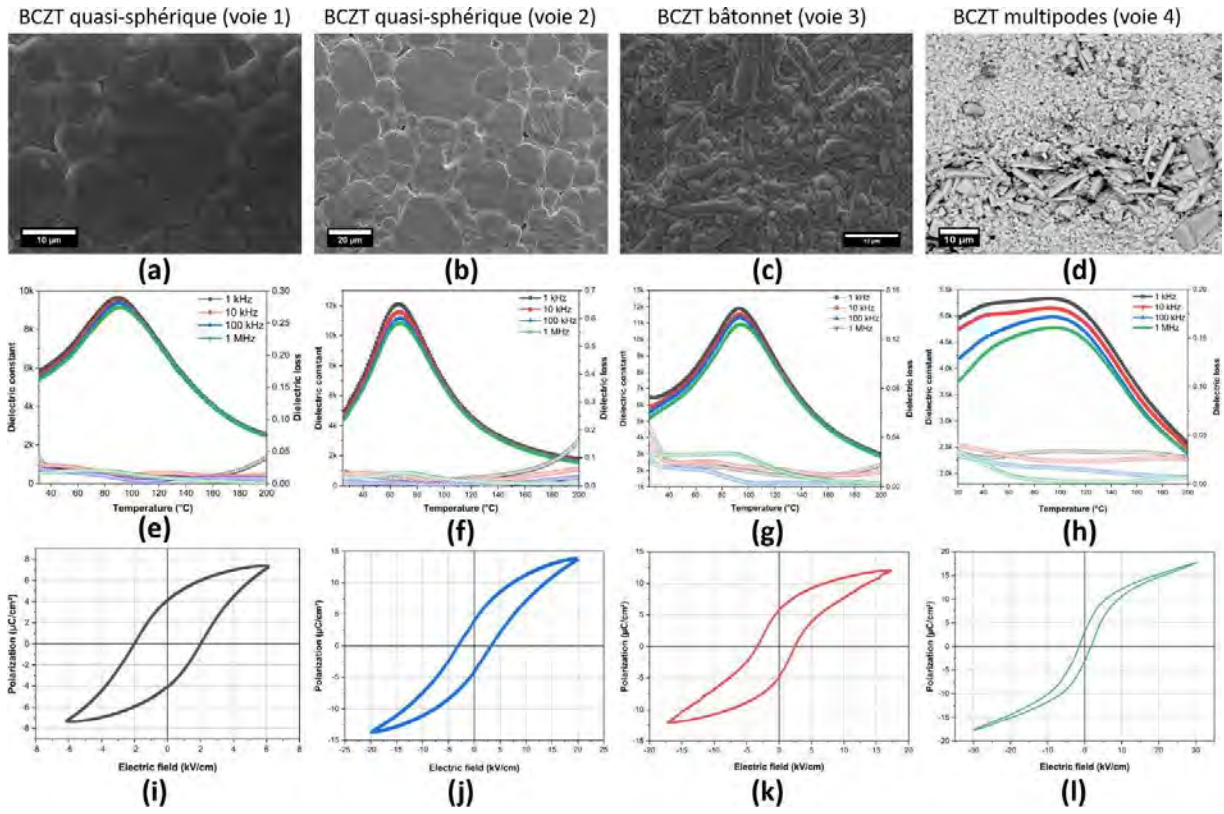


Figure 4. (a-d) Micrographies MEB-FEG, (e-h) propriétés diélectriques et (i-l) les boucles d'hystérésis P-E des céramiques BCZT frittées à 1250 °C/10 h. (Voie 1) nanoparticules BCZT issues par la synthèse solvothermale assistée par le surfactant SDS. (Voie 2) nanoparticules BCZT obtenues par la voie hydrothermale à 160 °C/24 h. (Voie 3) bâtonnets BCZT élaborés par la voie solvothermale assistée par le surfactant CTAB. (Voie 4) Multipodes de BCZT synthétisés par un traitement hydrothermal en deux étapes.

Afin de mieux illustrer les avantages du traitement hydrothermale à basse température pour l'élaboration de céramiques BCZT sans plomb (voie 2), le tableau 1 montre une étude comparative des propriétés diélectriques (constante diélectrique maximale ϵ_m et pertes diélectriques correspondantes : $\tan \delta$) et ferroélectriques (polarisation rémanente P_r , polarisation maximale P_{max} et le champ coercitif E_c) des céramiques BCZT élaborées par les différentes méthodes et conditions de synthèse utilisées, en fonction de leurs caractéristiques géométriques (taille moyenne des grains et la densité relative).

Du point de vue de la consommation d'énergie, la diminution importante de la température de synthèse des poudres BCZT pures et cristallines possédant propriétés diélectriques et ferroélectriques élevées, d'environ 1200 °C nécessaire dans le cas du procédé solide-solide à environ 150 °C dans le cas de la technique l'hydrothermale, soit une différence d'environ 950 °C, est un atout indéniable pour le développement des nanogénérateurs piézoélectriques. A cet égard, comme illustré dans le tableau 1,

les traitements hydrothermale et sol-gel-hydrothermale permettent la synthèse des céramiques BCZT avec des propriétés diélectriques et ferroélectriques améliorées. A titre d'exemple, la céramique B-160 possède une constante diélectrique maximale de 12085, supérieure à celle des céramiques BCZT élaborées par la méthode classique tout en conservant une faible perte diélectrique (tableau 1).

Comme déjà cité ci-dessus, l'amélioration de la densité d'énergie récupérable et de l'efficacité du stockage d'énergie exige des céramiques de grande rigidité diélectrique, de polarisation résiduelle réduite et de polarisation maximale élevée (équations (1), (2) et (3) ci-dessous) [17]. En d'autres termes, la densité de stockage de charge ($Q_c = P_{\max} - P_r$) dans un condensateur ferroélectrique calculée à partir des boucles d'hystérésis ferroélectrique à champ nul, doit être maximale pour obtenir un condensateur ferroélectrique de stockage d'énergie élevée [18]. Ces exigences sont rassemblées dans des céramiques BCZT élaborées par traitement hydrothermal. Le matériau B-160 obtenu selon cette voie peut résister à un champ électrique élevé (60 kV/cm) et possède une densité de stockage élevée $Q_c = 18,62 \mu\text{C}/\text{cm}^2$. Ainsi, nous pourrions conclure que la voie hydrothermale à basse température serait une méthode bénéfique à la conception des systèmes de récupération d'énergie avec des performances améliorées.

$$W_{tot} = \int_0^{P_{\max}} E dP, \quad (1)$$

$$W_{rec} = \int_{P_r}^{P_{\max}} E dP, \quad (2)$$

$$\eta(\%) = \frac{W_{rec}}{W_{tot}} \times 100, \quad (3)$$

Avec W_{tot} , W_{rec} et η sont la densité d'énergie totale, la densité d'énergie récupérée et l'efficacité énergétique, respectivement, tandis que P_{\max} , P_r , E et P représentent respectivement la polarisation maximale, la polarisation rémanente, le champ électrique et la polarisation.

Tableau 1. Comparaison des propriétés diélectriques et ferroélectriques des céramiques BCZT sans plomb rapportées dans cette étude avec d'autres rapportées dans la littérature en utilisant différentes conditions et méthodes de synthèse.

Conditions de synthèse			Taille des grains (μm)	Densité relative (%)	ϵ_m	$\tan \delta$	P_r	P_{max}	Q_c	E	Ref.
Méthode	Calcination	Frittage									
Hydrothermale	Non	1250 °C/10 h	22.1	97.1	12085	0.017	8.59	27.21	18.62	60	B-160
Sol-gel–hydrothermale	Non	1400 °C/2 h	-	95	9173	-	12.56	41.00	28.44	40	[19]
Hydrothermale	Non	1300 °C/3 h	12.09	-	7760	0.1	10.83	25.00	14.17	15	[16]
Solvothermale	1000 °C/4 h	1250 °C/10 h	6.6	96.4	9646	0.012	3.92	7.56	3.64	6.6	B-SDS
Solvothermale	1000 °C/4 h	1250 °C/10 h	-	95	11906	0.014	6.01	12.04	6.03	17	B_NR
Sol-gel	1000 °C/4 h	1420 °C/6 h	-	-	16480	0.015	11.60	17.76	6.16	30	[13]
Sol-gel	800 °C	1400 °C/2 h	-	95	8808	0.02	12.20	17.23	5.03	30	[20]
Sol-gel	1000 °C/4 h	1550 °C/2 h	10	97	20250	-	10.70	20.70	10.00	50	[21]
Sol-gel auto-combustion	1200 °C/2 h	1450 °C/2 h	3.4	97	-	-	7.38	15.50	8.12	20	[22]
Méthode Solide--solide	1250 °C/10 h	1500 °C/4 h	-	-	12181	-	6.32	25.35	19.03	106	[18]
Méthode Solide-solide	1200 °C	1350 °C	18.12	-	17120	0.023	10.20	19.71	9.51	60	[23]
Méthode Solide-solide	1150 °C/6 h	1400 °C/6 h	-	95	10615	-	8.21	18.53	10.32	50	[24]
Méthode Solide-solide	1147 °C/12 h	1427 °C/2 h	-	-	4762	0.022	4.35	6.53	2.18	8	[25]
Méthode Solide-solide	1350 °C et 1400 °C/6 h	1450 °C/4 h	-	94	-	-	5.48	16.06	10.58	21	[26]

III. Elaboration, caractérisation et propriétés des nanocomposites BCZT/PLA

En réponse au besoin de développer une nouvelle nanotechnologie respectueuse de l'environnement avec des propriétés diélectriques améliorées, de nouveaux matériaux composites céramiques/polymères nanostructurés combinant une faible perte diélectrique, une résistance à la rupture élevée du polymère et une constante diélectrique élevée des nanocharges céramiques sont de plus en plus étudiés pour des applications de stockage d'énergie [27,28]. Idéalement, les nanocharges en tant que particules contribuent à l'augmentation de la constante diélectrique du système nanocomposite par rapport au polymère en tant que matrice, sans compromettre les faibles facteurs de dissipation de la matrice polymère [29,30]. Plusieurs stratégies ont été utilisées pour maintenir les pertes diélectriques des nanocomposites à un faible niveau, y compris le développement de polymères à polarisation dipolaire rapide, l'amélioration de la dispersion des nanocharges et la fabrication de nanostructures avancées [31]. Comme ces défis incluent la nécessité de comprendre la chimie et la structure du polymère de charge, l'étude de leur interface devient un sujet de recherche attrayant [32,33]. La préparation des nanoparticules structurées cœur-coquille (core-shell) par polymérisation in situ initiée en surface a suscité un intérêt considérable en raison de ses avantages uniques : (i) les nanoparticules peuvent être bien encapsulées par des couches de polymère contrôlables en épaisseur, ce qui entraîne une réduction significative de l'énergie de surface des nanoparticules. (ii) les propriétés des nanocomposites peuvent être ajustées en adaptant les caractéristiques physiques de la coque polymère et/ou l'interaction entre la coque polymère et la matrice polymère [6,34–38].

Dans ce paragraphe, nous proposons d'élaborer des nanocomposites BCZT/PLA en dispersant le BCZT sous forme de charges dans le PLA en tant que matrice et d'étudier les propriétés en fonction de la fraction volumique de BCZT. Dans un premier temps, nous avons choisi le matériau B-160 sans plomb et sans calcination préalable comme charge pour les raisons suscitées. En outre, la morphologie de B-160 qui sera notée par la suite B_NP, est quasi-sphérique et pourrait être utilisée comme référence pour étudier l'influence de la morphologie sur les propriétés résultantes. Les nanopoudres B_NP ont été fonctionnalisées via la structuration core-shell en utilisant une couche de polydopamine (PDA) (Figure 5). Le succès de la structuration core-shell a été vérifié par les micrographies STEM-HAADF de la Figure 6a et b. Elles mettent en évidence le revêtement réussi des nanoparticules B_NP par PDA avec une épaisseur de coquille d'environ 15 à 25 nm.

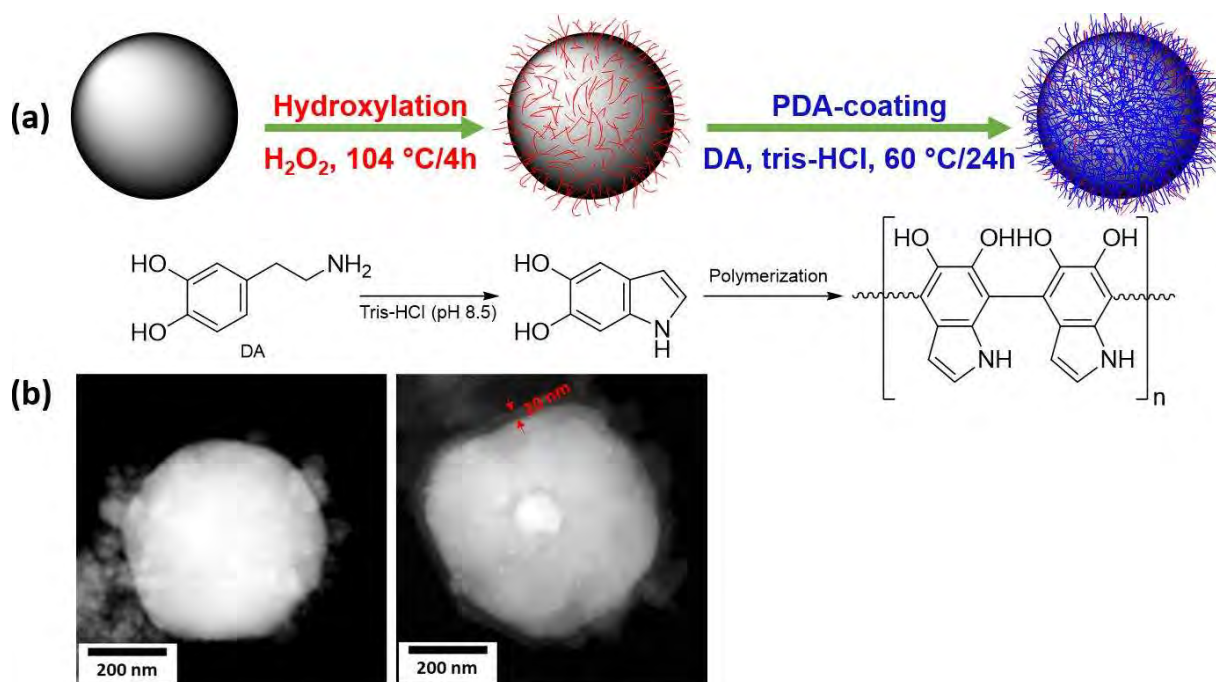


Figure 5. (a) Illustration schématique de la préparation des nanocharges B_NP@PDA structurées core-shell. (b) Micrographies STEM–HAADF d’une nanoparticule B_NP (à gauche) et nanoparticule B_NP@PDA (à droite) montrant l’épaisseur de couche PDA avec les lignes rouges.

Par la suite, des nanocomposites à haute permittivité diélectrique à base d'acide polylactique biodégradable (PLA) et des différentes nanocharges inorganiques de formes et d'arrangements variés (sphériques, bâtonnets et fils) ont été fabriqués avec succès. Les effets de la permittivité, du facteur de forme, de la nanocharge et de la structuration cœur-coquille sur la constante diélectrique effective du nanocomposite ont été explorés par une approche à la fois expérimentale et théorique. Nous avons constaté que l’augmentation de la permittivité effective des nanocomposites B_NP/PLA et B_NP@PDA/PLA s’accompagne d’une augmentation des pertes diélectriques. Cependant, les pertes diélectriques maximales restent relativement faibles au vu de l’augmentation importante de la permittivité (Figure 6). Il est à noter que l’augmentation de la permittivité effective, relativement élevée, mesurée reste faible par rapport à la valeur élevée attendue de la permittivité de la poudre B_NP quasi sphérique. Par ailleurs, et de manière surprenante, la fonctionnalisation B_NP@PDA n’a pas amélioré d’une façon significative les propriétés diélectriques des nanocomposites (permittivité effective et perte diélectrique) mais elle a un effet significatif à la fois sur les densités d’énergie totale et récupérée comme il sera décrit par la suite.

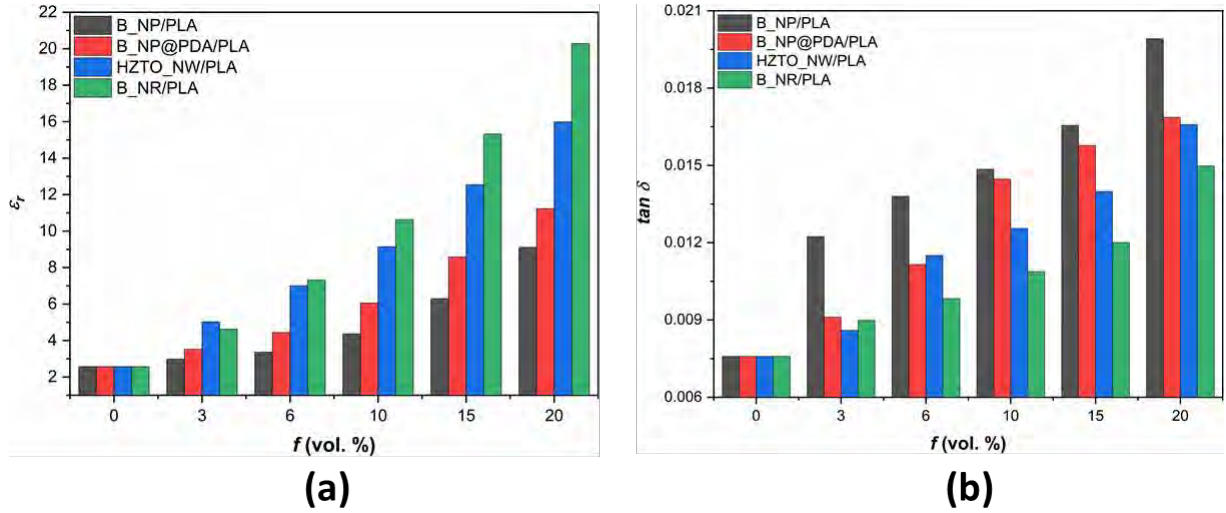


Figure 6. Effet de la fraction volumique des charges B_NP, B_NP @ PDA, HZTO_NW et B_NR sur les (a) ϵ_r et (b) $\tan \delta$ des nanocomposites à base de PLA.

Egalement, il est montré que les permittivités effectives mesurées montrent une dépendance linéaire avec la fraction volumique de BCZT (Figure 7). Ceci s'explique simplement par le fait que les domaines sont spatialement séparés et que les interactions électrostatiques entre chaque inclusion et ses voisins sont relativement faibles lorsque la fraction volumique des charges est inférieure au seuil de percolation. En effet, lorsque les inclusions sphériques ne se touchent pas, il existe une permittivité critique de la céramique à partir de laquelle la permittivité effective n'augmente pas même pour les céramiques à hautes permittivités. Cela est attribué au fait que le champ électrique a du mal à pénétrer dans les inclusions diélectriques déconnectées lorsque le contraste électrique entre B_NP et PLA devient élevé. En modifiant la forme des inclusions par rapport à la sphère et/ou lorsque la distribution des inclusions n'est pas aléatoire, le seuil de percolation diminue à mesure qu'il devient plus probable que les inclusions se touchent. Afin de pouvoir évaluer l'incidence du facteur de forme des charges sur les propriétés diélectriques des nanocomposites, nous avons suivi l'évolution de la permittivité effective théorique et expérimentale des nanocomposites en fonction du facteur de forme et de la fraction volumique de la charge B_NP (Figure 7). De manière très intéressante, les données expérimentales peuvent être ajustées avec des valeurs de permittivité B_NP très différentes mais des valeurs de facteur de forme relativement proches, voir par exemple les couples ($\epsilon_{B_NP} = 10000$, $\frac{c}{a} = 3.9$) et ($\epsilon_{B_NP} = 200$, $\frac{c}{a} = 5.5$). Il est à noter qu'une diminution drastique de la permittivité B_NP peut être compensée par une augmentation relativement faible du facteur de forme de B_NP. En conséquence, un paradigme entre la constante diélectrique et le facteur de forme de la charge émerge. Pour aller plus loin, deux types de charges céramiques possédant des propriétés différentes. Les nano-batônnets B_NR ayant une constante diélectrique élevée de 11906 et un facteur de forme moyen de 10, d'une part et les nanofils HZTO_NW possédant une constante diélectrique faible de 300 et un facteur de

forme élevé de 50, d'autre part. Ces charges, de même fraction volumique, ont été intégrées dans la matrice PLA et les résultats obtenus ont montré que l'augmentation du facteur de forme engendre une augmentation de la valeur de la permittivité diélectrique du nanocomposite (Figure 7). Ainsi, on peut conclure que l'amélioration des propriétés diélectriques d'un nanocomposite à base de charge de facteur de forme élevé est due à un seuil de percolation plus faible.

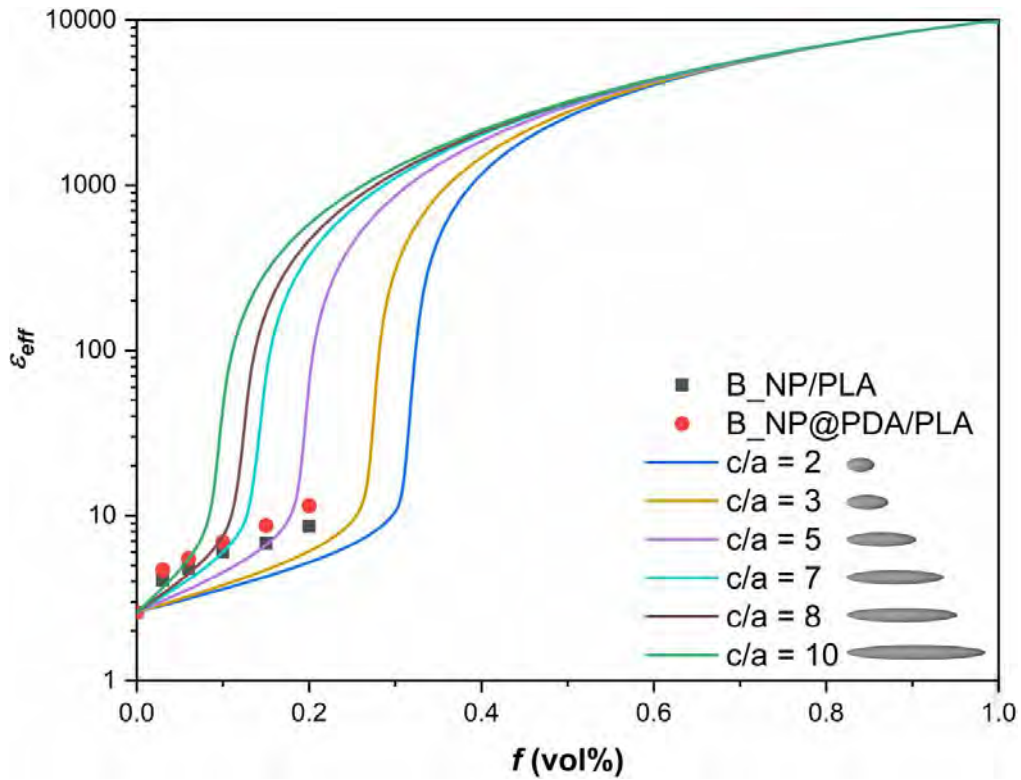


Figure 7. Evolution de la permittivité effective du nanocomposite B_NP/PLA en fonction du facteur de forme de la charge B_NP. Pour tous les calculs, la permittivité de la céramique B_NP a été considérée comme égale à 10000.

Les performances de stockage d'énergie des nanocomposites à base de PLA chargés avec les différentes poudres (quasi-sphériques avec et sans PDA, bâtonnets et fils) ont été évaluées à l'aide des boucles D-E (Figure 8). Une densité de stockage d'énergie élevée et une densité d'énergie récupérée de 3,63 et 1,80 J/cm³, respectivement, ont été obtenues dans des nanocomposites à base des charges en forme de bâtonnets. Par conséquent, l'utilisation des nanocharges avec un facteur de forme élevé et une constante diélectrique élevée s'avère bénéfique pour améliorer les performances de stockage d'énergie des nanocomposites à base de PLA comme illustré sur la Figure 9. Ainsi, les propriétés diélectriques résultantes et les performances de stockage d'énergie dans le nanocomposite céramique/polymère sont basées sur un compromis entre la constante diélectrique et le rapport de forme de la céramique.

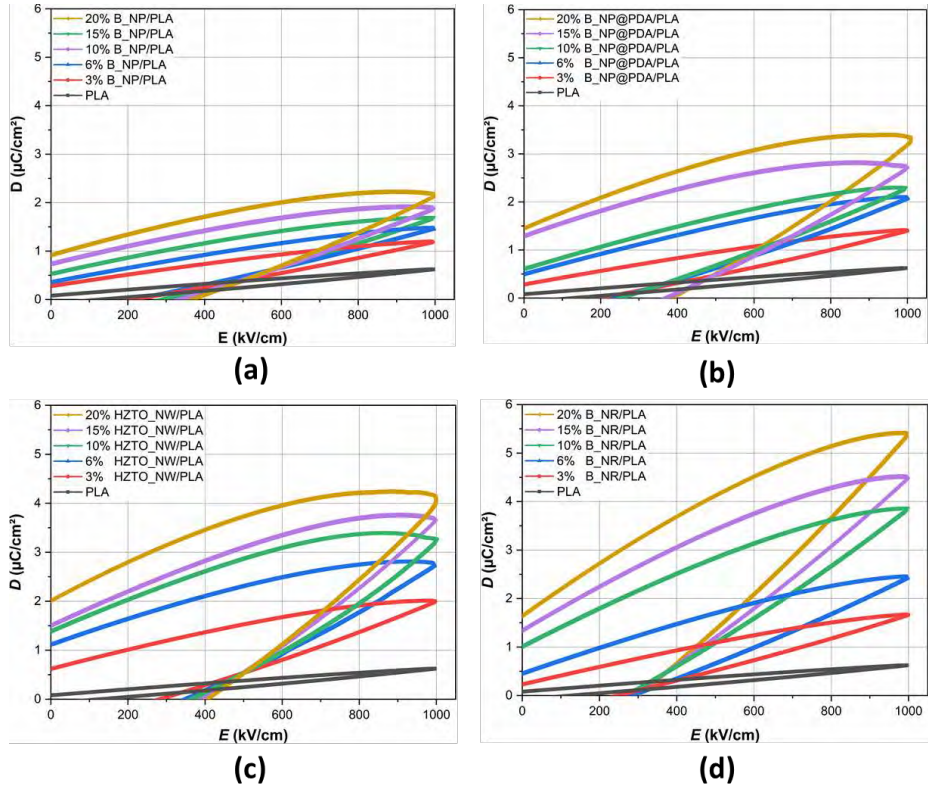


Figure 8. Boucles D-E des nanocomposites (a) B_NP/PLA, (b) B_NP@PDA/PLA, (c) HZTO_NW/PLA et (d) B_NR/PLA.

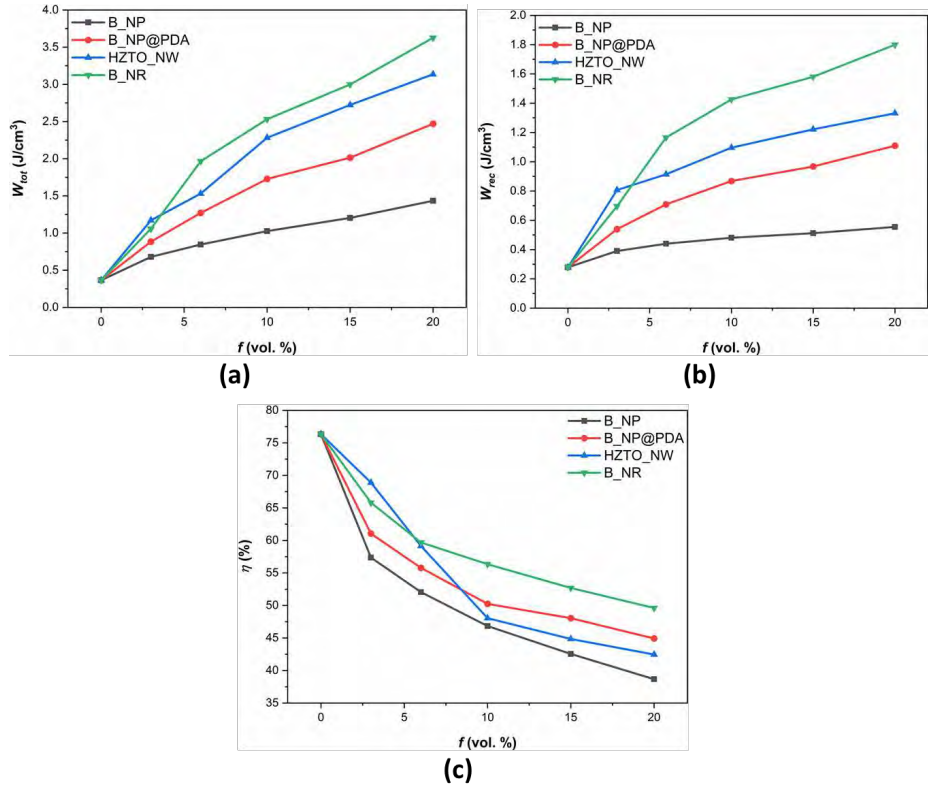


Figure 9. Les densités d'énergie (a) totale, (b) récupérée et (c) l'efficacité de stockage d'énergie des films nanocomposites à base de PLA.

A la fin de ce travail, l'aspect récupération (et conversion) d'énergie dans les nanocomposites BCZT/PLA a été étudié en utilisant le concept des nanogénérateurs piézoélectriques pour convertir l'énergie mécanique ambiante en énergie électrique. De même, les performances de sortie sous différents mouvements du corps humain ont été testées et la faisabilité de piloter des composants électroniques commerciaux a été vérifiée en utilisant le nanogénérateur piézoélectrique bio-flexible basé sur le nanocomposite 20% vol B_NP@PDA/PLA.

Malgré les excellentes propriétés piézoélectriques des céramiques, certains de leurs inconvénients tels que la rigidité, la fragilité, la toxicité, et le manque de flexibilité de conception limitent leur application dans les dispositifs de récupération d'énergie. Par contre, les polymères piézoélectriques constituent un meilleur candidat pour ces applications en raison de leur flexibilité mécanique, un traitement plus rapide, un coût de fabrication plus faible et la biocompatibilité de certains piézopolymères comme l'acide polylactique (PLA). Par conséquent, les composites piézoélectriques céramique/polymère suscite un engouement important du fait qu'ils combinent les avantages des piézocéramiques et des piézopolymères (la flexibilité mécanique, une tension appropriée avec une puissance de sortie suffisante, un coût de fabrication inférieur et un traitement rapide par rapport aux composites à base de céramique.

IV. Nanogénérateur piézoélectrique à base de film nanocomposite sans plomb pour la récupération d'énergie biomécanique

En raison de leurs robustesse et performances de sortie améliorées, les nanogénérateurs piézoélectriques (NGP) à base de nanocomposites céramiques/polymères sont au centre de développement de la nouvelle génération des sources mécaniques de récupération d'énergie [39–42]. Ces NGP pourraient piloter les systèmes de santé auto-alimentés tels que le moniteur et le stimulateur cardiaques, le moniteur de débit sanguin et le moniteur biomédical en temps réel [43–47].

Dans cette étude, un nanogénérateur de nanocomposite bio-flexible (BF-NGP) a été conçu en utilisant le film nanocomposite 20% vol B_NP@PDA/PLA. La tension en circuit ouvert (V_{OC}) et le courant de court-circuit (I_{SC}) ont été évalués. L'illustration schématique et l'image du dispositif générateur flexible BF-NGP sont présentées sur la Figure 10.



Figure 10. (a) Illustration schématique du générateur nanocomposite préparé et (b) image du dispositif flexible BF-NGP à base du nanocomposite 20% B_NP@PDA /PLA.

Comme la réponse piézoélectrique est la propriété clé des NGP, elle a été évaluée par la microscopie à force piézoélectrique (PFM) avant et après l'incorporation des nanoparticules B_NP@PDA dans la matrice PLA. La PFM est basée sur la détection d'une réponse piézoélectrique locale dans le matériau ferroélectrique à travers l'effet piézoélectrique inverse. Des réponses piézoélectriques représentées par les zones brillantes des figures 11 et 12 ont été détectées dans les NGPs avant et après l'incorporation des nanocharge BCZT@PDA.

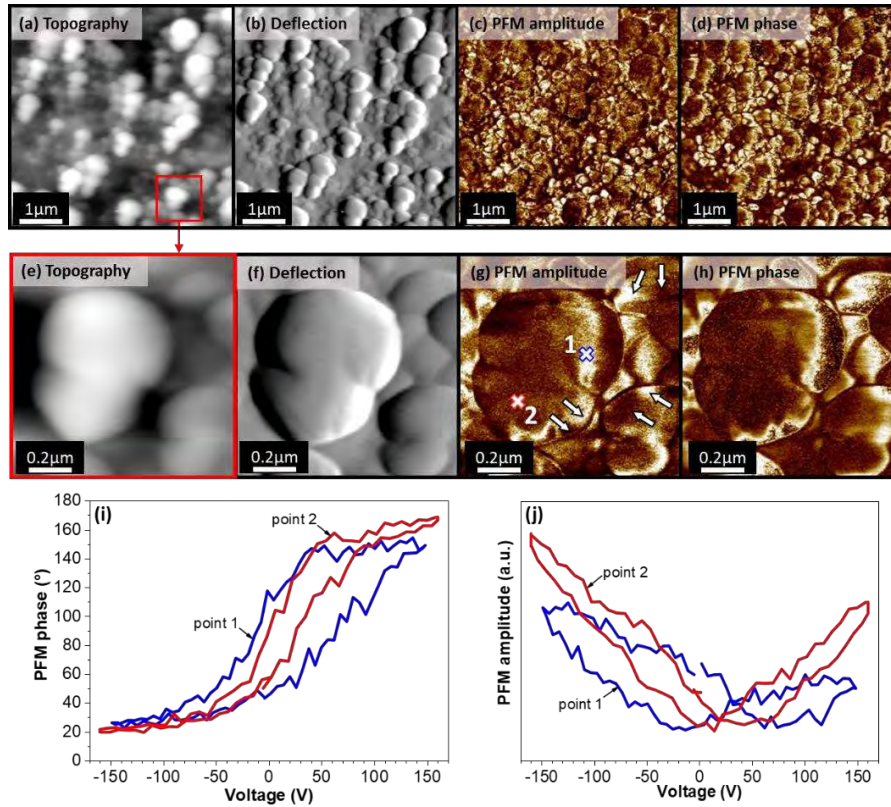


Figure 11. (a, e) La topographie, (b, f) déflection et (c, g) amplitude PFM hors plan, (d, h) images de phase des nanoparticules B_NP@PDA. Les boucles d'hystérésis locales de (i) phase et (j) d'amplitude PFM mesurées aux deux points 1 et 2 repérés par des croix sur l'image (g). Dans les deux images (i et j), un deuxième cycle est effectué.

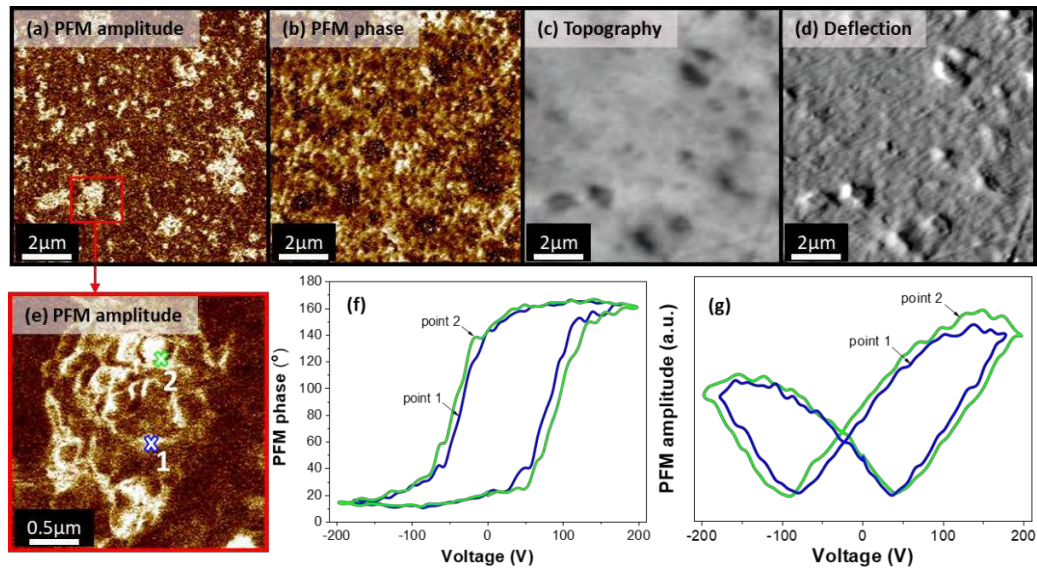


Figure 12. (a) Amplitude PFM hors plan, (b) images de phase avec (c) la topographie et (d) déflexion du film 20% B_NP@PDA/PLA. Dans l'image (a), les régions claires sont les îlots de poudre B_NP@PDA noyés dans la matrice PLA qui est plus sombre. Le grand grossissement d'un tel îlot est montré dans l'image (e). Les images (f) et (g) montrent la phase et l'amplitude des boucles d'hystérésis locales, respectivement, mesurées par PFM sur les deux points, marquées par les croix 1 et 2 dans l'image (e). Dans les deux images (f et g), un deuxième cycle est effectué.

En général, les NGPs sont utilisés pour récupérer de l'énergie mécanique dans une gamme de fréquences relativement basses comme les activités humaines, les vibrations mécaniques, etc. Dans ce cas, la contrainte mécanique joue un rôle essentiel dans la génération de la tension de sortie car la déformation de la structure flexible dépend de la contrainte mécanique appliquée. Nous avons évalué la contrainte mécanique issue par deux types d'impartitions humaines (le tapotement du doigt et le frappe à la main à fréquences fixes). Les contraintes mécaniques sous le tapotement du doigt et le la frappe à la main ont été estimées à 15 kPa et 177 kPa, respectivement.

Le BF-NGP conçu a permis de générer une tension en circuit ouvert de 14,4 V et un courant de court-circuit de 0,55 μ A par tapotement du doigt (Figure 13a, b). De plus, le BF-NGP a démontré une durabilité remarquable, une grande tenue mécanique et une tension de sortie stable, même après 14000 cycles à haute fréquence (Figure 13c). La densité de puissance maximale obtenue était d'environ 7,54 mW/cm³ à une faible charge résistive de 3,5 M Ω (Figure 13d). La faisabilité du BF-NGP a été vérifiée en déclenchant l'électronique commerciale (charge de condensateurs et allumage d'une LED) (Figure 14). Le BF-NGP pourrait charger un condensateur de 1 μ F pour stocker une énergie de 3,92 μ J en 115 s sous un léger tapotement du doigt. Ce travail démontre qu'une piézocéramique sans plomb associée à un piézopolymère biodégradable peut conduire à la conception des nanogénérateurs piézoélectriques bio-flexibles aux performances avancées et notamment utiles dans les dispositifs auto-alimentés.

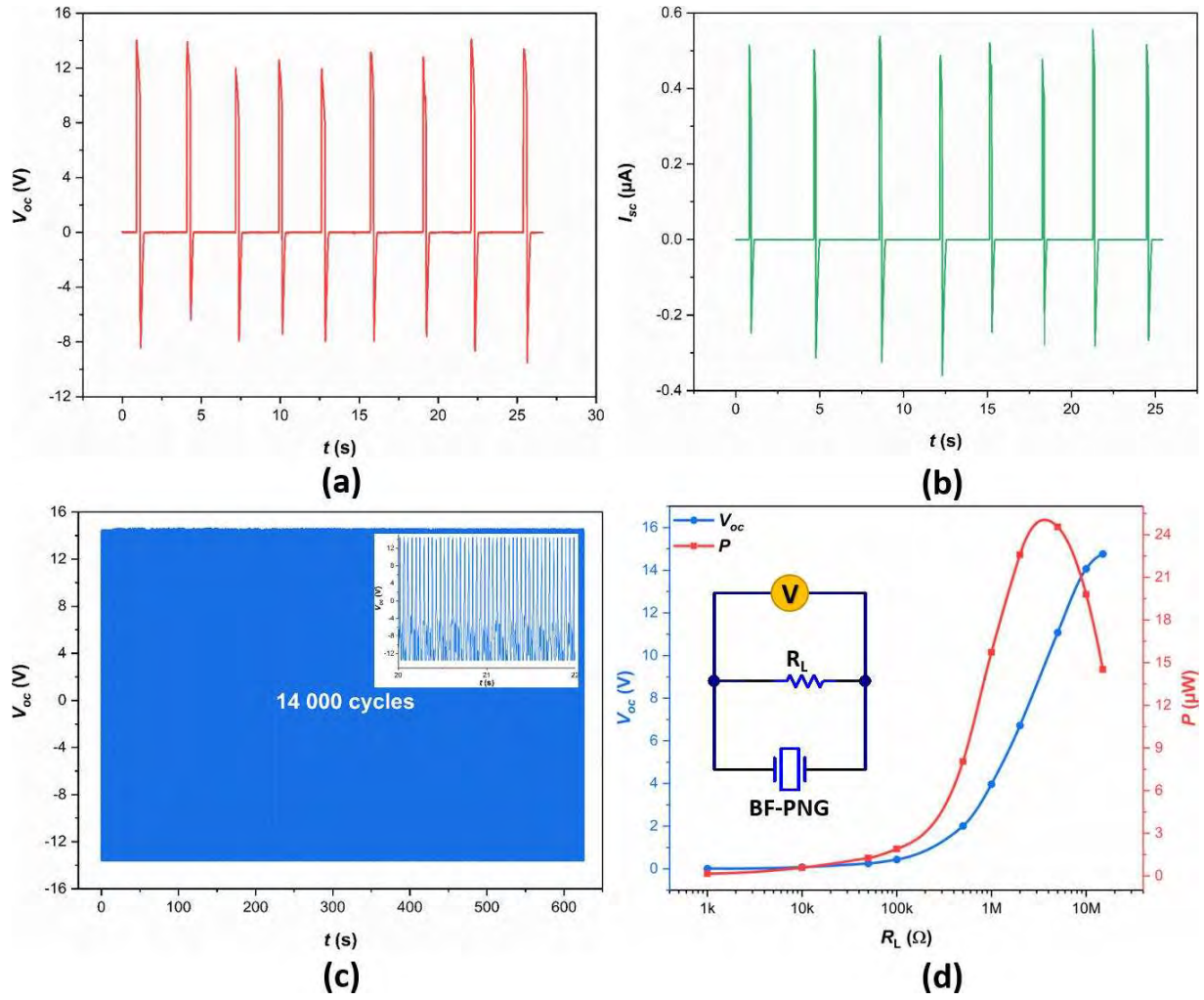


Figure 13. (a) La tension en circuit ouvert g n r e et (b) le courant de court-circuit du BF-NGP sous pression r p t e du doigt. (c) La stabilit  de la tension de sortie du dispositif BF-NGP sous 14000 cycles de tapotement sous une machine   coudre (l'encart ins r  montre une vue agrandie de la stabilit  de la tension). (d) La tension de sortie et la densit  de puissance g n r es par le BF-NGP   travers diverses r sistances (l'encart ins r  montre le sch ma de principe de la tension de sortie collect e).

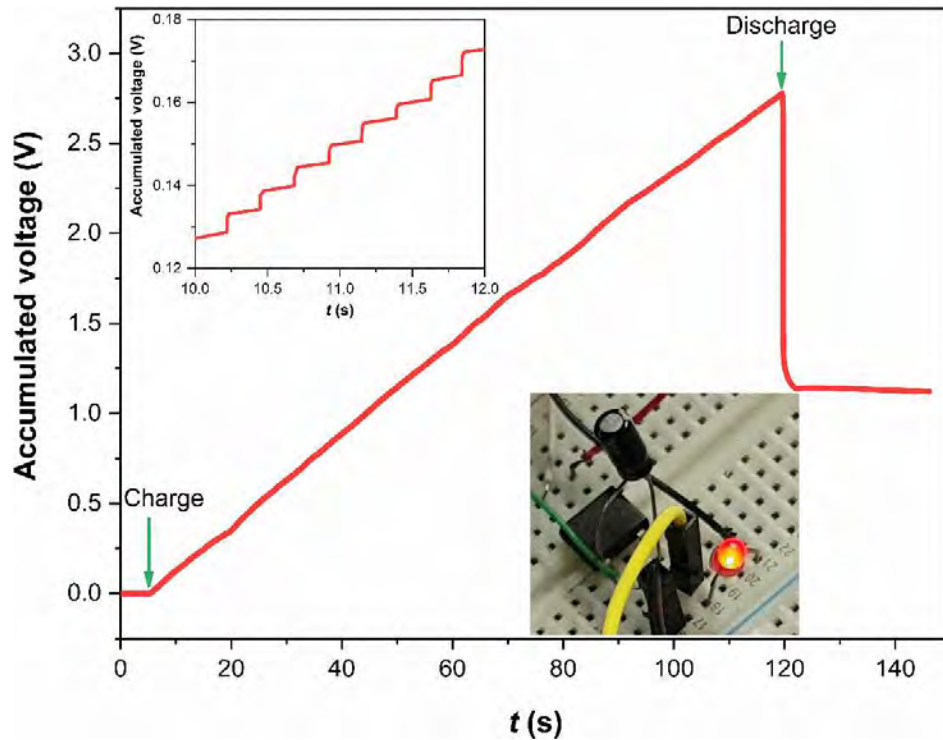


Figure 14. La courbe de charge de la tension de sortie d'un condensateur commercial de 1 μF par le BF-NGP sous tapotement à une fréquence de 4 Hz. L'encart supérieur montre un zoom des étapes de tension pendant la charge du condensateur. L'encart inférieur représente une photographie numérique d'une LED rouge alimentée par le condensateur chargé.

V. Conclusions et perspectives

Les technologies de stockage et de récupération d'énergie souffrent des performances modérées, de faible flexibilité et d'utilisation des composés non environnementaux. Ce travail a pour objectif la conception des nanocomposites céramiques/polymères flexibles et écologiques pour améliorer le stockage et la récupération d'énergie. Des procédés de synthèses contrôlées ont été utilisés pour élaborer les matériaux ferroélectriques BCZT avec différentes tailles et formes (nanoparticules sphériques, nanorods, morphologies anisotropes) et nanofils HZTO. Les propriétés diélectriques et ferroélectriques des céramiques frittées BCZT ont été examinées en fonction de la taille et de la forme des grains des céramiques. Nous avons constaté que la céramique BCZT à particules quasi-sphériques issue de la voie 2 et élaborée à 160 °C révélait des propriétés diélectriques et ferroélectriques améliorées par rapport aux autres céramiques BCZT.

Par la suite, des particules quasi-sphériques BCZT, des nanorods BCZT et des nanofils HZTO ont été incorporées dans la matrice de polymère PLA biodégradable. Les effets de la forme, de la disposition, de la constante diélectrique et du facteur de forme ont été étudiés en utilisant des modèles de la constante diélectrique effective des nanocomposites. Le paradigme entre la constante diélectrique

et le facteur de forme a été révélé par l'incorporation dans le PLA des nanorods BCZT possédant une constante diélectrique et un facteur de forme élevés, et des nanofils HZTO ayant un facteur de forme plus élevé mais une constante diélectrique plus faible. Nous avons constaté que pour améliorer les propriétés diélectriques du nanocomposite, il n'est pas nécessaire d'utiliser des charges céramiques à haute permittivité mais plutôt contrôler mieux leur géométrie dans le composite. Par la suite, les performances de stockage d'énergie (densité d'énergie totale, densité d'énergie récupérée et efficacité énergétique) des nanocomposites à base de PLA ont été évaluées. Une densité de stockage d'énergie élevée de $3,63 \text{ J/cm}^3$ et une densité d'énergie récupérée de $1,80 \text{ J/cm}^3$ ont été obtenues dans des nanocomposites à base de charges en forme de bâtonnets. Les résultats obtenus sont supérieurs à ceux rapportés dans les composites à base de matériaux écologiques et non-toxiques.

L'aspect de récupération d'énergie a été étudié en utilisant le concept des nanogénérateurs piézoélectriques pour convertir l'énergie mécanique ambiante en énergie électrique. A cet effet, un nanogénérateur piézoélectrique bio-flexible (BF-NGP) basé sur un film nanocomposite 20% BCZT@PDA/PLA a été conçu. Le BF-NGP pourrait générer une tension en circuit ouvert et un courant de court-circuit de 14,4 V et 0,55 μA , respectivement, sous un léger tapotement du doigt. En outre, une durabilité remarquable, une bonne tenue mécanique et une tension de sortie stable, même après 14000 cycles à haute fréquence, ont été démontrées dans le BF-NGP. De plus, une densité de puissance maximale notable de $7,54 \text{ mW/cm}^3$ à une faible charge résistive de $3,5 \text{ M}\Omega$ a été obtenue dans le BF-NGP par comparaison à celles d'autres nanocomposites céramique/polymère de la littérature. La faisabilité du BF-NGP a été testée en pilotant l'électronique commerciale (charge de condensateurs et allumage d'une LED). Plus intéressant encore, le BF-NGP pourrait piloter un condensateur de $1 \mu\text{F}$ pour stocker de l'énergie de $3,92 \mu\text{J}$ en 115 s sous un léger tapotement du doigt, ce qui le rend applicable aux capteurs et actionneurs biomédicaux tels que les stimulateurs cardiaques. En conclusion, ce travail démontre que la piézocéramique BCZT sans plomb en combinaison avec le piézopolymère biodégradable PLA peut conduire à une conception de nanocomposite bio-flexible avec des performances améliorées de stockage et de récupération d'énergies pour des applications dans des dispositifs auto-alimentés.

Dans ce travail de recherche, nous avons mis principalement l'accent sur les essais expérimentaux pour rechercher des corrélations entre la taille, la distribution de taille, la forme, la disposition et le facteur de forme des nanoparticule BCZT et les propriétés diélectriques et ferroélectriques des céramiques frittées et des nanocomposites. En fonction des résultats obtenus à l'issue de ce travail, les perspectives suivantes pourront être envisagées :

- l'étude de l'effet piézoélectrique direct et indirect des céramiques BCZT en vue d'améliorer les performances des nanocomposites BCZT/PLA pour les applications des condensateurs intégrés et des nanogénérateurs piézoélectriques,
- la conception des nanocomposites à base de nanofils BCZT_NW /PLA et étude de leurs propriétés diélectriques et de stockage d'énergie,
- l'étude des effets de l'orientation et du facteur de forme des charge B_NR et HZTO_NW sur les performances de stockage d'énergie des nanocomposites,
- pour l'application pratique des condensateurs de stockage d'énergie, la stabilité en température du stockage d'énergie récupérée des nanocomposites à base de PLA pourrait être aussi intéressante à étudier, parallèlement à la densité de puissance de ces nanocomposites.
- En outre, il est recommandé de modéliser et optimiser l'architecture du nanogénérateur piézoélectrique pour une meilleure conversion d'énergie mécanique.
- Enfin, pour des applications plus poussées, la génération d'énergie in vitro et par l'activité corporelle naturelle et l'environnement physiologique serait aussi importante à étudier pour les dispositifs implantables autonomes.

VI. Bibliographie

- [1] L. Yang, X. Kong, F. Li, H. Hao, Z. Cheng, H. Liu, J.F. Li, S. Zhang, Perovskite lead-free dielectrics for energy storage applications, *Prog. Mater. Sci.* 102 (2019) 72–108. doi:10.1016/j.pmatsci.2018.12.005.
- [2] Q. Chi, G. Liu, C. Zhang, Y. Cui, X. Wang, Q. Lei, Microstructure and dielectric properties of BZT-BCT/PVDF nanocomposites, *Results Phys.* 8 (2018) 391–396. doi:10.1016/j.rinp.2017.12.052.
- [3] L. Yao, Z. Pan, J. Zhai, G. Zhang, Z. Liu, Y. Liu, High-energy-density with polymer nanocomposites containing of SrTiO₃ nanofibers for capacitor application, *Compos. Part A Appl. Sci. Manuf.* 109 (2018) 48–54. doi:10.1016/j.compositesa.2018.02.040.
- [4] X. Huang, B. Sun, Y. Zhu, S. Li, P. Jiang, High-k polymer nanocomposites with 1D filler for dielectric and energy storage applications, *Prog. Mater. Sci.* 100 (2019) 187–225. doi:10.1016/j.pmatsci.2018.10.003.
- [5] W. Xia, Y. Yin, J. Xing, Z. Xu, The effects of double-shell organic interfaces on the dielectric and energy storage properties of the P(VDF-CTFE)/BT@HBP@PDA-Ag nanocomposite films, *Results Phys.* 11 (2018) 877–884. doi:10.1016/j.rinp.2018.10.046.
- [6] K. Bi, M. Bi, Y. Hao, W. Luo, Z. Cai, X. Wang, Y. Huang, Ultrafine core-shell BaTiO₃@SiO₂ structures for nanocomposite capacitors with high energy density, *Nano Energy.* 51 (2018) 513–523. doi:10.1016/j.nanoen.2018.07.006.
- [7] Z.H. Shen, J.J. Wang, Y. Lin, C.W. Nan, L.Q. Chen, Y. Shen, High-Throughput Phase-Field Design of High-Energy-Density Polymer Nanocomposites, *Adv. Mater.* 30 (2018) 1704380. doi:10.1002/adma.201704380.
- [8] C. Zhao, H. Wu, F. Li, Y. Cai, Y. Zhang, D. Song, J. Wu, X. Lyu, J. Yin, D. Xiao, J. Zhu, S.J. Pennycook, Practical High Piezoelectricity in Barium Titanate Ceramics Utilizing Multiphase Convergence with Broad Structural Flexibility, *J. Am. Chem. Soc.* 140 (2018) 15252–15260. doi:10.1021/jacs.8b07844.
- [9] V. V. Shvartsman, D.C. Lupascu, Lead-free relaxor ferroelectrics, *J. Am. Ceram. Soc.* 95 (2012) 1–26. doi:10.1111/j.1551-2916.2011.04952.x.
- [10] N.A. Hoque, P. Thakur, P. Biswas, M.M. Saikh, S. Roy, B. Bagchi, S. Das, P.P. Ray, Biowaste crab shell-extracted chitin nanofiber-based superior piezoelectric nanogenerator, *J. Mater.*

Chem. A. 6 (2018) 13848–13858. doi:10.1039/c8ta04074e.

- [11] C. Baek, J.H. Yun, H.S. Wang, J.E. Wang, H. Park, K. Il Park, D.K. Kim, Enhanced output performance of a lead-free nanocomposite generator using BaTiO₃ nanoparticles and nanowires filler, *Appl. Surf. Sci.* 429 (2018) 164–170. doi:10.1016/j.apsusc.2017.06.109.
- [12] W. Liu, X. Ren, Large piezoelectric effect in Pb-free ceramics, *Phys. Rev. Lett.* 103 (2009) 257602. doi:10.1103/PhysRevLett.103.257602.
- [13] Z. Wang, J. Wang, X. Chao, L. Wei, B. Yang, D. Wang, Z. Yang, Synthesis, structure, dielectric, piezoelectric, and energy storage performance of (Ba_{0.85}Ca_{0.15})(Ti_{0.9}Zr_{0.1})O₃ ceramics prepared by different methods, *J. Mater. Sci. Mater. Electron.* 27 (2016) 5047–5058. doi:10.1007/s10854-016-4392-x.
- [14] J. Shi, R. Zhu, X. Liu, B. Fang, N. Yuan, J. Ding, H. Luo, Large electrocaloric effect in lead-free(Ba_{0.85}Ca_{0.15})(Zr_{0.1}Ti_{0.9})O₃ ceramics prepared via citrate route, *Materials (Basel)*. 10 (2017) 1093. doi:10.3390/ma10091093.
- [15] Z. Hanani, D. Mezzane, M. Amjoud, S. Fourcade, A.G. Razumnaya, I.A. Luk'yanchuk, M. Gouné, Enhancement of dielectric properties of lead-free BCZT ferroelectric ceramics by grain size engineering, *Superlattices Microstruct.* 127 (2019) 109–117. doi:10.1016/j.spmi.2018.03.004.
- [16] S. Hunpratub, S. Maensiri, P. Chindaprasirt, Synthesis and characterization of Ba_{0.85}Ca_{0.15}Ti_{0.9}Zr_{0.1}O₃ ceramics by hydrothermal method, *Ceram. Int.* 40 (2014) 13025–13031. doi:10.1016/j.ceramint.2014.04.166.
- [17] Y. Huang, F. Li, H. Hao, F. Xia, H. Liu, S. Zhang, (Bi_{0.51}Na_{0.47})TiO₃ based lead free ceramics with high energy density and efficiency, *J. Mater.* 5 (2019) 385–393. doi:10.1016/j.jmat.2019.03.006.
- [18] V.S. Puli, D.K. Pradhan, I. Coondoo, N. Panwar, S. Adireddy, S. Luo, R.S. Katiyar, D.B. Chrisey, Observation of large enhancement in energy-storage properties of lead-free polycrystalline 0.5BaZr_{0.2}Ti_{0.8}O₃-0.5Ba_{0.7}Ca_{0.3}TiO₃ ferroelectric thin films, *J. Phys. D: Appl. Phys.* 52 (2019) 255304. doi:10.1088/1361-6463/ab161a.
- [19] X. Ji, C. Wang, S. Zhang, R. Tu, Q. Shen, J. Shi, L. Zhang, Structural and electrical properties of BCZT ceramics synthesized by sol–gel-hydrothermal process at low temperature, *J. Mater. Sci. Mater. Electron.* 30 (2019) 12197–12203. doi:10.1007/s10854-019-01578-5.
- [20] X. Ji, C. Wang, S. Li, S. Zhang, R. Tu, Q. Shen, J. Shi, L. Zhang, Structural and electrical

- properties of BCZT ceramics synthesized by sol–gel process, *J. Mater. Sci. Mater. Electron.* 29 (2018) 7592–7599. doi:10.1007/s10854-018-8751-7.
- [21] E. Chandrakala, J. Paul Praveen, B.K. Hazra, D. Das, Effect of sintering temperature on structural, dielectric, piezoelectric and ferroelectric properties of sol-gel derived BZT-BCT ceramics, *Ceram. Int.* 42 (2016) 4964–4977. doi:10.1016/j.ceramint.2015.12.009.
- [22] P. Jaimeewong, M. Promsawat, A. Watcharapasorn, S. Jiansirisomboon, Comparative study of properties of BCZT ceramics prepared from conventional and sol-gel auto combustion powders, *Integr. Ferroelectr.* 175 (2016) 25–32. doi:10.1080/10584587.2016.1199913.
- [23] K. Xu, P. Yang, W. Peng, L. Li, Temperature-stable MgO-doped BCZT lead-free ceramics with ultra-high energy storage efficiency, *J. Alloys Compd.* 829 (2020) 154516. doi:10.1016/j.jallcom.2020.154516.
- [24] X. Wang, P. Liang, X. Chao, Z. Yang, Dielectric Properties and Impedance Spectroscopy of MnCO₃-Modified (Ba_{0.85}Ca_{0.15})(Zr_{0.1}Ti_{0.9})O₃ Lead-Free Ceramics, *J. Am. Ceram. Soc.* 98 (2015) 1506–1514. doi:10.1111/jace.13481.
- [25] H. Kaddoussi, A. Lahmar, Y. Gagou, B. Manoun, J.N. Chotard, J.L. Dellis, Z. Kutnjak, H. Khemakhem, B. Elouadi, M. El Marssi, Sequence of structural transitions and electrocaloric properties in (Ba_{1-x}Cax)(Zr_{0.1}Ti_{0.9})O₃ceramics, *J. Alloys Compd.* 713 (2017) 164–179. doi:10.1016/j.jallcom.2017.04.148.
- [26] S. Patel, D. Sharma, A. Singh, R. Vaish, Enhanced thermal energy conversion and dynamic hysteresis behavior of Sr-added Ba_{0.85}Ca_{0.15}Ti_{0.9}Zr_{0.1}O₃ ferroelectric ceramics, *J. Mater.* 2 (2016) 75–86. doi:10.1016/j.jmat.2016.01.002.
- [27] L. Zhu, Exploring strategies for high dielectric constant and low loss polymer dielectrics, *J. Phys. Chem. Lett.* 5 (2014) 3677–3687. doi:10.1021/jz501831q.
- [28] C. Wu, X. Huang, L. Lv, G. Chen, J. Yu, L. Xie, P. Jiang, High-permittivity and low-dielectric-loss polymer composites based on TiO₂-nanorod functionalized carbon nanotubes, in: *Proc. 2012 IEEE Int. Conf. Cond. Monit. Diagnosis, C. 2012, IEEE, 2012: pp. 347–349.* doi:10.1109/CMD.2012.6416450.
- [29] T. Tanaka, Dielectric breakdown in polymer nanocomposites, in: *Polym. Nanocomposites Electr. Therm. Prop.*, Springer International Publishing, Cham, 2016: pp. 113–137. doi:10.1007/978-3-319-28238-1_5.
- [30] K. Yang, X. Huang, M. Zhu, L. Xie, T. Tanaka, P. Jiang, Combining RAFT polymerization

- and thiol-ene click reaction for core-shell structured polymer@BaTiO₃ nanodielectrics with high dielectric constant, low dielectric loss, and high energy storage capability, *ACS Appl. Mater. Interfaces*. 6 (2014) 1812–1822. doi:10.1021/am4048267.
- [31] Y. Huang, X. Huang, Dielectric loss of polymer nanocomposites and how to keep the dielectric loss low, in: *Polym. Nanocomposites Electr. Therm. Prop.*, Springer International Publishing, Cham, 2016: pp. 29–50. doi:10.1007/978-3-319-28238-1_2.
- [32] M. Arbatti, X. Shan, Z. Cheng, Ceramic-polymer composites with high dielectric constant, *Adv. Mater.* 19 (2007) 1369–1372. doi:10.1002/adma.200601996.
- [33] P. Barber, S. Balasubramanian, Y. Anguchamy, S. Gong, A. Wibowo, H. Gao, H.J. Ploehn, H.C. Zur Loye, Polymer composite and nanocomposite dielectric materials for pulse power energy storage, *Materials (Basel)*. 2 (2009) 1697–1733. doi:10.3390/ma2041697.
- [34] Y. Fan, X. Huang, G. Wang, P. Jiang, Core-Shell Structured Biopolymer@BaTiO₃ Nanoparticles for Biopolymer Nanocomposites with Significantly Enhanced Dielectric Properties and Energy Storage Capability, *J. Phys. Chem. C*. 119 (2015) 27330–27339. doi:10.1021/acs.jpcc.5b09619.
- [35] L. Xie, X. Huang, Y. Huang, K. Yang, P. Jiang, Core@Double-shell structured BaTiO₃-polymer nanocomposites with high dielectric constant and low dielectric loss for energy Storage Application, *J. Phys. Chem. C*. 117 (2013) 22525–22537. doi:10.1021/jp407340n.
- [36] M. Ejaz, V.S. Puli, R. Elupula, S. Adireddy, B.C. Riggs, D.B. Chrisey, S.M. Grayson, Core-shell structured poly(glycidyl methacrylate)/BaTiO₃ nanocomposites prepared by surface-initiated atom transfer radical polymerization: A novel material for high energy density dielectric storage, *J. Polym. Sci. Part A Polym. Chem.* 53 (2015) 719–728. doi:10.1002/pola.27485.
- [37] X. Huang, P. Jiang, Core-shell structured high-k polymer nanocomposites for energy storage and dielectric applications, *Adv. Mater.* 27 (2015) 546–554. doi:10.1002/adma.201401310.
- [38] Z. Pan, L. Yao, J. Liu, X. Liu, F. Pi, J. Chen, B. Shen, J. Zhai, Superior discharge energy density and efficiency in polymer nanocomposites induced by linear dielectric core-shell nanofibers, *J. Mater. Chem. C*. 7 (2019) 405–413. doi:10.1039/c8tc04555k.
- [39] M.A. Parvez Mahmud, N. Huda, S.H. Farjana, M. Asadnia, C. Lang, Recent Advances in Nanogenerator-Driven Self-Powered Implantable Biomedical Devices, *Adv. Energy Mater.* 8 (2018) 1–25. doi:10.1002/aenm.201701210.

- [40] D. Hu, M. Yao, Y. Fan, C. Ma, M. Fan, M. Liu, Strategies to achieve high performance piezoelectric nanogenerators, *Nano Energy*. 55 (2019) 288–304. doi:10.1016/j.nanoen.2018.10.053.
- [41] Y. Zhang, M. Wu, Q. Zhu, F. Wang, H. Su, H. Li, C. Diao, H. Zheng, Y. Wu, Z.L. Wang, Performance Enhancement of Flexible Piezoelectric Nanogenerator via Doping and Rational 3D Structure Design For Self-Powered Mechanosensational System, *Adv. Funct. Mater.* 29 (2019) 1904259. doi:10.1002/adfm.201904259.
- [42] Z. Zhou, Z. Zhang, Q. Zhang, H. Yang, Y. Zhu, Y. Wang, L. Chen, Controllable Core-Shell BaTiO₃@Carbon Nanoparticle-Enabled P(VDF-TrFE) Composites: A Cost-Effective Approach to High-Performance Piezoelectric Nanogenerators, *ACS Appl. Mater. Interfaces*. 12 (2020) 1567–1576. doi:10.1021/acsami.9b18780.
- [43] G.T. Hwang, H. Park, J.H. Lee, S. Oh, K. Il Park, M. Byun, H. Park, G. Ahn, C.K. Jeong, K. No, H. Kwon, S.G. Lee, B. Joung, K.J. Lee, Self-powered cardiac pacemaker enabled by flexible single crystalline PMN-PT piezoelectric energy harvester, *Adv. Mater.* 26 (2014) 4880–4887. doi:10.1002/adma.201400562.
- [44] F.W. Horlbeck, F. Mellert, J. Kreuz, G. Nickenig, J.O. Schwab, Real-world data on the lifespan of implantable cardioverter-defibrillators depending on manufacturers and the amount of ventricular pacing, *J. Cardiovasc. Electrophysiol.* 23 (2012) 1336–1342. doi:10.1111/j.1540-8167.2012.02408.x.
- [45] Z. Li, G. Zhu, R. Yang, A.C. Wang, Z.L. Wang, Muscle-driven in vivo nanogenerator, *Adv. Mater.* 22 (2010) 2534–2537. doi:10.1002/adma.200904355.
- [46] D.H. Kim, H.J. Shin, H. Lee, C.K. Jeong, H. Park, G.T. Hwang, H.Y. Lee, D.J. Joe, J.H. Han, S.H. Lee, J. Kim, B. Joung, K.J. Lee, In Vivo Self-Powered Wireless Transmission Using Biocompatible Flexible Energy Harvesters, *Adv. Funct. Mater.* 27 (2017) 1700341. doi:10.1002/adfm.201700341.
- [47] H. Feng, C. Zhao, P. Tan, R. Liu, X. Chen, Z. Li, Nanogenerator for Biomedical Applications, *Adv. Healthc. Mater.* 7 (2018) 1–18. doi:10.1002/adhm.201701298.

Acknowledgements

This joint thesis was conducted in collaboration with four groups: Innovative Materials, Energy and Sustainable Development (IMED-Lab) of Cadi Ayyad University in Morocco, l'Institut de Chimie de la Matière Condensée de Bordeaux (ICMCB) in France, Laboratoire de Physique de la Matière Condensée (LPMC) in France and Jožef Stefan Institute (JSI) in Slovenia.

Financial support was provided by the CNRST Priority Program (PPR 15/2015), European Union Horizon 2020 Research and Innovation actions MSCA-RISE-ENGIMA (No. 778072) and Slovenian Research Agency grant program (P1-0125).

First and foremost, I sincerely appreciate the almighty God for His graces, strength and sustenance from the beginning of my academic life up to this doctoral level. His benevolence has made me excel and successful in all my academic pursuits.

I am deeply indebted to my supervisors, Prof. Mohamed GOUNE, Prof. M'barek AMJOUD and Prof. Daoud MEZZANE for their guidance, expertise, constructive criticism, myriad useful suggestions, and valuable advice that greatly helped me to work on such topic. I would like to thank them for providing me the opportunity of working not only in their groups, but also the chance to collaborate with other researcher groups as well. I would like to express my deepest appreciation to my co-supervisor Prof. Mohammed LAHCINI for his unlimited guidance, insight and suggestions in the physico-chemistry of polymers and nanocomposites.

I would like to thank professors Mimoun EL MARSSI, Yaovi GAGOU, Anna G. RAZUMNAYA and Igor A. LUK'YANCHUK from LPMC (Amiens, France) for providing me the opportunity to work in their research group and for instructing me to Raman spectroscopy and ferroelectric measurements, and their discussions on ferroelectric materials. I would like to thank Mr. Sébastien FOURCADE for his kindness and his technical assistance in ICMCB (Bordeaux, France). I would like to thank Jaâfar GHANBAJA from Institut Jean Lamour (IJL, France) for the wonderful HRTEM and STEM images of BCZT multipodes. I would like to express my sincere gratitude to Prof. Abdelhadi ALIMOUSSA for his help in SAED patterns indexing. A huge gratitude is also addressed to Professors Zdravko KUTNJAK, Brigita ROŽIČ and Nikola NOVAK for giving me the chance to work in the Laboratory for calorimetry and dielectrics (JSI, Ljubljana, Slovenia). A special thanks to Prof. Matjaž SPREITZER, Dr. Marjeta MAČEK KRŽMANC and Mr. Damjan VENGUST from the Department of Advanced Materials (JSI, Ljubljana, Slovenia) for their great availability and discussions on 1D ferroelectric materials. I would like to express my sincere gratitude to Prof. Hana URŠIČ from the Department of Electronic Ceramics (JSI, Ljubljana, Slovenia) for the effort and time spent during the high-quality PFM analyses. Thank you all for your kindness and for sharing your knowledge and experience with me; it has been a honor and a great pleasure to work with you during my secondment in Jožef Stefan Institute.

Apart from the academic and technical training received during my thesis, I would like to express my deepest gratitude to Prof. Daoud MEZZANE and Ms. Soukaina MERSELMIZ

for their encouragements during my thesis writing and for the other important qualities and skills like self-motivation, time management, and leadership that I will always benefit from in my future career and life.

My special thanks go to my colleagues and friends Ilyasse IZANZAR, El-Houssaine ABLOUH, Adel ZYANE, Miloud CHEBBAY, Mohamed ILSOUK, and Taha EL ASSIMI for their kindness and for all the discussions, helps and collaborations.

A great thank to my teammates from IMED-Lab: Abdelmalek BRIK, Abderrahmane NABGUI, Ismail ADOUMAZ, Soukaina AJOUGUIM, Fatima Ezzahra BOUHARRAS, Jamal CHABBI, Oumayma JENNAH, Abserrahim IHYADN, Wafa MISRAR, and Hajar ZAITOUNI. I would also like to thank my colleagues from ICMCB: Samy AOUED, Iñaki CORNU, Maël PONTOREAU, Jonathan STEF, and Khawla ZRIKEM.

I associate my thanks also to Dejvid ČREŠNAR, Aleksander MATAVŽ, Marta LAVRIČ and Nikita DERETS for the unforgettable memories in Ljubljana.

Finally, I want to express my deepest thanks to my mother Sakina BAKHALEQ, my father Abdelaziz HANANI, and my brothers Ilyass, Walid and Nabil. Thank you for instilling in me the basic values of life and giving me every chance to succeed. Your love carries me and guides me every day. No words can express the love, esteem and respect that I have had always for you.

Zouhair HANANI

This doctoral dissertation is dedicated to my beloved parents and brothers for their love, encouragements, and support throughout my entire PhD life.

Contents

Abstracts	i
Contents	xxxiii
List of Figures	xxxix
List of Tables	xlvi
<u>General Introduction</u>	1
1 Overview of relaxor ferroelectric-based ceramic materials for energy storage and harvesting	4
1.1 Overall context	5
1.2 Generalities about ferroelectric materials	6
1.2.1 Definition	6
1.2.2 A short history of ferroelectric materials	7
1.2.3 Polarization	8
1.2.4 Origin of ferroelectricity: BaTiO ₃ as an example	9
1.2.5 Ferroelectricity, piezoelectricity and pyroelectricity	10
1.3 Ferroelectric based-ceramics for energy storage	12
1.3.1 Basic knowledge	12

1.3.1.1	Capacitance and permittivity	12
1.3.1.2	Stored energy density	14
1.3.1.3	Energy storage performance: the particular case of relaxor ferroelectric based-ceramic	15
1.3.1.4	Characterization methods	17
1.3.2	Properties of relaxor ferroelectric-based ceramic	20
1.3.3	Factors affecting the permittivity and the BDS	23
1.3.3.1	Grain size	23
1.3.3.2	Porosity	24
1.3.4	Ferroelectric ceramic/polymer composites	24
1.4	Ferroelectric based-ceramics for energy harvesting: towards piezoelectric nanogenerators	31
1.4.1	Background on piezoelectric effect	31
1.4.2	Piezoelectric nanogenerators (PNGs)	32
1.4.3	The first principle theory of nanogenerators	34
1.4.4	The working mechanism of a PNG	35
1.4.5	PNGs performance characterization	36
1.4.5.1	Open-Circuit Voltage V_{oc}	36
1.4.5.2	Short-Circuit Current I_{sc}	37
1.4.5.3	Maximum Power Output	37
1.4.6	PNG-based Piezoelectric ceramics	37
1.4.6.1	ZnO	37
1.4.6.2	PZT	38
1.4.6.3	BaTiO ₃	38
1.4.7	PNG-based ceramic/polymer composites	38

1.4.8	Some applications of PNGs	39
1.4.8.1	Tire condition monitoring	39
1.4.8.2	Smart wearable fabric	40
1.4.8.3	Implantable biomedical devices	41
1.5	BCZT lead-free relaxor ferroelectric and PLA as promising materials for energy storage and harvesting?	42
1.5.1	BCZT lead-free relaxor ferroelectric	42
1.5.1.1	Contextual elements	42
1.5.1.2	Structural properties	43
1.5.1.3	Elaboration of BZCT	45
1.5.1.4	Dielectric, ferroelectric and piezoelectric properties	47
1.5.1.5	Biocompatibility of BCZT ceramics	50
1.5.2	PLA as a biodegradable polymer	51
1.5.2.1	Contextual elements	51
1.5.2.2	PLA production	52
1.5.2.3	Transition from PVDF to PLA	53
1.6	Conclusions	56
2	Elaboration and Characterization of BCZT ceramics	57
2.1	Introduction	58
2.2	Synthesis of BCZT ceramics with different morphologies	58
2.2.1	BCZT near-spherical nanoparticles	58
2.2.1.1	Strategy N°1: Surfactant-assisted solvothermal	58
2.2.1.2	Strategy N°2: Very-low temperature hydrothermal	62
2.2.2	BCZT nanorods	66

2.2.2.1	Synthesis route: surfactant-assisted solvothermal	66
2.2.2.2	Thermal analysis: phase evolution and temperature of calcination	68
2.2.2.3	Structure and growth mechanism	69
2.2.3	Morphological transition: from cube to multipod BCZT	72
2.2.3.1	Synthesis route	72
2.2.3.2	Morphological transformations	73
2.2.3.3	Growth mechanism of BCZT multipods	80
2.3	Dielectric and ferroelectric properties of BCZT sintered ceramics	83
2.3.1	Microstructural state of sintered ceramics	83
2.3.1.1	BCZT near-spherical nanoparticles	83
2.3.1.2	BCZT rod-like ceramic	86
2.3.1.3	BCZT: Anisotropic morphologies	86
2.3.2	Dielectric and ferroelectric properties of sintered ceramics	87
2.3.2.1	BCZT near-spherical nanoparticles	87
2.3.2.2	BCZT rod-like ceramic	91
2.3.2.3	BCZT Anisotropic morphologies	92
2.4	Selection of the most promising BCZT ceramics	93
2.5	Conclusions	97
3	Elaboration, characterization and properties of BCZT/PLA nanocomposites	98
3.1	Context of the study	99
3.2	The near-spherical BCZT (B_NP)/PLA composite as a reference	100
3.2.1	Functionalization of BCZT nanoparticles (B_NP)	100
3.2.2	Elaboration of PLA-based nanocomposite films	102

3.2.3	Dielectric properties of nanocomposite films	104
3.2.3.1	Effects of frequency, volume fraction of fillers and functionalization: qualitative analysis	104
3.2.3.2	Effects of both volume fraction and aspect-ratio of fillers on the effective permittivity of the nanocomposite: quantitative analysis	107
3.2.3.3	Effects of the aspect-ratio of fillers on the effective permittivity of the nanocomposite: quantitative analysis	114
3.3	The permittivity <i>vs</i> the aspect ratio of the ceramic: a real paradigm? . . .	117
3.3.1	Dielectric properties	117
3.3.2	Energy storage performances	122
3.4	Conclusions	126
4	Lead-free Nanocomposite Piezoelectric Nanogenerator Film for Biomechanical Energy Harvesting	128
4.1	Context of the study	129
4.2	Fabrication of the BF-PNG	130
4.3	Local piezoelectric properties	131
4.4	Mechanical energy harvesting	133
4.4.1	Input mechanical forces measurement	133
4.4.2	Output electrical properties	134
4.4.3	Stability of the output voltage	136
4.4.4	Charge-storage capability	137
4.4.5	Energy harvesting performances	139
4.4.6	Feasibility demonstration	141
4.5	Conclusions	142

<u>Conclusions and suggested directions for future work</u>	144
I . Conclusions	145
II . Suggested directions for future work	146
<u>Bibliography</u>	148
<u>Appendices</u>	189
A. Structure and phase analysis	189
A. 1. X-ray diffraction	189
A. 2. Fourier-transform infrared spectroscopy	190
B. Ceramic bulk density measurement	190
C. Thermogravimetric analysis	191
D. Morphology and composition	191
D. 1. Scanning electron microscopy	191
D. 2. Transmission electron microscopy	192
E. Thickness measurement of the nanocomposite films	192
F. Dielectric measurements	192
G. P-E hysteresis loops	193
H. Piezoelectric force microscopy	193
I. Energy harvesting in the BF-PNG	194

List of Figures

1.1	Ferroelectric hysteresis loop.	9
1.2	Unit cell of a cubic BaTiO ₃ perovskite structure.	10
1.3	(a) Schematic representation of piezoelectricity, pyroelectricity and ferroelectricity on the basis of crystal symmetry and (b) Venn diagram showing how ferroelectrics fit into the different classes of dielectric materials.	12
1.4	A schematic representation of dielectric medium (a) without and (b) under electric field.	13
1.5	Schematic illustration of hysteresis loops for (a) linear dielectric, (b) normal ferroelectric and (c) relaxor ferroelectric. The green areas and red areas represent the recoverable energy density and dissipated energy density, respectively.	16
1.6	Schematic circuit of dielectric spectroscopy measurement.	17
1.7	Schematic circuit of dielectric spectroscopy measurement.	19
1.8	The temperature dependence of the real part of the dielectric permittivity measured at different frequencies for a single crystal of the canonical relaxor compound PMN [44].	21

1.9	(a-h) Breakdown phase evolution processes for composites having the same volume fraction of ceramic fillers under applied horizontal electric field using a phase-field model: (a-d) filled with nanoparticles and (e-h) filled with nanofibers. (i) Breakdown phase morphology in composites with different microstructures; (j) evolution of the breakdown phase fraction under an applied electric field in the z-direction; (k) BDS of the corresponding microstructures [68].	28
1.10	The outline contours of the numerically simulated electric field distortion in different ceramic/polymer composites: (a) BaTiO ₃ /PVDF, (b) BaTiO ₃ /P(VDF-TrFE-CTFE). (c) TiO ₂ /P(VDF-TrFE-CTFE) and (d) BaTiO ₃ /P(VDF-TrFE-CTFE) nanocomposite with BaTiO ₃ nanoparticles of larger size [99].	29
1.11	Schematic representation of the (a) direct and converse piezoelectric effects.	31
1.12	Schematic representation of the deformation modes of a piezoelectric material (a) longitudinal, (b) lateral, and (c) shear mode.	32
1.13	(a) Schematic diagram showing the design and structure of the piezoelectric nanogenerators [108] and (b) schematic definition of a nanowire and the coordination system [107].	33
1.14	Illustrations about the working mechanisms of a piezoelectric nanogenerator with the increase of the applied stress.	36
1.15	(a) Shape change of the tire in the contact patch, (b) a sketch of the nanogenerator, (c) simulating the tire's deformation, and (d) the location of the nanogenerator in tire [129].	40
1.16	(a) A photo and (b) the structure of the fabric nanogenerator, and (c) an LCD display driven by the nanogenerator [130].	40
1.17	(a) A single-wire-generator (SWG) attached to a live rat's heart (b) and (b) $I - V$ characteristics of the SWG [133].	41

1.18	(a) A representation of a self-powered artificial cardiac pacemaker, (b) a photograph of the heart stimulation test on a live rat by PMN-PT stimulator, and (c, d) the electrocardiogram (ECG) rate in a rat heart before the stimulation and after the stimulation [131].	42
1.19	Crystalline structure of BCZT lead-free relaxor ferroelectric.	44
1.20	Pseudo-binary phase diagrams of BCZT system proposed by (a) Liu and Ren [159], (b) Keeble et al. [135], and (c) phase diagram of $(\text{Ba}_{1-x}\text{Ca}_x)(\text{Zr}_{0.1}\text{Ti}_{0.9})\text{O}_3$ system reported by Fu et al. [160].	45
1.21	Effect of Zr content on the (a) dielectric, (b) ferroelectric and (c) piezoelectric properties in $(\text{Ba}_{0.85}\text{Ca}_{0.15})(\text{Zr}_x\text{Ti}_{1-y})\text{O}_3$ system [158].	48
1.22	(a) $P - E$ hysteresis loop for the 0.5BCT–0.5BZT samples with different average grain sizes fabricated from $5\text{ }\mu\text{m}$ powders, and (b) dependence of d_{33} value on average grain size for the samples of the 0.5BCT–0.5BZT composition fabricated from different powder particle sizes [157].	49
1.23	Three stereoisomers of lactide which lead to distinct PLA structures upon polymerization [199].	52
1.24	Synthesis methods for PLA [202].	53
1.25	Electrical properties of some biodegradable and conventional polymers. (a) relative permittivity, (b) loss tangent, (c) apparent conductivity and (d) DC breakdown strength [203].	55
2.1	Experimental procedure used in strategy N°1 to elaborate spherical BCZT nanoparticles.	59
2.2	TGA curves of B-0, B-CTAB and B-SDS raw powders.	60
2.3	XRD patterns of (a) as-prepared and (b) BCZT powders calcined at $1000\text{ }^\circ\text{C}/4\text{ h}$, the enlarged views of the peaks $2\theta \approx$ (c) 45° and (d) 66°	61
2.4	FESEM micrographs and nanoparticles size distribution histograms of B-0, B-CTAB and B-SDS calcined powders.	61

2.5	Experimental procedure used in strategy N°2 to elaborate spherical BCZT nanoparticles.	62
2.6	TGA curves of B-25, B-80 and B-160 raw powders.	63
2.7	(a) XRD patterns of BCZT powders synthesized from 25 to 240 °C, and enlarged peaks splitting at $2\theta \approx 45^\circ$ (b) and 65.5° (c).	64
2.8	FTIR spectra of BCZT powders synthesized from 25 to 240 °C.	65
2.9	FESEM micrographs and nanoparticles size distribution histograms of BCZT powders synthesized at different temperatures.	66
2.10	Schematic representation of the mechanisms of BCZT nanoparticles formation under hydrothermal processing: (a) <i>in situ</i> transformation and (b) dissolution-precipitation processes.	67
2.11	Experimental procedure used to elaborate BCZT nanorods.	68
2.12	Experimental procedure used to elaborate BCZT nanorods.	68
2.13	(a) XRD, (b) SAED patterns and (c) Rietveld refinement of BCZT powder calcined at 1000 °C/4 h.	69
2.14	FESEM micrograph of BCZT nanorods powder calcined at 1000 °C/4 h.	70
2.15	A plausible schematic representation of the formation of BCZT rod-like grains using rod-like micellar templates.	71
2.16	Experimental procedure for HZTO_NW elaboration.	72
2.17	Experimental procedure for the elaboration of shape-controlled BCZT nanostructures.	73
2.18	Variation of samples' weight as a function of the reaction time.	74
2.19	FESEM images indicating the effect of time on the morphogenesis of BCZT materials using 150 mM of Ba^{2+} and 26.5 mM of Ca^{2+} . (a) HZTO_NW, and after (b) 3 h, (c) 6 h, (d) 12 h, (e) 32 h and (f) 72 h of hydrothermal reaction.	75

2.20	FESEM images indicating the effect of A-site concentrations on the morphogenesis of BCZT materials after 18 h of hydrothermal reaction, using (a) 50 mM of Ba^{2+} and (b) 150 mM of Ba^{2+}	76
2.21	TEM image and EDX elemental mapping images of wires, cubes and multipods.	77
2.22	TEM image and EDS elemental mapping images of isolated (a) wires, (b) cubes and (c) multipods.	77
2.23	XRD patterns of different powders elaborated using (a) $\{[\text{Ba}^{2+}] = 5 \text{ mM}, [\text{Ca}^{2+}] = 8.8 \text{ mM}\}$ and (b) $\{[\text{Ba}^{2+}] = 150 \text{ mM}, [\text{Ca}^{2+}] = 26.5 \text{ mM}\}$, at various hydrothermal reaction times.	78
2.24	The composition of the elaborated samples at various hydrothermal reaction times using (a) $\{[\text{Ba}^{2+}] = 5 \text{ mM}, [\text{Ca}^{2+}] = 8.8 \text{ mM}\}$ and (b) $\{[\text{Ba}^{2+}] = 150 \text{ mM}, [\text{Ca}^{2+}] = 26.5 \text{ mM}\}$	78
2.25	FESEM micrographs of 50B72h and 150B72h samples.	79
2.26	TEM and SAED patterns of (a) HZTO nanowire, (b) CZTO cube, and (c) BCZT multipod.	80
2.27	(a-c) FESEM and (d-f) HRTEM images of various loose nanostructures using 150 mM of Ba^{2+} and 26.5 mM of Ca^{2+}	81
2.28	(a-c) FESEM and (d-f) HRTEM images indicating the morphogenesis of BCZT materials using 15mM of Ba^{2+} and 26.5 mM of Ca^{2+}	82
2.29	HRTEM images of (a) three edge-attached cubes and (b) two edge-attached cubes (SAED pattern in inset).	83
2.30	SEM micrographs and grain size distributions of B-0, B-CTAB and B-SDS ceramics sintered at 1250 °C/10 h.	84
2.31	SEM micrographs of (a) B-25, (b) B-80 and (c) B-160 ceramics sintered at 1250 °C/10 h and (d) variation of bulk and relative densities and grain size with synthesis temperature.	85
2.32	(a) SEM micrograph and corresponding statistical distribution of (b) length and (c) diameter of B_NR ceramic sintered at 1250 °C/10 h.	86

2.33	FESEM micrographs of (a) HZTO_NW, (b) 50B3h and (c) 50B24h ceramics sintered at 1250 °C/10 h.	87
2.34	Temperature dependence of dielectric constant and dielectric loss of (a) B-0, (b) B-CTAB and (c) B-SDS ceramics sintered at 1250 °C/10 h. (d) Room-temperature $P - E$ loops of BCZT ceramics.	89
2.35	(a) Comparison of the dielectric properties of BCZT ceramics at 1 kHz, and temperature dependence of dielectric constant and dielectric loss of (a) B-25, (b) B-80 and (c) B-160 ceramics sintered at 1250 °C/10 h.	90
2.36	(a) Temperature-dependence of dielectric constant and dielectric loss, and (b) room-temperature $P - E$ loop of B_NR ceramic	91
2.37	(a) Temperature-dependence of dielectric constant and dielectric loss, and (b) room-temperature $P - E$ loop of B_NR ceramic	92
2.38	Temperature-dependence of ε_r and $\tan\delta$ of (a) HZTO_NW and (b) 50B24h sintered ceramics. Room-temperature $P - E$ loops of (c) HZTO_NW and (d) 50B24h sintered ceramics.	94
3.1	Schematic illustration of the preparation of core-shell structured B_NP@PDA nanofillers.	101
3.2	STEM-HAADF micrographs of (a) B_NP nanoparticle, (b) B_NP@PDA nanoparticle showing PDA layer thickness with the red lines, and (c) TGA curves of B_NP and B_NP@PDA nanoparticles.	101
3.3	FTIR patterns of (a) B_NP, B_NP-OH, B_NP@PDA nanoparticles and (b) B_NP@PDA/PLA films.	103
3.4	FESEM images of the (a, b) surface and the (c, d) cross-section of 20 vol% B_NP/PLA and 20 vol% B_NP@PDA/PLA nanocomposite films, respectively.	105
3.5	Schematic illustrations of the dispersion of (a) B_NP and (b) B_NP@PDA fillers inside the PLA matrix.	106
3.6	(a, b) ε_r and (c, d) $\tan\delta$ of B_NP/PLA and B_NP@PDA/PLA nanocomposites, respectively.	107

3.7	Effect of the volume fraction of B_NP and B_NP@PDA fillers on the (a) ε_r and (b) $\tan\delta$ of PLA-based nanocomposites.	108
3.8	Evolution of the effective permittivity of the B_NP/PLA and B_NP@PDA/PLA composites as a function of volume fraction of B_NP as inclusion. Comparison with the lower and upper Wiener bounds defined from different value of the B_NP permittivity.	109
3.9	Evolution of the effective permittivity of the composite as a function of B_NP volume fraction for different values of B_NP permittivity. Comparison with the experimental data.	112
3.10	(a) Evolution of the internal field E_{int} (<i>via</i> the ratio $\frac{E_{int}}{E_{ext}}$) as a function of the B_NP permittivity. (b) Evolution of the polarizability α (<i>via</i> the ratio $\frac{\alpha}{a^3}$) as a function of the B_NP permittivity.	113
3.11	Evolution of the effective permittivity of the B_NP/PLA composite as a function the aspect ratio of the B_NP charge. For all calculations, the permittivity of the B_NP ceramic was considered equal to 10000.	115
3.12	Calculation of the evolution of the percolation threshold of B_NP into PLA as a function the aspect ratio of B_NP.	116
3.13	Calculation of the effective permittivity of the B_NP/PLA composite as a function of B_NP volume fraction for different couples (ε_{B_NP} , $\frac{c}{a}$). Comparison with experimental data.	117
3.14	FESEM images of the (a-c) surface and the (d-i) cross-section of HZTO_NW/PLA nanocomposite films at various volume fractions.	119
3.15	FESEM images of the (a) surface and the (b) cross-section of 3 vol% B_NR/PLA nanocomposite film.	120
3.16	(a, b) ε_r and (c, d) $\tan\delta$ of HZTO_NW/PLA and B_NR/PLA nanocomposites, respectively.	121
3.17	Effect of the volume fraction of B_NP, B_NP@PDA, HZTO_NW and B_NR fillers on the (a) ε_r and (b) $\tan\delta$ of PLA-based nanocomposites. . .	122

3.18	$D-E$ loops of (a) B_NP/PLA, (b) B_NP@PDA/PLA, (c) HZTO_NW/PLA and (d) B_NR/PLA nanocomposites.	123
3.19	(a) The U_{tot} , (b) U_{rec} and (c) η of the PLA-based nanocomposite films. . .	125
4.1	(a) Schematic illustration of the prepared composite generator and (b) a photograph of the flexible nanocomposite generator device (BF-PNG). . . .	130
4.2	The operating PFM setup used to measure the piezoelectric response in 20 vol% B_NP@PDA/PLA nanocomposite film schematically shown in the upper right corner (zoomed inset displays field-emission scanning electron microscope (FESEM) image of the nanocomposite film).	131
4.3	The topography (a, e) height, (b, f) deflection and out-of-plane PFM (c, g) amplitude, (d, h) phase images of B_NP@PDA nanoparticles. The PFM (i) phase and (j) amplitude local hysteresis loops measured in the two points 1 and 2 marked by crosses in panel (g). In both panels (i and j), a second cycle is shown.	132
4.4	Out-of-plane PFM (a) amplitude, (b) phase images with the topography (c) height and (d) deflection of 20 vol% B_NP@PDA/PLA film. In the panel (a), the bright regions are the B_NP@PDA powder islands embedded in the darker PLA matrix. The large magnification of such an island is shown in panel (e). The panels (f) and (g) show phase and amplitude of local hysteresis loops, respectively, measured by PFM in the two points, marked by crosses 1 and 2 in the panel (e). In both panels (f and g), a second cycle is shown.	133
4.5	The measured contact force under (a) finger tapping and (b) hand slapping.	134
4.6	The generated (a) V_{oc} and (b) I_{sc} of the BF-PNG under finger tapping. . .	135
4.7	Schematic illustration of the BF-PNG in an (a) original state, (b) when the stress is applied and (c) stress is released.	136
4.8	The output voltage stability tests of the BF-PNG device under (a) finger tapping and (b) under 14000 tapping cycles using a sewing machine (inset shows a magnified view of the voltage stability).	137

4.9	(a) The accumulated voltage across a single capacitor of 1 μF charged by the BF-PNG at 4 Hz of imparting frequency under finger tapping and hand slapping, (b) the maximal output voltage and the equivalent stored energy (inset schematic circuit diagram of capacitor charging).	138
4.10	Repeated charging and discharging shown for the (a) 1 μF and (b) 2.2 μF commercial capacitors charged by the BF-PNG at 23 Hz of sewing machine tapping frequency (insets show the zoomed portion of a charging curve). .	140
4.11	The output voltage and power density generated by the BF-PNG across various resistors (inset shows the schematic circuit diagram of the harvested output voltage).	141
4.12	The output voltage charging curve of a 1 μF commercial capacitor by the BF-PNG under finger tapping at a frequency of 4 Hz. The upper inset shows an enlarged plot of voltage steps during capacitor charging. The lower inset depicts a digital photograph of a glowing red LED powered by the charged capacitor. (b) Schematic circuit diagram for the measurement of the accumulated voltage across the capacitor and for the LED lighting. .	143
I.1	Contact force measurement under finger tapping.	194
I.2	Open-circuit voltage (V_{oc}) generation under gentle finger tapping.	195
I.3	Stability of the open-circuit voltage (V_{oc}) using a sewing machine.	195
I.4	Capacitor charging by finger tapping.	196
I.5	Capacitor charging by hand slapping.	196
I.6	LED powering by successive finger impartation.	197

List of Tables

2.1	Structural parameters obtained from Rietveld refinement of BCZT calcined powder.	70
2.2	Comparison of dielectric (at 1 kHz) and microstructure properties of the top three BCZT ceramics elaborated in this work.	95
2.3	Comparison of the dielectric and ferroelectric properties of lead-free BCZT ceramics reported here with others reported in literature using different synthesis conditions and methods.	96
3.1	Physico-chemical properties of Ingeo™ Biopolymer 6201D.	103
3.2	Comparison of the dielectric (at 1 kHz) and microstructure properties of B_NP, HZTO_NW and B_NR sintered ceramics at 1250 °C/10 h.	118
4.1	Comparison of the energy harvesting performances of BF-PNG with other PNGs reported in the literature.	142

General Introduction

Driven by the growing environmental concerns, miniaturization, flexibility, high performance and low cost for energy storage and energy harvesting applications, novel and unique concepts have been studied recently. In this regard, the integration of energy harvesting and storage devices is currently considered to be one of the most important energy-related technologies for self-powered devices. Actually, lead-based ferroelectrics such as lead zirconate titanate (PZT) ceramics are the most successful piezoelectric materials in practical applications due to their excellent ferroelectric and piezoelectric properties. These lead-based are widely used in sensors, ultrasonic generators, resonators, actuators, etc. Though, in view of the concern with environmental pollution and human health, worldwide environmental considerations are demanding the elimination of lead-based materials from all the consumer items. Accordingly, the replacement of Pb-based materials by the homologs with comparable piezoelectric properties but without lead is an emergent task. In 2009, high piezoelectric coefficient ($d_{33} \sim 620$ pC/N) in $0.5\text{BaZr}_{0.2}\text{Ti}_{0.8}\text{O}_3 - 0.5\text{Ba}_{0.7}\text{Ca}_{0.3}\text{TiO}_3$ (BZT-0.5BCT, BCZT) ceramic through the construction of a morphotropic phase boundary (MPB), was reported in the literature. Such large value, comparable to lead-based materials like soft lead PZT, makes lead-free BaTiO_3 -based ferroelectric ceramics and its derivatives as potential candidates for energy applications. However, since its discovery, the majority of published works was based on high temperature solid-state reaction to make pure and crystalline BCZT powders, due to its simplicity and capability to obtain enhanced dielectric, ferroelectric and piezoelectric performances. Subsequently, BCZT ceramics were elaborated by soft chemistry routes like sol-gel, citrate reaction, solvothermal and hydrothermal. However, relative high temperature was needed to obtain pure and crystalline

BCZT powders. Besides, the nucleation and growth of BCZT from the organometallic, ionic or oxide, carbonate or salt precursors results, generally, in the formation of isometric morphologies (spherical or cubic shapes), which offer inferior electrical properties compared to the anisometric particles (rods, wires).

On other hand, ceramic-based energy storage devices suffer from the flexibility and the low energy storage density due to the low breakdown strength (BDS). To overcome this drawback, ceramic/polymer composite approach is an alternative to be explored due to the high flexibility and large DBS of the polymers. Moreover, from energy harvesting consideration, to alleviate the disadvantages of ceramic-based systems, such as rigidity, brittleness, lower voltage coefficient, and lack of design flexibility, ceramic-polymer combination offers the mechanical flexibility, faster processing, adaptability for large mechanical forces, suitable voltage with sufficient power output, alongside with the lower fabrication cost. Nevertheless, the majority of the current ceramic/polymer composites are relying on the combination of the lead-based or lead-free ceramics with petrol-based, not eco-friendly and nonbiodegradable polymers, such as polyethylene, polypropylene, polyethylene terephthalate, and especially fluoropolymers like polyvinylidene fluoride and its derivatives.

The first chapter provides a literature survey, where an overview of ferroelectric-based ceramic materials for both energy storage and harvesting is given. After introducing the basic knowledge in ferroelectric materials, we are interested in both dielectric and piezoelectric properties of relaxor ferroelectric based-ceramic materials. After, the ferroelectric based-ceramic/polymer nanocomposites as materials for energy storage and harvesting is investigated. A particular attention is paid to $\text{Ba}_{0.85}\text{Ca}_{0.15}\text{Zr}_{0.1}\text{Ti}_{0.9}\text{O}_3$ (BCZT), a lead-free relaxor ferroelectric and polylactic acid (PLA), a biodegradable polymer as possible constituents of the nanocomposite.

The second chapter deals with the synthesis of nanostructured lead-free BCZT nanoparticles having different sizes, size distributions and morphologies (near-spherical, rods and multipods). The synthesis routes studied are mainly based on surfactant-assisted solvothermal, low temperature hydrothermal and two-steps hydrothermal routes. The

ferroelectric properties of BCZT sintered ceramics were studied as a function of both process and metallurgical parameters. Then, the best candidates for ceramic/polymer encapsulation were selected.

The third chapter of this work focusses on the elaboration of ceramics/polyactic acid (PLA) nanocomposites and their properties. The effects of the core-shell structuration and functionalization of BCZT, aspect ratio and dielectric constant of ceramics on the effective dielectric constant of the composites are studied and discussed. From an experimental and theoretical coupled-approach some important conclusions are drawn regarding the influence of both the aspect ratio and the dielectric constant of the ceramics on the dielectric constant of the ceramic/PLA composites. Finally, the energy storage performances (total energy density, recovered energy density and energy efficiency) of PLA-based nanocomposites are studied using dielectric displacement–electric field ($D - E$) hysteresis loops. The chapter four is focused on the energy harvesting performances of BCZT/PLA nanocomposites. The concept of piezoelectric nanogenerators to convert the ambient mechanical energy to electrical energy is used. For this purpose, the outputs performances under different human body motions are tested, and the feasibility to drive commercial electronics are verified, using the self-poled and bio-flexible piezoelectric nanogenerator based on BCZT@PDA/PLA nanocomposite.

Overview of relaxor ferroelectric-based ceramic materials for energy storage and harvesting

Contents

1.1	Overall context	5
1.2	Generalities about ferroelectric materials	6
1.3	Ferroelectric based-ceramics for energy storage	12
1.4	Ferroelectric based-ceramics for energy harvesting: towards piezoelectric nanogenerators	31
1.5	BCZT lead-free relaxor ferroelectric and PLA as promising materials for energy storage and harvesting?	42
1.6	Conclusions	56

1.1 Overall context

The growing demand in size-reduced mobile electronic devices which can be connected among each other at any time invites us to consider the following issue. All these promising new technologies with increased functions do, however, require an (or many) external power supply (ies). And batteries, which remain actually the main power source, have many disadvantages in that specific context: their relatively high volume and weight, their power density which is limited and their relatively long charge and discharge time. In order to address these disadvantages, there would be two promising avenues. The first is the development of new materials or systems limited in both size and weight that can harvest at least one energy source such as mechanical, heat and light into electrical energy. The physical phenomena involved in this conversion can be piezoelectricity, thermoelectricity and photoelectricity. The second is the development of new materials or systems limited in both size and weight with high electrical energy storage performance.

On those aspects i.e. harvesting and storage, relaxor ferroelectric perovskite materials would be a credible alternative. Regarding the “harvesting” aspect, the electric current is generally generated by internal polarization. As a consequence, the output power of energy harvester is improved with increasing polarization density. While conventional materials have a low polarization density, the polarization density can be increased by using ferroelectric perovskite materials since they can have a strong and permanent polarization. Concerning the “storage” aspect, relaxor ferroelectric perovskite materials can also be seen as dielectric materials that can store and release electrical energy through dielectric polarization and depolarization. It is worth noting that the energy-storage density of dielectric materials is determined by both electrical displacement and electric field. It can be established that the energy-storage density depends on both the dielectric permittivity and the breakdown strength; the latter representing the highest electric field applicable to the material. As a consequence of this, the permittivity and the breakdown strength are the two most critical parameters for achieving the maximum energy density. In a general manner, dielectric perovskite materials have a high permittivity which is however counterbalanced by a low breakdown strength. Their low breakdown strength limits

thus their energy-storage density and hinders their development at a larger scale. The nanocomposite approach would address these challenges. It consists of combining the high dielectric constant of ferroelectric based-ceramic and the high breakdown strength of polymer for reaching high energy-storage density. In that case, the choice of both the ceramic and the polymer is prime of necessity.

Although the perovskites with the general formula ABO_3 is an important class of ferroelectric materials, the most high-performance ferroelectric perovskites materials used in industry contain lead, a toxic and environmentally unfriendly element. Similarly, the majority of polymers used in high dielectric constant (high- k) nanocomposites are petrol-based, not eco-friendly and many of them are not biodegradable, such as polyethylene, polypropylene, polyethylene terephthalate, and especially fluoropolymers like polyvinylidene fluoride and its derivatives.

In the following literature survey, we will give an overview of ferroelectric-based ceramic materials for both energy storage and harvesting. After providing the basic knowledge, we will interest in both dielectric and piezoelectric properties of relaxor ferroelectric based-ceramic materials. Some avenues will be given through this chapter for improving these properties. Particularly, the interest in considering the ferroelectric based-ceramic/polymer nanocomposites as materials for energy storage and harvesting will be highlighted. We will give a particular attention to $Ba_{0.85}Ca_{0.15}Zr_{0.1}Ti_{0.9}O_3$ (BCZT), a lead-free relaxor ferroelectric and polylactic acid (PLA), a biodegradable polymer as possible constituents of the nanocomposite.

1.2 Generalities about ferroelectric materials

1.2.1 Definition

Ferroelectrics are polar materials that possess at least two equilibrium orientations of the spontaneous polarization vector in the absence of an external electric field, and in which the spontaneous polarization vector may be switched between those orientations by an

electric field. In other words, the spontaneous polarization of the ferroelectrics is reversible when applying an external electric field. These materials are called “ferroelectrics” by analogy to ferromagnetic materials which have spontaneous magnetization and exhibit some similarities such as hysteresis loops, Curie temperature (T_C). The prefix, ferro, meaning iron (Fe), was used to describe the property despite the fact that most ferroelectric materials do not contain iron [1].

1.2.2 A short history of ferroelectric materials

In 1912, Erwin Schrödinger first proposed the term ferroelectricity [2]. However, the discovering of ferroelectricity goes to Joseph Valasek in 1920 after his study of the magnetic properties of ferromagnetics and the dielectric properties of Rochelle salt (Potassium sodium tartrate tetrahydrate, $\text{KNaC}_4\text{H}_4\text{O}_6 \cdot 4\text{H}_2\text{O}$ [3, 4]. In 1935, KH_2PO_4 (KDP) was found by Busch and Scherrer and was followed by some of its isomorphs. During the World War II, these materials were used in sonar devices because of their piezoelectric properties. Busch suggested the hydrogen bonds between adjacent oxygen atoms to be responsible for ferroelectricity in KDP. Besides, it was believed that hydrogen bonds were indispensable for ferroelectricity. Barium Titanate (BaTiO_3) the first man-made perovskite ferroelectric was discovered in 1942 and 1944 in Russia, Japan and the United States. The initial reports were based on doping studies of TiO_2 with BaO , which produced ceramic materials with enhanced dielectric permittivities, and in 1941, high dielectric constant (> 1200) in BaTiO_3 was observed by Thurnauer and Deaderick [5]. In the mid-1940s, Wul and Goldman established that the high dielectric constant BaTiO_3 ceramics was originated from its ferroelectric properties [6]. The discovery of ferroelectricity in BaTiO_3 ceramics was extremely important for two main reasons. First, it was demonstrated for the first time that ferroelectricity could exist in simple oxide materials. Second, ferroelectricity was shown to be not necessarily associated with hydrogen bonding. This finding opened up new outlooks of application for ferroelectric materials, leading to significant interest in other types of ferroelectrics [7]. More than a century after the discovery of ferroelectricity, some significant progress in the miniaturization of electronics devices were made because of the

rapid development of nanoferroelectric components such as ultrasonic medical composites, high displacement piezoelectric actuators, thin and thick films for piezoelectric applications and integrated circuits [4, 8–13].

1.2.3 Polarization

When a material is subjected to an external electric field, the induced polarization (P) is linearly proportional to the magnitude of the applied external electric field (E), which is known as dielectric polarization. Above T_C , ferroelectric materials are at a paraelectric state. In this case, a nonlinear polarization is present versus an external electric field. As a result, electric permittivity, according to the slope of the polarization curve, is no longer constant. At the ferroelectric state, besides the nonlinearity, a spontaneous nonzero polarization was present, as $E = 0$. Because the spontaneous polarization can be reversed by a sufficiently strong electric field, it is dependent on the currently applied electric field and the history as well, thus leading to the presence of the hysteresis loop [1]. Fig. 1.1 shows a schematic plot of polarization versus electric field ($P - E$) in a typical ferroelectric material, through which the characteristic parameters, such as spontaneous polarization (P_s), remnant polarization (P_r) and coercive field (E_c) can be determined. At $E > 0$, the total polarization in the crystal increases as the polarizations in different dipolar regions are aligned. Eventually, it reaches a saturation point (P_s) where the only further increase in P is that due to the relative permittivity of the material. The elimination of the electric field ($E = 0$) results a remnant polarization (P_r). At $E < 0$, the polarization reduces until it reaches zero at the coercive field ($-E_c$). A further negative increase in the field leads to a reverse saturation polarization ($-P_s$). When the field returns to zero the crystal is left with a negative remnant polarization ($-P_r$). Increasing the field once more increases the polarization from $-P_r$ to zero at E_c , and then to P_s , completing the ferroelectric hysteresis loop.

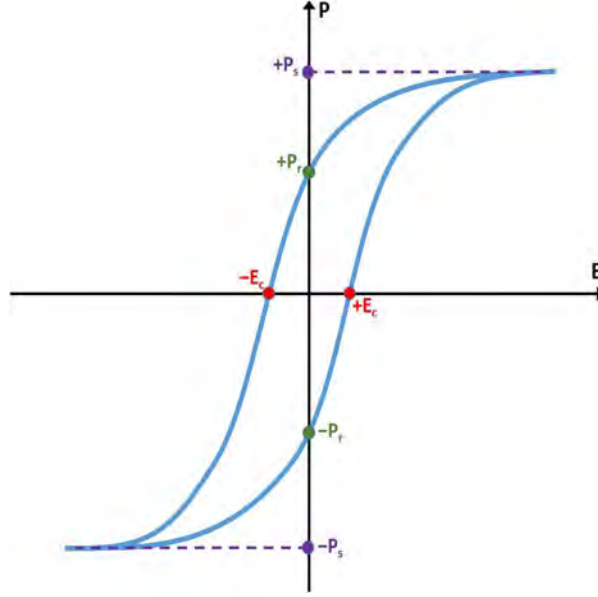


Figure 1.1: Ferroelectric hysteresis loop.

1.2.4 Origin of ferroelectricity: BaTiO₃ as an example

BaTiO₃ is a member of the perovskite family based on the mineral CaTiO₃, as predicted from fundamental crystal chemical principles described by Goldschmidt [14]. BaTiO₃ is the first known simple ferroelectric oxide and remains today a model material for the study of ferroelectricity. Its simple perovskite type structure, its ferroelectricity in a wide range of temperatures including ambient temperature, its dielectric and piezoelectric properties make BaTiO₃ a suitable material for industrial application. To understand the origin of ferroelectricity in BaTiO₃ materials, it is worthy to recall the particularities of the perovskite structure in BaTiO₃. Above the Curie temperature, BaTiO₃ is cubic with a cell side of about 4 Å, and contains one formula-unit per cell. Ba ions occupy cube corner positions (0, 0, 0), Ti ions sit at the body center positions ($\frac{1}{2}$, $\frac{1}{2}$, $\frac{1}{2}$), and O anions are located at face-centered positions such as (0, $\frac{1}{2}$, $\frac{1}{2}$), ($\frac{1}{2}$, 0, $\frac{1}{2}$) and ($\frac{1}{2}$, $\frac{1}{2}$, 0), as depicted in Fig. 1.2. Ba ions are coordinated by twelve oxygens, while Ti ions are coordinated by six oxygens in octahedral coordination.

The origin of the ferroelectricity in BaTiO₃ was intensively discussed [15–22]. Among the countless theories put forward to answer this question, it should retain firstly that of Megaw who attributed the origin of ferroelectricity to a small change of bond character

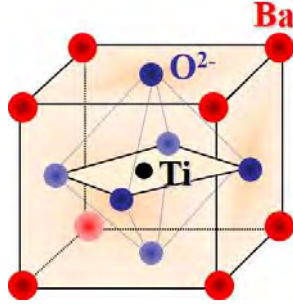


Figure 1.2: Unit cell of a cubic BaTiO_3 perovskite structure.

occurring in a structure whose geometry is compatible with either ionic or homopolar binding [15]. In BaTiO_3 , it was postulated that the TiO_6 octahedra are large enough for the central ion Ti^{4+} . This results in a great mobility of the latter and consequently a significant polarizability of the network. In contrast, other theories assume that it is the oxygen ions that make the greatest displacements [16]. The appearance of ferroelectricity in a large number of compounds whose lattice contains TiO_6 octahedra allowed early to recognize the particular importance of this group. Afterwards, Mason and Matihias supposed that the Ti ion has six equilibrium positions around the center of the TiO_6 octahedron; these six symmetrical positions are equivalent in the paraelectric phase [17]. Below the Curie temperature, inside each unit cell, the Ti^{4+} ions move in only one of the six possible orientations so that it appears in this direction a dipole moment. Simultaneously the crystal lengthens in this direction relative to the other two and becomes tetragonal. Then, Devonshire has attempted a purely thermodynamic approach to deduce the behavior of BaTiO_3 below T_C by introducing a free energy function of the crystal [18]. This approach is based on the earlier ideas of Landau, Ginzberg and Lifshitz and invoked the point group symmetry and nonlinear elasto-dielectric coupled interactions with electrostriction and piezoelectric coefficients [23, 24]. The resulting Landau-Ginzberg-Devonshire theory (LGD) of ferroelectrics is still the most powerful tool for the understanding of ferroelectrics.

1.2.5 Ferroelectricity, piezoelectricity and pyroelectricity

There is an ambiguous relationship between the electric dipoles and crystal lattice in a ferroelectric material. Accordingly, the variation in lattice parameters could change the

strength of the dipoles, namely the strength of the spontaneous polarization. In turn, when a ferroelectric material is made into a capacitor without the application of an external field across it, the variation of this latter leads to a change in the surface charge, which causes current flow across the ferroelectric material [1, 4]. There are three stimuli that can be used to change the lattice structure of a ferroelectric material, i.e. (i) mechanical force, (ii) electric field and (iii) temperature. The generation of surface charge as a result of the application of an external stress is known as piezoelectricity, the variation of spontaneous polarization under applied electric field is defined as ferroelectricity, while the change in spontaneous polarization in response to the change in temperature is named as pyroelectricity.

To better understand the ferroelectricity, it is necessary to link it with piezoelectricity and pyroelectricity, because they have interesting interrelationships in terms of crystal structures [1]. The crystal structure of a material must be acentric (non-centrosymmetric) for it to show piezoelectricity, and be both acentric and possess a unique axis of symmetry (polar) for it to be pyroelectric [4]. As depicted in Fig. 1.3a, all crystals can be categorized into 32 different classes, and 11 of them possess a center of symmetry. Of the remaining 21 acentric classes, all except one exhibit a polarization change when subjected to mechanical stress and hence are piezoelectric [6]. Ten of these 20 classes possess a unique axis of symmetry and an electric polarization exists within the structure in the absence of an applied field. The electric polarization in these polar materials changes with temperature, making them pyroelectric. As they are acentric, they also show piezoelectric behavior [1, 4]. On one hand, the polarization in a ferroelectric material is similar to that in a pyroelectric one. On the other hand, these two polarizations are different, because ferroelectric polarization is reversible by an external applied electric field. Therefore, ferroelectricity is defined as the presence of spontaneous polarization that is reversible by an external electric field [25]. Fig. 1.3b summarizes the interrelationship among piezoelectric, pyroelectric, and ferroelectric materials.

In the Landolt–Börnstein data collection, ferroelectric materials are classified into three major groups; according to their chemical composition and crystal structure [26]. These three ferroelectrics groups are (i) inorganic crystals oxides, (ii) inorganic crystals

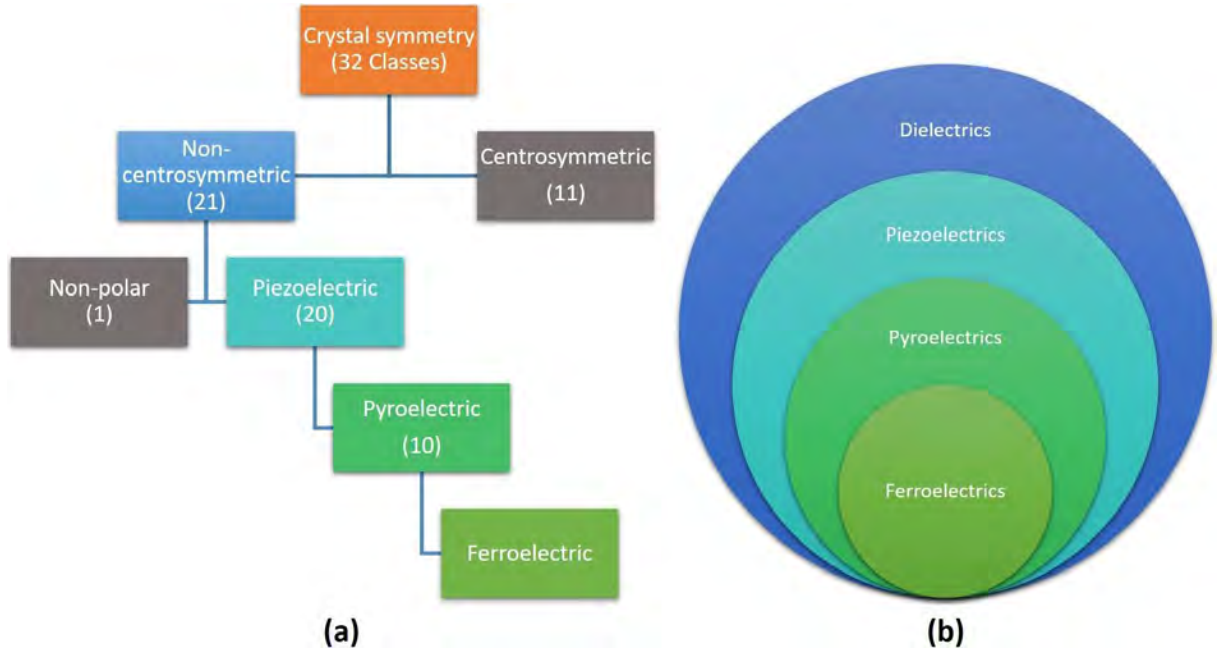


Figure 1.3: (a) Schematic representation of piezoelectricity, pyroelectricity and ferroelectricity on the basis of crystal symmetry and (b) Venn diagram showing how ferroelectrics fit into the different classes of dielectric materials.

non-oxides, and (iii) organic crystals, liquid crystals and polymers. Among these groups, the oxide-based ferroelectrics especially the ABO_3 perovskite-type family, are certainly the most expansively studied.

1.3 Ferroelectric based-ceramics for energy storage

1.3.1 Basic knowledge

1.3.1.1 Capacitance and permittivity

A ferroelectric ceramic can be seen as a dielectric material in which polarization remains permanently, even after removing the applied electric field. It is an electrical insulator that can be polarized by an applied electric field (Fig. 1.4). When a dielectric is placed in an electric field, electric charges do not flow through the material as they do in an electrical conductor but only slightly shift from their average equilibrium positions causing

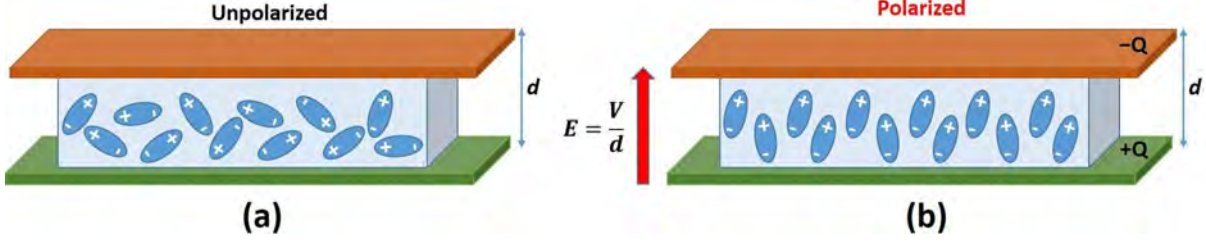


Figure 1.4: A schematic representation of dielectric medium (a) without and (b) under electric field.

dielectric polarization. Because of dielectric polarization, positive charges are displaced in the direction of the field and negative charges shift in the direction opposite to the field. This creates an internal electric field that reduces the overall field within the dielectric itself. The ability of the dielectric materials to store energy is attributed to the polarization, i.e. electric field-induced separation and alignment of the electric charges, which can result in an increase in capacitance. There are several polarization mechanisms, including electronic, ionic, molecular (dipole), and interfacial (space-charge) polarization. In general, application of a field to each of these mechanisms in a normal state will cause a displacement of charge which results in a polarization in the direction of the field. The dielectric material is a capacitor which store electric charges $\pm Q$ (in coulombs) on the surfaces between which the potential difference V (in volts) is applied according to the Eq. 1.1,

$$Q = CV \quad (1.1)$$

where C (in farads) is the capacitance of the system, referring to how much electric charge can be stored in a capacitor. The relationship between C and dielectric constant (ε) is given by the Eq. 1.2,

$$C = \frac{\varepsilon_r \varepsilon_0 A}{d} \quad (1.2)$$

where ε_0 is the dielectric constant of the free space ($8.854 \times 10^{-12} F/m$), A (in meters) is the area of the electrical conductor, d (in meters) is the thickness of the dielectric layer, and ε_r is the dielectric constant of the dielectric material.

1.3.1.2 Stored energy density

When an external voltage is applied, charges with opposite sign and equal magnitude are accumulated at the electrodes. This process is called the charging process. The charges form an internal electric field with a direction opposite to the external electric field. The internal electric field increases as the accumulated charges increase. The charging process will be finished when the internal electric field induced by the accumulated charges (Q) is equal to the external field ($\frac{V}{d}$). ($\frac{Q}{V}$) is equal to the C of the capacitor. In the charging process, the charges are moved by the external electric field, and electrostatic energy is stored in the dielectric layer. The stored energy can be calculated by Eq. 1.3,

$$W = \int_0^{Q_{max}} V dq \quad (1.3)$$

where Q_{max} is the maximum charge when the charging process is finished. dq is the increment of charge. One of the figure-of-merits (FOMs) of energy-storage electrostatic capacitors is energy density (U_{tot}), which measures the “capability” of energy-storage performance. It can be expressed by the ratio between the stored energy and the volume of the capacitor as described by the Eq. 1.4,

$$U_{tot} = \frac{W}{Ad} = \frac{\int_0^{Q_{max}} V dq}{Ad} = \int_0^{D_{max}} E dD \quad (1.4)$$

where D is the electrical displacement in the dielectric layer and E_{max} is the maximum electric field induced by the accumulated charges, which equals the external electric field. For dielectrics with high permittivity, D ($D = \varepsilon_0 \varepsilon_r E$) is very close to the polarization P . Thus, Eq. 1.4 can be rewritten as follow,

$$U_{tot} = \int_0^{P_{max}} E dP = \int_0^{E_{max}} \varepsilon_0 \varepsilon_r E dE \quad (1.5)$$

Thus, it is clearly shown that the energy density depends directly on both permittivity and breakdown strength (BDS). Thus, the energy density of any capacitor can be enhanced by increasing the permittivity, the BDS, or both. Another remark is that, for a linear dielectric with a permittivity that is independent of the electric field, Eq. 1.5 can be expressed as,

$$U_{tot} = \frac{1}{2} \varepsilon_0 \varepsilon_r E^2 \quad (1.6)$$

In that specific case, the energy density is proportional to the permittivity of the dielectric and the square of the applied electric field. Thus, the dielectrics possessing high BDS are more promising in the quest to achieve high energy density because of the square relation between energy density and BDS.

1.3.1.3 Energy storage performance: the particular case of relaxor ferroelectric based-ceramic

At this stage, it is interesting to come-back to the Eq. 1.5. The energy density can be easily obtained from the polarization *vs* electric field ($P - E$) curves by integrating the area between the polarization axis and the $P - E$ curve. As shown in Fig. 1.5, the green-colored area is equal to the recoverable energy density, which corresponds to the released energy density in the discharging process. The red-colored area is equal to the dissipated energy density, which is due to the losses in the dielectric. The total area of the two parts equals the total energy density stored in the charging process.

Linear dielectrics usually possess low permittivity, low dielectric loss, and high BDS. The permittivity of an ideal linear dielectric is independent of the electric field. In other words, their polarization increases linearly with increasing electric field, without hysteresis, as shown in Fig. 1.5a. All the stored energy in the charging process can be released from the dielectric in the discharging process. Many polymers such as polypropylene and polyphenylene sulfide are linear dielectrics and their energy density was reported to be around 1-2 J/cm³ [27]. Some alkaline earth (Ba, Ca, Sr) zirconates and hafnates can also be categorized as linear dielectrics [28]. For example, CaZrO₃ ceramic possess low permittivity (around 30) low loss (<0.1%). Glass is also another type of linear dielectric [29].

In a general manner, the ferroelectric based-ceramics can be considered as non-linear dielectrics. Their permittivity evolves as a function of electric field. They possess high permittivity and dielectric loss with a large remnant polarization as shown in Fig. 1.5b. As a consequence, the recoverable energy density is small. In addition, most of ferroelectric ceramics exhibit low BDS and are thus not suitable for energy storage applications. However, relaxor ferroelectric ceramics are drawing much attention for energy storage applications

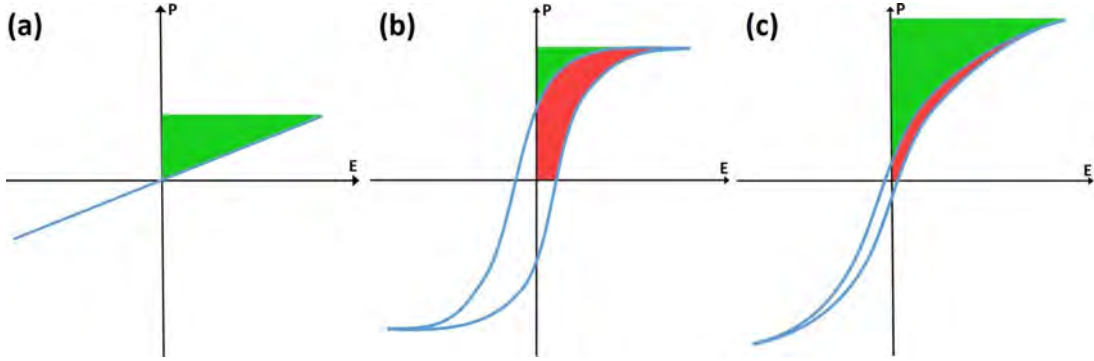


Figure 1.5: Schematic illustration of hysteresis loops for (a) linear dielectric, (b) normal ferroelectric and (c) relaxor ferroelectric. The green areas and red areas represent the recoverable energy density and dissipated energy density, respectively.

owing to their outstanding dielectric and ferroelectric properties. Like conventional ferroelectrics, relaxor ferroelectric ceramics also exhibit large permittivities and saturation polarizations, but possess broad frequency-dependent peak of the temperature-dependent dielectric susceptibility, lower remnant polarizations and slimmer hysteresis loops (see Fig. 1.5c) due to the nanodomains in relaxor ferroelectric (take less energy to align). These properties are essential for realizing extremely high energy densities and efficiencies [30–32]. The high energy storage density in relaxor ferroelectric ceramics is due to the diffuse phase transition [33]. Consequently, ferroelectricity can be detected in a certain temperature range in relaxor ferroelectrics, which has improved their thermal stability. While applying high electric field to obtain high energy density, an increase in the conduction of the material will lead to dielectric/polarization loss and ultimately will reduce the fraction of energy that can be recovered during a discharge. Such a loss of energy, i.e., the energy being dissipated by the hysteresis loss, will lead to temperature heat generation in the capacitor, deteriorating its thermal stability and lifetime [34]. It is thus worth noting that both the energy dissipated by the hysteresis loss (U_H) and the maximum power density (P_{max}) delivered depends on the dielectric loss *via* the Eqs. 1.7 and 1.8, respectively. Besides, the power density is a benchmark for capacitors used in pulse-power applications, which measures the “speed” of the energy storage/release process.

$$U_H = \pi \epsilon_0 \epsilon_r E^2 \tan \delta \quad (1.7)$$

$$P_{max} = \frac{\pi f \epsilon_0 \epsilon_r E^2}{2 \tan \delta} \quad (1.8)$$

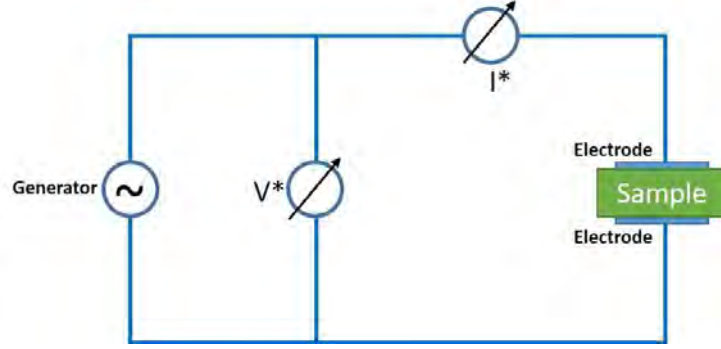


Figure 1.6: Schematic circuit of dielectric spectroscopy measurement.

As a partial conclusion, the main avenues for improving both the energy storage and energy efficiency of relaxor ferroelectric based-ceramics is to optimize their electrical breakdown strength, dielectric constant and dielectric loss.

1.3.1.4 Characterization methods

1.3.1.4.1 Dielectric spectroscopy

To determine the dielectric properties (dielectric constant ϵ_r , dielectric loss tangent or dissipation factor $\tan\delta$) of a dielectric material, the dielectric spectroscopy is used. In this analytic technique, the relaxation and conduction phenomena occurring in a dielectric material are studied as a function of frequency ($\omega = 2\pi f$) at a given temperature. The principle of measurement is based on the application of a sinusoidal voltage V^* (of frequency f) across a dielectric material resulting in a complex current I^* in the material with a phase shift by a phase angle φ . Fig. 1.6 illustrates the schematic circuit of dielectric spectroscopy measurement with a capacitor containing two parallel electrodes separated by a dielectric material of thickness d placed in between them.

The measured impedance of a capacitor is given by $Z^* = Z' + iZ'' = \frac{V^*}{I^*}$, which is related to complex permittivity as $\epsilon^*(\omega) = \epsilon' + i\epsilon'' = \frac{-i}{\omega Z^*(\omega) C_0}$. Thus, from dielectric spectroscopy, complex permittivity is obtained as $\epsilon^*(\omega) = \epsilon' + i\epsilon'' = \frac{C^*(\omega)}{C_0}$. where, C_0 is the capacitance of a capacitor with free space in between parallel plates, C^* is the capacitor with a dielectric material, ϵ' and ϵ'' are real and imaginary parts of permittivity, respectively.

The dielectric constant of a material represents the ability of this material to store charges. The higher the dielectric constant of a material is, the greater its power to store charges is. But the ability to store electrical charges also depends on the geometric parameters of the material. Thus, the capacity of an empty planar capacitor with surface electrodes A , separated by a distance d is equal to,

$$\epsilon_r = \frac{dC}{A\epsilon_0} \quad (1.9)$$

Moreover, the dielectric loss of the dielectric material, which is resulted from distortional, dipolar, interfacial, and conduction loss could be evaluated using the dielectric spectroscopy. The distortional loss is related with electronic and ionic polarization mechanisms. The interfacial loss originates from the excessive polarized interface induced by the fillers and specifically the movement or rotation of the atoms or molecules in an alternating electric field. The conduction loss is attributed to the dc electrical conductivity of the materials, representing the flow of actual charge through the dielectric materials [27]. The dielectric loss material is a property independent on the geometry of capacitor and denotes the energy loss in the dielectric resulting from space charge distortion, dipolar, interfacial-ionic motion, and conduction losses. It is usually expressed as the loss tangent ($\tan\delta$) or dissipation factor (DF) which can be defined as,

$$DF = \tan\delta = \frac{\epsilon''}{\epsilon'} \quad (1.10)$$

1.3.1.4.2 Ferroelectric measurement techniques

The polarization in a material cannot be directly measured by electrical means. However, we can measure the charge flowing through an external circuit. The most used method for hysteresis loop measurement is based on Sawyer and Tower circuit [35, 36]. It includes some seminal measurements on Rochelle salt. A schematic of the experimental setup using an oscilloscope is shown in Fig. 1.7. The applied voltage across the sample is attenuated by a resistive divider, R_1 , R_2 . The sample capacitances, C_{sample} , is connected in series with a shunt capacitor, C_{shunt} , so that the charge flowing onto both is the same. The oscilloscope is connected to measure the voltage across the shunt capacitor. A high-quality low leakage shunt capacitor provides a stable and linear relationship between charge and

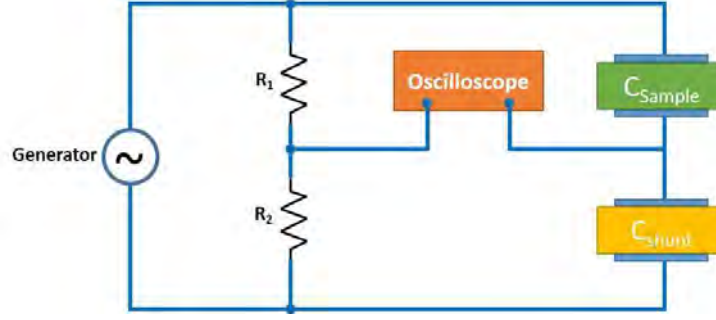


Figure 1.7: Schematic circuit of dielectric spectroscopy measurement.

voltage so that the measured voltage can be converted to a charge by multiplying by the capacitance. For better approximation this will be equal to the charge on the sample. The shunt capacitor is usually chosen to have a capacitance much larger than that of the sample. Therefore, the $P - E$ loops, is the fingerprint of ferroelectrics, should be carefully employed to identify ferroelectrics together with current-electric field ($I - E$) measurement.

1.3.1.4.3 Breakdown strength (BDS)

BDS is one of the key parameters characterizing the performance for energy storage usage. BDS can be defined as the maximum electric field that a dielectric material can withstand without the current flowing through it reaching uncontrollable values. The voltage corresponding to the breakdown is referred to the breakdown voltage (V_{BD}). Apart from the nature of a material, the breakdown process depends on the thickness of a sample (d), the temperature of measurement, relative humidity, molecular defects, structure/shape of electrodes and also the kind of voltage application (AC, DC, impulse). Breakdown field (E_{BD}) of a dielectric is given by the Eq. 1.11,

$$E_{BD} = \frac{V_{BD}}{d} \quad (1.11)$$

Usually, the BDS is measured by applying an increasing DC voltage to the samples to the point of failure. A two-parameter Weibull distribution is commonly employed for characterizing the dielectric breakdown strength. The cumulative distribution function of the Weibull distribution is given by the Eq. 1.12,

$$P(E_i) = 1 - e^{-(\frac{E_i}{E_w})^m} \quad (1.12)$$

where $P(E_i)$ represents the cumulative breakdown probability for a certain electric field, E_i is the BDS of each sample, E_w is the Weibull characteristic BDS, which corresponds to the BDS at 63.2% probability of breakdown ($P(E_w)=63.2\%$), and m is the Weibull modulus, which is a measure of the reliability of the data. For reliable evaluation of the dielectric strength, the plot of Weibull distribution of BDS is described by [37, 38],

$$X_i = \ln E_i \quad (1.13)$$

$$Y_i = \ln \left(\ln \left(\frac{1}{1-p} \right) \right) \quad (1.14)$$

$$P_i = \frac{i}{n+1} \quad (1.15)$$

where X_i , Y_i , and P_i are the variables of the Weibull distribution functions, E_i is the measured dielectric breakdown strength for the i^{th} specimen in the experiments and n is the sum of the specimens. Usually, X_i and Y_i were linearly dependent.

1.3.2 Properties of relaxor ferroelectric-based ceramic

Normal ferroelectric materials like BaTiO_3 own high constants which decrease sharply around the Curie temperature (T_C) because of the tetragonal/cubic phase transition [39]. Hence, only in a narrow temperature range the substantial dielectric and energy storage properties can be observed, which decreases brutally the thermal-stability of BaTiO_3 -based devices [40, 41]. To overcome this drawback, researchers focused on systems with a diffuse ferroelectric phase transition like relaxor ferroelectrics due to the broad operating temperature [42]. The term ferroelectric with a “diffuse phase transition” (DPT) appeared in the literature for the first time by Smolenskii and Isupov in 1954 [43], and have attracted continued interest due to their unusual properties. Relaxor ferroelectric is often observed in solid solutions or in compounds in which a site is occupied by two or more cations. It is the case for example of a lot of perovskite, pyrochlore and quadratic tungsten bronze compounds, e.g., $\text{Pb}(\text{Mg}_{1/3}\text{Nb}_{2/3})\text{O}_3$ (PMN), $\text{Pb}(\text{Zn}_{1/3}\text{Nb}_{2/3})\text{O}_3$ (PZN), $(\text{Pb},\text{La})(\text{Zr},\text{Ti})_3$ (PLZT), $\text{Bi}_2(\text{Mg}_{2/3}\text{Nb}_{4/3})\text{O}_7$, $(\text{Ba},\text{Sr})(\text{Nb},\text{Ta})_2\text{O}_6$, and $\text{Ba}_{0.85}\text{Ca}_{0.15}\text{Zr}_{0.1}\text{Ti}_{0.9}\text{O}_3$ (BCZT).

Relaxor ferroelectrics are characterized by: (i) a broad maximum in temperature dependence of the dielectric permittivity, whose position, T_m , is shifted to lower temperatures

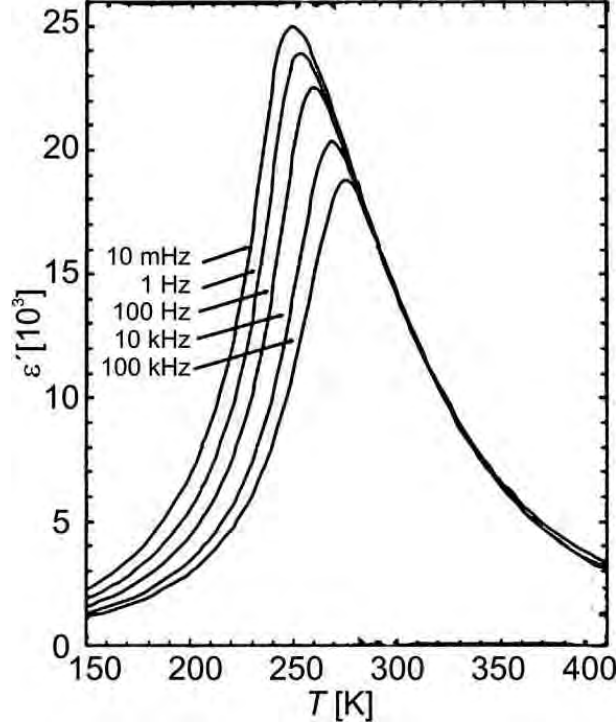


Figure 1.8: The temperature dependence of the real part of the dielectric permittivity measured at different frequencies for a single crystal of the canonical relaxor compound PMN [44].

as the frequency of the probing field decreases (Fig. 1.8); (ii) a slow degeneration of the hysteresis loop as the temperature increases, indicating that the spontaneous polarization does not disappear suddenly at T_m as it is for a classical ferroelectric such as BaTiO_3 , but decays more gradually to zero at a temperature far above the value of T_C ; and (iii) an absence of apparent symmetry change as the temperature is lowered down the DPT without any applied external field. To explain the relaxor behavior, Smolenskii et al. proposed the existence of composition fluctuations [45]. Because of the dependence of T_m with the composition, different microregions of the crystal have different transition temperatures. Therefore, the global phase transition of the crystal consists in a great number of phase transitions of the microregions and is consequently observed in a wide temperature range. This induces an intimate mixture of ferroelectric (polar) and paraelectric (non-polar) regions, in a wide temperature range. Unlike the long-range ordered state with macroscopic polarization in normal ferroelectrics, short-range ordered polar nanoregions (PNRs) appear in relaxors [46–49].

Inducing the polar nanoregions (PNRs) to reduce the P_r and decreasing the grain size to submicron scale to improve the electric breakdown strength have gained attention to achieve high energy density and efficiency in dielectric capacitors for high power energy storage [50–52]. Recently, Yan et al. constructed $(1-x)\text{Bi}_{0.5}\text{Na}_{0.5}\text{TiO}_3 - x\text{SrNb}_{0.5}\text{Al}_{0.5}\text{O}_3$ ceramics by introducing the Sr^{2+} ion and $(\text{Al}_{0.5}\text{Nb}_{0.5})^{4+}$ complex-ion into A-site and B-site of BNT ceramic, respectively, to induced PNRs [53]. Superior energy storage properties with W_{rec} of 6.64 J/cm^3 and η of 96.5% and ultra-high-power density of 131.75 MW/cm^3 can be achieved simultaneously when $x=0.20$.

Though, relaxor ferroelectric systems are relatively limited and the majorities are lead-containing compositions [54]. Pb-based relaxors like PMN, PZN and PLZT were intensively investigated for energy-storage applications due to their excellent dielectric and ferroelectric properties. Nevertheless, the lead-containing ferroelectric materials are suffering from the health safety issue related to the lead-caused high-toxicity [55–57], despite their remarkable properties. Consequently, there is a current upsurge in research on the development of lead-free ferroelectric materials with comparable properties to replace lead-based materials [58–60]. This includes: $(\text{K}_{0.5}\text{Na}_{0.5})\text{NbO}_3$ (KNN), $(\text{Bi}_{0.5}\text{Na}_{0.5})\text{TiO}_3$ (BNT), BiFeO_3 (BFO), BaTiO_3 (BT) and $(1-x)\text{BaZr}_{0.2}\text{Ti}_{0.8}\text{O}_3 - \text{Ba}_{0.7}\text{Ca}_{0.3}\text{TiO}_3$ based compositions. Ogihara et al. reported high energy storage density of 6.1 J/cm^3 at 730 kV/cm and relatively low permittivity of 700 at 1 kHz in $0.7\text{BaTi}_3 - 0.3\text{BiScO}_3$ (BT-BS) thick film at room temperature [61]. With addition of $(\text{K}_{0.5}\text{Bi}_{0.5})\text{TiO}_3$ to the BT-BS system, the permittivity could rise further to 1670, where the energy density was reported to be 4 J/cm^3 at 220 kV/cm as observed by Lim et al. [62]. Of particular interest, relaxors with high energy efficiency $>96.5\%$ was found to exhibit minimal electric field dependence, due to their negligible remnant polarization and high insulating characteristics. Wang et al. reported enhanced energy storage density of 1.13 J/cm^3 at 143.5 kV/cm and high energy efficiency of 95.8 in $\text{BaTiO}_3 - \text{Bi}(\text{Mg}_{2/3}\text{Nb}_{1/3})\text{O}_3$ ceramics [63]. Puli et al. observed a giant energy storage density of 93.52 J/cm^3 at an applied electric field of 3470 MV/cm in $0.5\text{BaZr}_{0.2}\text{Ti}_{0.8}\text{O}_3 - 0.5\text{Ba}_{0.7}\text{Ca}_{0.3}\text{TiO}_3$ (BZT–BCT) thin films [64].

1.3.3 Factors affecting the permittivity and the BDS

Generally, the dielectric properties (dielectric permittivity, dielectric loss, breakdown strength) depends on various factors such as temperature, intensity and frequency of electric field, humidity, radiation effect, mechanical stress etc. For instance, an applied DC voltage reduces the dielectric constant while an applied AC voltage within a reasonable range tends to increase dielectric constant. Besides, the presence of humidity and moisture affects the important parameters of dielectric materials. It reduces the dielectric strength of the material to a great extent, and the temperature coefficient for loss factor may have either positive or negative sign, depending upon moisture content. An increase in loss angle is also a worse result of humidity. This topic is beyond this study. In this work we aim to describe the effects of grain size and porosity on the dielectric permittivity and the breakdown strength in ferroelectric materials.

1.3.3.1 Grain size

The grain size is known to affect the dielectric permittivity of the material with maximum properties reported for grain sizes in the 0.8–1 μm size range. This is a result of (i) the trend toward increasing permittivity because of the increase in internal stress when grains decrease in size [65]. As the grain size decreases, the number of domains that can be supported within a grain also decreases, resulting in an increase in internal stress and an increase in relative permittivity. When the grain size is below a critical size (1 μm or less), the grain is single domain and a higher internal stress is expected. (ii) The increase in the proportion of grain boundaries, resulting in an increase in the volume fraction of degraded material, thus causing a reduction in relative permittivity. Finally, at very small grain sizes the internal stresses may even suppress the Curie temperature phase transformation decreasing the relative permittivity.

The BDS of ceramics are found to increase as the grain size decreases [66, 67]. It was reported that the BDS have an exponential decay relationship with the grain size, i.e., $BDS \propto (\text{grain size})^{-a}$, with exponent values being in the range of 0.2–0.4 [68]. This can

be explained by the depletion space charge layers that build up at the grain boundaries in ceramics, leading to high resistivity of the grain boundary. The grain boundaries give rise to depletion regions, which can act as barriers for the charge carriers transporting across the grain boundaries. Though, it was reported that the grain size itself does not have a huge direct effect on the BDS of the material, as the atomic structure is unchanged (except at extreme small sizes) [69]. It does, however, affect the proportion and nature of grain boundaries and pores. As grains become larger, pores are also likely to be larger and more likely to be open in nature due to reduced sintering.

1.3.3.2 Porosity

Open porosity may increase the dielectric permittivity if charged species adsorb onto pore surfaces [69]. In addition, the presence of porosity may allow some of the stress associated with the enhancement of relative permittivity in ferroelectrics to be relieved, thus resulting in a decrease in properties [70]. This effect is likely to be negligible in comparison to the removal of material from the system. Nevertheless, the effect of porosity on the BDS will be markedly different depending on whether it is open or closed. With closed porosity, each pore is isolated from the next. When open porosity is present, the individual pores are connected together, forming a network from one side of the film to the other. Open porosity can lead to adsorption of conductive species which significantly reduces breakdown strength [69]. Therefore, the microstructure of ferroelectric materials has a large effect on the dielectric properties. Generally speaking, dense ceramics with fine and uniform grains have high BDS. Therefore, fine-grain ceramics with high density may feature slim hysteresis loops and high BDS, which are beneficial to the energy storage performance, including the energy density and efficiency.

1.3.4 Ferroelectric ceramic/polymer composites

Ferroelectric ceramics own high dielectric constant, however, their high dielectric loss, low breakdown strength, poor processability and lack of flexibility significantly limit their

application in energy storage or insulation technologies [39, 71]. An ideal high- k material will not only have a high dielectric constant but also will display low dielectric loss, high breakdown strength, and good processability [72–75]. The term high- k dielectric refers to a material with a high dielectric constant as compared to silicon dioxide. In general, it is difficult to find a single material combining all the desirable properties for practical applications. Polymers usually have a high breakdown strength and ease of processing, but most have a low dielectric constant [76–78]. It is clear that increasing electrical breakdown strength and enhancing dielectric constant are the two efficient paths for obtaining higher energy storage density, while these two paths are always inconsistent, according to the Eq. 1.16 [79]. Thus, the higher the permittivity is, the lower the electromechanical breakdown strength is. Hence, it is reasonable to harness the advantages of both polymers and ceramics to design advanced high- k with enhanced electrical properties [80, 81].

$$E_{EM} = 0.6 \sqrt{\frac{Y}{\varepsilon_0 \varepsilon_r}} \quad (1.16)$$

Here E_{EM} electromechanical breakdown strength, the factor 0.6 corresponds to the point where mechanical instability occurs and Y is Young’s modulus.

Usually, the composites do not exhibit the expected properties (possessing high permittivity and high BDS simultaneously). There are many factors affecting the dielectric properties of the composites, such as the volume fraction, dispersion, and orientation of the fillers. Even if, a high-volume fraction of ceramic fillers provides enhanced permittivity of the composites, the BDS of the composites decreases monotonically as the filler volume fraction increases due to the filler’s percolation and the porosity of the composite [82]. Furthermore, the dispersion of the nanofillers inside the polymer matrix could affect the dielectric properties of the composites. Since, the surface energy of particles increases significantly with decreasing size down to the nanoscale, this results in the agglomeration of the nanoparticles which become separated from the polymer matrix [83]. To overcome this drawback, surface treatment of the ceramic nanofillers by surfactant is usually used in the synthesis process [84]. However, most of the surfactants and polymers are only physisorbed on particles by electrostatic attraction or by Van der Waals forces, and the residual surfactant could lead to high leakage current and dielectric loss, however, thus greatly decreasing the BDS [85]. Chang et al. proposed an efficient approach to

derive hydroxyl groups on the surface of barium titanate nanoparticles to improve its chemical modification ability [86]. Several strategies have been devoted for nanoparticles surface modification including hydroxylation [86–90], coupling agents [91], liquid-crystalline polymers [92], and other organic molecules [93, 94], to improve the performance of high- k polymer nanocomposites. However, these methods still have some limitations in realizing the full potential of high- k polymer nanocomposites because the modifiers themselves usually do not play a significant role in the property enhancement of the nanocomposites. Additionally, the orientation of ceramic filler, especially nanofibers and nanoplates, in the polymer matrix also affects the macroscopic properties of the ceramic-polymer composites. Another significant factor is the aspect ratio of the nanofibers, where a higher aspect ratio gives rise to a higher dielectric constant of the composite [95]. In zero-directional (0D) nanofillers, to achieve a high-permittivity nanocomposite, a high-volume fraction (>50 vol%) of nanoparticles is required. Nevertheless, this can cause low mechanical flexibility and reduced breakdown strength of the nanocomposite. However, while dispersing one-directional filler with high aspect ratio in the polymer matrix, improved dielectric properties and energy storage performances are obtained with respect to the 0D ceramic fillers. To predict the breakdown phase evolution under applied electric fields, Shen et al. performed a 2D simulation in BaTiO₃/PVDF composite [96]. The BaTiO₃ nanoparticles are randomly distributed in the polymer matrix, while the nanofiber orientation is perpendicular to the applied electric field (Figs. 1.9a–h). It is found that the breakdown paths tend to penetrate the nanofibers instead of going around them, due to the fact that the breakdown path cannot penetrate nanofibers until the applied field surpasses a critical value, a composite filled with nanofibers possesses higher BDS than one with nanoparticles. Moreover, Shen et al. demonstrated that the BDS of composites can also be impacted by the orientation of the ceramic fillers, where nanofibers and nanosheets parallel to the composite surface can enhance the BDS of the composite (Figs. 1.9i–k) [96]. It is concluded that higher energy storage performance of polymer-ceramic composites can be expected if the surfaces of the ceramic fillers are well-modified and their orientation is well-controlled. Recently, Zhang et al. reported a high energy density of 25.5 J/cm³ in BaTiO₃ nanofibers/P(VDF-HFP) nanocomposites by controlling the distribution and

orientation of the nanofillers [97].

Another reason for the inconsistency between the real and expected dielectric properties of a composite is the mismatch of relative permittivity between the ceramic fillers and polymer matrix, which often leads to the development of an inhomogeneous electric field distribution throughout the composite. This generally leads to local electric field intensification and interfacial polarization and thus to a significant reduction of the breakdown strength of dielectric composites [98–100]. In detail, nanoparticles of high permittivity act as electrical defect centers in filled polymers. Such defect centers effectively distort the distribution of electric field, making the local electrical field in the matrix much higher than the average electric field. This field expulsion lowers the overall energy storage because it results in the breakdown of the polymer at an electric field much lower than the intrinsic BDS of the polymer. Dang et al. numerically simulated the electric field distortion in various inorganic/polymer nanodielectric materials, as shown in Fig. 1.10, and observed that for composites with the same shape, size and distribution of the filler, the larger permittivity contrast in the two phases creates a larger local field distortion [99]. Moreover, as compared with the small-particle-filled polymer composite, a larger size of filler would be prone to inducing a higher degree of field intensification (see Figs. 1.10b, d). These results indicate that homogenous inclusion of small nanoparticles with comparable permittivities to the polymer matrix can effectively create dielectric homogeneity in the nanocomposites. Otherwise, ceramic/polymer composites are applied in high-temperature ranges to a restricted degree due to the low glass transition temperature (T_g) of the polymer and increased losses at elevated temperature. In addition, a temperature dependence of the dielectric properties of the ceramic component is also to be taken into account. Moreover, the low T_g and high thermal expansion of the polymer matrix limit the operational temperature range of the composites. Li et al. thermally crosslinked the divinyltetramethyldisiloxane-bis(benzocyclobutene) (BCB) in the presence of boron nitride nanosheets (BNNSs), and compared the dielectric and energy storage properties of the composite c-BCB/BNNS with some high-temperature polymer films like polyetherimide and polyimide, and found that the c-BCB/BNNS exhibited higher energy density and efficiency with good temperature stability (from room temperature to 250 °C) [75]. The

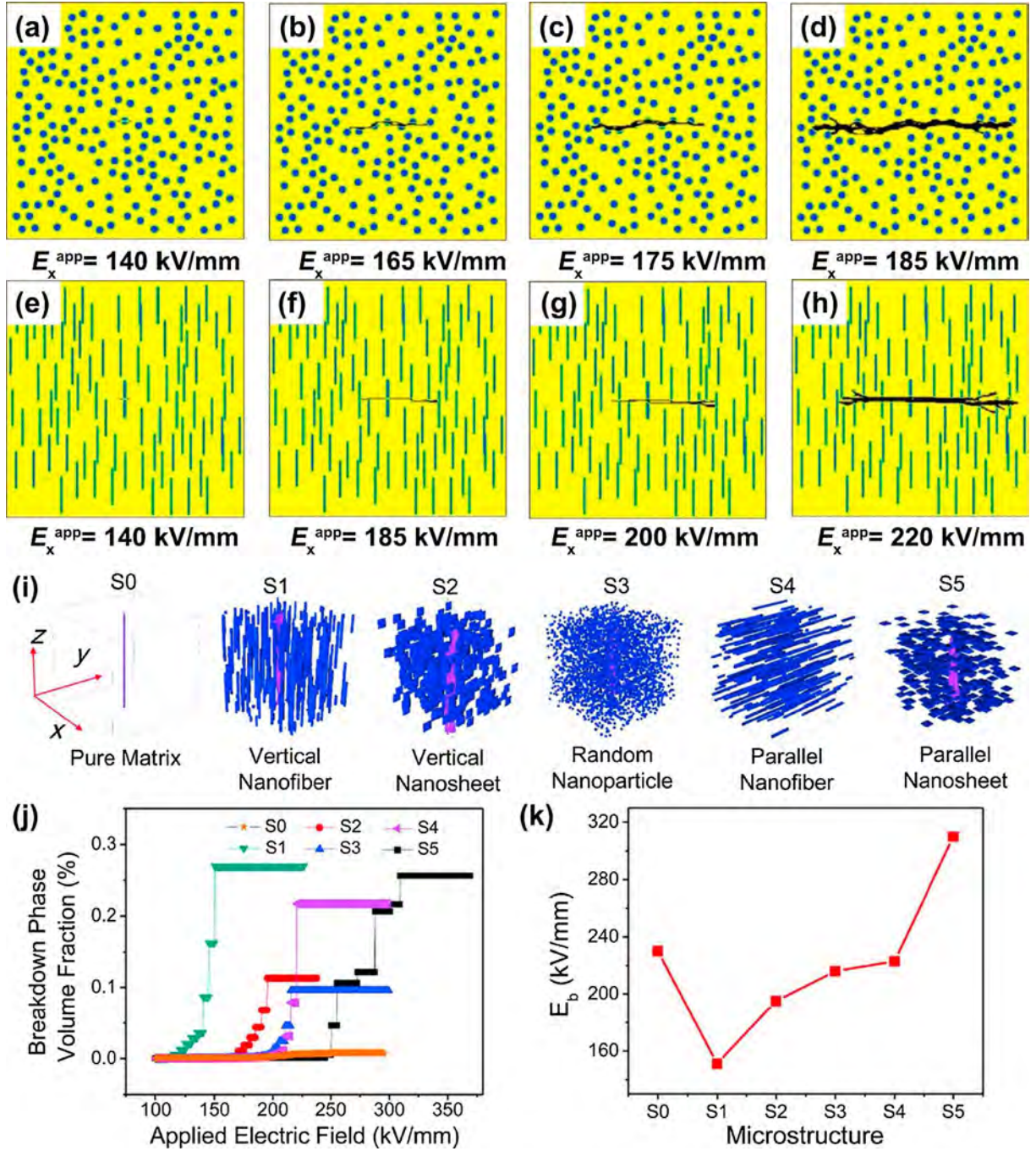


Figure 1.9: (a-h) Breakdown phase evolution processes for composites having the same volume fraction of ceramic fillers under applied horizontal electric field using a phase-field model: (a-d) filled with nanoparticles and (e-h) filled with nanofibers. (i) Breakdown phase morphology in composites with different microstructures; (j) evolution of the breakdown phase fraction under an applied electric field in the z-direction; (k) BDS of the corresponding microstructures [68].

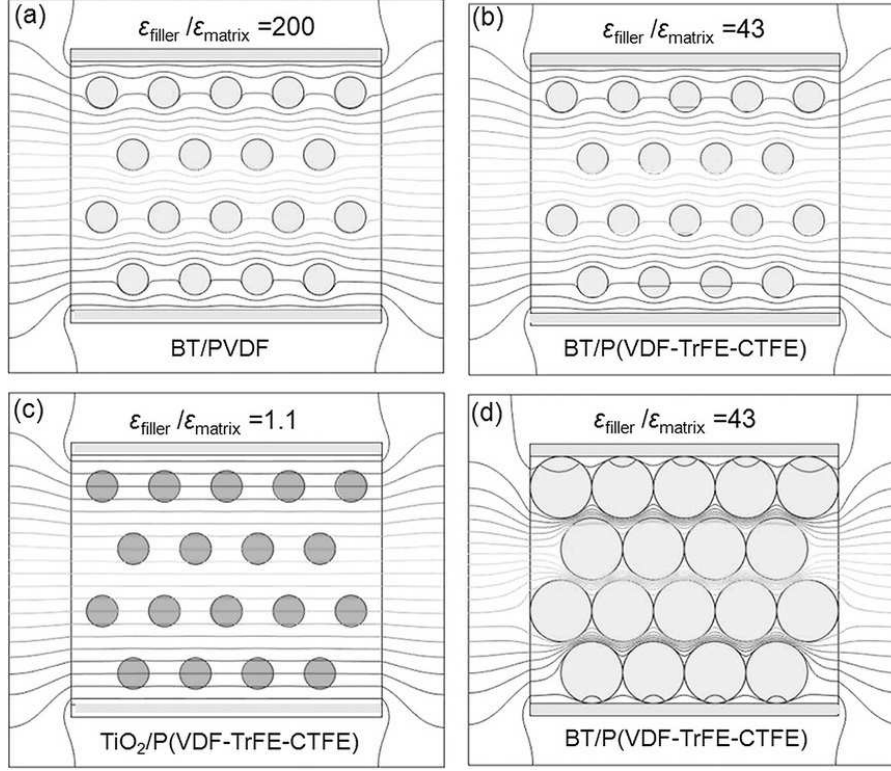


Figure 1.10: The outline contours of the numerically simulated electric field distortion in different ceramic/polymer composites: (a) BaTiO₃/PVDF, (b) BaTiO₃/P(VDF-TrFE-CTFE). (c) TiO₂/P(VDF-TrFE-CTFE) and (d) BaTiO₃/P(VDF-TrFE-CTFE) nanocomposite with BaTiO₃ nanoparticles of larger size [99].

good temperature stability is attributed to the improved thermal conductivity due to the presence of boron nitride nanosheets (BNNSs). In addition, the Young's modulus is increased owing to the introduced BNNSs. According to Eq. 1.16, the enhanced Young's modulus impedes the occurrence of electromechanical breakdown. Therefore, embedding fillers with high thermal conductivity in polymers is a potential strategy to enhance the thermal stability of the energy storage density.

Then again, compared to the composite material, a pristine polymer cannot have all the excellent properties like mechanical strength, low coefficient of thermal expansion, low friction during relative motion, shock resistance to externally applied loads, lower thermal or chemical degradation, etc. Fillers have significant roles in changing properties of many polymers. The effect of fillers on properties of the composites depends on their particle size, shape, and quantity as well as on their interaction with the polymer matrix. Alignment techniques are very useful to align low fraction of nanofillers in polymer

composites. Better improvement in mechanical, thermal, and electrical properties could be attained along the filler aligned direction. Srivastava et al. prepared $\text{CaCu}_3\text{Ti}_4\text{O}_{12}$ (CCTO) and $\text{Ca}_{1-3x/2}\text{La}_x\text{Cu}_3\text{Ti}_4\text{O}_{12}$, $x = 0.05$ (LaCCTO) PVDF-based composites, and observed that the Young's modulus value increased to 1154 and 1363 MPa for PVDF-20C and PVDF-20LaC composites, respectively, compared to 920 MPa in neat PVDF [101]. This increment was attributed to good interaction between stiffer ceramic and PVDF matrix thus making composites stiffer than pure PVDF. Besides, elongation at breaking point decreased from 30% in case of PVDF to 16% and 14% in case of PVDF-20CCTO and PVDF-20LaCCTO composites, respectively. Ceramic particles act as defects from macroscopic point of view which inhibit the PVDF chains from packing with each other and result in the reduction in elongation at breaking point in the composites.

Ceramic/polymer composites were extensively investigated for energy storage applications. Xie et al. prepared uniform morphology BaTiO_3 nanowires with high aspect ratio (>100) *via* stirring hydrothermal method, and fabricated $\text{BaTiO}_3/\text{P}(\text{VDF-CTFE})$ nanocomposite films by solution casting method using dopamine modified [102]. At 3 vol% of BaTiO_3 nanowires, a maximum dielectric displacement of $9 \mu\text{C}/\text{cm}^2$ under the electric field of 3000 kV/cm, and an enhanced energy density of $8.4 \text{ J}/\text{cm}^3$ at 2700 kV/cm were achieved. Zhang et al. reported the synthesis of BaTiO_3 nanofibers with different aspect ratio by a two-step hydrothermal method, investigated the dielectric properties and the and energy storage of the $\text{BaTiO}_3/\text{P}(\text{VDF-HFP})$ nanocomposites [103]. It was found that the BaTiO_3 nanofiber's aspect ratio increased the dielectric constant and the maximum electric displacement of the nanocomposites, while the breakdown strength decreased. The nanocomposites with highest aspect ratio of BaTiO_3 nanofibers showed a high energy storage density of $15.48 \text{ J}/\text{cm}^3$. Chi et al. prepared BCZT nanofibers with high aspect ratio by electrospinning technique, and fabricated BCZT/PVDF nanocomposite films [104]. It was observed that BCZT with large aspect ratio helps the composites to polarize at a higher field strength, hence higher polarization strength was obtained in the composites. The energy density of 3 vol% BCZT/PVDF composite was $3.08 \text{ J}/\text{cm}^3$ at 3000 kV/cm. Beside the incorporation of 1D nanofiller into the polymer matrixes improve the energy density at low concentration, due to the enhancement of local fields, 1D materials possess a

smaller specific surface, which is beneficial for decreasing the surface energy and alleviating the agglomeration of the nanofillers in the polymeric matrixes.

1.4 Ferroelectric based-ceramics for energy harvesting: towards piezoelectric nanogenerators

1.4.1 Background on piezoelectric effect

The piezoelectric effect is a unique property of certain crystals which generate an electric field or a current if they are subjected to physical constraints and vice versa. The direct piezoelectric effect was discovered by the brothers Pierre Curie and Jacques Curie in 1880, when conversion of mechanical energy into electrical energy [105]. The same effect has been observed in reverse by Gabriel Lippmann in 1881, when an electric field is imposed on the crystal, a stress on its structure is induced (converse piezoelectric effect) as illustrated in Fig. 1.11. The piezoelectric effect occurs in most classes of noncentrosymmetric crystals, in which electric dipole moments can be induced as a result of applied stress. The most

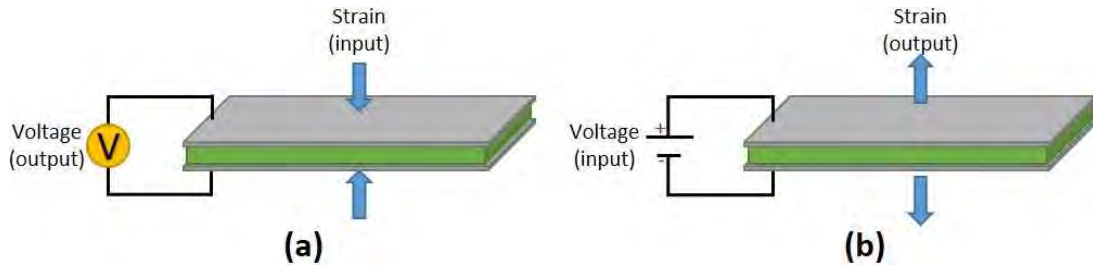


Figure 1.11: Schematic representation of the (a) direct and converse piezoelectric effects.

commonly used piezoelectric coefficient, d_{ij} , is the ratio of the surface charge per unit of mechanical stress applied for the direct effect (mostly used in sensors) (Eq. 1.17), and the ratio of the deformation to the electric field for the opposite effect (mostly used in actuators) (Eq. 1.18).

$$d_{ij} = \frac{D_i}{\sigma_{ij}} \quad (1.17)$$

$$d_{ij}^* = \frac{S_j}{E_i} \quad (1.18)$$

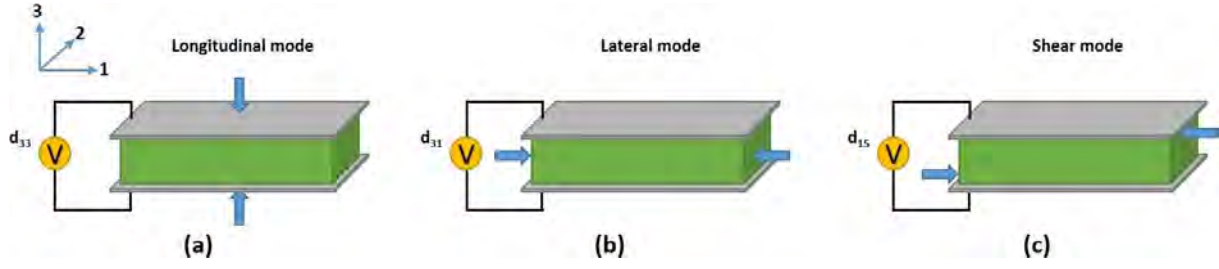


Figure 1.12: Schematic representation of the deformation modes of a piezoelectric material (a) longitudinal, (b) lateral, and (c) shear mode.

Here, D_i , σ_{ij} , S_j , E_i are dielectric displacement, applied stress, strain developed, and applied electric field.

These coefficients are expressed in Eqs. 1.17 and 1.18 with the notation of Voigt to indicate the direction of polarization and the direction of the mechanical stress according to the i and j axes, respectively. The three important operation modes of a piezoelectric are illustrated in Fig. 1.12. The piezoelectric voltage coefficient g_{ij} is another important coefficient in piezoelectric materials. It signifies the electric field developed along the i -axis when the piezoceramic is stressed along the j -axis.

$$g_{ij} = \frac{d_{ij}}{\varepsilon_0 \varepsilon_{ij}} \quad (1.19)$$

Another important parameter of a piezoelectric material is the electromechanical coupling coefficient k_{ij} , which evaluates the ability of a material to convert mechanical energy into electrical energy and vice versa. It is between 0 and 1 and must be as high as possible. This coefficient is defined as follows,

$$k_{ij} = \frac{d_{ij}}{\sqrt{k_i \varepsilon_{ij}}} \quad (1.20)$$

1.4.2 Piezoelectric nanogenerators (PNGs)

Piezoelectric nanogenerators (PNGs) are growing as a promising technology for harvesting random mechanical energy into electric energy through nanometer-scale piezoelectric materials. Contrary to chemical batteries, PNGs are eco-friendly and can provide sustainable electrical energy [106]. The first piezoelectric nanogenerator was developed in 2006 by Wang et al. [107]. It is a simple device that uses zinc oxide (ZnO) nanowires to

convert mechanical energy into electrical energy. The operating principle is illustrated in Fig. 1.13. When the nanowires are deformed by weak mechanical forces, piezoelectric potentials are generated at the upper and lower ends of the nanowires. Pulse currents are generated by external circuits to convert mechanical energy into electrical energy. This method of using nanowires to generate electrical energy under the action of external forces embodies the energy generation function of materials at the nanoscale. The work of Wang is widely credited as the starting point for nanostructured piezoelectric harvesting systems. Since 2006, various PNGs have been designed using piezoelectric materials to convert mechanical energy into electrical energy. Zhu et al. compressed the PMMA-coated ZnO nanorod array grown on Si with a linear motor. An open-circuit voltage up to 37 V after rectification through a bridge rectifier and a short-circuit current density of $12 \mu\text{A}/\text{cm}^2$ were produced [109]. Though, the PNGs based on rigid substrates could harvest the energy mainly from compression. Thus, the design of alternative device based on flexible substrates, which could be strained through bending method to extract a large amount of energy from a range of situations is highly desired. In 2008, Xu et al. developed a PNG based on a single ZnO nanowire fixed horizontally on a flexible substrate generated an alternating voltage of 65 mV during the periodic folding process [110]. In 2012, Park et al. introduced a new concept of PNG based on a composite film PNG formed by combining BaTiO₃ nanoparticles incorporated into the polydimethylsiloxane (PDMS) polymer matrix produced an output voltage and current of 3.2 V and 350 nA respectively [111]. These high-outputs were originated from the excellent piezoelectric properties of BaTiO₃ and the flexibility of PDMS. During the same year, an PNG formed of a piezoelectric matrix based

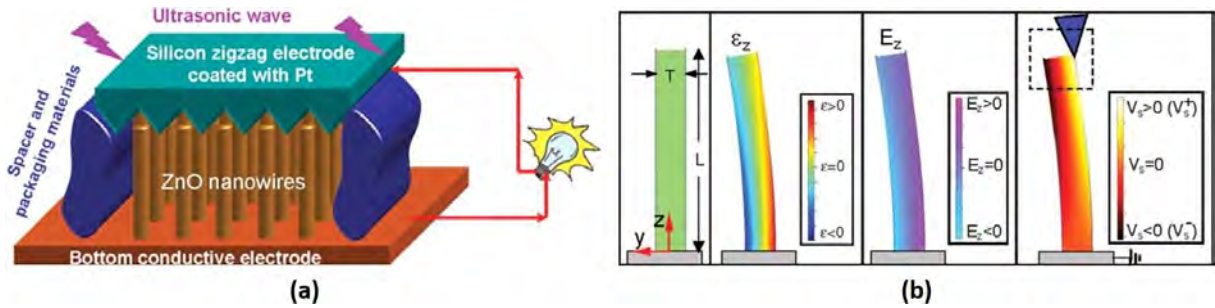


Figure 1.13: (a) Schematic diagram showing the design and structure of the piezoelectric nanogenerators [108] and (b) schematic definition of a nanowire and the coordination system [107].

on ZnO was developed delivering an output voltage sufficient to drive portable microelectronic devices [111]. There exist about 200 piezoelectric materials for energy harvesting applications out of which piezo-ceramics (mainly PZT and BaTiO₃) have attracted major attention due to their better piezoelectric properties as compared to other piezoelectric materials [112].

1.4.3 The first principle theory of nanogenerators

The driving force for the nanogenerator is Maxwell's displacement current, which is caused by a time variation of the electric field plus a media polarization term. For power generation, the polarization should contain a term that is contributed by the strain field such as surface contact electrification (e.g., triboelectric effect) and the piezoelectric effect, which is independent of the presence of an electric field. To explain the contribution made by contact electrification-induced electrostatic charges in Maxwell's Equations, an additional term P_s was added in the displacement vector D ($D = \varepsilon_0 E + P + P_s$) by Wang in 2017 [113, 114]. Here, the first term polarization vector P is due to the existence of an external electric field, and the added term P_s is mainly due to the existence of the surface charges that are independent of the presence of electric field.

The reformulated Maxwell's Equations are:

$$\nabla \cdot D' = \rho' \quad (1.21)$$

$$\nabla \cdot B = 0 \quad (1.22)$$

$$\nabla \cdot E = -\frac{\partial B}{\partial t} \quad (1.23)$$

$$\nabla \cdot H = J' + \frac{\partial D'}{\partial t} \quad (1.24)$$

where $D' = \varepsilon_0 E + P$, and the volume charge density (ρ') and the density of current density (J') can be redefined as,

$$\rho' = \rho - \nabla \cdot P_s \quad (1.25)$$

$$J' = J + \frac{\partial P_s}{\partial t} \quad (1.26)$$

Then, the newly revised Maxwell's displacement current (J_D) can be calculated as,

$$J_D = \frac{\partial D}{\partial t} = \varepsilon_0 \frac{\partial E}{\partial t} + \frac{\partial P_s}{\partial t} \quad (1.27)$$

Here, the first term $\varepsilon_0 \frac{\partial E}{\partial t}$ represents the displacement current due to time variation electric field and the electric-induced medium polarization, and it can generate the corresponding magnetic field. This is known as the origin of the electromagnetic wave, which was first proposed by Maxwell. This component of displacement current has driven developing radio, radar, TV and long-distance wireless communication in the last century. The second term, $\frac{\partial P_s}{\partial t}$, is the displacement current due to nonelectric field but owing to external strain field. This term contributes to the output current of nanogenerators and is related to the driving force (the Wang term). Nanogenerators could have extensive applications in internet of things (IoT), blue energy, and even big data, which will impact the world for the future. Nanogenerators could be regarded as another important application of Maxwell's equations in energy and sensors (after the electromagnetic wave theory and technology).

1.4.4 The working mechanism of a PNG

The working principle of a PNG is illustrated in Fig. 1.14. An insulator piezoelectric material is covered by a top and bottom electrodes on its two surfaces (Fig. 1.14a). A vertical mechanical deformation results in the generation of piezoelectric polarization charges at the two ends of the material (Fig. 1.14b). An increase of the applied force results in higher polarization charge density (Fig. 1.14c). The electrostatic potential created by the polarization charges is balanced by the flow of electrons from one electrode to the other through an external load. This is the process of converting mechanical energy into electric power. If the density of the piezoelectric polarization charges on the surface is $\sigma_p(z)$, and the corresponding charge density of free electrons in the electrode is $\sigma(x)$, which is a function of the thickness of the piezoelectric material z with considering the strain introduced by applied force [114].

1.4.5 PNGs performance characterization

Such new device designs present a new range of challenges for testing and reporting of performance. Output from these devices has been reported in a variety of ways. Most commonly the open-circuit voltage (V_{oc}) and/or short-circuit current (I_{sc}) or current density ($J_{sc} = I_{sc}/area$) is reported versus time as an impulsive strain is induced in the device. Sometimes the peak values are used to calculate the peak power ($P_{peak} = V_{oc-peak} \times I_{sc-peak}$) or equivalent values per area or per volume.

1.4.5.1 Open-Circuit Voltage V_{oc}

When a PNG is subjected to mechanical force, which results in a change in polarization, this change in polarization corresponds to charge build-up that can be measured as generated voltage, according to Eq. 1.28. Open-circuit voltage is the term commonly used to describe generated voltage from a device when a load is not connected across its terminals. During open-circuit voltage measurement, the current passing through the device circuitry is minimum (ideally zero current).

$$V_{oc} = \frac{d_{ij}}{\varepsilon_0 \varepsilon_{ij}} \sigma_{ij} g_e \quad (1.28)$$

From Eq. 1.28, it is found that the open circuit voltage (V_{oc}) is proportional to the applied stress σ_{ij} , the piezoelectric coefficient d_{ij} , and the gap distance between electrodes g_e .

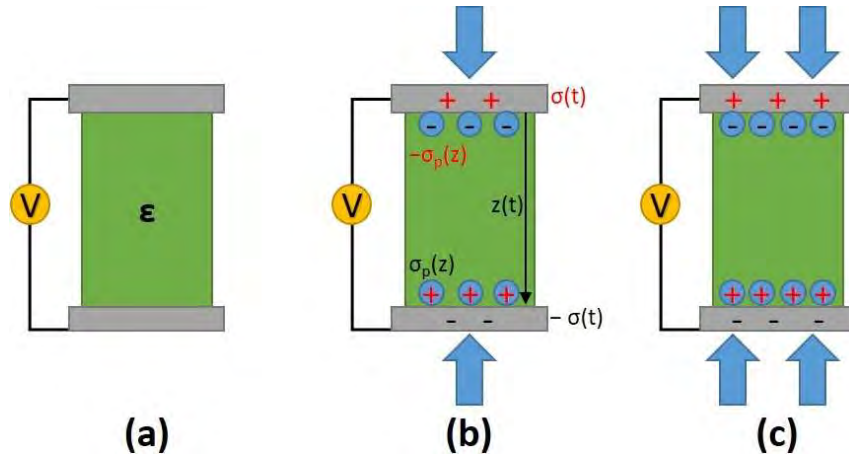


Figure 1.14: Illustrations about the working mechanisms of a piezoelectric nanogenerator with the increase of the applied stress.

1.4.5.2 Short-Circuit Current I_{sc}

The strain-induced charge displacement in the PNG causes voltage output generation, and the current output from the piezoelectric material depends on the conductivity of material. Therefore, the current flows due to free-charge carriers present in the piezoelectric material. The flow of current is measured across the device terminals. The condition at which the current is measured across minimum impedance (ideally zero impedance) is called short-circuit current. At short-circuited condition a load is not connected across PNG terminals and the terminals are effectively connected across a short-circuit.

1.4.5.3 Maximum Power Output

Energy harvesters present a source impedance to the load circuit, and power output is maximized when the load impedance is matched to the source impedance. Therefore, to evaluate the maximum power of a PNG, it is common to vary the load impedance to find the maximum power point.

1.4.6 PNG-based Piezoelectric ceramics

1.4.6.1 ZnO

As stated before, zinc oxide is the first material that has been studied for the manufacture of PNGs [107]. ZnO is an important functional material due to its optical, semiconductor and piezoelectric properties. Its chemical composition, the size of its particles and its morphology are easy to control. In addition, the piezoelectric effect generated by the ZnO nanowires causes spontaneous polarization of the charges, thereby converting mechanical energy into electrical energy and temporarily storing energy in the nanowires. Although PNG-based ZnO can generate relatively low voltages and currents, which cannot really meet the energy requirements of microelectronic devices. This is due to the fact that the ZnO material itself has poor piezoelectric characteristics, therefore it is necessary to find alternative materials [106, 115, 116].

1.4.6.2 PZT

Piezoelectric materials based on lead zirconate titanate (PZT) have excellent piezoelectric properties. It should be noted that good crystallinity and high dielectric constants are the major criteria sought for the design of the PNGs [117, 118]. Due to the high piezoelectricity of the PZT material, the performance of PZT-based PNGs exceeds that of ZnO. However, the lead element in PZT has extremely toxic effects on human health and the environment. Therefore, PZT materials cannot be widely used in microelectronic systems and devices [119]. Research is therefore directed towards piezoelectric materials based on lead-free materials with piezoelectric properties comparable to those of PZT [55, 57, 120].

1.4.6.3 BaTiO₃

So far, researchers have developed many lead-free materials such as barium titanate (BaTiO₃), sodium and potassium niobate (KNN, KNaNiO₃), bismuth titanate (BTO, Bi₄Ti₃O₁₂) and bismuth sodium titanate (BNT, BiNaTiO₃). These ecological materials are possible alternatives to improve energy recovery. However, the piezoelectric performances of PNGs based on KNN, BTO and BNT are limited [121]. Thus, research has turned to BaTiO₃ with excellent piezoelectric properties and biocompatibility. In addition, this oxide has a much higher piezoelectric coefficient than that of ZnO [116], and can convert very low mechanical energy into electricity [10]. However, its dielectric and piezoelectric properties are weak in comparison with those of PZT. To overcome this problem, the researchers proposed the chemical doping solution of BaTiO₃ in order to improve its piezoelectric coefficient [106, 122, 123].

1.4.7 PNG-based ceramic/polymer composites

Despite the excellent piezoelectric properties of ceramics, some of their disadvantages such as rigidity, brittleness, toxicity, high density, lower voltage coefficient, and lack of design flexibility limit their energy-related application to some extent. Piezoelectric

polymers serve as a better candidate for concerned applications satisfying most of the abovementioned criteria. The mechanical flexibility, faster processing, lower fabrication cost, and biocompatibility of piezo-polymers like polyvinylidene fluoride (PVDF) and its copolymers, cellulose and their derivatives, polylactic acids (PLA), polyurethanes (PU), polyimides (PI) outspread their applications to several, energy-related systems [112]. Consequently, polymeric piezoelectric composites for energy harvesting applications are considered a significant research field which provides the convenience of mechanical flexibility, suitable voltage with sufficient power output, lower manufacturing cost, and rapid processing compared to ceramic-based composites [106,124–126]. In 2017, a composite film-based PNG formed from BaTiO₃ nanocubes immersed in the PDMS showed improved output performance (voltage: 126.3 V and current: 77.6 μ A [127]. This material paved the way for portable, continuously powered electronic devices. In 2018, the output performance of an ultra-flexible PNG, prepared from a composite of BaTiO₃ nanoparticles and PVDF (polyvinylidene fluoride), was 7 V and 2500 nA, which made the PNGs more important and more promising for practical applications [128].

1.4.8 Some applications of PNGs

1.4.8.1 Tire condition monitoring

PNGs can be used as a self-powered sensor for tire condition monitoring. In this regard, Hu et al. have integrated a PNG on the inner surface of a tire, the deformation of this latter when moving the vehicle could be exploited and converted into electrical output signals [129]. In conformity with the working area (1.5 cm \times 0.5 cm) of the device, a maximum power output density of 70 μ W/cm³ was obtained. Since the change in tire pressure and vehicle speed can cause the PNG deformation and deformation speed to change, it can be used both as a tire pressure sensor and as a vehicle speed sensor. Fig. 1.15 shows the shape change of the tire in the contact patch, a sketch of the nanogenerator, simulating the tire's deformation, and the location of the nanogenerator in the tire.

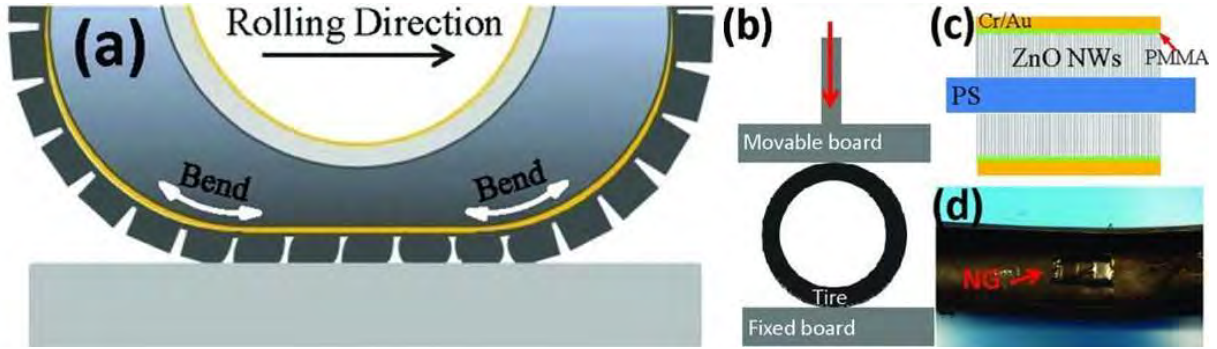


Figure 1.15: (a) Shape change of the tire in the contact patch, (b) a sketch of the nanogenerator, (c) simulating the tire's deformation, and (d) the location of the nanogenerator in tire [129].

1.4.8.2 Smart wearable fabric

Smart clothes can be woven by integrating piezoelectric materials in the fabric to convert the mechanical energy of human body motion into electric energy. matrix. Zhang et al. developed a two-dimensional fabric-like nanogenerator based on three kinds of fibers including BaTiO_3 nanowire-PVC hybrid piezoelectric fibers, conventional cotton threads and copper wires (Fig. 1.16) [130]. It was reported that, by attaching the fabric nanogenerator on an elbow pad which was bended by human arms, the nanogenerator can generate 1.9 V output voltage and 24 nA output current and the output are large enough to power an LCD display (Fig. 1.16c).

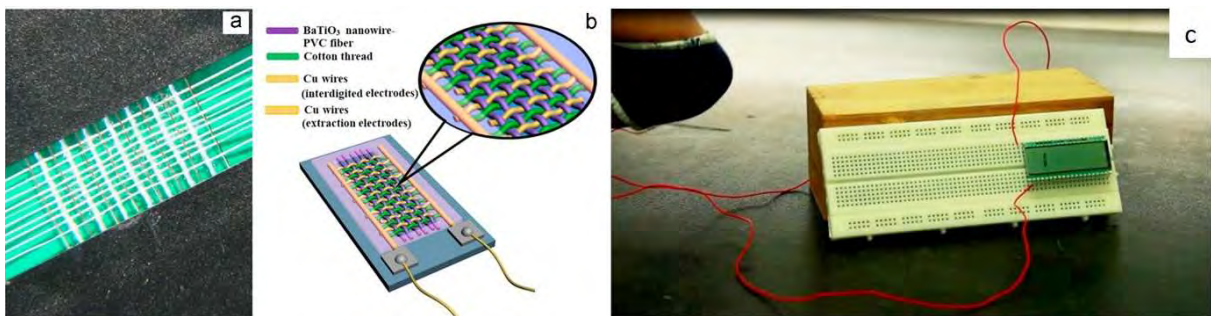


Figure 1.16: (a) A photo and (b) the structure of the fabric nanogenerator, and (c) an LCD display driven by the nanogenerator [130].

1.4.8.3 Implantable biomedical devices

Implantable medical devices have shown a rapid progress in recent years to the advancement of state-of-the-art medical practices. Though, the toxicity of chemical batteries fails to meet the power supply needs of the commonly used equipment to operate, which may restrict their application for *in vivo* applications. Moreover, these batteries of the implantable medical devices need to be changed every 7 to 10 years or even every 3 to 6 years for an implantable cardioverter defibrillator [131, 132], by surgical processes once expired, causing physical and psychological infuriation to patients and rising healthcare financial problems. Several implantable PNGs were designed to drive self-powered, wireless healthcare systems (hearth monitor, pacemaker energizer, nerve-cell stimulator, blood flow monitor, and real-time biomedical monitor). Li et al. built a nanogenerator based on a single piezoelectric ZnO fine wire that can harvest power from heart beating and breathing in a living rat under *in vivo* conditions (Fig. 1.17) [133]. PNGs were also served to control the real-time functional electrical stimulation heart beating utilizing electronic signals for contracting the heart muscles. Hwang et al. designed high-performance crystalline $(1 - x)\text{Pb}(\text{Mg}_{1/3}\text{Nb}_{2/3})\text{O}_3 - \text{PbTiO}_3$ (PMN-PT) for real-time powering of a cardiac pacemaker [131]. The used the electrical response of the implanted PNG to stimulate the heartbeat of a live rat without any other energy supply (Fig. 1.18).

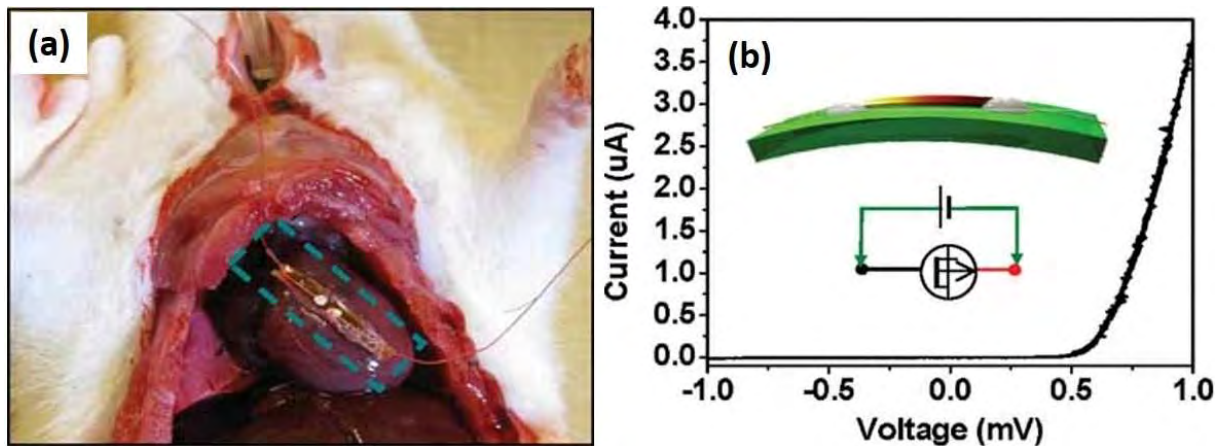


Figure 1.17: (a) A single-wire-generator (SWG) attached to a live rat's heart (b) and (b) $I - V$ characteristics of the SWG [133].

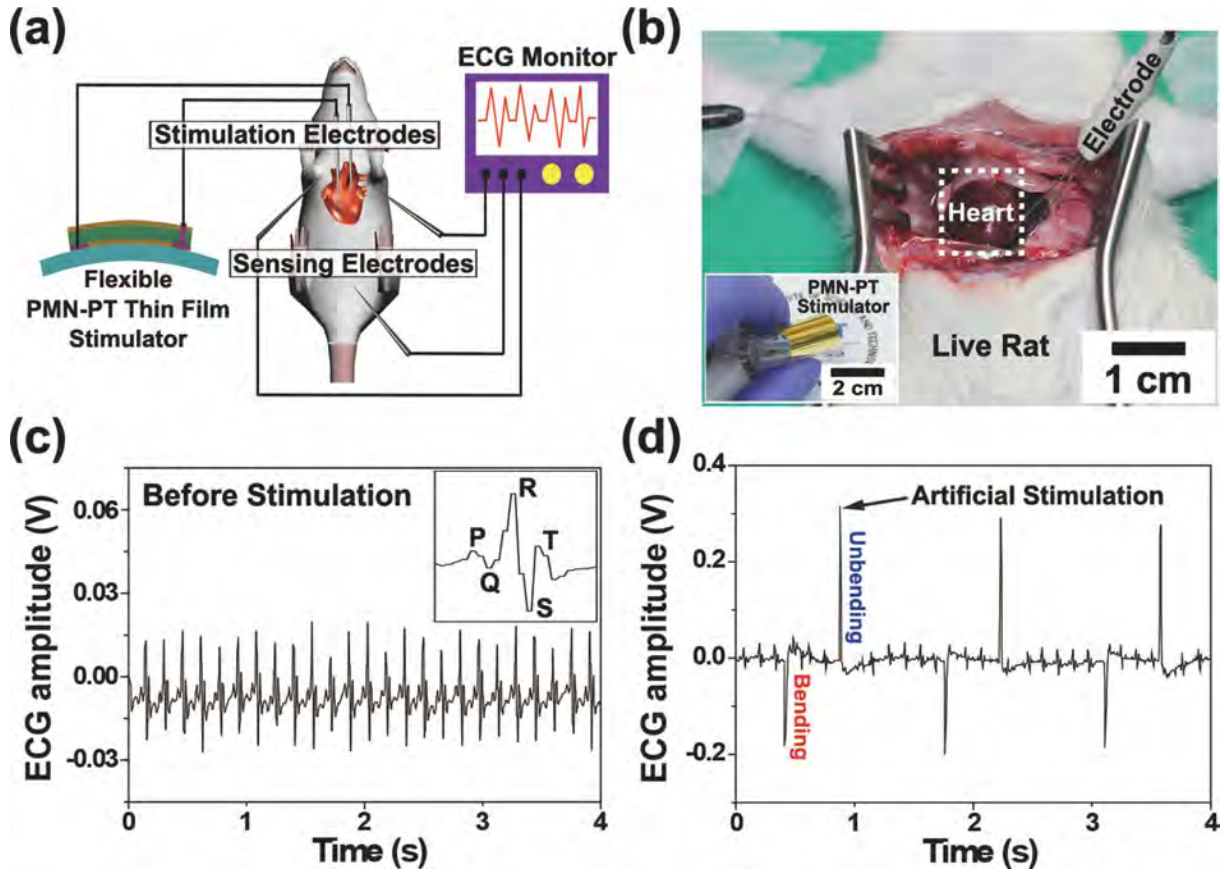


Figure 1.18: (a) A representation of a self-powered artificial cardiac pacemaker, (b) a photograph of the heart stimulation test on a live rat by PMN-PT stimulator, and (c, d) the electrocardiogram (ECG) rate in a rat heart before the stimulation and after the stimulation [131].

1.5 BCZT lead-free relaxor ferroelectric and PLA as promising materials for energy storage and harvesting?

1.5.1 BCZT lead-free relaxor ferroelectric

1.5.1.1 Contextual elements

Over the past 50 years, PZT ceramics have become the most successful piezoelectric materials in practical applications (sensors, ultrasonic generators, resonators, actuators, etc.) due to their excellent ferroelectric and piezoelectric properties [134–136]. However,

in view of the concern with environmental pollution and human health, worldwide environmental considerations are demanding the elimination of lead-based materials from all the consumer items [57, 134, 137]. This led to intensive research to find the appropriate alternative material to lead-based ceramics [57, 138]. Among this class of eco-friendly ceramics, BaTiO_3 with perovskite structure ABO_3 was extensively investigated by dint of its excellent dielectric and piezoelectric properties [139, 140]. In this purpose, BaTiO_3 is usually regarded as one of potentially promising lead-free ceramics, which was the first material practically, used to fabricate piezoelectric ceramics [58]. It is widely employed in modern technologies such as mobile electronic devices, and hybrid electric vehicles [139, 140]. Furthermore, BaTiO_3 is also a bioceramic material which does not contain any toxic or volatile elements, and its properties can be easily tailored by versatile engineering [141–143]. Pure BaTiO_3 possess high-temperature coefficient of capacitance near the T_C due to the transition from the tetragonal to the cubic phase, which results narrow dielectric peak and restricts the temperature range of application. The addition of heteroatoms can serve to form solid solutions to shift the transition temperature. BaTiO_3 , however, is limited to use as a piezoelectric material, due to multiple ferroelectric-ferroelectric phase transitions and the resulting significant temperature dependence of piezoelectric properties. From both fundamental and technical point of view, it is thus important to pay attention to BCZT a derivative of BaTiO_3 .

1.5.1.2 Structural properties

Chemical substitutions at the Ba^{2+} and Ti^{4+} sites are made to tailor the properties to meet a variety of device and performance requirements. Doping BaTiO_3 by Ca^{2+} to form $\text{Ba}_{1-x}\text{Ca}_x\text{TiO}_3$ (BCT) solid solutions have been extensively studied and used for several applications in electronic devices owing to their dielectric, ferroelectric and piezoelectric properties. This substitution caused a slight change in the TC with increasing calcium concentration, but strongly lowers the orthorhombic/tetragonal ($T_{O/T}$) transition temperature [144, 145], whereas it can improve the temperature stability of the piezoelectric properties for several practical applications [146–149]. Besides, the Zr^{4+} introduction in

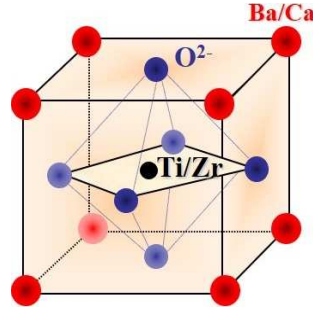


Figure 1.19: Crystalline structure of BCZT lead-free relaxor ferroelectric.

BCT to form $\text{Ba}_{1-x}\text{Ca}_x\text{Zr}_y\text{Ti}_{1-y}\text{O}_3$ (BCZT) system, expands the perovskite lattice because of the rather large radius difference between Zr^{4+} (0.72 Å) and Ti^{4+} (0.605 Å) [145, 150–154]. Consequently, the lattice distortion leads to improve the strain level and enhanced the piezoelectric effect in BCZT ceramic [155, 156]. Additionally, enhanced dielectric and ferroelectric properties were reported in BCZT [157, 158]. The crystalline structure of BCZT ceramics is depicted in Fig. 1.19.

In 2009, Liu and Ren established the first structural phase diagram of the $(1 - x)\text{BaZr}_{0.2}\text{Ti}_{0.8}\text{O}_3 - x\text{Ba}_{0.7}\text{Ca}_{0.3}\text{TiO}_3$ system, abbreviate as BCT–BZT (BCZT) as displayed in Fig. 1.20a [159]. The existence of rhombohedral (*R*)/tetragonal (*T*) and tetragonal (*T*)/cubic (*C*) phase transitions for the composition 0.5BCT–BZT, and the presence of a triple point composition near 57 °C, where *R*, *T* and *C* phases coexist were reported [159]. Four years after, and contrary to the unusual *R*/*T* phase transition reported by Liu and Ren [159], Keeble et al. re-investigated the structural phase diagram of BCZT system by using high-resolution synchrotron X-ray diffraction techniques, and have observed an intermediate orthorhombic (*O*) phase, isostructural to that present in the parent phase, BaTiO_3 , and identified the previously assigned *R*/*T* transition as a *O*/*T* transition (Fig. 1.20b) [135]. The *R*/*O* transition coalescing with the previously observed triple point, forming a phase convergence region was reported. Rietveld refinements confirm that the phase sequence observed in 0.5BCT–BZT and 0.4BCT–BZT is identical to that observed in BaTiO_3 , i.e., $R3m \rightarrow Amm2 \rightarrow P4mm \rightarrow Pm-3m$. Afterward, Fu et al. established a simplified phase diagram of $(\text{Ba}_{1-x}\text{Ca}_x)(\text{Zr}_{0.1}\text{Ti}_{0.9})\text{O}_3$ system (Fig. 1.20c) [160]. It was found that substitution of Ba by Ca ions can slightly increase the *T*/*C* phase transition temperature and strongly decrease the *O*/*T* and *R*/*O* transitions.

1.5. BCZT LEAD-FREE RELAXOR FERROELECTRIC AND PLA AS PROMISING MATERIALS FOR ENERGY STORAGE AND HARVESTING?

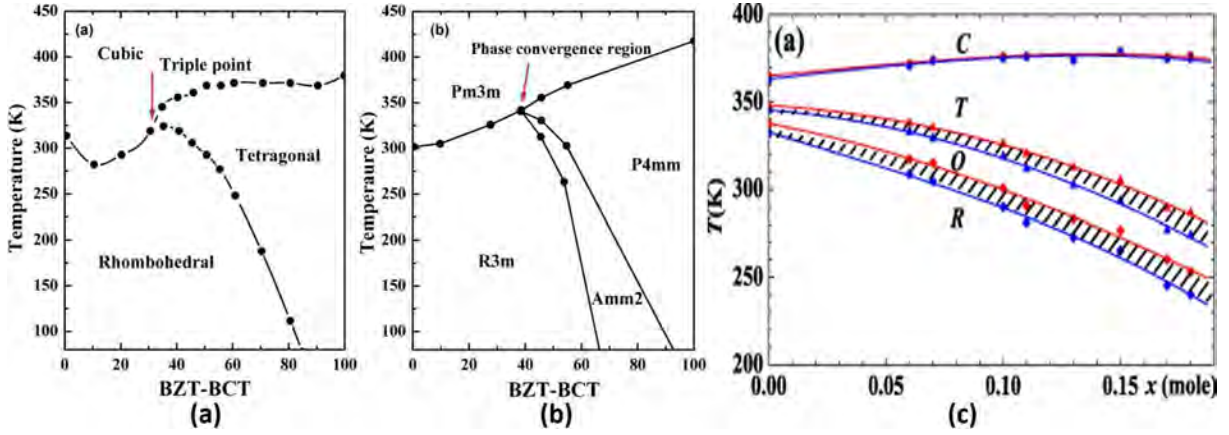


Figure 1.20: Pseudo-binary phase diagrams of BCZT system proposed by (a) Liu and Ren [159], (b) Keeble et al. [135], and (c) phase diagram of $(\text{Ba}_{1-x}\text{Ca}_x)(\text{Zr}_{0.1}\text{Ti}_{0.9})\text{O}_3$ system reported by Fu et al. [160].

1.5.1.3 Elaboration of BZCT

Since its discovery by Liu and Ren [159], a large and growing body of literature is based on high temperature synthesis to make pure and crystalline BCZT powder [138, 161, 162]. The first published synthesis of BCZT complex composition was based on solid-state reaction at high temperatures (calcination at 1350 °C and sintering between 1450 – 1500 °C) due to its simplicity and capability to obtain enhanced dielectric, ferroelectric and piezoelectric performances [159, 163, 164]. Kaddoussi et al. studied the structural, dielectric, ferroelectric, piezoelectric and electrocaloric properties in $(\text{Ba}_{1-x}\text{Ca}_x)(\text{Zr}_{0.1}\text{Ti}_{0.9})\text{O}_3$ solid-solution elaborated by solid-state [151]. BCZT samples were obtained by calcination at 1150 °C/12 h, and sintering at 1430 °C/2 h. Subsequently, BCZT ceramic was elaborated by soft chemistry routes like sol-gel [161], citrate reaction [122], solvothermal [152] and hydrothermal [165]. However, relative high temperature is needed to obtain pure and crystalline BCZT powder. Praveen et al. have elaborated $\text{Ba}_{0.85}\text{Ca}_{0.15}\text{Zr}_{0.1}\text{Ti}_{0.9}\text{O}_3$ ceramic by sol-gel processing, and the single-phase perovskite structure appeared at high temperature (700 °C) alongside with some impurity peaks [138]. Hsieh et al. have synthesized $\text{Ba}_{0.95}\text{Ca}_{0.05}\text{Zr}_{0.1}\text{Ti}_{0.9}\text{O}_3$ ceramic, using Pechini polymeric precursor method with a calcination temperature of 700 °C [166]. Zhan et al. have reported the elaboration $\text{Ba}_{0.95}\text{Ca}_{0.05}\text{Zr}_{0.3}\text{Ti}_{0.7}\text{O}_3$ ceramics by a citrate method followed by thermal treatment at 650 °C [167]. Jaimeewong et al. outlined a comparative study of two BCZT ceramics

synthesized by solid-state and sol-gel auto combustion methods at 1200 °C and 900 °C, respectively [168].

Hydro/solvothermal synthesis of nanostructures have attracted much attention for the elaboration of supported or free-standing ferroelectric ceramic with highly improved properties [169, 170]. This low cost and eco-friendly technique can provide an efficient design of ferroelectric nanomaterials with specifically tailored architectures with an appropriate size and shape [9, 169, 171–175]. Few works have reported the preparation of $\text{Ba}_{0.85}\text{Ca}_{0.15}\text{Zr}_{0.1}\text{Ti}_{0.9}\text{O}_3$ ceramic through hydrothermal techniques. Hunpratub et al. prepared $\text{Ba}_{0.85}\text{Ca}_{0.15}\text{Zr}_{0.1}\text{Ti}_{0.9}\text{O}_3$ by hydrothermal processing at 240 °C/16 h under different alkaline mediums, however, pseudo-cubic BCZT samples with some crystalline impurities like BaZrO_3 and CaTiO_3 were obtained [165]. Ji et al. reported the effects of synthesis time on the structure, morphology and size distribution of the powders of BCZT ceramic elaborated by sol-gel-hydrothermal reaction at 180 °C, however, high sintering-temperature (1400 °C) was required to obtain enhanced dielectric, ferroelectric and piezoelectric properties [176].

It is worthy to note that the abovementioned works, suffer from high-temperature elaboration to obtain pure and crystalline BCZT powders due to the low reactivity of Zr ions [177, 178], and/or high-temperature sintering to achieve enhanced electrical properties. Furthermore, the obtained BCZT powders were mainly synthesized in spherical shape. It was stated that the dielectric, ferroelectric and piezoelectric properties and the energy storage performances are highly affected by the shape of the ferroelectric material, hence, many works have attempted to elaborate BCZT ceramics with different morphologies namely nanowires and nanofibers [104, 179–182]. Zhou et al. prepared BCZT nanowires (BCZT-NWs) *via* two-steps hydrothermal processing, studied the piezoelectric properties of single BCZT-NW by piezoresponse force microscopy (PFM), and designed a cantilever based on BCZT-NW and PDMS for energy harvesting [170]. Besides, it was found that the peak power density could be enhanced 9 times by using BCZT-NWs instead of BCZT nanoparticles. Chary et al. elaborated large aspect ratio BCZT nanofibers (BCZT-NFs) by electrospinning technique, however, the perovskite phase was formed above 500 °C with a small percentage of secondary phase (BaCO_3), and pure BCZT-NFs were obtained at

600 °C [182]. The obtained BCZT-NFs exhibited low dielectric constant of 210 around $T_C = 108.8$ °C due to the porous structure of the nanofibers mat.

1.5.1.4 Dielectric, ferroelectric and piezoelectric properties

Since 2009, several researchers have focused on the phase boundaries and electrical properties of BCZT ceramics. Wu et al. studied the composition dependence of the dielectric, ferroelectric and piezoelectric properties of $(\text{Ba}_{0.85}\text{Ca}_{0.15})(\text{Zr}_x\text{Ti}_{1-y})\text{O}_3$ system [158]. It was stated that the ceramics with $y = 0.10$ exhibit the highest permittivity peak due to the two phases existence (Fig. 1.21a). It was showed also the strong dependence of the ferroelectric properties on the Zr content in BCZT ceramics through the plot of $2P_r$ and $2E_c$ values as a function of Zr at room temperature (Fig. 1.21b). The $2P_r$ increases gradually, reaches a maximum value at $y = 0.10$, and then decreases with further increasing the Zr content. This result confirms that the BCZT ceramics with the coexistence of two phases at near room temperature have a higher $2P_r$ value than those of the ceramics with other compositions. However, their $2E_c$ values decrease with increasing the Zr content. Meanwhile, the Zr-content dependence of the piezoelectric properties was also investigated as shown in Fig. 1.21c. The maximum d_{33} and k_p values are situated for the ceramic with $y = 10\%$, which is induced by the coexistence of two phases at near room temperature. This implies that the proximity of the phase transition temperature to near room temperature plays more important roles in enhancing piezoelectric properties of BCZT ceramics [158].

Bai et al. reported a detailed investigation of a wide range of processing factors, including composition (e.g. ratio of BZT to BCT), sintering conditions (temperature and cooling rate), particle size of the calcined ceramic powder, structure and microstructure (e.g. phase, lattice parameters, density and grain size), and their effect on the piezoelectric properties. BCZT system process enhanced electrical properties [157]. It was found that the degree of tetragonality (c/a) of the tetragonal phase was independent of sintering regime. High dielectric constant was observed in 0.7BZT–0.3BCT ceramic. In 0.5BCT–0.5BZT $\text{Ba}_{0.85}\text{Ca}_{0.15}\text{Zr}_{0.1}\text{Ti}_{0.9}\text{O}_3$ composition where the O and T phases coexist showed higher piezoelectric properties manifested by a piezoelectric coefficient d_{33} between 300 and

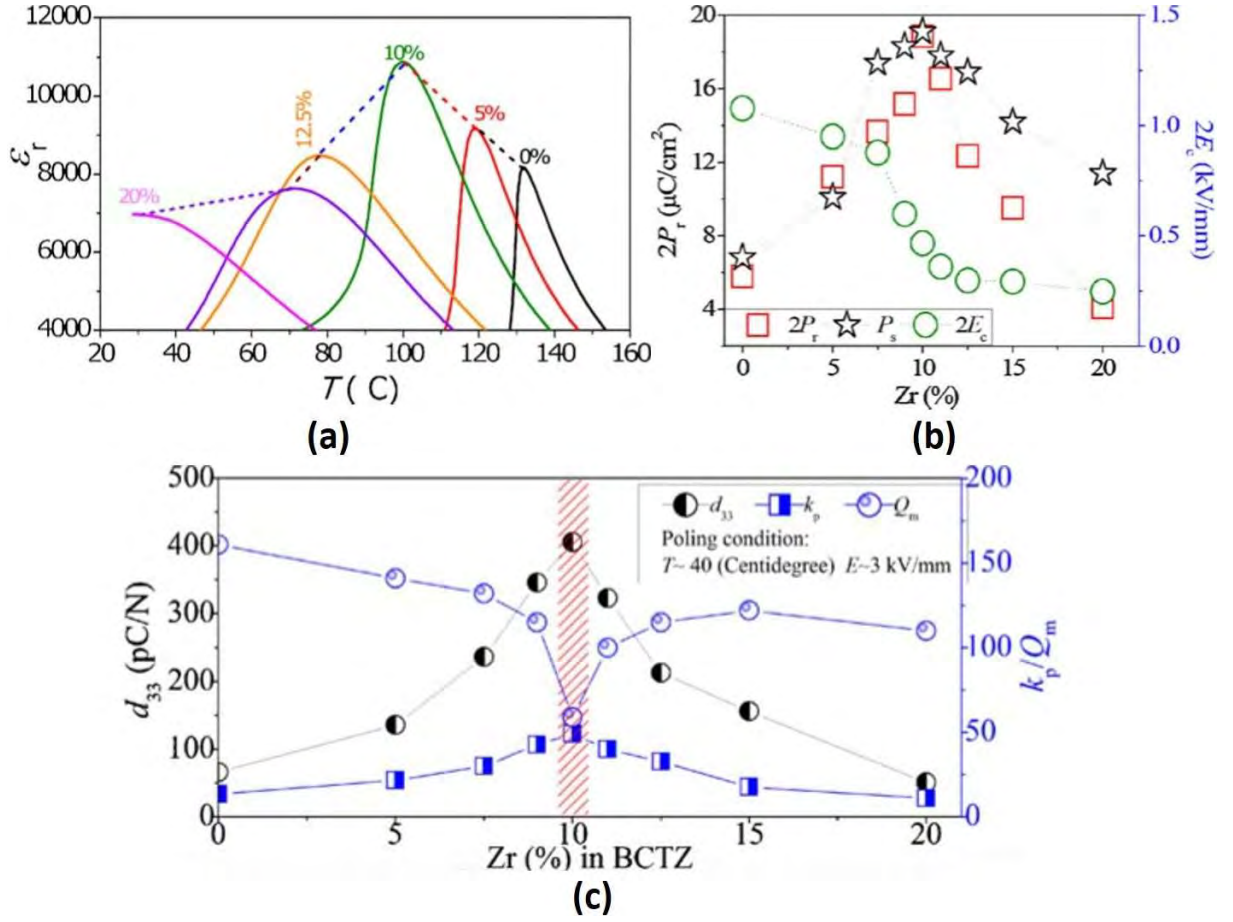


Figure 1.21: Effect of Zr content on the (a) dielectric, (b) ferroelectric and (c) piezoelectric properties in $(\text{Ba}_{0.85}\text{Ca}_{0.15})(\text{Zr}_x\text{Ti}_{1-y})\text{O}_3$ system [158].

500 pC/N, which is comparable to those reported by Liu and Ren [159]. Moreover, in 0.5BCT–0.5BZT composition made from 5 μm powder, that increasing the average grain size enhanced the remnant polarization, while the coercive electric field stayed the same were observed, and a further increase in the grain size from 33.1 to 33.5 μm results a slight reduction in polarization (Fig. 1.22a). Meanwhile, the variations in the d_{33} values with the average grain size indicated that the particle size of the ceramic powder affected the general magnitude of the d_{33} values, and powders with high c/a ratio displayed enhanced the piezoelectric response (Fig. 1.22b) [157]. These results were in good agreement with those obtained by Castkova et al. using the same BCZT composition $(\text{Ba}_{0.85}\text{Ca}_{0.15}\text{Zr}_{0.1}\text{Ti}_{0.9}\text{O}_3)$ [183]. Besides, it was reported that BCZT ceramic possess low dielectric loss $\sim 1\text{--}3\%$, which is encouraging to obtain high-efficiency energy storage density [34, 152, 163, 184, 185].

1.5. BCZT LEAD-FREE RELAXOR FERROELECTRIC AND PLA AS PROMISING MATERIALS FOR ENERGY STORAGE AND HARVESTING?

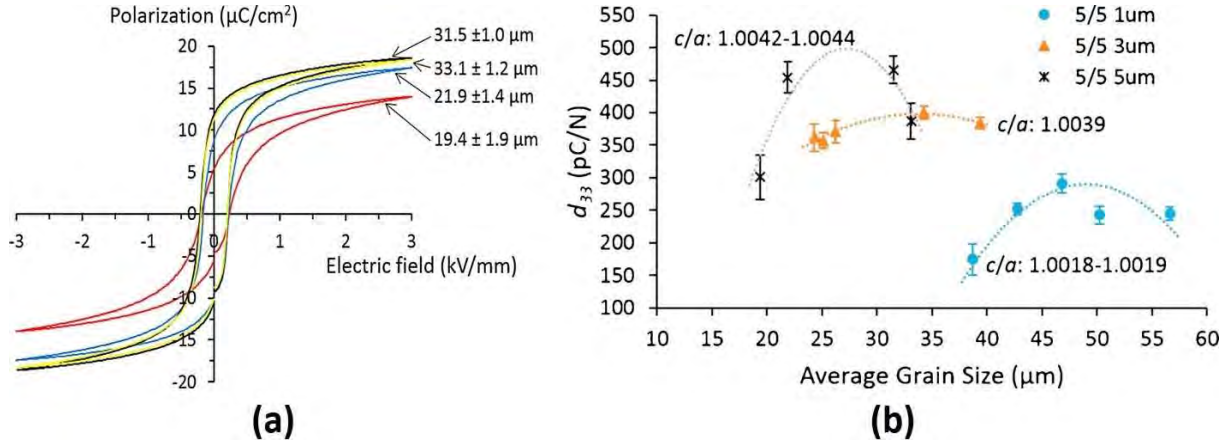


Figure 1.22: (a) $P - E$ hysteresis loop for the 0.5BCT–0.5BZT samples with different average grain sizes fabricated from 5 μm powders, and (b) dependence of d_{33} value on average grain size for the samples of the 0.5BCT–0.5BZT composition fabricated from different powder particle sizes [157].

To enhance the dielectric, ferroelectric and piezoelectric properties of BCZT ceramics, the basic approach of this achievement relies on placing the composition of the material to the proximity of the Morphotropic Phase Boundary (MPB) [138, 186]. The instability of the polarization state at the phase transition regions allows a significant polarization variation under external stress or electric field. As a result, the properties of BCZT ceramics related to polarization change, such as dielectric permittivity and piezoelectric coefficients, can be enhanced significantly [187]. Liu and Ren reported non-Pb ceramics of $\text{Ba}_{0.85}\text{Ca}_{0.15}\text{Zr}_{0.1}\text{Ti}_{0.9}\text{O}_3$ (BCZT) with extremely high ϵ_r of 18 000 and d_{33} of 620 pC/N at the MPB [159]. The high piezoelectricity can be ascribed to the phase boundary starts from a tricritical triple point composed of paraelectric cubic phase, ferroelectric rhombohedral, and tetragonal phases. Such a phase boundary has a flattened energy landscape and consequently leads to a low energy barrier for polarization rotation [155, 159, 188]. Nevertheless, many researchers reported the piezoelectric constant of this composition around 200–350 pC/N. It is well known that microstructure and the properties may differ greatly in ceramics with the same composition fabricated with different processes, even if the same technique but different processing parameters. It will be interesting to study how the microstructure and electrical properties of BCZT ceramics depends on different preparation method and processing condition. Researchers are focusing on various strategies namely grain size engineering, doping, preparation techniques, etc.,

to design BCZT ceramics with enhanced properties. Tang et al. studied the effect of grain size on the electrical properties of BCZT ceramics [189]. It was found that, as the grain size decreased, the maximum dielectric constant decreased and the transition temperature increased. Furthermore, some researchers have investigated the effects of small concentration of dopants such as Pr, Ce, Cu, La, Zn, Y, etc. into 0.5BCT–0.5BZT ceramics, to reduce the sintering temperature and improve the electrical properties. Wu et al. studied that the ZnO (0.06 mol%) modified 0.5BCT–0.5BZT ceramics exhibit good piezoelectric properties ($d_{33} \sim 521$ pC/N and $k_p \sim 47.8\%$) and dielectric constant of 4500 [190]. However, the addition of ZnO significantly reduced the T_C of 0.5BCT–0.5BZT ceramics and increased the grain size, because ZnO is responsible for enhancing the grain growth. Jaimeewong et al. investigated the effect of CoO and Fe₂O₃ dopant on phase, microstructure and ferroelectric properties of BCZT ceramics with the formula of Ba_{0.85}Ca_{0.15}Zr_{0.1}(Ti_{1-x}Co_x)O₃ and Ba_{0.85}Ca_{0.15}Zr_{0.1}(Ti_{1-x}Fe_x)O₃ where $x=0, 0.01$, and 0.03 [191]. It was stated that a small doping of BCZT with Co and Fe could enhance the dielectric and piezoelectric properties and lower the processing temperature.

BCZT relaxor ferroelectric ceramics are drawing much attention for energy storage applications and electrocaloric cooling devices owing to their outstanding dielectric and ferroelectric properties [192, 193]. Zhan et al. achieved an energy storage density of 590 mJ/cm³ and storage efficiency of 72.8% in Ba_{0.95}Ca_{0.05}Zr_{0.3}Ti_{0.7}O₃ ceramics under 160 kV/cm [167]. Meanwhile, Puli et al. examined the energy density properties in $(1-x)\text{BaZr}_{0.2}\text{Ti}_{0.8}\text{O}_3 - x\text{Ba}_{0.7}\text{Ca}_{0.3}\text{TiO}_3$ ($x=0.10, 0.15, 0.20$) system, and observed at $x=0.15$, enhanced energy storage density and high energy storage efficiency of 680 mJ/cm³ and 72.8%, respectively, by using an electric field of 170 kV/cm [139]. In a recent study, Puli et al. observed an energy storage density in Ba_{0.85}Ca_{0.15}Zr_{0.1}Ti_{0.9}O₃ bulk ceramics, of 1.33 J/cm³ but with moderate energy efficiency of 52.27% [64].

1.5.1.5 Biocompatibility of BCZT ceramics

Another key factor in lead-free BCZT piezoelectric ceramics to design eco-friendly energy storage and harvesting devices, is its biocompatibility. This family of piezoelectric ceramics

may be the key to functionalizing current implant designs, as they exhibit mechanically generated electric surface potentials. Therefore, they can be used to mimic the bone's ability to generate electrical potentials under a mechanical load without applying any external power source [194, 195]. Scarisoreanu et al. proved for the first time that BCZT coatings on Kapton polymer substrates could provide optimal support for osteogenic differentiation of mesenchymal stem cells in the bone marrow [196]. Moreover, Poon et al. investigated the potential of BCZT as implant materials in *in vitro* environment [195]. It was found that BCZT ceramic exhibits low cytotoxicity with human osteoblast and endothelial cells as well as high piezoelectric responses. It was concluded that BCZT ceramic is a promising material for biomedical applications, and could open the possibility to functionalize existing bone replacement implant designs to improve implant ingrowth and long-term stability.

1.5.2 PLA as a biodegradable polymer

1.5.2.1 Contextual elements

Poly(lactic acid) or polylactide (PLA) was discovered in 1932 by Carothers (DuPont) who produced a low molecular weight product by heating lactic acid under vacuum. PLA is a biodegradable, biocompatible, non-toxic and ecological thermoplastic aliphatic polyester derived from a natural organic acid. PLA and its derivatives degrade easily in the environment from six months to two years, unlike conventional plastics such as PE and PS which persist between 500 and 1000 years [197]. This completely biodegradable biopolymer has high tensile strength (70 MPa) and can be recycled from 7 to 10 times [198]. PLA melts at a lower temperature between 160 and 190 °C and has a glass transition temperature between 60 and 65 °C. Moreover, PLA can also be recycled to its monomer by thermal depolymerization or by hydrolysis. PLA can be processed by injection molding, extrusion, film spinning and casting, providing easy access to a wide architectural range of PLA materials. Three stereoisomers of lactide can be formed, namely *D,D*-lactide (*D*-lactide), *L,L*-lactide (*L*-lactide) and *D,L*-lactide (or *meso*-lactide). Polymerization of lactic acids

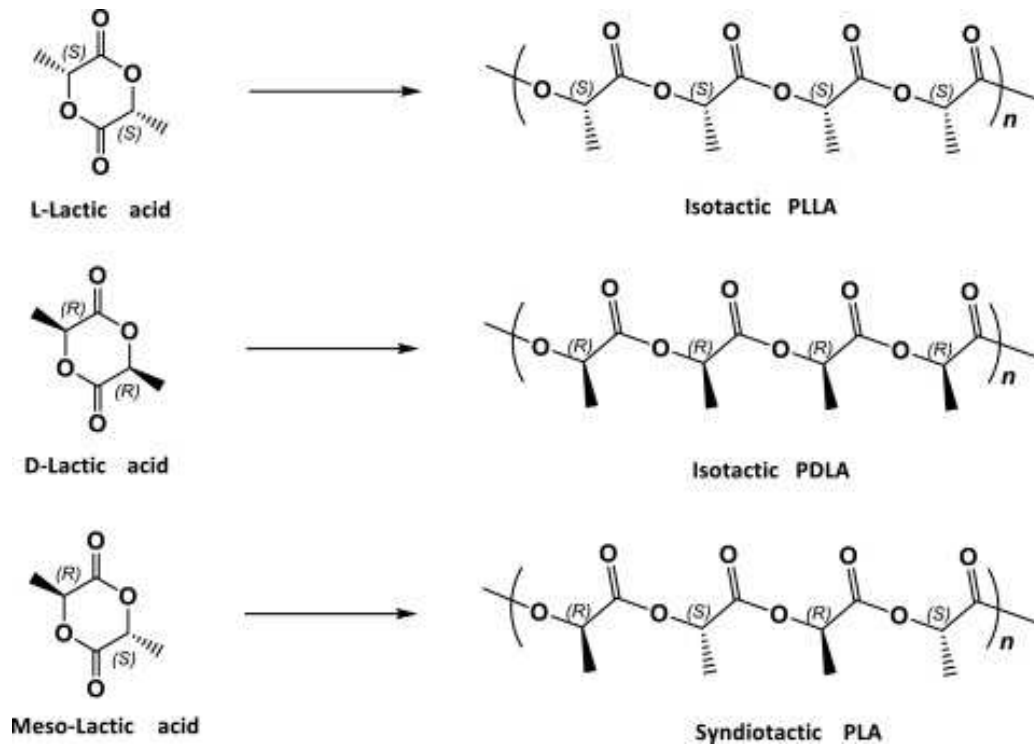


Figure 1.23: Three stereoisomers of lactide which lead to distinct PLA structures upon polymerization [199].

(or lactides) leads to isotactic, syndiotactic and atactic/heterotactic PLA primary structures as shown in Fig. 1.23 [199].

1.5.2.2 PLA production

PLA can be prepared by different polymerization process from lactic acid including: polycondensation, ring opening polymerization and by direct methods like azeotropic dehydration and enzymatic polymerization. Currently, direct polymerization and ring opening polymerization are the most used production techniques [200]. Fig. 1.24 shows the main methods for PLA synthesis. The direct condensation polymerization method is based on esterification of monomers by the aid of some solvents and released water is removed using progressive vacuum and high temperatures. Although, it is not easy to obtain PLA with high molecular weight and good mechanical *via* this method. However, the precondensates (prepolymers) could be used for the preparation of biodegradable glues or lacquers, since the $-OH$ and $-COOH$ end groups allow cross-linking with suitable

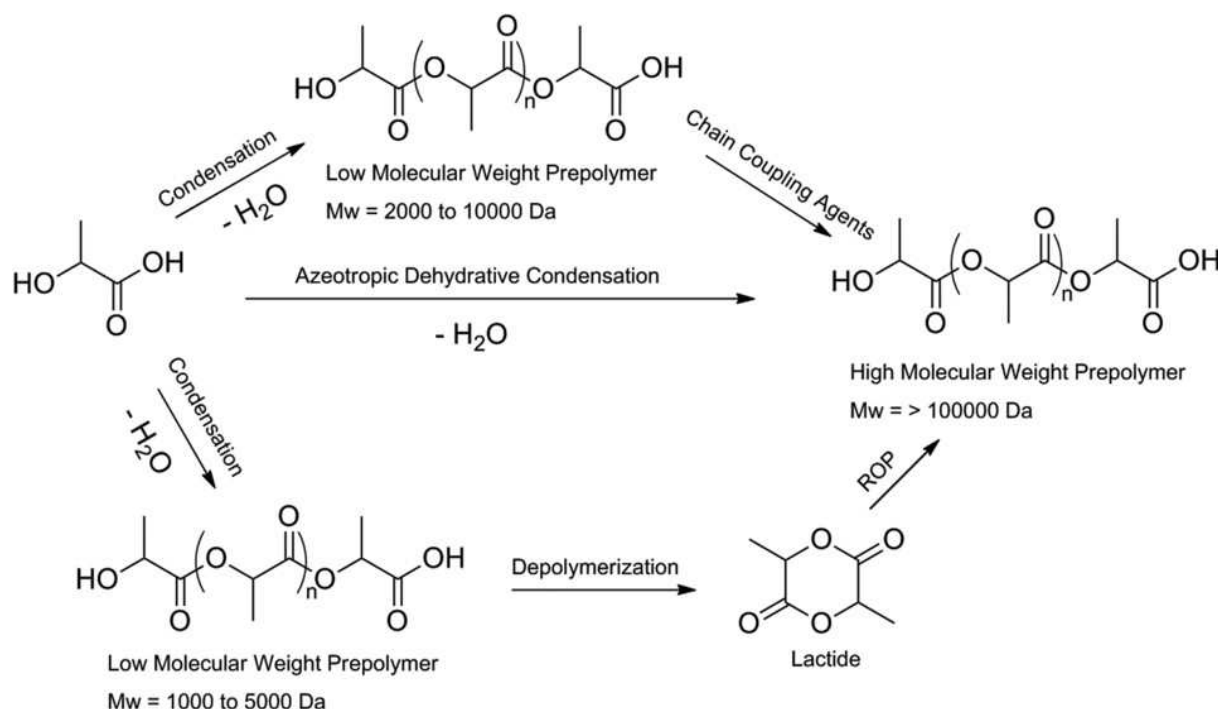


Figure 1.24: Synthesis methods for PLA [202].

inorganic or organic multivalent additives [201].

To produce PLA with high molecular weight, direct polycondensation in an azeotropic solution and polymerization through lactide formation are used. The polymerization through lactide formation is occurred by ring opening of the lactic acid cyclic dimer (lactide) in the presence of catalyst. This process consists of three steps: polycondensation, depolymerization and ring opening polymerization. However, this route requires additional steps of purification which is relatively complicated and expensive [200]. The direct polycondensation in an azeotropic solution relies on the fact that the azeotropic solution helps to decrease the distillation pressures and facilitates PLA separation from the solvent by application of molecular sieves [201].

1.5.2.3 Transition from PVDF to PLA

Fig. 1.25 compares the electrical properties of some biodegradable polymers including PLA and some conventional polymers reported in [203], and those of Solef® PVDF film (Solvay).

The relative permittivities of biodegradable are comparable to those of conventional polymers (Fig. 1.25a), due to the presence of polar carbonyl and hydroxyl groups in their structures [204]. PLA shows a relative permittivity around 3, closer to some conventional polymers used in electrical cables like PE and PP, and very far from PVDF. Despite the biodegradable polymers exhibit high value of losses, PLA has the lowest level of dissipation factor (Fig. 1.25b) and exhibits low dielectric loss as compared to PVDF and epoxy resin. Concerning the apparent conductivity, only PLA could be argued for competing with classical polymers like LDPE and PVDF (Fig. 1.25c). The rest of the biodegradable polymers shows high level of apparent conductivity. The DC breakdown strength of PLA is higher than all other biodegradable polymers and even high compared with some conventional polymers like LDPE and PVDF (Fig. 1.25d). According to these results, the electric properties PLA are enhanced compared to other biodegradable polymers, and even it can compete conventional polymers like LDPE and PVDF. which make it very promising biopolymer for the fabrication of ceramic/polymer nanocomposites for electrical insulation and energy storage applications. From energy harvesting view, PLA is becoming a popular candidate for energy harvesting applications owing to its higher piezoelectric properties. The carbonyl groups present in PLA structure induces polarity and it shows a d_{14} value of 10 pC/N without additional poling step in its crystalline structure [112, 205]. Varga et al. investigated the piezoelectric responses of PLA/BaTiO₃ composite fiber mats prepared by electrospinning and reported a d_{33} value of ~ 0.5 nC/N and compression modulus $Y \sim 10^4$ – 10^5 Pa which broadened its applications from active implants to smart textiles [206]. Additionally, the authors reported that finger tapping of a 0.15 μm thick 2 cm \times 2 cm area mat was capable of powering a small LCD. Besides, Ando et al. prepared piezoelectric PLLA fabric from poly(*L*-lactic acid) yarns [207]. The twist yarn was prepared from the left-handed helical fibers (S-yarn) and the reverse twist yarn was prepared from right-handed helical fibers (Z-yarn). A piezoelectric constant of $d_{14}=10$ pC/N was observed for 1% applied shear displacement. The authors explained that generation of the electric field due to extension and contraction of the twisted yarns leads to the strong antibacterial effect of the as-prepared fabric. Thus, PLA and PLLA based systems opened new avenues for piezoelectric textiles. Advanced characterization

1.5. BCZT LEAD-FREE RELAXOR FERROELECTRIC AND PLA AS PROMISING MATERIALS FOR ENERGY STORAGE AND HARVESTING?

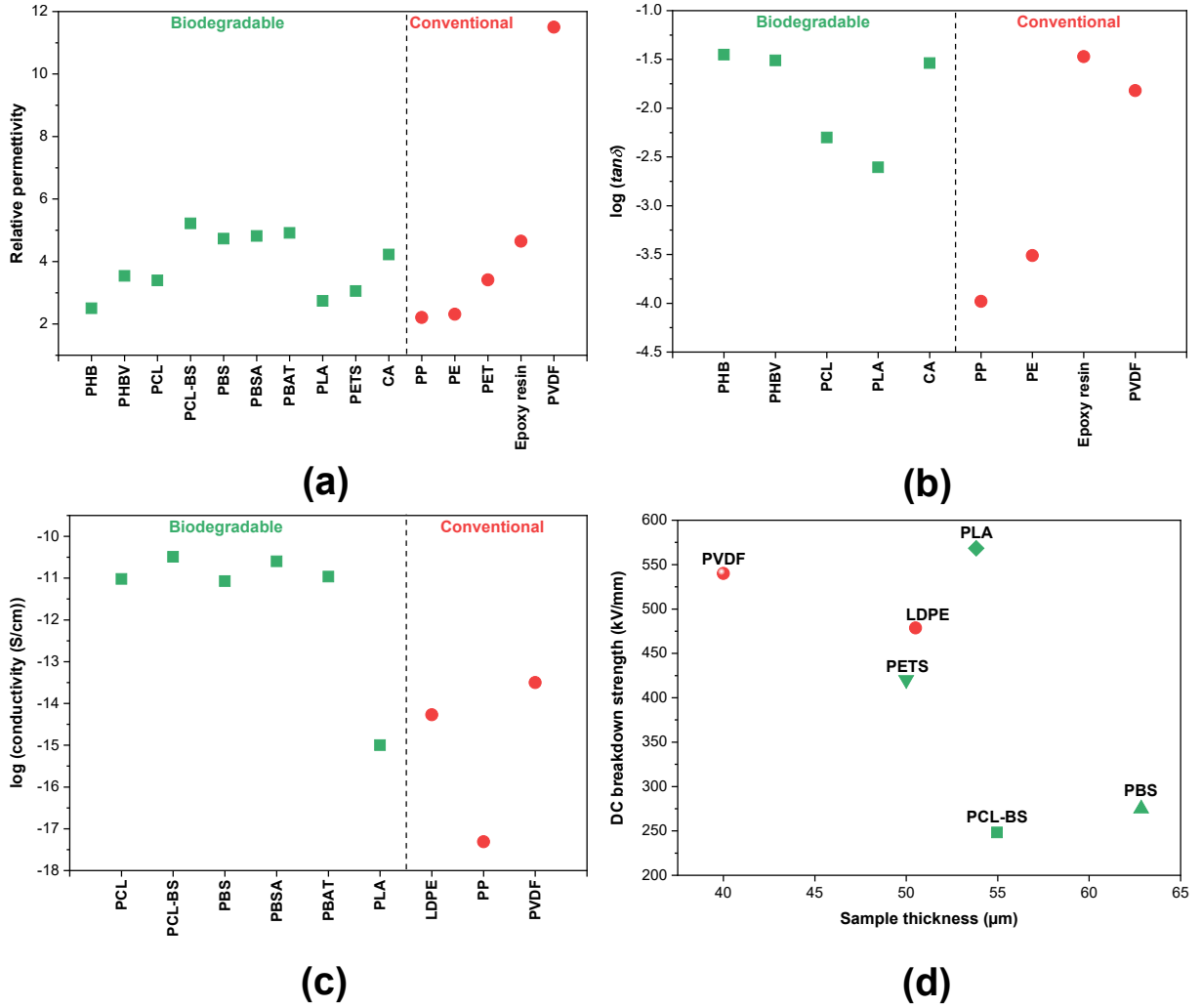


Figure 1.25: Electrical properties of some biodegradable and conventional polymers. (a) relative permittivity, (b) loss tangent, (c) apparent conductivity and (d) DC breakdown strength [203].

techniques further enabled direct observation of PLLA piezoelectricity at the micro/nano-scale [208, 209]. Smith et al. reported the first direct observation of shear piezoelectricity in highly crystalline and oriented PLLA nanowires by PFM [208]. The nanowires in confined anodized aluminum oxide (AAO) template, where the nanoconfinement promoted crystallinity that was proved to be 70%. Under PFM, significant deflection was seen in the lateral signal along the nanowire while only sharp vertical response was detected at the edge of nanowire, indicating a strong shear piezoelectricity. Deflection gradient under AC voltage sweeping gave an estimated d_{14} around 8 pC/N, the same as that of bulk materials. In a recent study, Li et al. prepared PLLA/Graphene electrospun composite nanofibers

for wearable sensors applications [205]. The maximum V_{OC} and I_{SC} of the wearable sensors were 184.6V and 10.8 μ A, respectively. The response generated by touching the bioelectronic skin can be converted to a digital signal. It is worth noting that contrary to polyvinylidene fluoride (PVDF) or Polydimethylsiloxane (PDMS) based PNGs, which require a poling process before testing the PNG, PLA exhibits a different piezoelectric response than PVDF or PDMS, and more interestingly, PLLA can expose its piezoelectric properties without polarization. Hence, PLA is expected to be a critical material for achieving high sensitivities for small sensors [205].

1.6 Conclusions

Ferroelectric based-ceramics are very promising materials for both energy storage and harvesting applications because of their particular polarization and depolarization properties. Ferroelectric ceramics own high dielectric constant and large piezoelectric coefficient d_{33} . However, their high dielectric loss, low breakdown strength, poor processability and lack of flexibility limit their application in energy storage or harvesting technologies. Contrary, polymers generally have a high breakdown strength and ease of processing, but most have a low dielectric constant. The nanocomposite approach consists of combining the advantages of both polymers and ceramics to design. For this purpose, the choice of both the ceramic and the polymer is prime of necessity. It can be only made on toxicity, ecological and performance considerations. As such, BCZT as ceramic and PLA as polymer offer interesting opportunities. BCZT is a biocompatible ceramic having high dielectric constant and enhanced piezoelectric properties. PLA is a biodegradable and flexible piezopolymer having high breakdown strength and relatively low dielectric loss. Thus, embedding BCZT ceramic inside PLA polymer could be beneficial to design flexible eco-friendly high- k nanocomposites with enhanced electrical properties for energy storage and energy harvesting technologies.

CHAPTER

2

Elaboration and Characterization of BCZT ceramics

Contents

2.1	Introduction	58
2.2	Synthesis of BCZT ceramics with different morphologies . .	58
2.3	Dielectric and ferroelectric properties of BCZT sintered ce- ramics	83
2.4	Selection of the most promising BCZT ceramics	93
2.5	Conclusions	97

2.1 Introduction

In this chapter, we are interested in innovative synthesis routes for BCZT ceramic. In general terms, it consists of coupling both solvothermal and hydrothermal process and using specific surfactants. Different strategies were proposed to elaborate pure BCZT ceramics having different morphologies. The physical phenomena involved in the formation of BCZT were also discussed. Finally, the dielectric properties (dielectric constant and dielectric loss) of BCZT ceramics were measured after sintering at 1250 °C for 10 h. The most promising BCZT ceramic were selected on the basis of its dielectric properties.

2.2 Synthesis of BCZT ceramics with different morphologies

2.2.1 BCZT near-spherical nanoparticles

2.2.1.1 Strategy N°1: Surfactant-assisted solvothermal

2.2.1.1.1 Synthesis route

This approach involves the use of cationic surfactant (cetyltrimethylammonium bromide, $C_{19}H_{42}BrN$, CTAB) and anionic surfactant (sodium dodecyl sulfate, $NaC_{12}H_{25}SO_4$, SDS). Fig. 2.1 displays the experimental procedure used in this approach. In the following section, B-CTAB and B-SDS refer to samples elaborated using CTAB and SDS surfactant, respectively, while B-0 sample denotes sample without addition of any surfactant. B-0, B-CTAB and B-SDS powders were obtained through single-step solvothermal synthesis, by controlled reaction at room temperature between calcium nitrate tetrahydrate, zirconium n-propoxide, barium acetate and titanium (IV) isopropoxide. First, an appropriate amount of barium acetate was dissolved in glacial acetic acid. Calcium nitrate tetrahydrate was dissolved in 2-ethoxyethanol. Second, the two solutions were mixed in a 50 mL-round-bottom flask equipped with a magnetic stirrer. Third, titanium (IV) isopropoxide and

2.2. SYNTHESIS OF BCZT CERAMICS WITH DIFFERENT MORPHOLOGIES

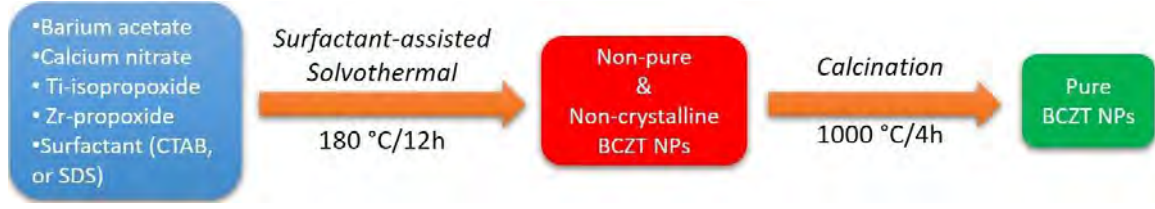


Figure 2.1: Experimental procedure used in strategy N°1 to elaborate spherical BCZT nanoparticles.

zirconium n-propoxide were added quickly to the reaction medium according to the mass-balance imposed by the stoichiometry of $\text{Ba}_{0.85}\text{Ca}_{0.15}\text{Zr}_{0.1}\text{Ti}_{0.9}\text{O}_3$ (BCZT). Next, 15 mM of CTAB or SDS was added to each solution with an additional 1 hour of continuous stirring at room temperature. The obtained mixtures were transferred separately to 30 mL-Teflon-lined stainless-steel autoclaves at 180 °C in an oven for 12 h. After the reaction was completed, the sealed autoclaves were cooled naturally to room temperature. The resulting white precipitates were collected by centrifugation at 12000 rpm for 10 min, and washed several times with deionized water and ethanol. Then, the final products were dried at 100 °C for 12 h.

2.2.1.1.2 Thermal analysis: phase evolution and temperature of calcination

The thermal decomposition of the B-0, B-CTAB and B-SDS products issued from solvothermal processing was analyzed using thermogravimetric analysis (TGA), and the results are shown in Fig. 2.2. Two consecutive weight losses at temperatures between 40–230 °C is due to dehydration and dehydroxylation phenomena. The weight loss between 230–390 °C is associated to the thermal decomposition of various organic compounds. This weight loss is remarkably noticed in B-CTAB raw powder. The weight losses between 600–800 °C are attributed to the formation and crystallization of BCZT phase [138, 186, 210–212]. Finally, the mass loss remains constant after 920 °C. Based on these analyzes, the temperature of 1000 °C was selected as the calcination temperature for BCZT powders. It is worth noting that the weight loss in BCZT-based surfactants are higher than that without any surfactant due to the existence of organic molecules.

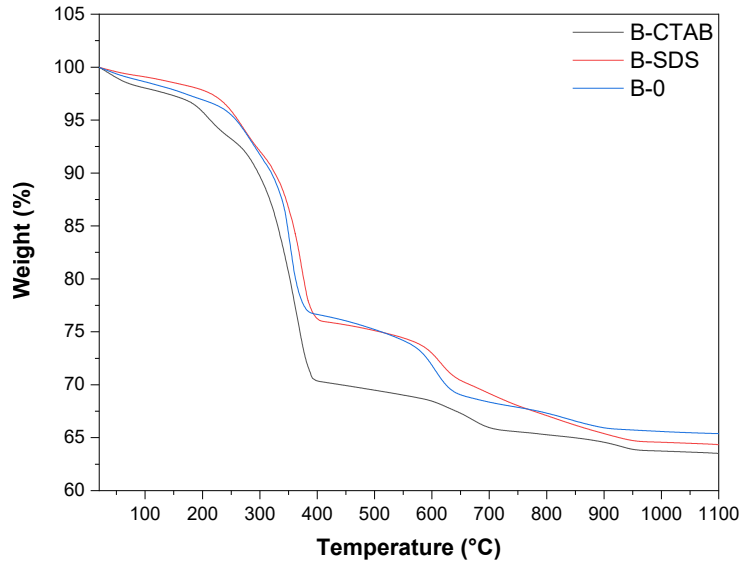


Figure 2.2: TGA curves of B-0, B-CTAB and B-SDS raw powders.

2.2.1.1.3 Structure and phase analysis

The XRD patterns obtained at room temperature for B-0, B-CTAB and B-SDS as-prepared and calcined powders at 1000 °C/4 h are illustrated in Fig. 2.3. It is worth noting that the as-prepared powders are not crystallized in perovskite phase (Fig. 2.3a), hence the calcination step is essential to obtain crystalline BCZT powders. After calcination, all BCZT powders are formed with a pure perovskite phase, without any secondary phase peaks (Fig. 2.3b). The peak splitting around $2\theta \approx 45^\circ$ indicates the presence of the tetragonal phase (Fig. 2.3c). However, the formation of the triplet around $2\theta \approx 66^\circ$ suggests also the presence of the orthorhombic phase (Fig. 2.3d). The co-existence of tetragonal and orthorhombic phases at room temperature was also reported by others researchers [135, 159, 213, 214]. As stated before, a calcination step at 1000 °C/4 h is crucial to obtain crystalline BCZT powders. Hence, a second strategy was envisaged in order to avoid any such high temperature of treatment and to elaborate near-spherical BCZT ceramics.

2.2.1.1.4 Nanoparticles morphology

Fig. 2.4 shows the FESEM micrographs of B-0, B-CTAB and B-SDS calcined powders at 1000 °C/4 h. In all samples, agglomerated near-spherical-shaped BCZT nanoparticles are formed with an average nanoparticle size of 80, 85 and 110 nm, for B-0, B-CTAB and

2.2. SYNTHESIS OF BCZT CERAMICS WITH DIFFERENT MORPHOLOGIES

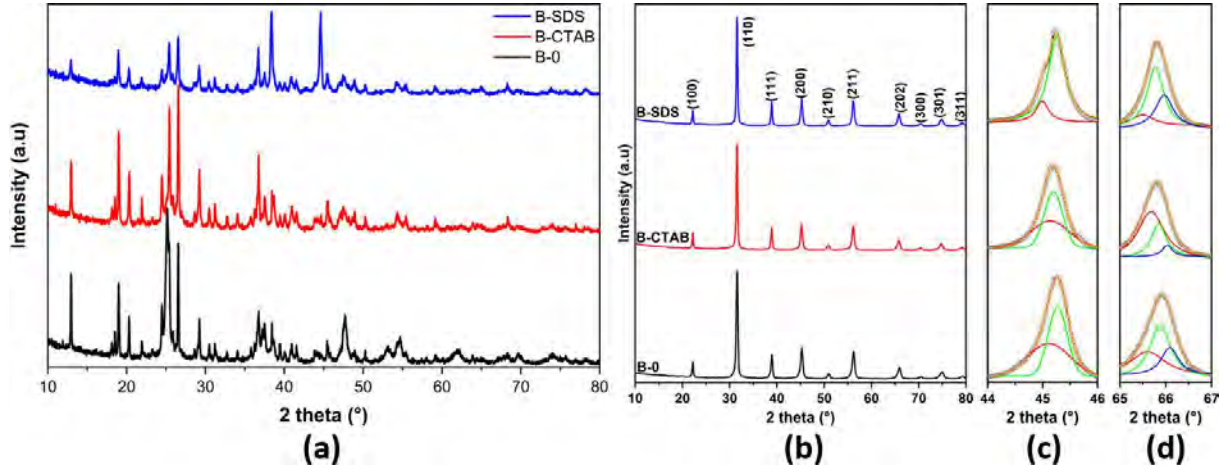


Figure 2.3: XRD patterns of (a) as-prepared and (b) BCZT powders calcined at 1000 °C/4 h, the enlarged views of the peaks $2\theta \approx$ (c) 45° and (d) 66°.

B-SDS powders, respectively. In B-0 and B-SDS powders, the majority of nanoparticle sizes are ranged between 60 and 80 nm for B-0 and 80 and 120 nm for B-SDS. However, a large nanoparticle size distribution between 50 and 110 nm with the presence of small nanoparticles ≤ 40 nm are observed in B-CTAB powder. Accordingly, the use of surfactant can be beneficial to adjust the nanoparticle size and the nanoparticle size distribution in BCZT powders. The grain size distributions of BCZT nanoparticles were determined by intercept method using ImageJ software.

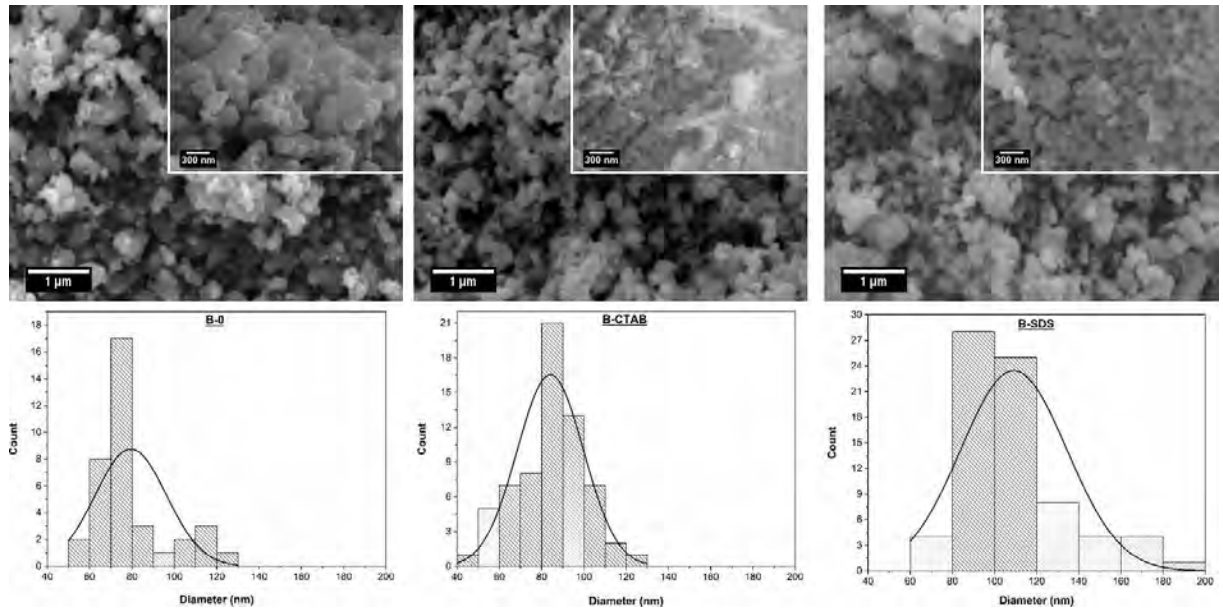


Figure 2.4: FESEM micrographs and nanoparticles size distribution histograms of B-0, B-CTAB and B-SDS calcined powders.

2.2.1.2 Strategy N°2: Very-low temperature hydrothermal

2.2.1.2.1 Synthesis route

As shown in Fig. 2.5, this method involves the elaboration of pure and crystalline BCZT powders through sol-gel followed by a single-step hydrothermal synthesis in high alkaline medium. Explicitly, under inert atmosphere (N_2), appropriate amounts of titanium (IV) isopropoxide and zirconium n-propoxide were added to isopropanol. After 1 hour of vigorous stirring, distilled water was added into the solution dropwise to produce a gel designated $Zr_{0.1}Ti_{0.9}O_2$ (ZTO). This was washed several times and dried at 80 °C for 12 hours to obtain ZTO powder. Next, a stoichiometric quantity of ZTO powder was dispersed in 100 mL of NaOH (10 M) solution for 1 hour. Meanwhile, calcium nitrate tetrahydrate and barium acetate were dissolved in 50 mL of distilled water. Then, the two solutions were mixed together in a 250 mL-round-bottom flask equipped with a magnetic stirrer for 3 hours under nitrogen flow. After, the suspension obtained was transferred to a Teflon-lined stainless-steel autoclave, purged with nitrogen, sealed and heated at 25, 40, 80, 120, 160 and 240 °C for 24 h and designated B-25, B-40, B-80, B-120, B-160 and B-240, respectively. After the reaction was completed, the sealed autoclave was cooled down to room temperature. The resulting white precipitates were collected by centrifugation at 12000 rpm for 10 min, and washed several times with distilled water and ethanol. Then, the final products were dried at 100 °C for 12 hours.

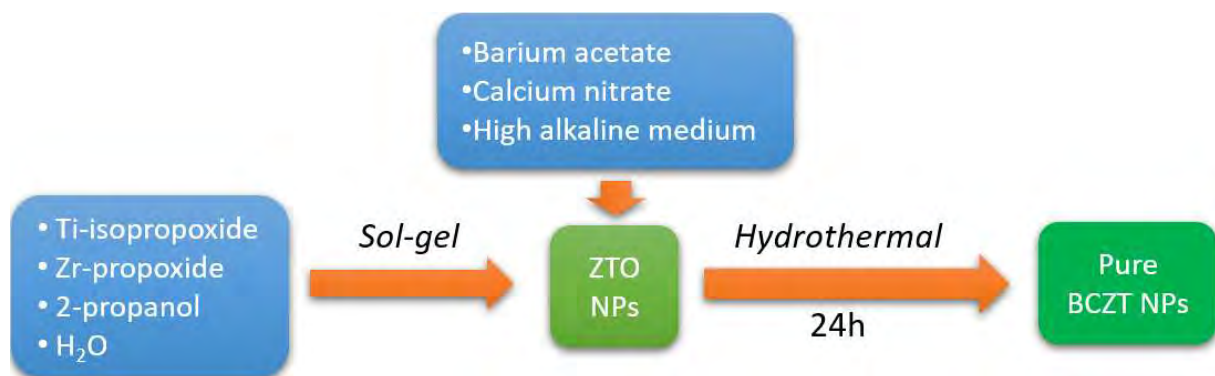


Figure 2.5: Experimental procedure used in strategy N°2 to elaborate spherical BCZT nanoparticles.

2.2.1.2.2 Thermal analysis and phase evolution

The thermal evolutions of the as-prepared BCZT powders *via* low-temperature hydrothermal processing are shown in Fig. 2.6. Two consecutive weight losses at temperatures between 30–250 °C are due to dehydration and dehydroxylation phenomena. The weight loss between 250–500 °C is associated to the thermal decomposition of different organic compounds. This weight loss is higher in the powder elaborated at 25 °C. The mass loss remains constant after 500 °C. More interestingly, the absence of the weight loss above 600 °C, attributed to the formation and crystallization of perovskite phase, as observed in the powders elaborated by the first strategy, and the low total weight loss in the powders issued by this strategy, indicate that BCZT perovskite phase was formed at low-temperature.

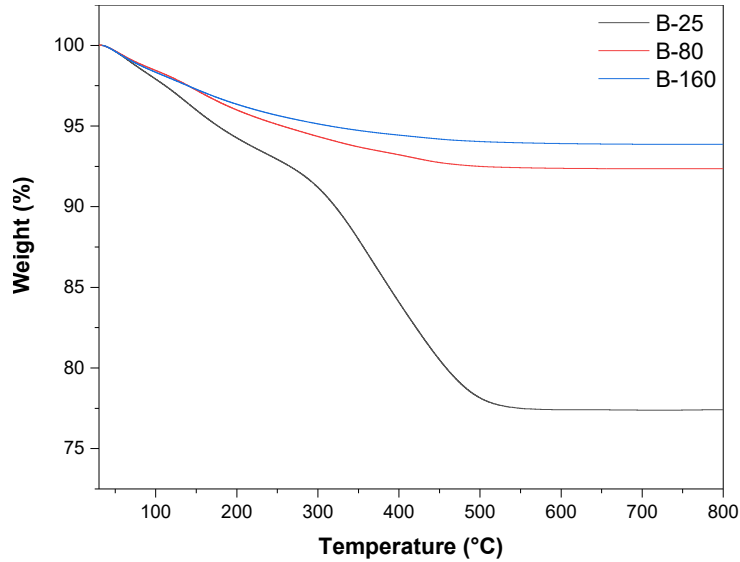


Figure 2.6: TGA curves of B-25, B-80 and B-160 raw powders.

2.2.1.2.3 Structure and phase analysis

Fig. 2.7a reveals the XRD patterns of BCZT powders elaborated at different temperatures. It is observed that all BCZT powders possess a perovskite phase, without any secondary phase peaks including B-25 elaborated at room temperature. The peaks-splitting similar to those reported by Sahoo et al. are observed at $2\theta \approx 45^\circ$ (Fig. 2.3b) and 65.5° (Fig. 2.7c) [214]. This indicates that all BCZT powders are formed at the Morphotropic Phase Boundary (MPB) with the coexistence of orthorhombic and tetragonal phases [58, 135, 213, 214]. Meanwhile, the diffraction peaks of all samples shift to higher 2θ

values by increasing the hydrothermal temperature, due to a decreasing of BCZT unit cell, and/or the reduction of defects and structural relaxation [215, 216]. Moreover, the peaks broadening observed after increasing the reaction temperature can be attributed to strain on the cell parameters issued from the cationic disorder (substitution of Ba^{2+} by Ca^{2+}) [151].

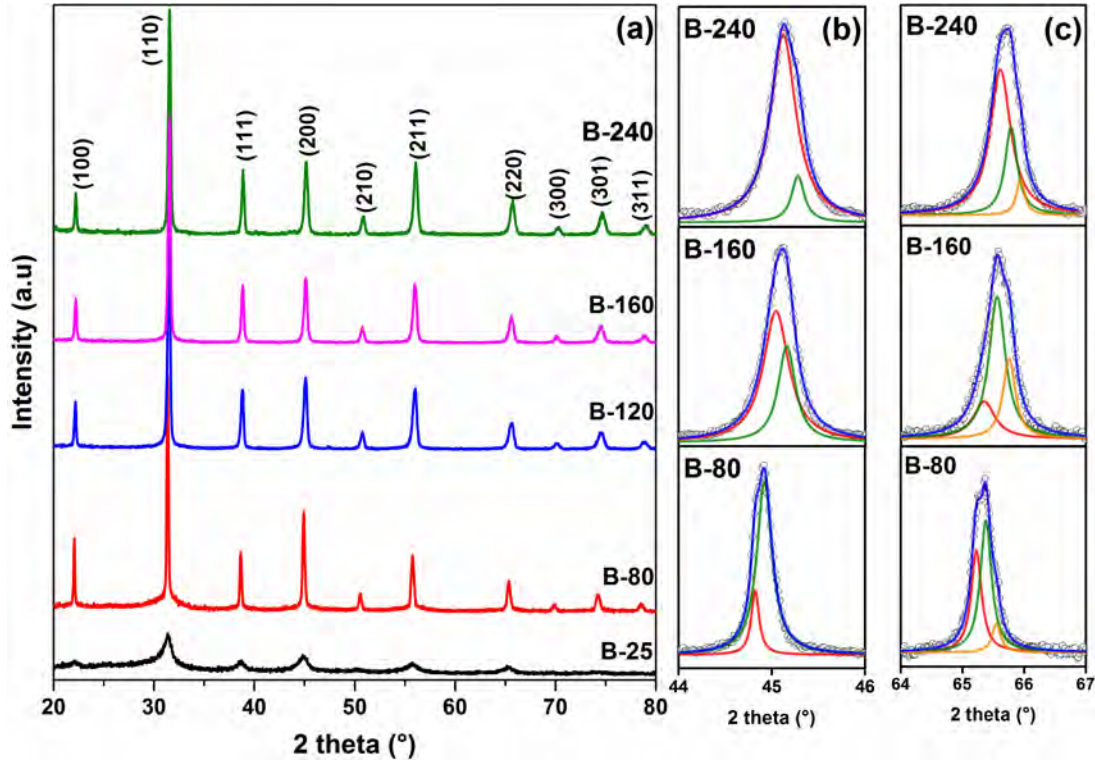


Figure 2.7: (a) XRD patterns of BCZT powders synthesized from 25 to 240 °C, and enlarged peaks splitting at $2\theta \approx 45^\circ$ (b) and 65.5° (c).

To have an insight on the purity of the elaborated powders, FTIR measurements were performed. Fig. 2.8 depicts FTIR spectra of BCZT powders synthesized at different temperatures. The absorption peaks between 850 and 1230 cm^{-1} observed in B-25 are attributed to carbonates compounds. A broad absorption band appeared at about 3400 cm^{-1} is assigned to stretching vibrations of M–OH groups (M: Ba, Ca, Zr, and Ti). It is worth noting that an obvious attenuation of the peaks corresponding to carbonate (CO_3^{2-}), hydroxyl (OH) and carboxylate (COOH) groups is clearly seen after increasing the temperature. Whilst, an increase in the intensity of the absorption M–O band located between 500 and 650 cm^{-1} is accompanied to the increase of thermal treatment [217].

These results indicate that pure BCZT can be obtained over 80 °C, and corroborate those obtained in XRD measurements suggesting the enhancement of the crystallinity of samples with the increase of temperature.

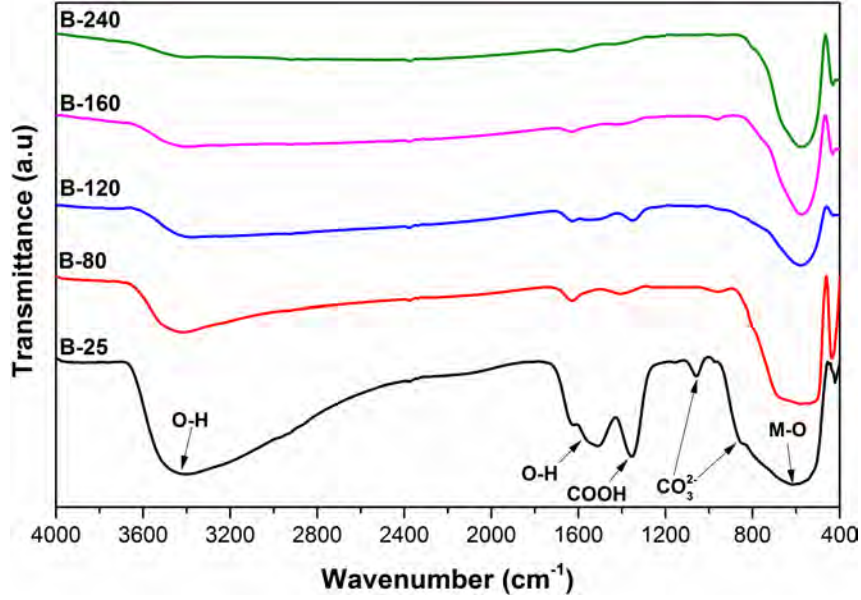


Figure 2.8: FTIR spectra of BCZT powders synthesized from 25 to 240 °C.

Fig. 2.9 displays the FESEM micrographs and nanoparticle size distribution histograms of BCZT powders synthesized at different temperatures. Agglomerated near-spherical nanoparticles are observed. After rising the treatment temperature from 40 °C to 80 °C, mature and spherical shaped BCZT nanoparticles are formed with increased nanoparticle size from 145 nm to 160 nm, respectively. Consequently, combining both sol-gel and hydrothermal processes is a promising route to prepare the pure and high-crystalline BCZT powders at very low-temperature (80 °C).

During hydrothermal treatment, ZTO powder prepared by sol-gel process can serve as the nuclei of BCZT crystals. The most plausible mechanisms governing the hydrothermal synthesis of BCZT powders consist in the *in situ* transformation (Fig. 2.10a) and/or dissolution-precipitation processes (Fig. 2.10b) [218, 219]. The first involves a mutual reaction between ZTO and Ba/Ca ions to form BCZT layer for barium and calcium diffusion until ZTO nanoparticles have completely reacted. However, the second one results from a dissolution-precipitation mechanism involving the break of Ti–O and Zr–O

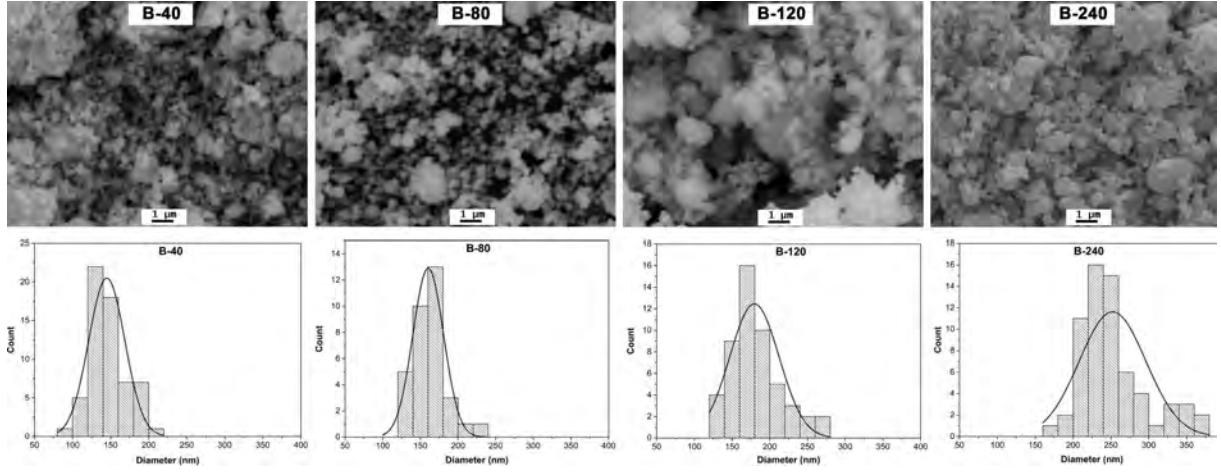


Figure 2.9: FESEM micrographs and nanoparticles size distribution histograms of BCZT powders synthesized at different temperatures.

bonds *via* hydrolytic attack to form titanium and zirconium complexes ($\text{Me}(\text{OH})_x^{4-x}$, Me: Ti/Zr) that easily react with barium and calcium ions to form homogeneous and/or heterogeneous BCZT nucleations, which agglomerate to create BCZT nanoparticles.

2.2.2 BCZT nanorods

2.2.2.1 Synthesis route: surfactant-assisted solvothermal

BCZT powder was obtained by CTAB-assisted solvothermal synthesis as shown in Fig. 2.11. First, an appropriate amount of barium acetate was dissolved in glacial acetic acid. Calcium nitrate tetrahydrate and zirconyl chloride octahydrate were dissolved each alone in 2-methoxyethanol. Second, the three solutions were mixed in a two-neck round bottom flask. In the third stage, titanium (IV) isopropoxide was added synchronously dropwise to the reaction medium using an isobaric dropping funnel. To control BCZT microstructure, 30 mM of CTAB surfactant was introduced. The obtained solution was transferred to a 30 mL-Teflon-lined stainless-steel autoclave at 180 °C in an oven for 12 h. After the reaction was completed, the sealed autoclave was cooled in the air. The resulting product was washed sequentially with ethanol for several times. Then, the final product was dried at 100 °C for 12 hours.

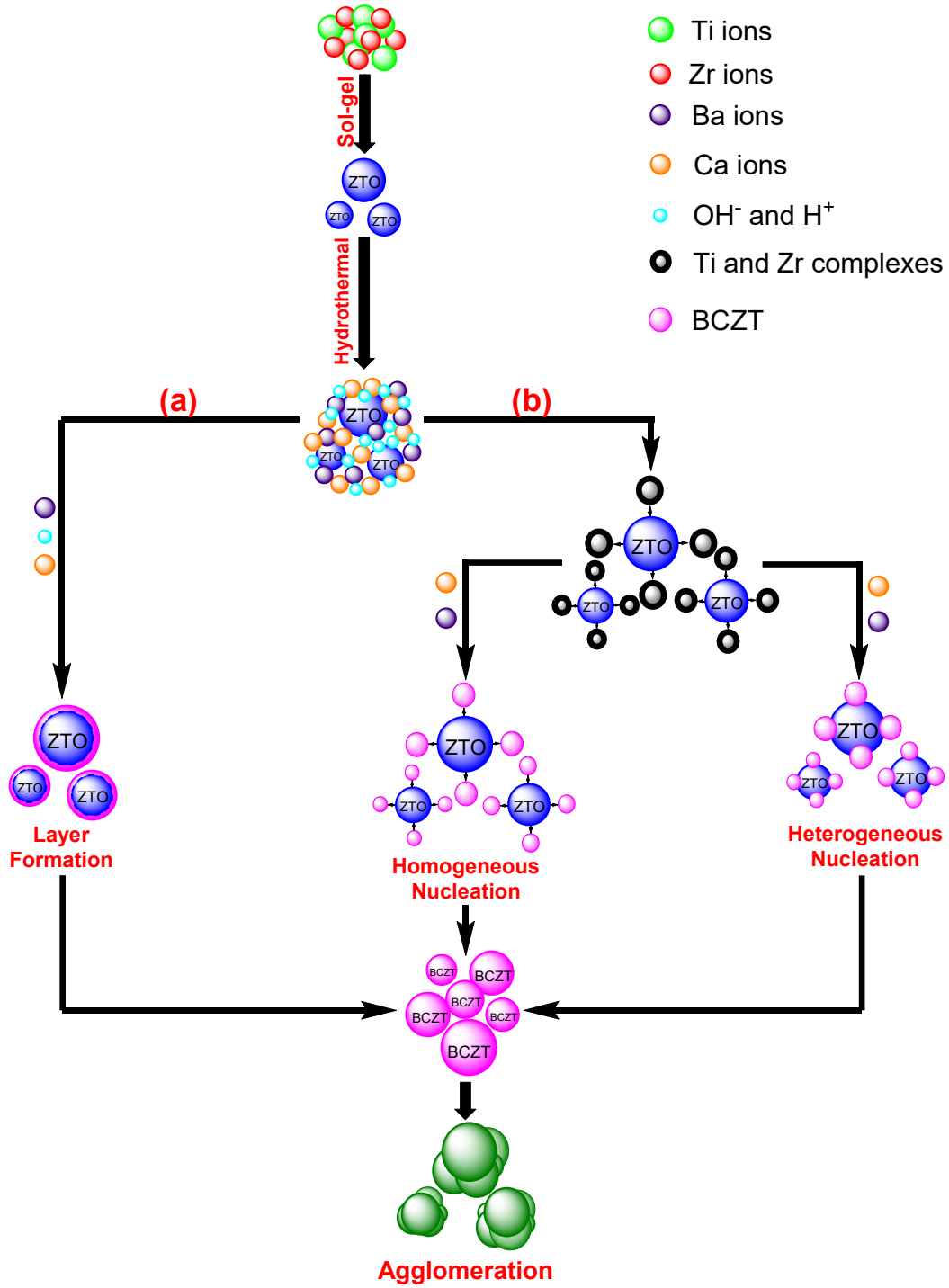


Figure 2.10: Schematic representation of the mechanisms of BCZT nanoparticles formation under hydrothermal processing: (a) *in situ* transformation and (b) dissolution-precipitation processes.

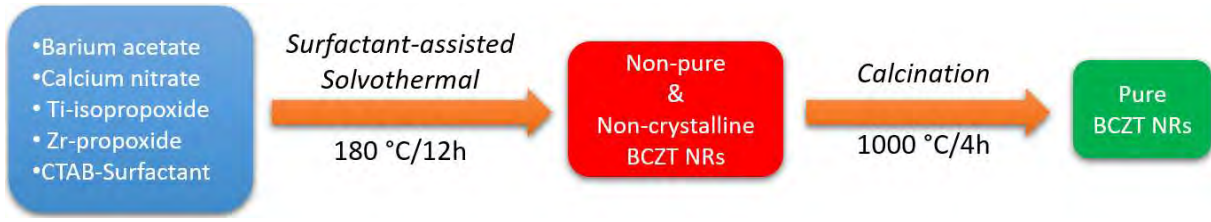


Figure 2.11: Experimental procedure used to elaborate BCZT nanorods.

2.2.2.2 Thermal analysis: phase evolution and temperature of calcination

The typical thermal decomposition behavior of the BCZT raw material is shown in Fig. 2.12. The first weight loss at temperatures between 40–160 °C and the second weight loss in the range of 160–230 °C can be attributed to desorption of physically adsorbed water (dehydration phenomena) and to the chemisorbed water (dehydroxylation phenomena) respectively. The fourth loss between 580 °C and 800 °C is a marker of the formation and crystallization of BCZT phase [138]. This behavior suggests the temperature transformation of non-crystalline BCZT into crystalline BCZT. It is worth noting that the mass loss remains constant after 800 °C. Based on this, the temperature of 1000 °C was selected as the calcination temperature for the formation of pure and crystallized BCZT.

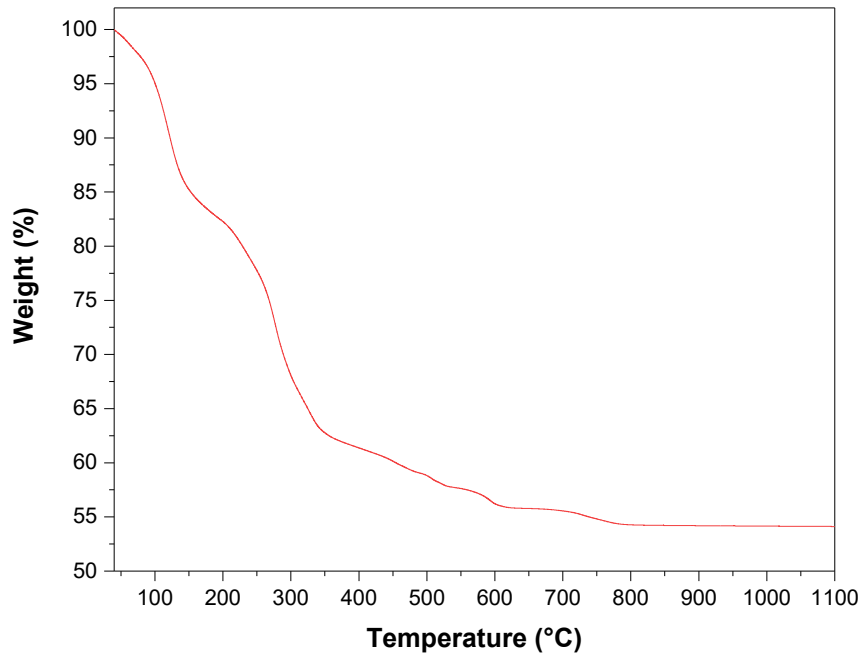


Figure 2.12: Experimental procedure used to elaborate BCZT nanorods.

2.2.2.3 Structure and growth mechanism

The XRD pattern obtained for BCZT calcined powder is shown in Fig. 2.13a. It was observed that BCZT powder was formed in a pure perovskite phase, without any trace of crystalline impurities. All diffraction peaks can be indexed based on the standard model X-ray polycrystalline tetragonal BaTiO_3 (JCPDS card no. 96-901-4669) with the space group $P4mm$. The characteristic tetragonal reflection (110) was observed at $2\theta = 31.65^\circ$. BCZT powder have a tetragonal symmetry demonstrated by the peaks (002) and (200) splitting [138, 143, 220, 221]. Inserted figure illustrates clearly the splitting of these peaks in the 2θ range 44° – 46° . Fig. 2.13b depicts Selected Area Electron Diffraction (SAED) patterns of BCZT calcined powder. The d-spacings calculated from the measured ring diameters i.e. 2.834, 2.313, 1.999 and 1.634 Å correspond to (110), (111), (002), and (211) planes, respectively. These results are in good agreement with those obtained by X-ray diffraction.

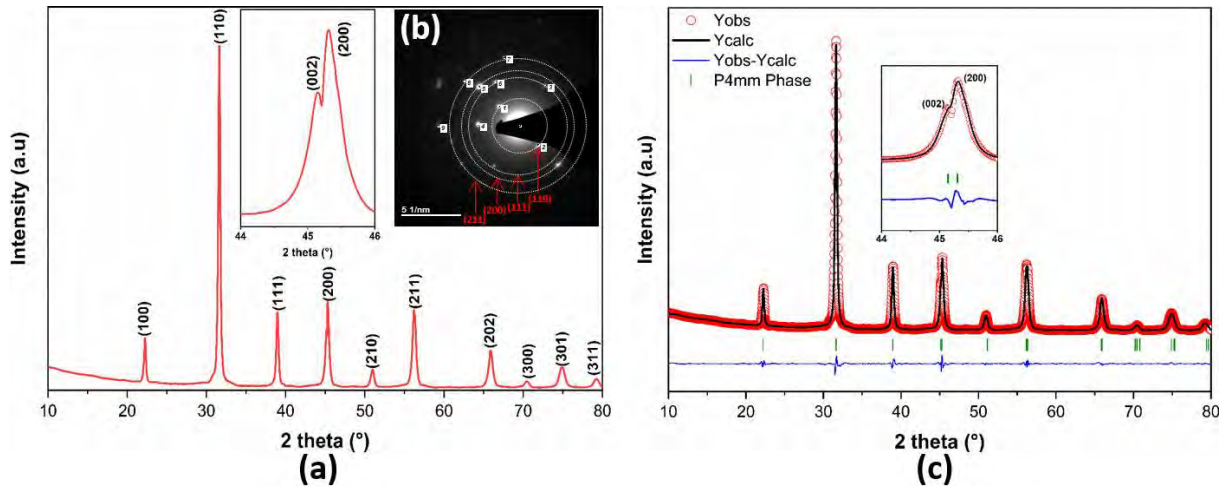


Figure 2.13: (a) XRD, (b) SAED patterns and (c) Rietveld refinement of BCZT powder calcined at 1000 °C/4 h.

Phase analysis BCZT calcined powder was performed in the light of $P4mm$ space group as shown in Fig. 2.13c. The refinement performed by FullProf Suite software indicates that the diffraction data of BCZT powder collected at room temperature have mainly a tetragonal phase ($P4mm$). In the Rietveld refinements, Ba and Ca ions are supposed to share the same crystallographic A-site of the BCZT perovskite structure. Similarly,

Table 2.1: Structural parameters obtained from Rietveld refinement of BCZT calcined powder.

Lattice parameters (Å)	Angles (°)	Volume (Å ³)	Atomic positions (x, y, z)			χ^2	Space group	c/a
$a = 3.9942(3)$	$\alpha = \beta = \gamma = 90$	64.039	Ba/Ca	0.0000	0.0000	0.0167(3)	$P4mm$	1.0050
$b = 3.9942(6)$			Zr/Ti	0.5000	0.5000	0.4964(5)		
$c = 4.0141(2)$			O1	0.5000	0.5000	-0.0381(6)		
			O2	0.5000	0.0000	0.5595(2)		

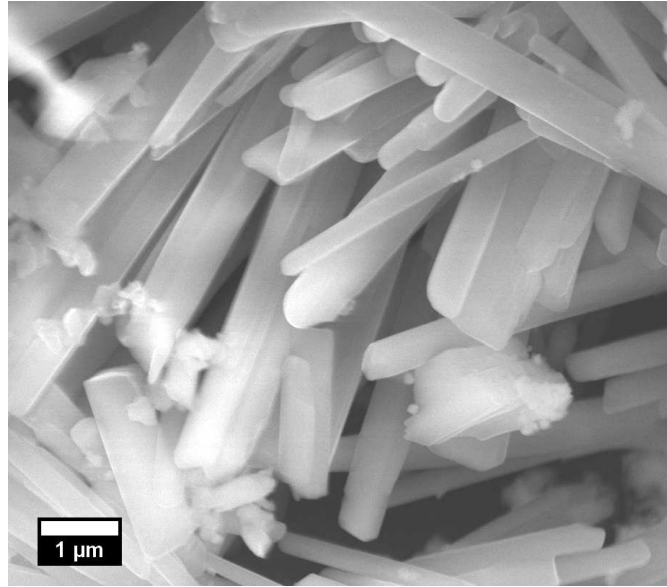


Figure 2.14: FESEM micrograph of BCZT nanorods powder calcined at 1000 °C/4 h.

Ti and Zr ions are positioned at the same B-site [138]. Table 1 indicates the lattice parameters, atomic positions and space group obtained after refinement. These parameters are comparable to those reported in the literature [138, 222]. The degree of tetragonality (c/a) at room temperature of BCZT is 1.0050. This value is in good agreement with those of Liu and Ren [159] and Praveen et al. [138] which are 1.0050 and 1.0049, respectively.

Fig. 2.14 presents FESEM micrograph of the elaborated BCZT powder. Mainly rod-like particles with smooth surface with an average diameter and length of 0.45 μm and 4.25 μm , respectively, with the corresponding aspect ratio around 10 (average length/average diameter), were observed. Besides that, very small amount of BCZT nanoparticles that were not yet transformed into BCZT rods were noticed.

2.2. SYNTHESIS OF BCZT CERAMICS WITH DIFFERENT MORPHOLOGIES

The plausible mechanism of the formation of BCZT rod-like particles is depicted in Fig. 2.15. It's known that the CTAB (cationic surfactant) has a critical micelle concentration (CMC) arranging between 0.9–1.0 mM [223]. Above this CMC, a transition from spherical micelles to rod-like micelles occurred, and the size of the micelles increased with the increase of CTAB concentration [224]. In our system, the concentration of CTAB is 30 mM, which is much higher than its CMC. As Fig. 2.14 illustrates, surfactant molecules are tending to assemble into rod-like micelles. Because of BCZT high surface energy and hydrophilic character due to functionalization with -OH groups, they are able to incorporate hydrophobic groups of CTAB (CTA^+), leading to the formation of $CTA^+ - BCZT - CTA^+$ system which coagulate to form a stable 1D nanorod structure [225, 226]. It should be noted that the microenvironment and packing for micelle-bound molecules in rod-shaped micelles are heterogeneous and are shown as spherical “end caps” and the cylindrical central part. The head group spacing is reduced in the cylindrical part of the rod-shaped micelle due to attenuation of charge interactions at high ionic strength [227].

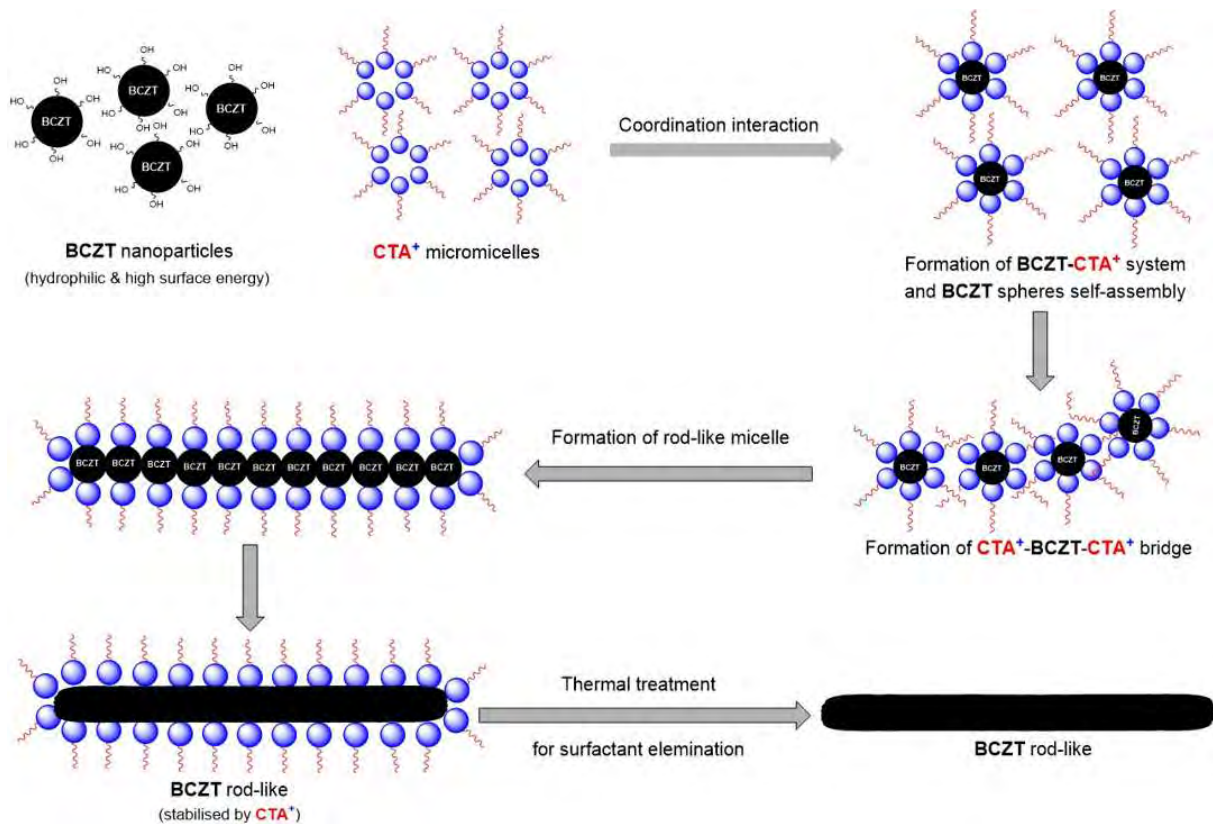


Figure 2.15: A plausible schematic representation of the formation of BCZT rod-like grains using rod-like micellar templates.

2.2.3 Morphological transition: from cube to multipod BCZT

2.2.3.1 Synthesis route

To design nanostructured lead-free BCZT ceramics of complex morphologies, a two-steps hydrothermal processing was used. The first step involves the elaboration of the HZTO_NW which serves as inorganic template for BCZT preparation. Then, the reaction of HZTO_NW and barium and calcium salts. To produce $\text{H}_2(\text{Zr}_{0.1}\text{Ti}_{0.9})_2\text{O}_7$ nanowires (HZTO_NW), which serves as inorganic template for BCZT preparation, 5 g of ZTO nanoparticles, was dispersed in 100 mL of 10 M NaOH aqueous solution in a 150 mL-Teflon-lined stainless-steel autoclave by stirring for 1 h. After sealing and heating at 240 °C for 48 h, the autoclave was cooled down to room temperature. The resulting white fluffy suspension was collected by filtration and soaked in 0.2 M HCl for 10 h in order to convert NaZTO to HZTO. The obtained product was centrifuged at 4000 rpm for 10 min, washed several times with DI water and ethanol, filtered to obtain a fluffy product, then freeze-dried for 48 h. Fig. 2.16 presents the main steps used for the elaboration of HZTO_NW.

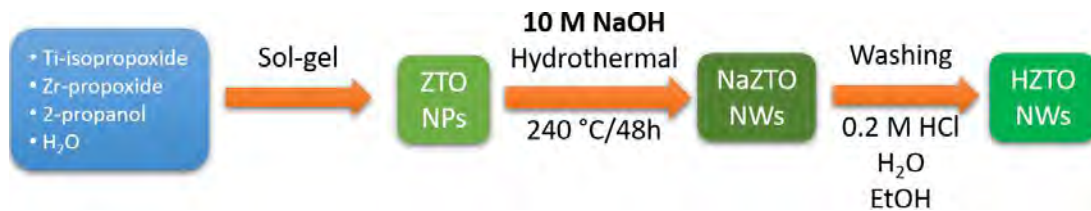


Figure 2.16: Experimental procedure for HZTO_NW elaboration.

BCZT nanostructures were prepared through hydrothermal reaction of HZTO_NW, barium acetate and calcium nitrate as depicted in Fig. 2.17. Under inert atmosphere (N_2), 150 mg of HZTO_NW was dispersed in 35 mL of barium acetate (50 mM or 150 mM) and calcium nitrate tetrahydrate (8.8 mM or 26.5 mM) solution and 0.1 M of potassium hydroxide. Next, the suspension was sonicated for 10 min to break the agglomeration. After, the final solution was purged with N_2 , transferred into a 50 mL-Teflon-lined stainless-steel autoclave, sealed and heated at 180 °C for different hydrothermal time, starting from 3 h to 72 h. After the hydrothermal reaction was completed, the sealed autoclave was

2.2. SYNTHESIS OF BCZT CERAMICS WITH DIFFERENT MORPHOLOGIES

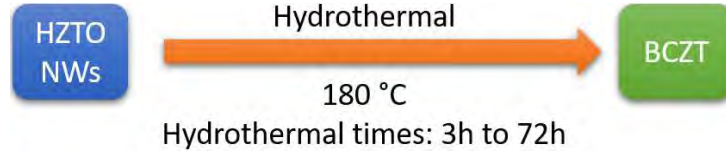


Figure 2.17: Experimental procedure for the elaboration of shape-controlled BCZT nanostructures.

cooled down to room temperature. The resulting white precipitates were collected by centrifugation at 5000 rpm for 10 min, soaked in 0.2 M HCl for 4 h, and washed several times with 0.2 M HCl, DI water and ethanol. Then, the final products were dried at 80 °C for 12 h. The prepared samples were designated as xByh, where x refers to Ba^{2+} concentration (50 mM or 150 mM) and y denotes the reaction time in hour. For instance, 50B18h corresponds to a sample elaborated using 50 mM of Ba^{2+} at 18 h of hydrothermal reaction time.

2.2.3.2 Morphological transformations

2.2.3.2.1 Weight-gain

The weight gain as a function of time give a macroscopic insight of the transformation kinetics of HZTO_NW in the presence of barium and calcium species. Fig. 2.18 gives such an evolution for two different conditions of barium/calcium concentration. Both curves show a similar behavior, Δm raises rapidly with time, and evolve slowly from 12 h to 32 h, then become stable from 32 h to 72 h of hydrothermal reaction. However, the kinetics is more rapid and the equilibrium weight gain is higher for the highest barium concentration. It is worth noting that the diffusion behavior is to describe the weight change as a function of square root of diffusion time. Accordingly, in this study, this kind of data presentation was also employed to have an insight on the diffusion of barium and calcium species to HZTO_NW.

2.2.3.2.2 Effect of reaction time

Fig. 2.19 represents the effect of time on the morphology of BCZT samples using 150 mM of Ba^{2+} and 26.5 mM of Ca^{2+} . HZTO_NW highly anisotropic shape are formed

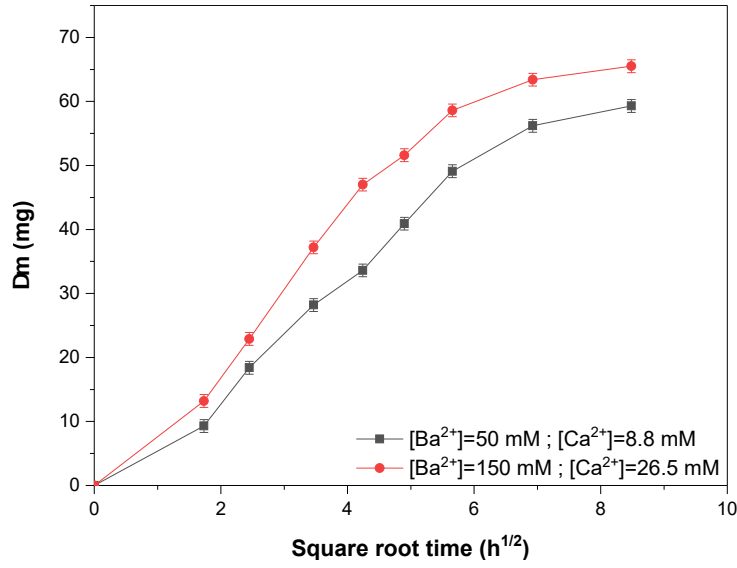


Figure 2.18: Variation of samples' weight as a function of the reaction time.

with various widths and lengths, with aspect ratio exceeding 50 (Fig. 2.19a). After 3 h of hydrothermal reaction, small cubes are grown on the surface of HZTO template (Fig. 2.19b). A further increasing in reaction time leads to boosted epitaxial growth of cubes on the surface of HZTO wires and multipods on the cubes faces until a complete covering of the HZTO template by these nucleations (cubes and multipods) (Fig. 2.19c). With increasing reaction time, the wire-like shape is progressively lost, while the coarsening of rough wires alongside with morphology degeneration and increasing amounts of loose nanoparticles are observed (Figs. 2.19d-f).

2.2.3.2.3 Effect of A-site concentration

Fig. 2.20 depicts the effect of A-site ions concentrations on the morphogenesis of BCZT materials after 18 h of hydrothermal reaction. In both samples, the formation of heterogeneous nucleation on the surface of HZTO template is observed. At low Ba^{2+} and Ca^{2+} concentrations, wires with rough surface covered with dendritic crystals and loose dendritic nanoparticles (multipods) are observed, however, the dominance of cubes on the surface of the template with the presence of loose cubic nanoparticles are detected. Accordingly, A^{2+} -concentration plays a vital role on the morphogenesis of the observed nanostructures [175]. Therefore, a thorough analyses of the composition and the crystallographic characteristics of each morphology will be discussed elsewhere.

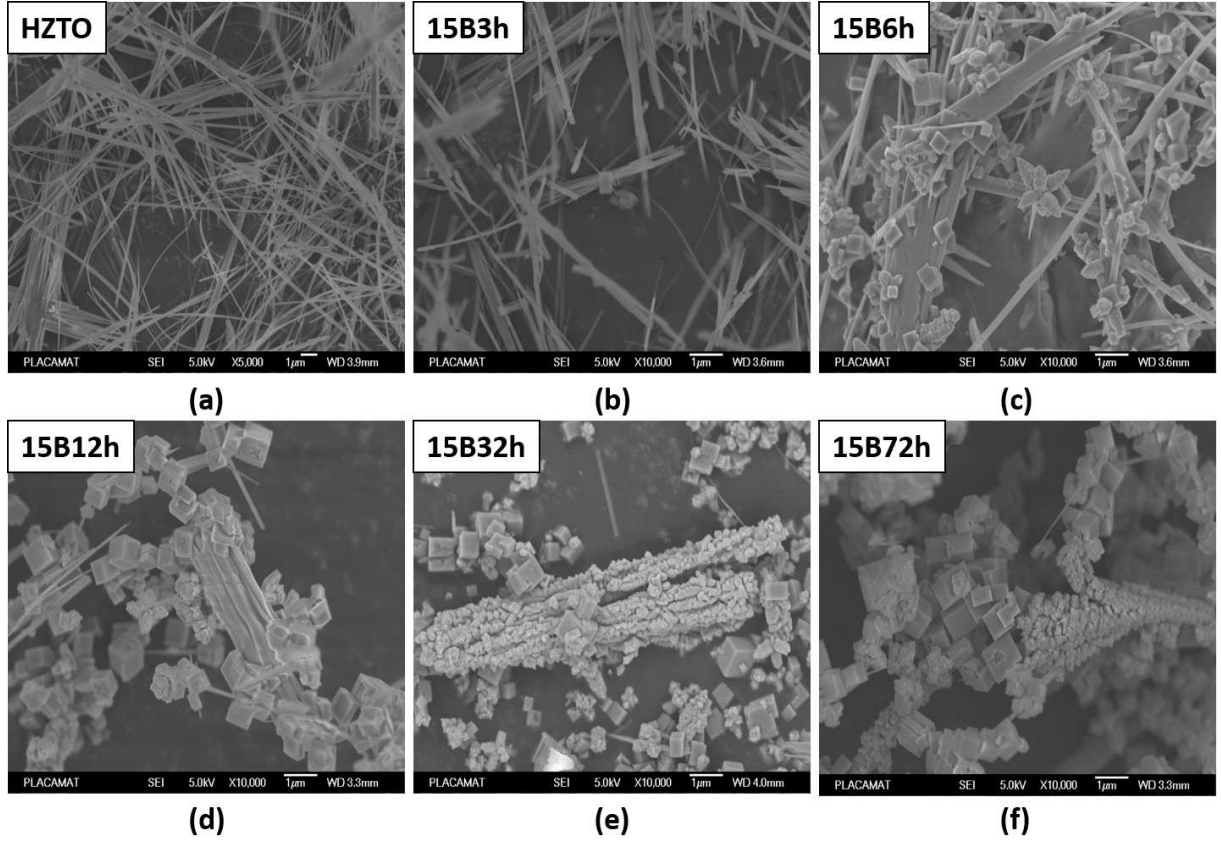


Figure 2.19: FESEM images indicating the effect of time on the morphogenesis of BCZT materials using 150 mM of Ba^{2+} and 26.5 mM of Ca^{2+} . (a) HZTO_NW, and after (b) 3 h, (c) 6 h, (d) 12 h, (e) 32 h and (f) 72 h of hydrothermal reaction.

2.2.3.2.4 Composition, structure and phases analysis

Compositional analysis of the resulting morphologies is probed energy dispersive X-ray spectroscopy (EDS). EDS elemental mapping images could provide the distribution of Zr, Ti, Ca, Ba and O elements in the different phases. As observed in Figs. 2.21 and 2.22, the Zr, Ti, and O elements constitute the whole wires in the HZTO_NW and Zr, Ti, Ca, and O elements constitute the entire cubes, however, Ba covers mainly the multipods. Hence, it can be concluded that the wires are HZTO_NW, the cubes constitute $\text{CaZr}_y\text{Ti}_{1-y}\text{O}_3$ (CZTO), $\text{Ca}_3(\text{Zr}_y\text{Ti}_{1-y})_2\text{O}_7$ ($\text{C}_3(\text{ZrTi})_2\text{O}_7$) and the multipods constitute BCZT phase. It is worth noting that some multipods exhibit small amounts of Ca. The structural properties of each phase are determined in the following paragraph.

The XRD patterns of powders elaborated using $[\text{Ba}^{2+}] = 50 \text{ mM}$ $[\text{Ca}^{2+}] = 8.8 \text{ mM}$ and $[\text{Ca}^{2+}] = 150 \text{ mM}$, $[\text{Ca}^{2+}] = 26.5 \text{ mM}$ at various hydrothermal reaction times are

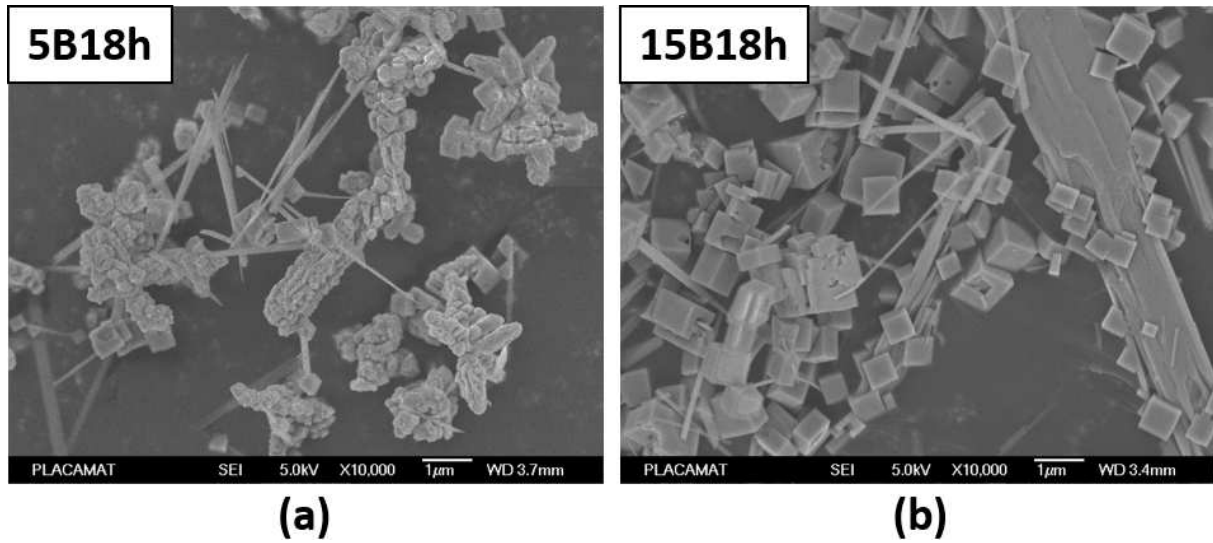


Figure 2.20: FESEM images indicating the effect of A-site concentrations on the morphogenesis of BCZT materials after 18 h of hydrothermal reaction, using (a) 50 mM of Ba^{2+} and (b) 150 mM of Ba^{2+} .

shown in Figs. 2.23a, b, respectively. The XRD patterns in can be indexed to monoclinic ($C2/m$), orthorhombic ($Pbnm$), orthorhombic ($Ccm21$) and tetragonal ($P4mm$), for HZTO, CZTO, $\text{C}_3(\text{ZrTi})_2\text{O}_7$ ($\text{C}_3(\text{ZrTi})_2\text{O}_7$) and BCZT, respectively. It is observed that whatever the A-site concentrations BCZT, unreacted HZTO_NW, secondary phases CZTO and $\text{C}_3(\text{ZrTi})_2\text{O}_7$ are simultaneously present in all samples. Moreover, the intermediate CZTO and $\text{C}_3(\text{ZrTi})_2\text{O}_7$ phases is remarkably pronounced at high-concentration A-site (Fig. 2.23b). After increasing the reaction time, a reduction of the unreacted HZTO_NW and the increasing of CZTO and $\text{C}_3(\text{ZrTi})_2\text{O}_7$ phases were noticed.

The previous observations were quantified to identify the amount of each phase in any sample as shown in Figs. 2.24a, b. It is found that the desirable BCZT phase with large amount is obtained in samples using low-concentration A-site, and especially at reaction time of 6 and 12 h. After increasing the reaction time, the quantity of BCZT phase decreases, and the unreacted HZTO_NW is reduced. Meanwhile, the secondary phases CZTO and $\text{C}_3(\text{ZrTi})_2\text{O}_7$ increase. At elevated reaction time (72 h), BCZT phase still present with an amount of 55%. At high-concentration A-site, the maximum amount of BCZT is found to be 60% at 3 h of reaction. However, after expanding hydrothermal reaction time, a drop of the quantity of BCZT and an increase of the secondary phases

2.2. SYNTHESIS OF BCZT CERAMICS WITH DIFFERENT MORPHOLOGIES

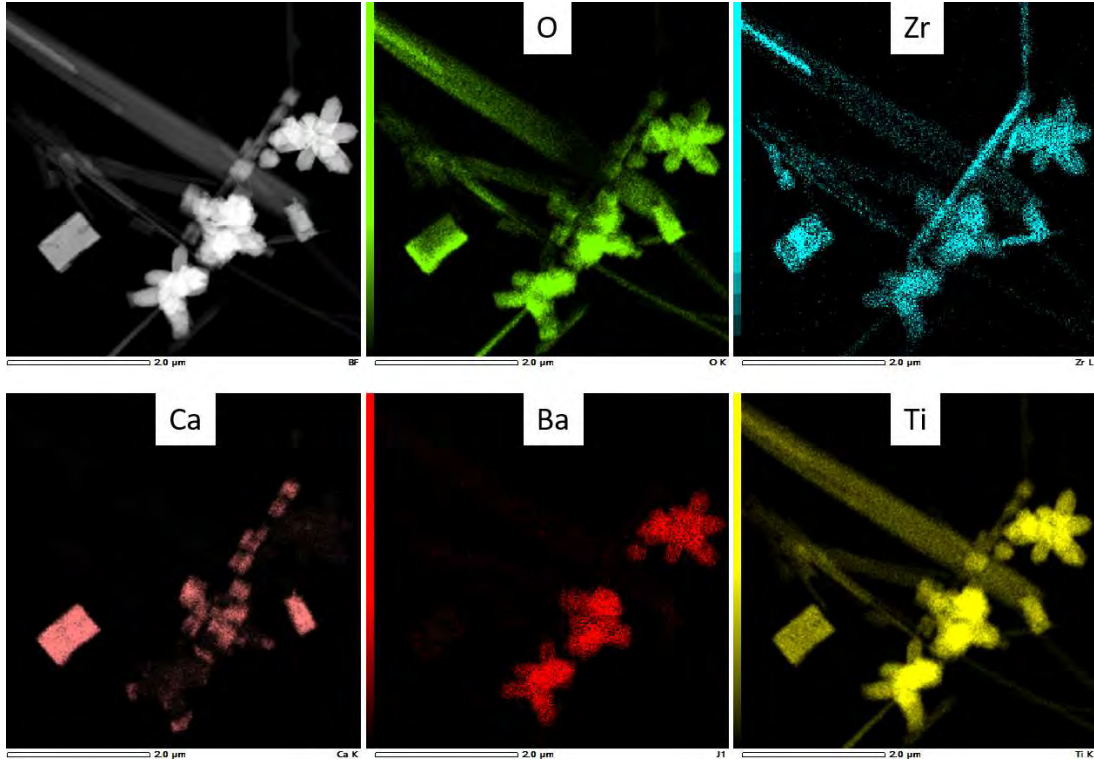


Figure 2.21: TEM image and EDX elemental mapping images of wires, cubes and multipods.

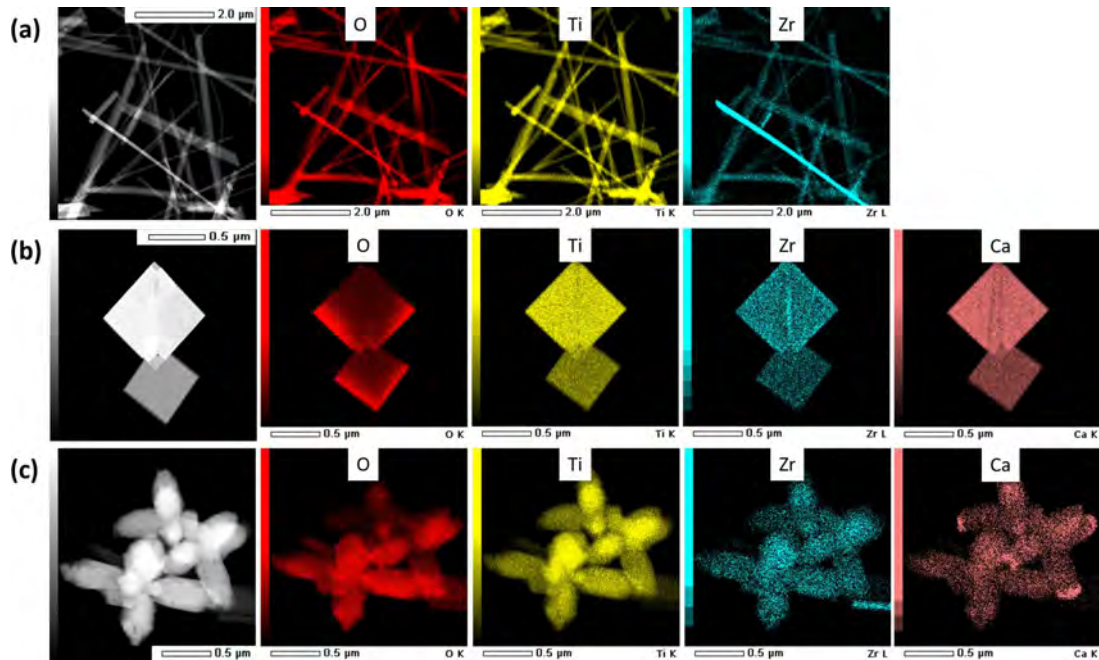


Figure 2.22: TEM image and EDS elemental mapping images of isolated (a) wires, (b) cubes and (c) multipods.

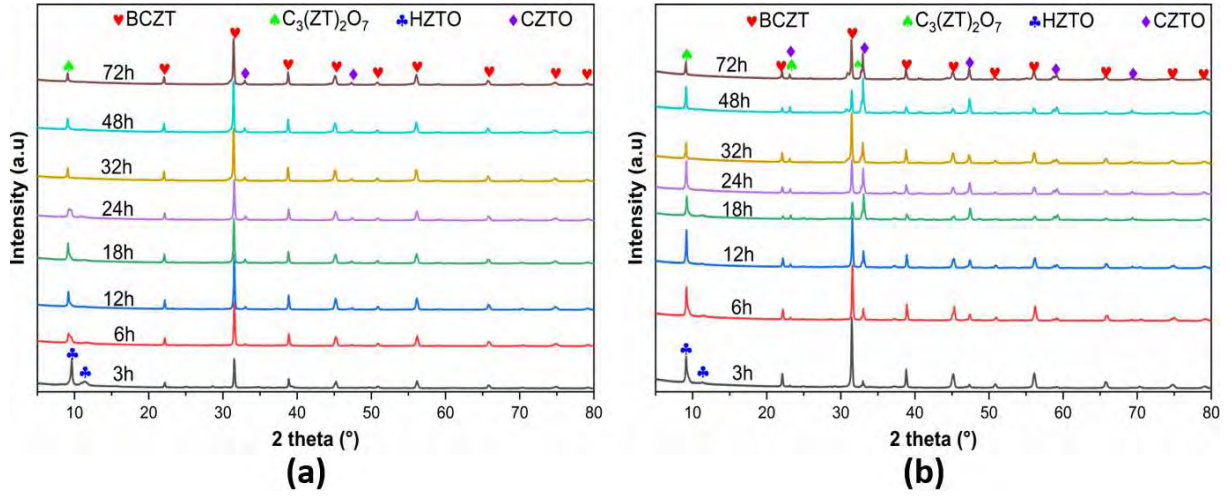


Figure 2.23: XRD patterns of different powders elaborated using (a) $\{[Ba^{2+}] = 5 \text{ mM}, [Ca^{2+}] = 8.8 \text{ mM}\}$ and (b) $\{[Ba^{2+}] = 150 \text{ mM}, [Ca^{2+}] = 26.5 \text{ mM}\}$, at various hydrothermal reaction times.

CZTO and $C_3(ZrTi)_2O_7$ were noticed (Fig. 2.24b). Therefore, no single-phase BCZT is obtained through this processing, and the use of low-concentration A-site and low reaction time ($\leq 12 \text{ h}$) could help to obtain large amount of BCZT phase in the sample.

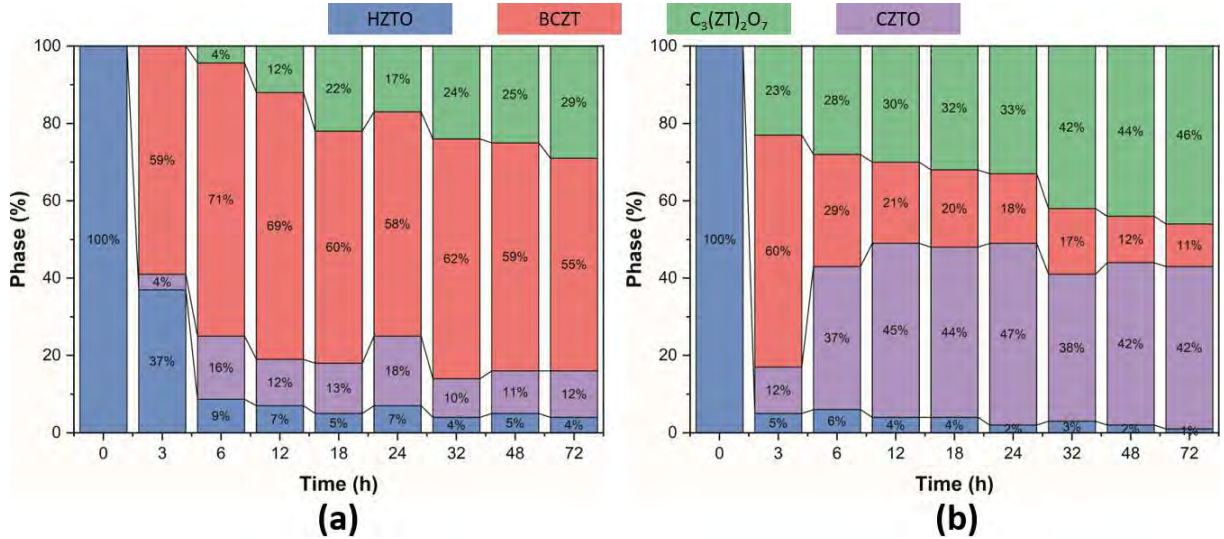


Figure 2.24: The composition of the elaborated samples at various hydrothermal reaction times using (a) $\{[Ba^{2+}] = 5 \text{ mM}, [Ca^{2+}] = 8.8 \text{ mM}\}$ and (b) $\{[Ba^{2+}] = 150 \text{ mM}, [Ca^{2+}] = 26.5 \text{ mM}\}$.

To have an insight on the morphological characteristics of the samples elaborated at prolonged reaction time, Figs. 2.25a, b display FESEM micrographs of 50B72h and 150B72h samples, respectively. It is observed that 50B72h is composed essentially with

2.2. SYNTHESIS OF BCZT CERAMICS WITH DIFFERENT MORPHOLOGIES

multipods, wires, degenerated morphologies and small number of cubes (Fig. 2.25a), however, 150B72h sample is based on cubes, degenerated morphologies and small number of multipods (Fig. 2.25b).

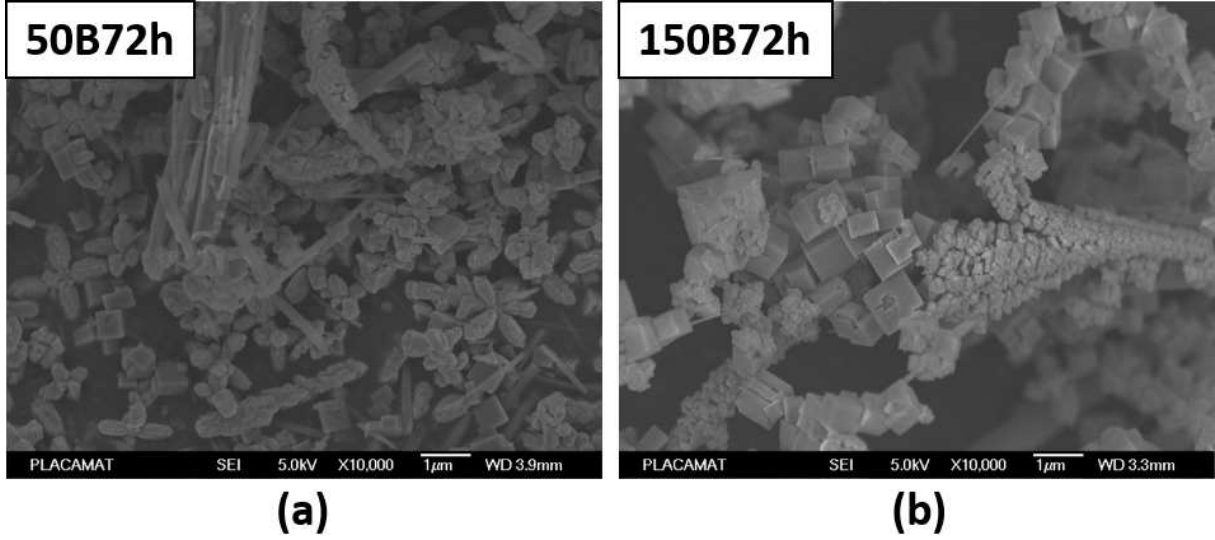


Figure 2.25: FESEM micrographs of 50B72h and 150B72h samples.

It was found that the structure and morphological studies provide important insights into the co-existence of simultaneous phases during the preparation of the samples. To distinguish these phases, SAED diffraction patterns were collected for each morphology. The SAED patterns clearly show that the obtained products possess single-crystalline structures as seen in Fig. 2.26. According to the SAED patterns, HZTO nanowire, CZTO cube and BCZT multipod are all single-crystal phase and well crystalline. As shown in Fig. 2.26a, SAED spot distances of the HZTO nanowire are found to be 9.0163 \AA and 3.9302 \AA , which are indexed as (001) and (400) planes, respectively. Likewise, the SAED spot distances of the CZTO cube are calculated to be 0.55 \AA and 0.55 \AA , which are consistent with the (100) and (010) planes, respectively (Fig. 2.26b). Also, the lattice spacings determined from the diffraction spots of the SAED of BCZT multipod are found to be 3.999 \AA and 2.834 \AA , which correspond to (100) and (011) planes, respectively (Fig. 2.26c). The corresponding zone axis of each SAED pattern is indicated in the top-left corner of each figure. The SAED diffraction patterns are in good agreement with the obtained results of XRD analyses.

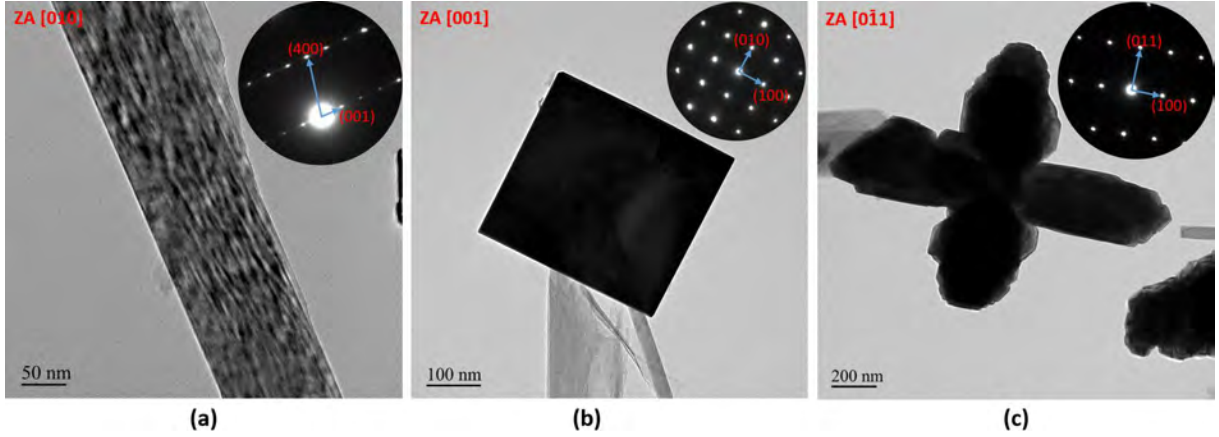


Figure 2.26: TEM and SAED patterns of (a) HZTO nanowire, (b) CZTO cube, and (c) BCZT multipod.

2.2.3.3 Growth mechanism of BCZT multipods

On the basis of the morphology observations, the domination of the heterogeneous nucleation (cubes and multipods) on the surface of HZTO, leading to the formation of polycrystalline wires with a rough surface, dendritic crystals and some loose nanoparticles (cubes and multipods) (Figs. 2.27d-f) indicate that a topochemical transformation of the HZTO template to the BCZT perovskite materials was not happened. Hence, a dissolution–precipitation processes is occurred rather than ionic exchange during the hydrothermal reaction. The most plausible mechanism for the formation of cubes and multipods nanostructures is as follow. First, primary cubes with good crystallinity, sharp corners and edges and smooth surface (Fig. 2.27d) decorate the HZTO template *via* heteroepitaxial growth. These cubes reorient under the influence of the interaction potentials and align along a preferred crystallographic direction, leading to the formation of mesocrystals rather than random aggregates while preserving the initial wire-like morphology of HZTO (Figs. 2.28a, d). After nucleation, the successive growth of nuclei strongly determines the shape of the nanomaterials, which is thermodynamically driven by the decreasing surface free energy of the generated particles. The nucleation of the cubes on the surface of HZTO_NW only proceeds at some special sites like as reported by Kalyani et al. [228]. The cubes reorientation step is essential to remove the free energy barrier to aggregation [229, 230]. Some of these self-assembly cube arrays, with a size between 200 – 500 nm, are tightly bound together, and some of them were grown at a certain distance

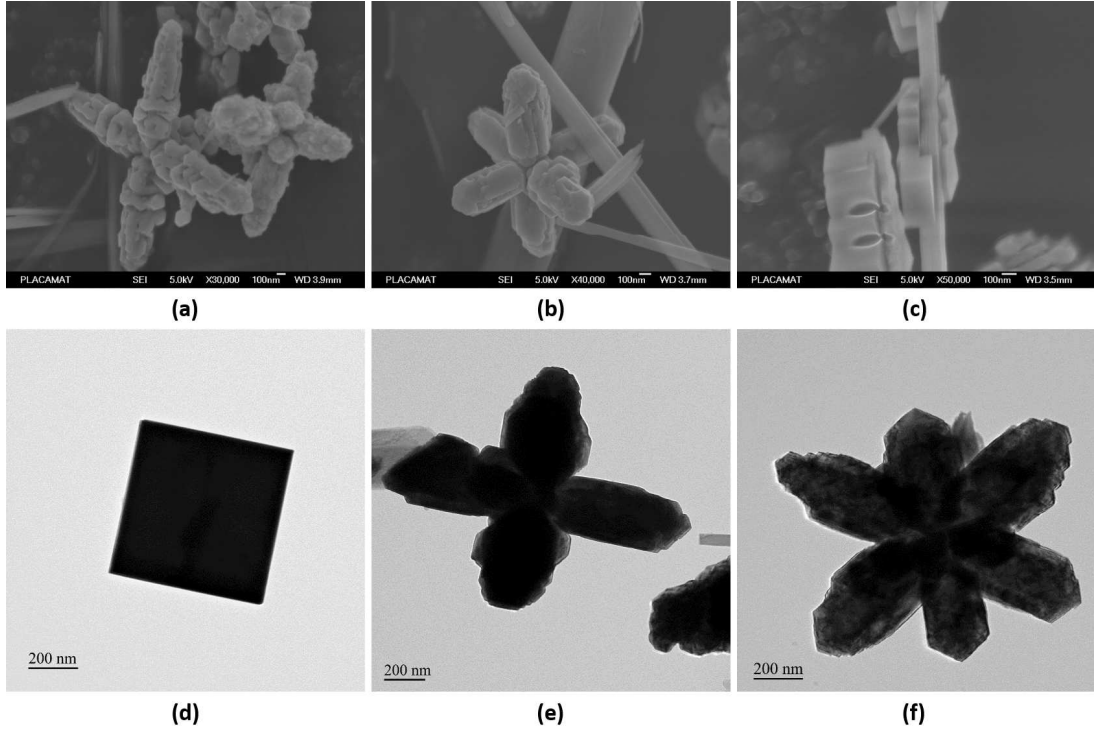


Figure 2.27: (a-c) FESEM and (d-f) HRTEM images of various loose nanostructures using 150 mM of Ba^{2+} and 26.5 mM of Ca^{2+} .

from HZTO surface. When the diameter of the HZTO template is small enough, two rows of perovskite nanocubes will nucleate on opposite surfaces of the wire as seen in Fig. 2.27c. More interestingly, two or more nanocubes nuclei are directly fusing together with an edge-to-edge fashion to form larger crystallites, sharing a common crystallographic orientation and uniting at the planar interfaces *via* a process called oriented attachment (Fig. 2.29) [231, 232]. Generally, for the cubic phase, the relative surface energies (γ) are in the order of $\gamma_{\{111\}} < \gamma_{\{100\}} < \gamma_{\{110\}}$ among the lowest index planes [233]. The presence of inorganics or organics in the solution during the crystal growth process can modify the relative order of surface energies [234]. The presence of Ba^{2+} ions could slightly modify the surface energy, and the crystal growth now along $\langle 100 \rangle$ direction is much faster than that along the $\langle 111 \rangle$ and $\langle 110 \rangle$ directions, because the $\{100\}$ facets bore the lowest energy.

Yet again, to lower the surface energy, the faces of cubes with $\langle 100 \rangle$ directions act as nucleation site for BCZT multipods (Figs. 2.28b, e) with four to six pods with different growth levels can be observed (Fig. 2.27a, b, d, e), which grow perpendicular to cubic 100

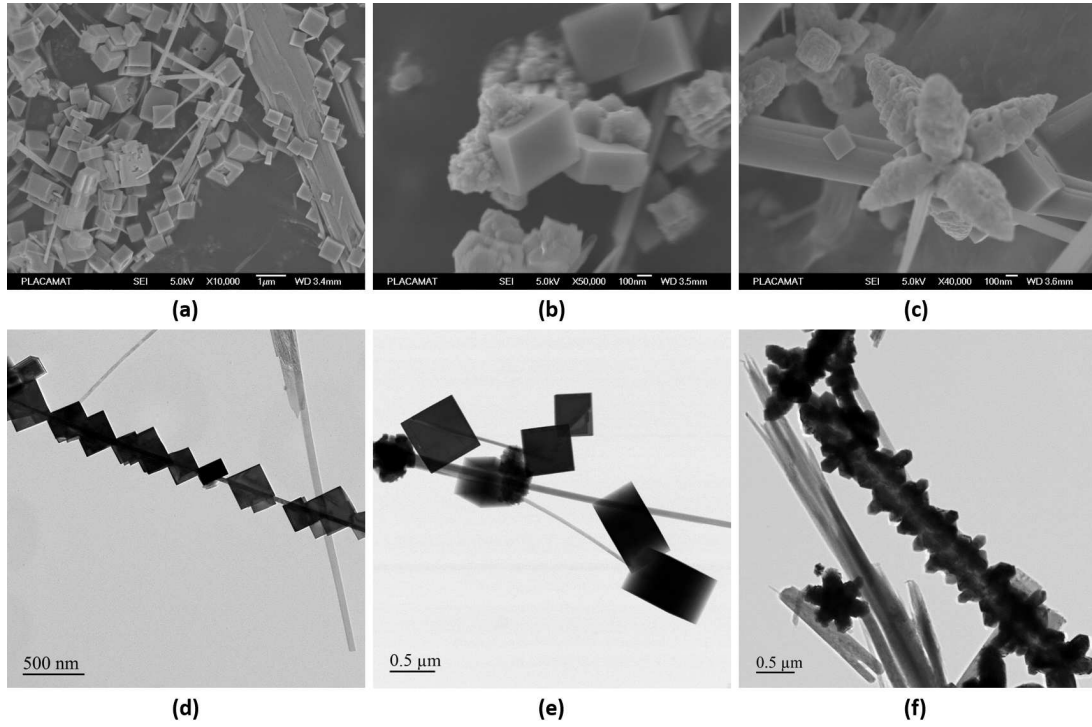


Figure 2.28: (a-c) FESEM and (d-f) HRTEM images indicating the morphogenesis of BCZT materials using 15mM of Ba^{2+} and 26.5 mM of Ca^{2+} .

faces while preserving the same orientation (Fig. 2.28c, f). The octahedral particle is a thermodynamic product with the lowest surface energy and is easily obtained as soon as the octahedral growth habit is controlled and the reaction time is long enough [235]. The successive morphological evolution depends on the density of surface nuclei. As soon as the HZTO template is totally consumed, a powder composed of loose particles (cubes and multipods) and irregular aggregates is obtained with almost complete loss of the initial wire morphology. The resulted loose particles (cubes and multipods) can be originated from the lattice mismatch or the crystallographic incompatibility between HZTO_NW and CZTO and BCZT products [228,236]. A similar evolution was reported in refs [228,229,237]. These results indicate that BCZT 1D nanostructures cannot be obtained by using HZTO_NW as templates in hydrothermal process at least under stagnant conditions. It is worthy to note that, despite several attempts to form BCZT nanowires, the topochemical transformation of HZTO_NW in the presence of barium and calcium species by ion exchange could not be obtained. This suggests that the Ba/Ca ions exchange reaction, reported by Zhou et al. as an effective template-assisted synthesis method for the preparation of single phase BCZT

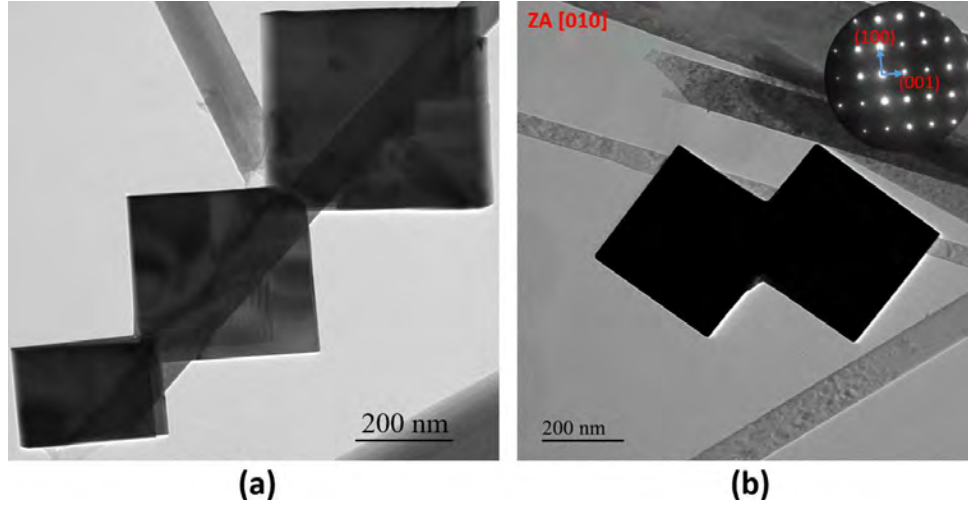


Figure 2.29: HRTEM images of (a) three edge-attached cubes and (b) two edge-attached cubes (SAED pattern in inset).

nanowires can only occurs in some special experimental conditions and is incompatible with an interface-driven dissolution and crystallization process [170].

2.3 Dielectric and ferroelectric properties of BCZT sintered ceramics

2.3.1 Microstructural state of sintered ceramics

2.3.1.1 BCZT near-spherical nanoparticles

2.3.1.1.1 Strategy N°1: Surfactant-assisted solvothermal

Fig. 2.30 displays the SEM micrographs and grain size distributions of B-0, B-CTAB and B-SDS ceramics sintered at 1250 °C/10 h. B-0 sample exhibits a Gaussian distribution of grain size characterized by a mean grain size of 3.6 μm . The grain size distributions of BCZT ceramics were determined by intercept method using ImageJ software. The grains are shown to be poly-faceted and the presence of inter-granular pores were highlighted (Fig. 2.30a). B-CTAB ceramic has a morphology relatively different to that observed in B-0. It is characterized by the presence of two types of grains: non-uniform poly-facets

and relatively uniform spheroids. The grains are characterized by a lognormal distribution around the smallest sizes (around 1 μm) (Fig. 2.30b). The resulting mean grain size was measured to be 2.7 μm . It is worthy to mention that B-0 and B-CTAB have large different grain size distribution. The porosity in B-CTAB ceramic is much lower compared to B-0. Indeed, the small spheroidal grains (60 – 1000 nm) are inlayed in the boundaries of coarse grains and occupy the pores created during the sintering of B-CTAB sample. B-SDS ceramics exhibit a Gaussian distribution of grain size characterized by a mean grain size of 6.6 μm . The grain boundaries are well defined and few faceted (Fig. 2.30c). Finally, a high value of relative density was calculated in B-SDS ceramics (96.4%) followed by B-CTAB (95.2%) and B-0 (93.1%). This corroborates SEM results, where the distribution of pores decreases in B-CTAB and B-SDS ceramics.

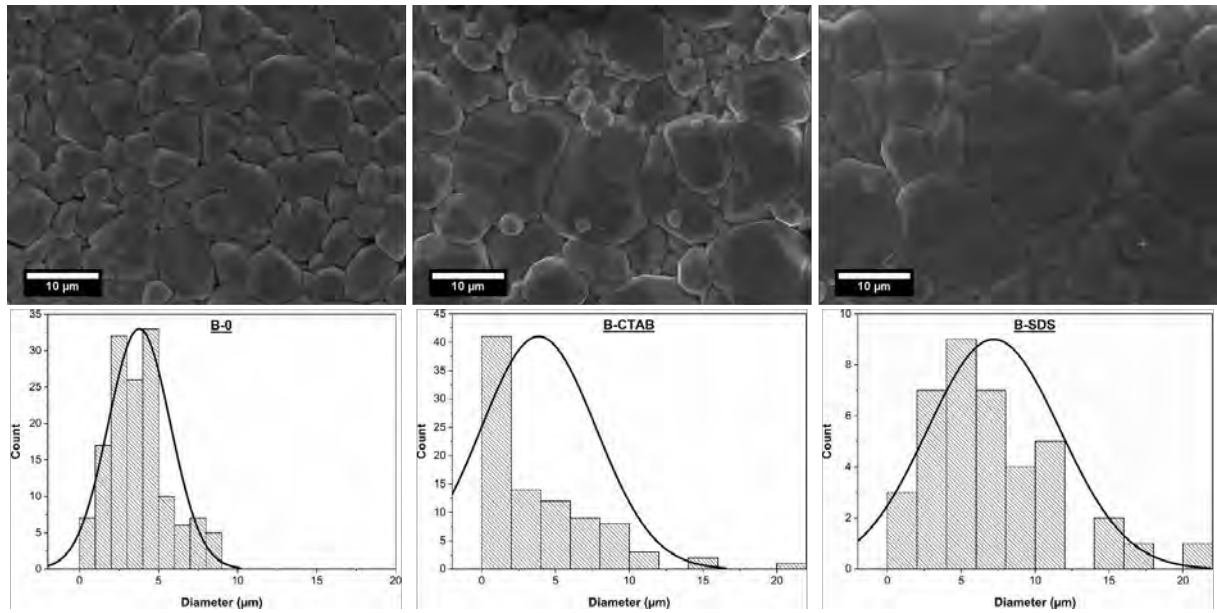


Figure 2.30: SEM micrographs and grain size distributions of B-0, B-CTAB and B-SDS ceramics sintered at 1250 °C/10 h.

2.3.1.1.2 BCZT near-spherical nanoparticles: Strategy N°2

Fig. 2.31 exhibits the SEM micrographs and the variation of bulk and relative densities and grain size with synthesis temperature for BCZT ceramics sintered at 1250 °C/10 h. B-25 exhibits small grain (Fig. 2.31a), however, B-80 shows the presence of small and coarse spheroidal grains (Fig. 2.31b). Contrary to B-25 and B-80, B-160 ceramic exhibits

2.3. DIELECTRIC AND FERROELECTRIC PROPERTIES OF BCZT SINTERED CERAMICS

a well-defined grain boundary with coarse and flatten grains leading to an enhancement of bulk and relative densities (Figs. 2.31c, d). In B-160 ceramic, the bulk density was found to be 5.62 g/cm³, which correspond to 97.1% of the theoretical density (5.79 g/cm³). It was observed that, after sintering process, by increasing the hydrothermal temperature, the grain size of the sintered ceramic increase, which led to an enhancement of the dielectric properties of the ceramic at elevated hydrothermal temperature. For example, the dielectric constant was boosted from 2242 to 12085 after increasing the hydrothermal reaction temperature from 25 to 160 °C, by increasing the grain size from 0.8 μm to 22.1 μm .

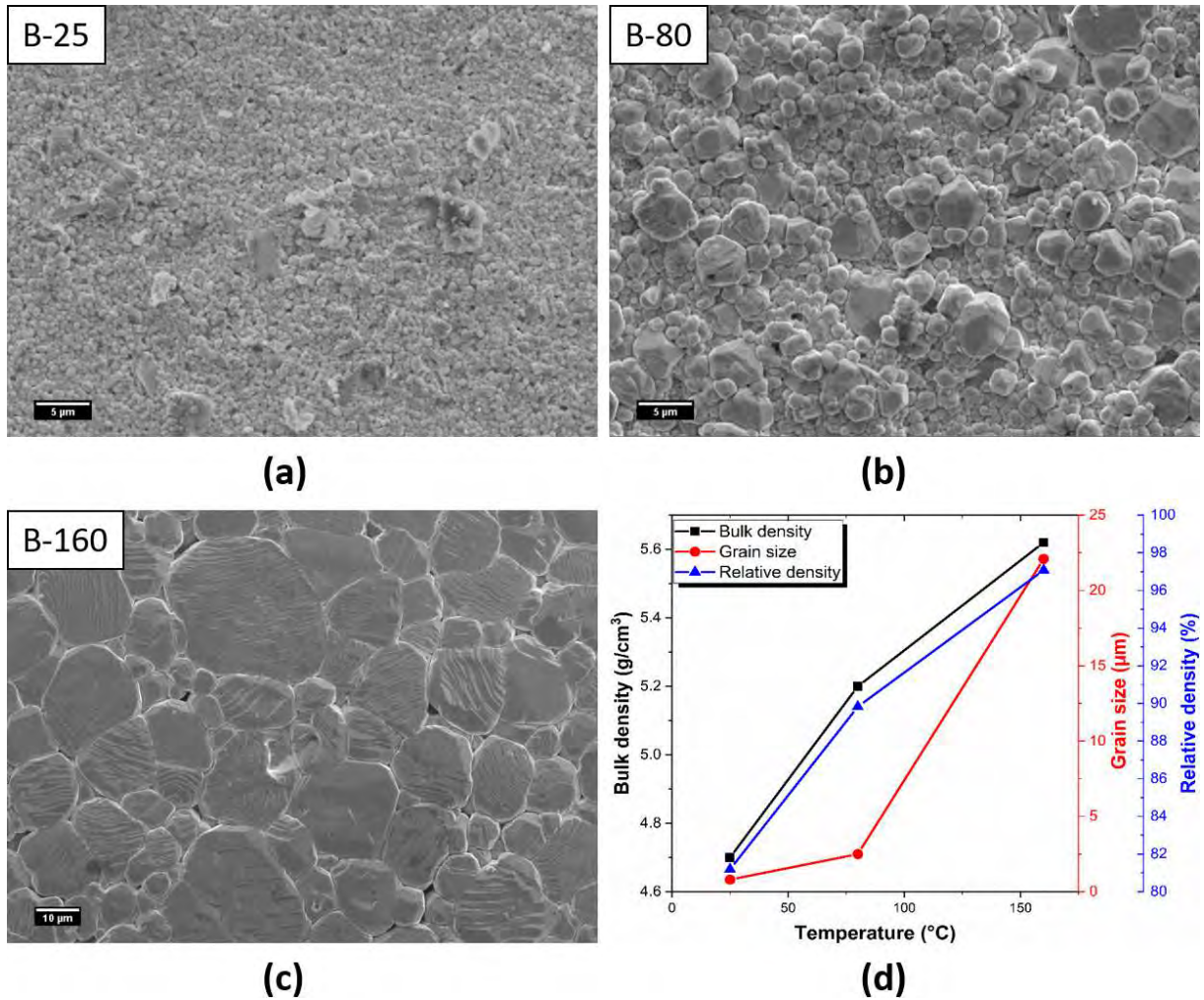


Figure 2.31: SEM micrographs of (a) B-25, (b) B-80 and (c) B-160 ceramics sintered at 1250 °C/10 h and (d) variation of bulk and relative densities and grain size with synthesis temperature.

2.3.1.2 BCZT rod-like ceramic

Fig. 2.32 displays SEM micrograph and the corresponding statistical distribution of length and diameter of rod-like BCZT ceramic (B_NR) ceramic sintered at 1250 °C/10 h. The microstructure reveals tightly bonded and well-defined rod-like grains with no obvious porosity, corresponding to a high relative density (D_r) of up 95% (bulk density of 5.50 g/cm³). The average length and diameter of the rod-like grains were 5.2 μ m and 1.35 μ m respectively. Hence, an average aspect ratio of about 4.

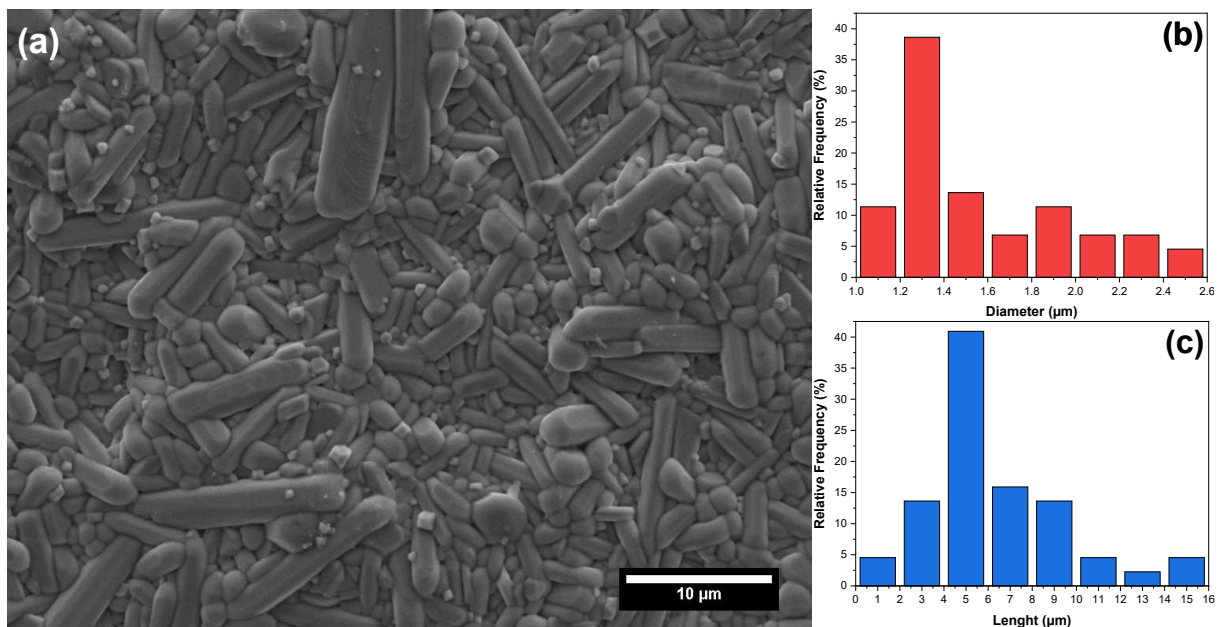


Figure 2.32: (a) SEM micrograph and corresponding statistical distribution of (b) length and (c) diameter of B_NR ceramic sintered at 1250 °C/10 h.

2.3.1.3 BCZT: Anisotropic morphologies

Fig. 2.33 exhibits FESEM micrographs of HZTO_NW and 50B24h ceramics sintered at 1250 °C/10 h. In both ceramics the initial morphologies were transformed to completely fragmented nanoparticles. Microstructure with fine grains where pores are clearly presented are observed in HZTO_NW sintered ceramic (Fig. 2.33a). Concerning 50B24h ceramics, it was concluded before that 50B24h powder was formed with multiple phases, i.e. nanowires and large amounts of cubes and multipods. Hence, backscattered electrons detector (BSE)

was used to visualize the composition fluctuation in each phase after sintering process at 1250 °C/10 h (Fig. 2.33b). The observed darkest regions correspond to CZTO and/or $C_3(\text{ZrTi})_2\text{O}_7$ phases and the brightest ones corresponds to BCZT phase.

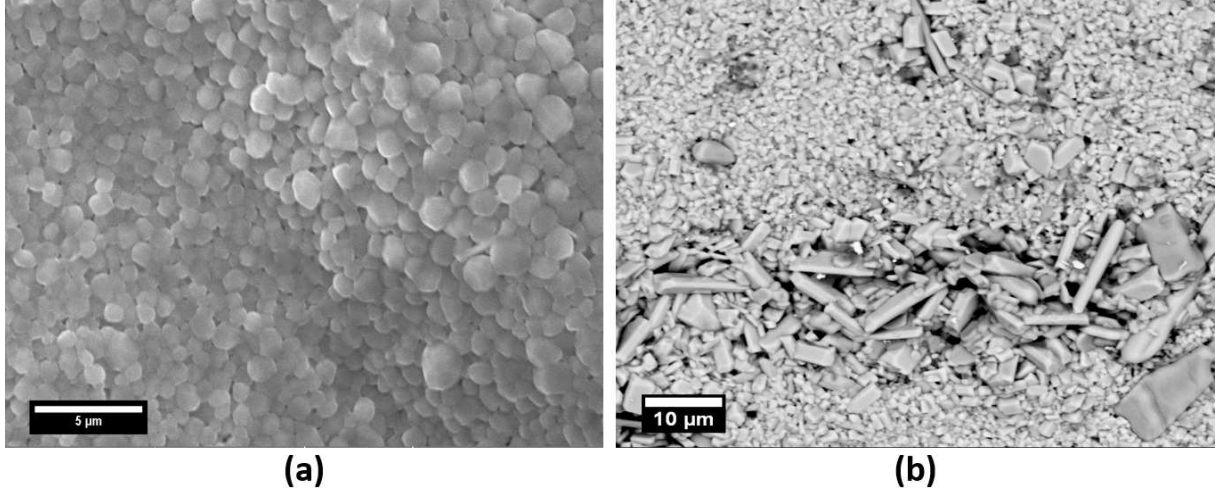


Figure 2.33: FESEM micrographs of (a) HZTO_NW, (b) 50B3h and (c) 50B24h ceramics sintered at 1250 °C/10 h.

2.3.2 Dielectric and ferroelectric properties of sintered ceramics

2.3.2.1 BCZT near-spherical nanoparticles

2.3.2.1.1 Strategy N°1: Surfactant-assisted solvothermal

Figs. 2.34a-c show the temperature dependence of the dielectric constant and dielectric loss at various frequencies for sintered BCZT pellets at 1250 °C/10 h. All samples exhibit a broad dielectric anomaly associated with tetragonal/cubic (T/C) phase transition around 90 °C. This dielectric broadening is due to compositional fluctuations and micro-inhomogeneity [238]. Meanwhile, all peak temperatures are dependent on the frequency and shift to high temperature with frequency increasing. In other words, all BCZT ceramics exhibit a relaxor behavior [239, 240]. The enhanced dielectric properties are observed in B-SDS ceramic, where the dielectric constant (ϵ_r) and dielectric loss ($\tan\delta$) are enhanced with 80% and 70% compared to B-0 ceramic. The reasons behind the enhancement of the dielectric properties in B-CTAB and B-SDS ceramics compared to B-0 ceramics could be

interpreted in two ways. (i) Traditionally, it has been argued that the increase in grain size of sintered ceramics enhances their dielectric properties [241, 242]. In B-SDS ceramics, the dielectric properties are enhanced after increasing the grain size from 3.6 to 6.6 μm . (ii) In B-CTAB ceramics, the increased dielectric constant was accompanied by a decreasing in grain size as described in Devonshire's phenomenological theory [65, 168]. Moreover, it was believed that the increase in density contributed to the enhancement of the dielectric constant [243]. As revealed in density measurements and SEM micrographs, the smaller particles could fill the gaps between the larger grains (Fig. 2.30b). This could result in increases in a degree of the packing and thus an enhancement of densification during the sintering process [244]. These suggest that the presence of surfactants exerts a favorable influence on the densification process. Consequently, dielectric properties were enhanced even at small-grained BCZT ceramics.

Besides, Fig. 2.34d shows the room-temperature polarization hysteresis loop ($P - E$) of the BCZT ceramics. The remnant polarization (P_r) increases from 2.85, 3.53 to 4.13 $\mu\text{C}/\text{cm}^2$ for B-0, B-CTAB and B-SDS, respectively. However, the coercive field (E_c) decreases from 2.48, 2.14 to 2.00 kV/cm for B-0, B-CTAB and B-SDS, respectively. B-SDS ceramic exhibits enhanced ferroelectric properties, hence, the addition of surfactant could affect grain size which results in an enhancement of the ferroelectric properties.

2.3.2.1.2 BCZT spherical nanoparticles: Strategy N°2

Fig. 2.35a compares the temperature-dependence of the dielectric constant and dielectric loss at 1 kHz of B-25, B-80 and B-160 ceramics sintered at 1250 $^{\circ}\text{C}/10$ h. All samples exhibit a broad dielectric anomaly associated with tetragonal/cubic (T/C) phase transition. Meanwhile, the dielectric losses of all samples decrease gradually when increasing measurement temperature to 40 $^{\circ}\text{C}$, then remain constant and after they increase (Inset of Fig. 2.35a). The overall dielectric properties at 1 kHz of all ceramics are summarized in Table 1. The temperature dependence of the dielectric constant and the dielectric loss of all BCZT ceramics at various frequencies are shown in Fig. 2.35b–d. The dielectric properties were enhanced with increasing hydrothermal temperature. Despite the low sintering temperature of B-160 ceramic, the maximal value of the dielectric constant

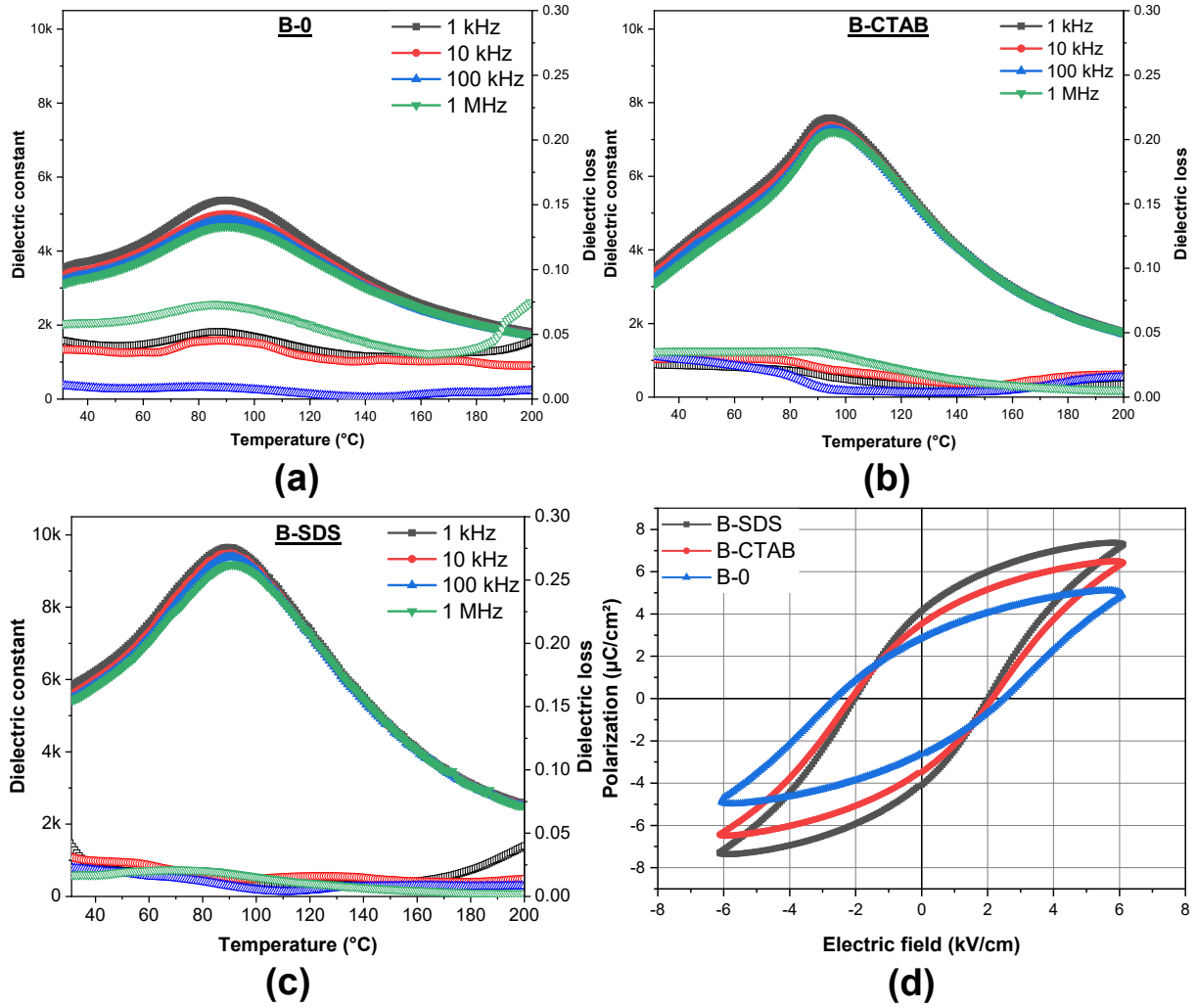


Figure 2.34: Temperature dependence of dielectric constant and dielectric loss of (a) B-0, (b) B-CTAB and (c) B-SDS ceramics sintered at 1250 °C/10 h. (d) Room-temperature $P - E$ loops of BCZT ceramics.

reached a value of 12085, which is much higher than that reported in other works using hydrothermal [165] or sol-gel hydrothermal routes [176]. Moreover, for all BCZT samples the peak temperatures are frequency-dependent and shifted to higher temperature with increasing frequency (reminiscent of relaxor behavior) [239, 240].

To gain insights on the ferroelectric properties of BCZT ceramics, room-temperature $P - E$ loops under 20 kV/cm were plotted in Fig. 2.36a. Interestingly, it is demonstrated that the ceramic elaborated at room temperature (B-25) exhibits a ferroelectric behavior evidenced by the $P - E$ hysteresis loops. P_r increases from 0.81 to 2.80 and 4.52 $\mu\text{C}/\text{cm}^2$ for B-25, B-80 and B-160, respectively. In contrast, E_c decreases from 3.63 to 3.97 and

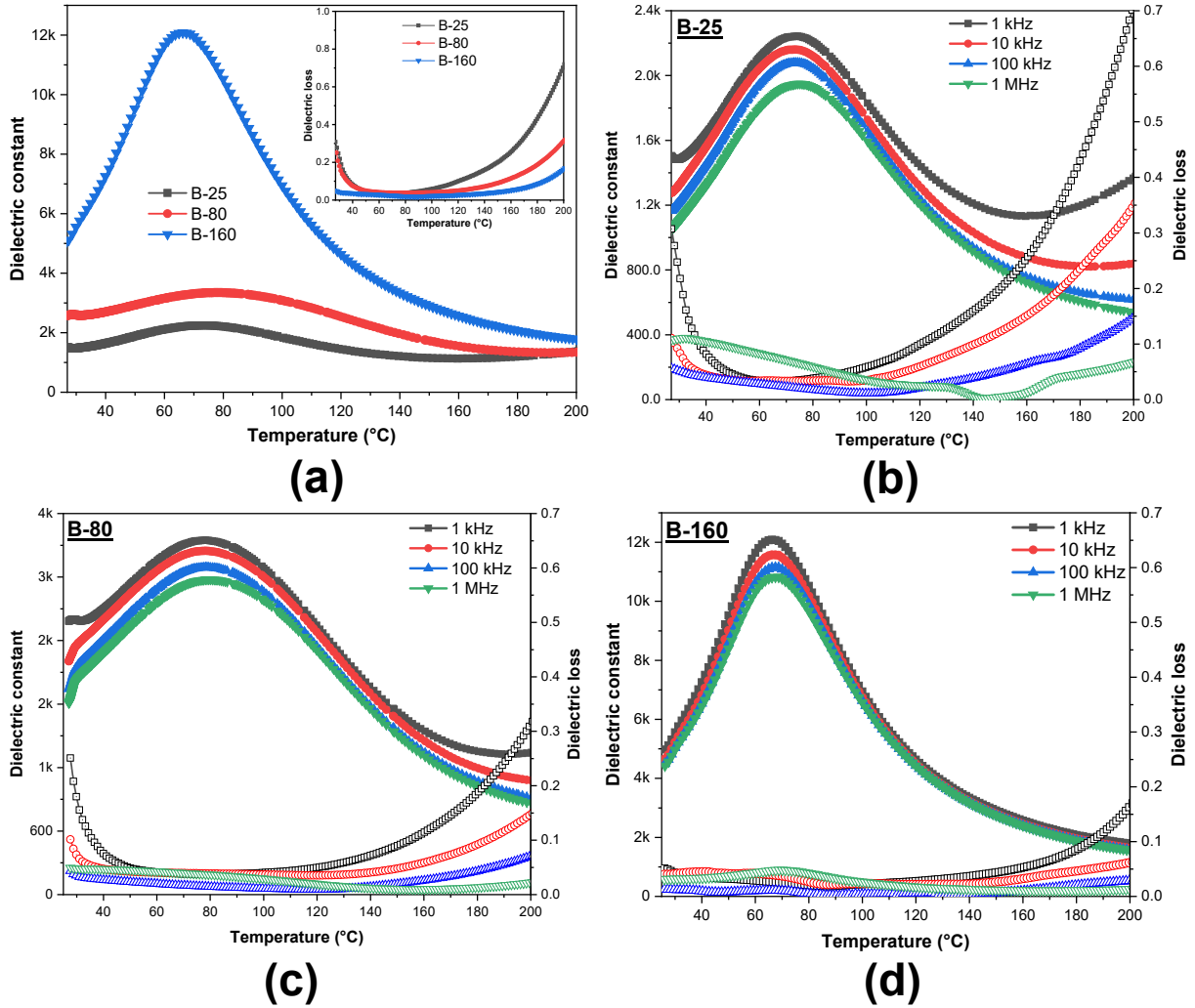


Figure 2.35: (a) Comparison of the dielectric properties of BCZT ceramics at 1 kHz, and temperature dependence of dielectric constant and dielectric loss of (a) B-25, (b) B-80 and (c) B-160 ceramics sintered at 1250 °C/10 h.

3.21 kV/cm for B-25, B-80 and B-160, respectively. It is well known that the ferroelectric properties are highly depended on parameters like grain size, grain size distribution, grain shape, phase transition, ionic radii and defect concentration [245–247]. The ceramics with large grains have been reported to exhibit larger P_r and small E_c [136, 243, 248]. Since, the smaller grains in ferroelectric ceramics inhibit the formation of large ferroelectric domains, consequently, the effective contribution to the total polarization is reduced [249, 250]. Moreover, the grain boundary affects the polarization, since the grain boundary is a low-permittivity region, i.e. the grain boundary has poor ferroelectricity. Therefore, the polarization of the grain boundary may be low, or even zero. Space charges in the grain

boundary exclude polarization charge on the grain surface, and a depletion layer on the grain surface can be formed. This results in the polarization discontinuity on the grain surface resulting in the depolarization field, hence polarization decreases [248]. The density of grain boundaries increases as the grain size decreases. Consequently, the remnant polarization decreases as the grain size decreases. Therefore, by increasing the synthesis temperature, which increases the grain size results in an enhancement of the ferroelectric properties.

Interestingly, the non-saturated $P - E$ loop in B-160 ceramic can help to further increase in the applied electric field. Fig. 2.36b depicts the hysteresis loops of B-160 ceramic at various electric fields from 10 to 60 kV/cm. It is shown that B-160 ceramic exhibits enhanced ferroelectric properties, the maximal polarization (P_{max}) and P_r increase with the increasing of the applied electric field. Under 60 kV/cm, P_{max} and P_r achieved 27.21 and 8.59 $\mu\text{C}/\text{cm}^2$, respectively.

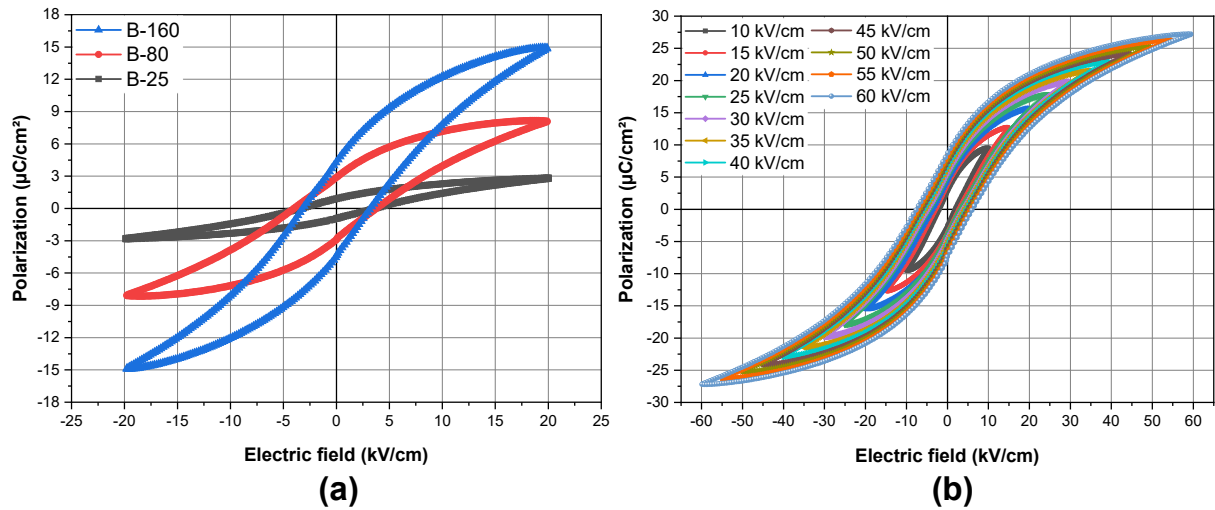


Figure 2.36: (a) Temperature-dependence of dielectric constant and dielectric loss, and (b) room-temperature $P - E$ loop of B_NR ceramic

2.3.2.2 BCZT rod-like ceramic

Fig. 2.37a displays the temperature-dependence of ε_r and $\tan\delta$ of B_NR ceramic at various frequencies from room temperature to 200 $^{\circ}\text{C}$. The dielectric constant increases as increasing temperature and reaches the maximum at the T_C . A broad anomaly at

93 °C associated to the T/C phase transition was observed [152, 161, 251]. The broad maximum observed is due to the overlap of several ferroelectric and non-ferroelectric regions [252]. Furthermore, with increasing frequency, the maximum dielectric constant decreases and Curie temperature shifts toward higher temperatures, indicating a relaxor behavior with strong frequency dispersion [240]. Compared to BCZT ceramic with spherical grains, i.e. B-CTAB ceramics exhibiting dielectric constant and dielectric loss of 7584 and 0.016, respectively, B_NR demonstrates enhanced ϵ_r and $\tan\delta$ of 11906 and 0.014, respectively. Hence, tailoring BCZT ceramic with large aspect ratio could enhance its dielectric properties [182, 253]. Meanwhile, Fig. 2.37b displays $P - E$ hysteresis loop of B_NR ceramic at room temperature. A slim $P - E$ hysteresis loop with P_r of 6.01 $\mu\text{C}/\text{cm}^2$ and E_c of 2.46 kV/cm is observed.

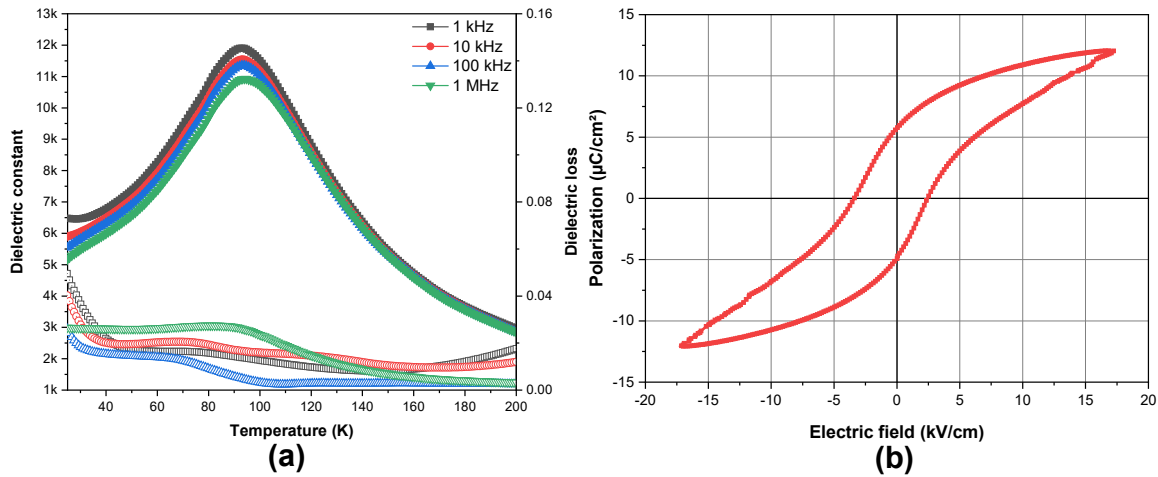


Figure 2.37: (a) Temperature-dependence of dielectric constant and dielectric loss, and (b) room-temperature $P - E$ loop of B_NR ceramic

2.3.2.3 BCZT Anisotropic morphologies

The temperature-dependence of ϵ_r and $\tan\delta$ of HZTO_NW and 50B24h sintered ceramics at 1250 °C/10 h are depicted in Fig. 2.38. In HZTO ceramic, the dielectric constant increases with temperature due to the weakening of the binding force between molecules/atoms to increase in temperature, permitting the molecules/atoms to vibrate more and more, which in turn increases the polarization, and hence, increases the dielectric constant (Fig. 2.38a) [254]. The increased dielectric constant value at lower frequencies is possibly related

to the contribution from the space charge/interfacial polarization. However, high values of dielectric losses are observed. The dielectric loss peak temperature increases to reach a maximum then decreases. Concerning 50B24h, a colossal-like behavior was noticed, where ε_r exhibits a slightly-constant values from room-temperature to T_C , then gradually decreases (Fig. 2.38b). The bump around 40 °C corresponds to orthorhombic–tetragonal (O/T) phase transition. In both samples, the observed broad anomaly is associated to the T/C phase transition [161]. Moreover, as seen in other BCZT samples (spherical and rod-like nanoparticles), with increasing frequency, the maximum of ε_r decreases and T_C shifts toward higher temperatures, indicating a relaxor behavior with strong frequency dispersion [240].

Meanwhile, Figs. 2.38c, d display room-temperature $P - E$ loops of HZTO_NW and 50B24h sintered ceramics, respectively. In HZTO_NW, a ferroelectric response of a lossy capacitor, where the area within the loop is proportional to the loss tangent of the device, and the slope proportional to the capacitance is observed. The loss can be due to dielectric hysteresis or leakage current or both [255]. However, 50B24h ceramic show a different trend where a slim hysteresis loop is observed with low P_r , P_{max} and E_c of 3.08 $\mu\text{C}/\text{cm}^2$, 17.68 $\mu\text{C}/\text{cm}^2$ and 1.61 kV/cm. The slimmest hysteresis loop is characteristic of relaxor ferroelectric with fine grained microstructure [256]. Moreover, the presence of $\text{CaZr}_y\text{Ti}_{1-y}\text{O}_3$ (CZTO), $\text{Ca}_3(\text{Zr}_y\text{Ti}_{1-y})_2\text{O}_7$ ($\text{C}_3(\text{ZrTi})_2\text{O}_7$) in 50B24h powder has promoted the relaxor behavior in BCZT ceramic. Since, $\text{C}_3(\text{ZrTi})_2\text{O}_7$ was reported to exhibit the largest polarization among the known hybrid improper ferroelectrics and ultra-lower coercive field [257, 258].

2.4 Selection of the most promising BCZT ceramics

To achieve our objective relaying on the elaboration of BCZT/polymer nanocomposite for energy storage application, we attempted to select the best BCZT ceramic owning excellent dielectric properties. Table 2 compares the synthesis conditions, the grain size averages, relative densities and the dielectric properties at 1 kHz of the top three lead-free

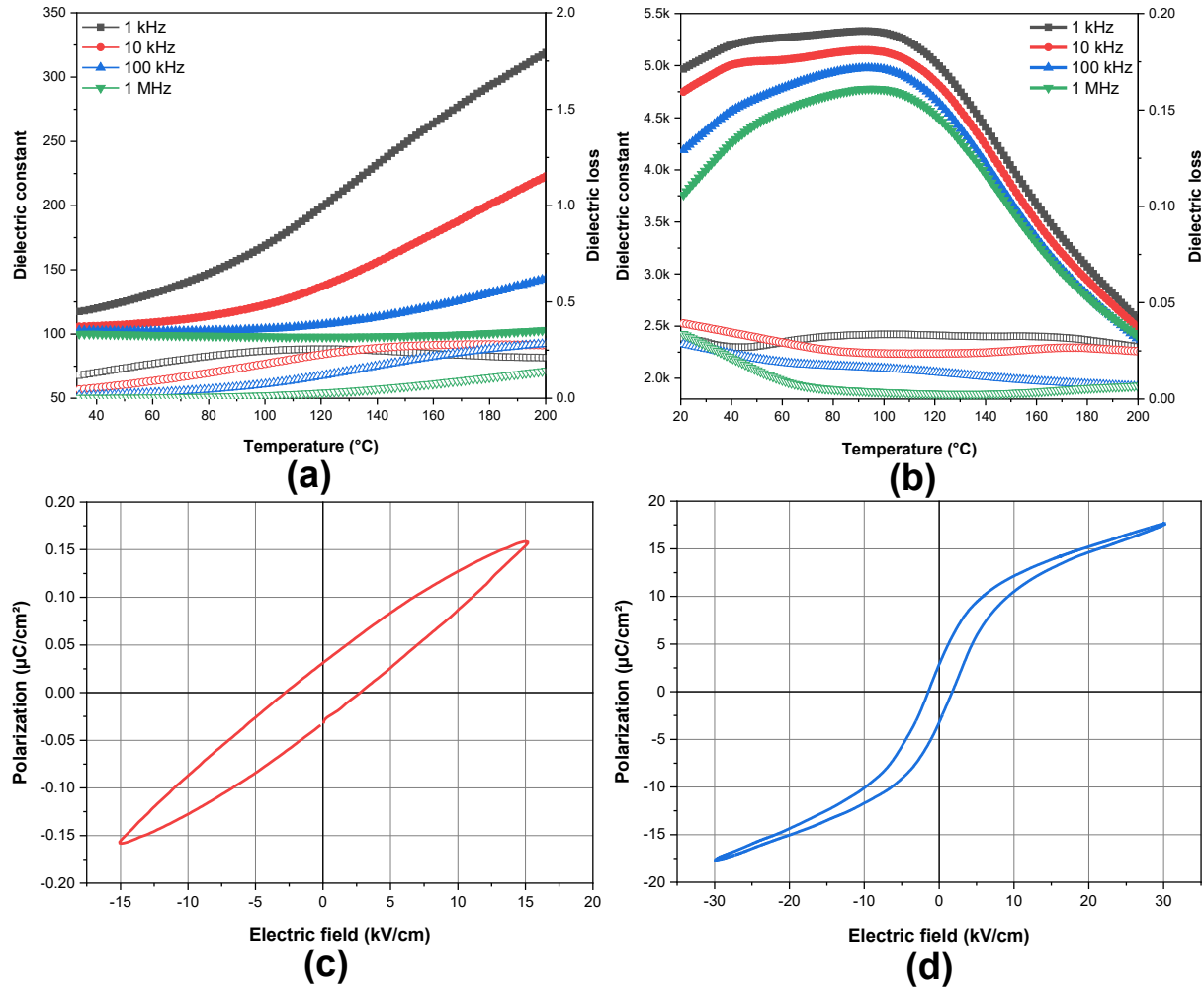


Figure 2.38: Temperature-dependence of ϵ_r and $\tan\delta$ of (a) HZTO_NW and (b) 50B24h sintered ceramics. Room-temperature $P - E$ loops of (c) HZTO_NW and (d) 50B24h sintered ceramics.

BCZT ceramic elaborated in this work. All samples demonstrated improved dielectric properties; with a slight-improvement in B-160 sample (dense ceramic (97.1%) with high grain size (22.1 μm) and enhanced dielectric properties ($\epsilon_m = 12085$ and $\tan\delta = 0.017$) compared to other BCZT ceramics cited in Table 2. However, in a view of the concern with energy consumption during the preparation of BCZT samples, B-SDS and B_NR require a calcination step at 1000 °C/4 h to obtain pure and crystalline powders. Hence, a favorable attention might be made to the B-160 sample since it was obtained at low temperature (160 °C) and without calcination. In the following section, the ferroelectric properties as well as the energy storage performances of B-160 ceramic will be thoroughly discussed.

2.4. SELECTION OF THE MOST PROMISING BCZT CERAMICS

Table 2.2: Comparison of dielectric (at 1 kHz) and microstructure properties of the top three BCZT ceramics elaborated in this work.

Sample	Synthesis conditions			Grain size (μm)	Relative density (%)	ε_m	$\tan\delta$
	Method	Calcination	Sintering				
B-160	Hydrothermal	No	1250 °C/10 h	22.1	97.1	12085	0.017
B-SDS	SDS-solvothermal	1000 °C/4 h	1250 °C/10 h	6.6	96.4	9646	0.012
B_NR	CTAB-solvothermal	1000 °C/4 h	1250 °C/10 h	12.09	95.0	11906	0.014

To further illustrate the advantages of the low-temperature hydrothermal processing in lead-free BCZT ceramics elaboration (strategy N°2), Table 3 summarizes the grain size average, relative density, dielectric and ferroelectric properties of $\text{Ba}_{0.85}\text{Ca}_{0.15}\text{Zr}_{0.1}\text{Ti}_{0.9}\text{O}_3$ (BCZT) ceramic elaborated by different conditions of synthesis and methods. From energy consumption view, the synthesis temperature of BCZT powders with high dielectric and ferroelectric properties could be decreased to a low temperature of 160 °C, which is about 1000-1200 °C lower when compared with solid-state reaction and 640-840 °C lower when compared with sol-gel methods respectively. Among the advantage of “calcination-free” in hydrothermal and sol-gel-hydrothermal processing, these strategies allow the synthesis of BCZT ceramics with enhanced dielectric and ferroelectric properties. For instance, B-160 ceramic processes a maximal dielectric constant of 12085 higher than BCZT ceramics elaborated by solid-state and sol-gel-hydrothermal processing, while keeping low dielectric loss. Moreover, from energy storage consideration, large dielectric breakdown strength, a reduced remnant polarization and large maximal polarization will lead to improved recoverable energy density and energy storage efficiency [259]. In other words, the charge storage density ($Q_c = P_{max} - P_r$) in a ferroelectric capacitor calculated from the ferroelectric hysteresis loops at zero field, must be maximal to obtain high energy storage ferroelectric capacitor [64]. These requirements are gathered in BCZT ceramics elaborated by hydrothermal processing. B-160 could withstood high electric field (60 kV/cm) and shows $Q_c = 18.62 \mu\text{C}/\text{cm}^2$. Hence, low-temperature hydrothermal route could be suitable for the design of energy harvesting systems with improved performances.

Table 2.3: Comparison of the dielectric and ferroelectric properties of lead-free BCZT ceramics reported here with others reported in literature using different synthesis conditions and methods.

<i>Method</i>	Synthesis conditions		Grain size (μm)	Relative density (%)	ϵ_m	$\tan\delta$	P_r ($\mu\text{C}/\text{cm}^2$)	P_{max} ($\mu\text{C}/\text{cm}^2$)	Q_c ($\mu\text{C}/\text{cm}^2$)	E (kV/cm)	Ref.
	<i>Calcination</i>	<i>Sintering</i>									
Hydrothermal	No	1250 °C/10 h	22.1	97.1	12085	0.017	8.59	27.21	18.62	60	B-160
Sol-gel+hydrothermal	No	1400 °C/2 h	-	95	9173	-	12.56	41.00	28.44	40	[176]
Hydrothermal	No	1300 °C/3 h	12.09	-	7760	0.1	10.83	25.00	14.17	15	[165]
Solvothermal	1000 °C/4 h	1250 °C/10 h	6.6	96.4	9646	0.012	3.92	7.56	3.64	6.6	B-SDS
Solvothermal	1000 °C/4 h	1250 °C/10 h	-	95	11906	0.014	6.01	12.04	6.03	17	B_NR
Sol-gel	1000 °C/4 h	1420 °C/6 h	-	-	16480	0.015	11.60	17.76	6.16	30	[161]
Sol-gel	800 °C	1550 °C/2 h	-	95	8808	0.02	12.20	20.70	5.03	30	[260]
Sol-gel	1000 °C/4 h	1450 °C/2 h	10	97	20250	-	10.70	20.70	10.00	50	[261]
Sol-gel	1000 °C/4 h	1500 °C/2 h	3.4	97	-	-	7.38	15.50	8.12	20	[262]
Sol-gel auto-combustion	1200 °C/10 h	1500 °C/4 h	-	-	12181	-	6.32	25.35	19.03	106	[64]
Solid-state	1200 °C	1350 °C	18.12	-	17120	0.023	10.20	19.71	9.51	60	[262]
Solid-state	1150 °C/6 h	1400 °C/6 h	-	95	10615	-	8.21	18.53	10.32	50	[263]
Solid-state	1147 °C/12 h	1427 °C/2 h	-	-	4762	0.022	4.35	6.53	2.18	8	[151]
Solid-state	1350 °C and 1400 °C/6 h	1450 °C/4 h	-	94	-	-	5.48	16.06	10.58	21	[164]

2.5 Conclusions

To conclude with, BCZT ceramics with different shapes, sizes and size distributions were elaborated by solvo/hydrothermal processing. BCZT spherical nanoparticles were synthesized using two strategies: (i) solvothermal and (ii) low-temperature sol-gel-hydrothermal routes. The first one was relayed on the use of surfactants to better control the grain size of BCZT powders, however, a calcination-step at 1000 °C/4 h was required to obtain pure and crystalline BCZT powders. To overcome this drawback, another strategy was designed based on sol-gel to obtain ZTO nanoparticles and hydrothermal reaction between ZTO and barium and calcium salts. For the first time, BCZT nanocrystalline powders were found at very-low temperature including room-temperature. Afterwards, BCZT ceramic with rod-like shape (B_NR) was elaborated using surfactant-assisted solvothermal processing using higher surfactant (CTAB) concentration. Later, lead-free BCZT hierarchically nanostructured ceramics were design using two-steps hydrothermal processing. First, HZTO_NW which serves as inorganic template for BCZT preparation were elaborated by hydrothermal processing. Then, reaction of HZTO_NW and barium and calcium salts to synthesize BCZT multipods. The growth mechanism of BCZT multipods was relaying on the nucleation of CZTO cubes on HZTO_NW template surface then perpendicular nucleation of BCZT multipods on the cubes' faces. It was found that the A-site precursor's concentrations play a key role on the formation of BCZT multipods, and the desirable BCZT phase was obtained in samples using low barium and calcium concentrations. Subsequently, the dielectric and ferroelectric properties of BCZT sintered ceramics at 1250 °C/10 h were examined for each powder (spherical nanoparticles, nanorods and anisotropic morphologies). The effects of grain size and grain shape of BCZT ceramics on the dielectric properties were discussed. Later, it was found that BCZT ceramic (B-160) based on spherical nanoparticle powder, elaborated at 160 °C by the low-temperature sol-gel-hydrothermal processing (strategy N°2) exhibited enhanced dielectric and ferroelectric properties compared to the other types of BCZT ceramics. Basing on these findings B-160 ceramic could be a promising candidate to be embedded in PLA matrix to prepare BCZT/PLA nanocomposite films for energy harvesting applications.

CHAPTER

3

Elaboration, characterization and properties of BCZT/PLA nanocomposites

Contents

3.1	Context of the study	99
3.2	The near-spherical BCZT (B_NP)/PLA composite as a ref- erence	100
3.3	The permittivity <i>vs</i> the aspect ratio of the ceramic: a real paradigm?	117
3.4	Conclusions	126

3.1 Context of the study

In response to the need to develop a new environmentally friendly nanotechnology with improved dielectric properties, novel nanostructured hybrid materials combining low dielectric loss and high breakdown strength of the polymer and high dielectric constant of the ceramic nanofillers are currently investigated for applications [264, 265]. Ideally, nanofillers as particles contribute to the increase in dielectric constant of the composite system with respect to polymer as matrix, without compromising the low dissipation factors of polymer matrixes [74, 266]. Several strategies have been used to keep the dielectric losses of nanocomposites low, including development of polymers with fast dipole polarization, improvement of the nanofiller dispersion and fabrication of advanced nanostructures [73]. As these challenges include the need to understand the chemistry and structure of the load-polymer, the study of their interface become an attractive research topic [100, 267]. The preparation of core-shell structured nanoparticles by surface-initiated *in situ* polymerization has aroused significant interest because of its unique advantages: (i) the nanoparticles can be well encapsulated by controllable polymer layers in thickness, resulting in significant reduction in the surface energy of nanoparticles. (ii) The properties of the nanocomposites can be adjusted by adapting the physical properties of the polymeric shell and/or the interaction between the polymeric shell and the polymer matrix [80, 268–271].

In this chapter, we propose to elaborate BCZT/PLA nanocomposites by dispersing BCZT as charges into PLA as matrix and to study the properties as a function of BCZT volume fraction. As a first step, we finally choose the lead-free B-160 ceramic as charge for many reasons. First, it exhibits excellent dielectric, ferroelectric and energy storage performances as sintered. Second, it was obtained at low temperature (160 °C) and without any calcination steps. Finally, the morphology of B-160 is near-spherical and could be used as a reference for studying the influence of morphology on resulting properties. The potentialities of functionalization were also explored. Indeed, the B-160 nanopowder functionalized *via* the core-shell structuration by using polydopamine layer (PDA) were embedded in the PLA matrix by the solvent casting method. The effect of the

core-shell structuration on the dielectric and energy storage performances of BCZT/PLA nanocomposites was then investigated.

3.2 The near-spherical BCZT (B_NP)/PLA composite as a reference

3.2.1 Functionalization of BCZT nanoparticles (B_NP)

In follow, B_NP refers to BCZT near-spherical powder elaborated by hydrothermal processing at 160 °C/24h. To enhance the chemical interactions between BCZT nanoparticles and the PLA matrix, the surface of the nanoparticles was pretreated. Fig. 3.1 displays the different processes during the functionalization of B_NP nanoparticles. The B_NP powder was first dispersed in the hydrogen peroxide (H_2O_2) by ultrasound for 30 minutes and then refluxed at 104 °C/4 h. The obtained hydroxylated product (B_NP-OH) was recovered by centrifugation and then dried under vacuum at 80 °C/12 h. Subsequently, the hydroxylated B_NP nanoparticles were coated with a PDA shell by air oxidation of dopamine, to form B_NP@PDA according to the reaction in Fig. 3.1. For that purpose, 2 g of the B_NP powder was dispersed in 100 ml of the Tris-HCL (0.01 M) by ultrasound for 15 min. A solution of 0.01 M dopamine was added to this suspension followed by another sonication cycle for 15 min. The pH of the dopamine aqueous solution was buffered to 8.5 by adding the 0.01 M Tris-HCL. After 24 h of reaction at reflux at 60 °C, a black powder B_NP@PDA was recovered by centrifugation, purified by washing with demineralized water and dried at 80 °C for 24 hours.

The STEM-HAADF micrographs of Figs. 3.2a, b evidence the successful coating of the B_NP nanoparticles by PDA with a shell thickness about 15-25 nm. Meanwhile, Fig. 3.2c exhibits TGA data of the weight changes of B_NP and B_NP@PDA nanoparticles. The first weight loss between 30 °C to 150 °C is due to dehydration (adsorbed water). The second loss between 150 °C and 500 °C corresponds to the thermal decomposition of various organic compounds including the PDA layer. Above 500 °C the weight loss for

3.2. THE NEAR-SPHERICAL BCZT (B_NP)/PLA COMPOSITE AS A REFERENCE

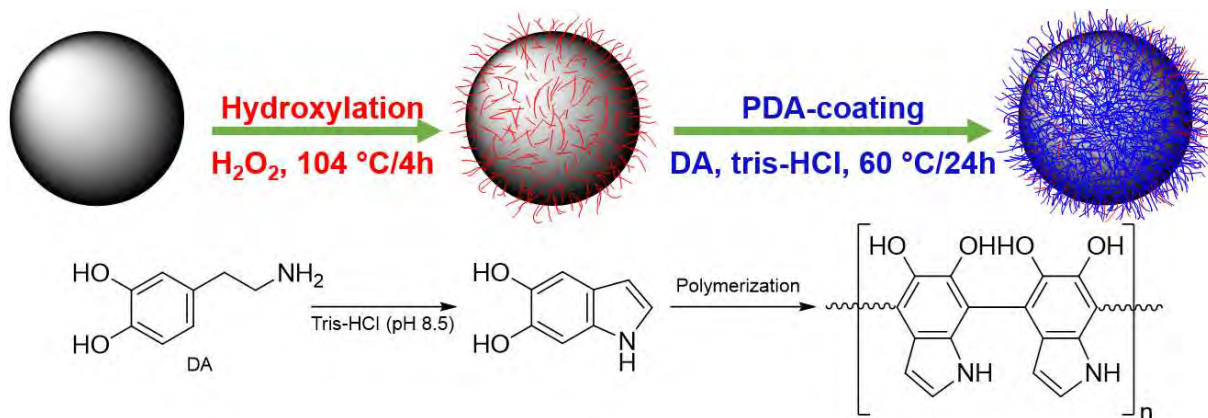


Figure 3.1: Schematic illustration of the preparation of core-shell structured B_NP@PDA nanofillers.

both compounds remains constant. The total weight loss is 6.13% and 9.95% for B_NP and B_NP@PDA, respectively. The weight percentage of the functional PDA layer was obtained by comparison of the B_NP and B_NP@PDA TGA data. Based on the total weight loss values, the mass percentage of the PDA coating layer is approximately 3.82 wt%, which prove the effective modification of B_NP nanoparticles in this work.

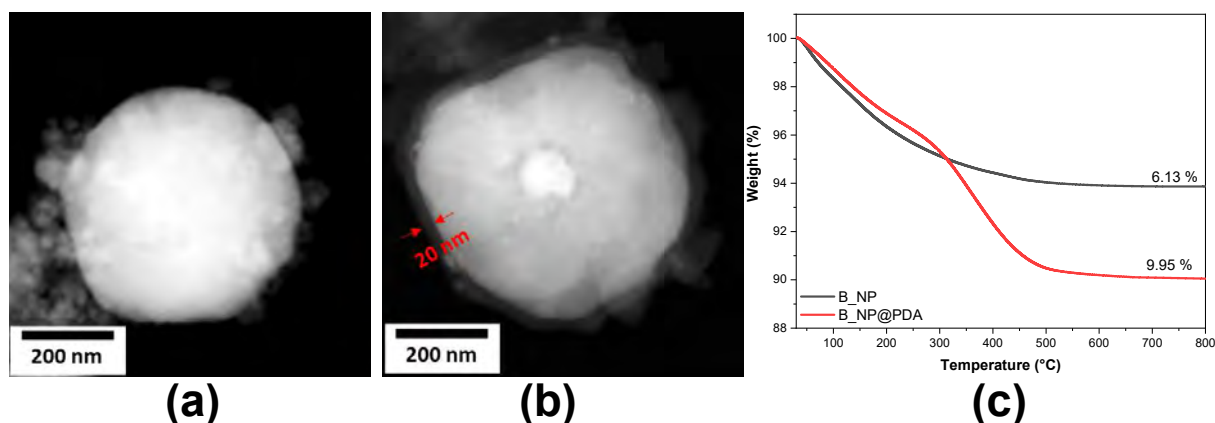


Figure 3.2: STEM-HAADF micrographs of (a) B_NP nanoparticle, (b) B_NP@PDA nanoparticle showing PDA layer thickness with the red lines, and (c) TGA curves of B_NP and B_NP@PDA nanoparticles.

It has been reported that the surface of barium titanate based powders contain hydroxyl groups ($-\text{OH}$) [87,272], however, the content of $-\text{OH}$ groups is too low to have a significant impact on the surface reactivity with the dispersants. Therefore, the hydroxylation of the particles surface is important precondition for effective functionalization of B_NP nanopowders [87,272]. Fig. 3.3a shows a superposition of infrared spectra of B_NP

powders before and after hydroxylation with hydrogen peroxide (H_2O_2). After treatment of the powder, a broad absorption band, due to the elongation vibrations of the MO–H groups (M stands here for Ba, Ca, Zr and Ti), is observed at around 3440 cm^{-1} and confirmed by the increasing intensity of the absorption band M–O and/or deformation outside the plane of the OH groups, situated between 500 and 650 cm^{-1} . This highlights the successful functionalization of B_NP surface by hydroxyls groups to form B_NP–OH nanoparticles [273]. Moreover, Fig. 3.3a depicts the surface functionalization of B_NP–OH by PDA layer. The observed peaks ranging from 1060 cm^{-1} to 1200 cm^{-1} refer to the bond $-C\equiv N$ of secondary amine [274], and the peak at 1380 cm^{-1} is assigned to the phenolic C–O–H vibration [275]. In addition, the absorption peaks at wavenumbers of 1630 , 1490 , 1265 and 1100 cm^{-1} correspond to the vibrations of the N–H, C=C, C–N and C–O bonds, respectively [71]. The broad peak centered at 3430 cm^{-1} is attributed to the vibrations of aromatic C–H bonds, N–H amine bonds and non-functionalized $-O-H$ groups. The increasing peaks from 3000 cm^{-1} to 3680 cm^{-1} correspond to the bond of $-OH$ and $-NH-$ of coated PDA [274]. Infrared spectroscopy was also used to confirm the success of the B_NP@PDA/PLA preparation. Fig. 3.3b shows the FTIR spectra of PLA and B_NP@PDA/PLA nanocomposite films. It can be seen that a new peak at 1760 cm^{-1} appeared in the infrared spectra of B_NP@PDA/PLA, which is attributed to C=O stretching vibrations of the PLA ester groups. In addition, new absorption bands were also found at 1190 – 1110 cm^{-1} , indicating the symmetric, stretching-vibration C–O–C groups of the PLA and also the appearance of the broad M–OH peak around 3440 cm^{-1} due to the functionalization of the surface of the loads [276, 277].

3.2.2 Elaboration of PLA-based nanocomposite films

PLA with reference Ingeo™ Biopolymer 6201D was purchased from NatureWorks® and its physico-chemical properties were listed in Table 1. 10 g of PLA beads was purified by several solubilization/precipitation (recrystallization) cycles in dichloromethane and methanol, respectively, followed by drying in vacuo at $50\text{ }^{\circ}\text{C}/12\text{ h}$.

3.2. THE NEAR-SPHERICAL BCZT (B_NP)/PLA COMPOSITE AS A REFERENCE

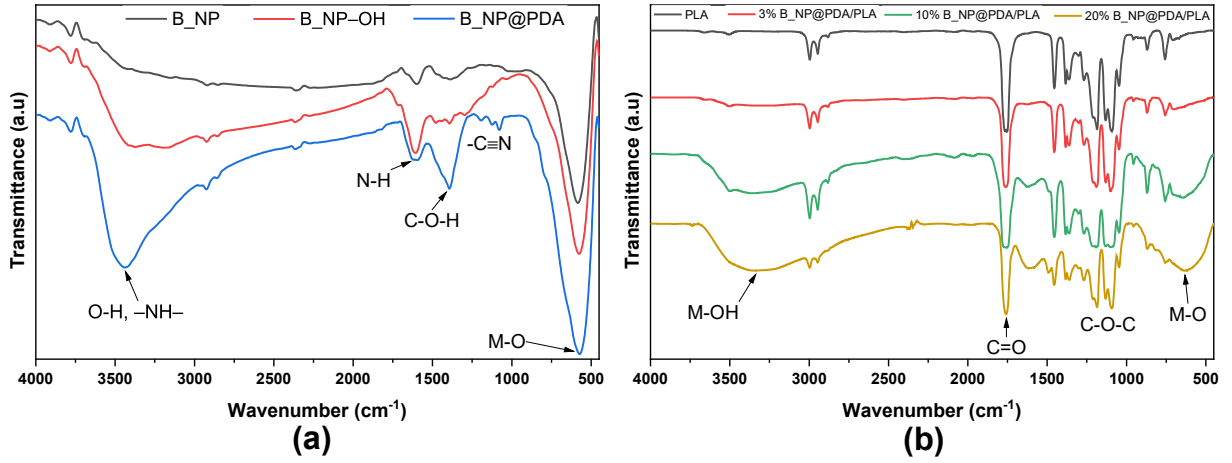


Figure 3.3: FTIR patterns of (a) B_NP, B_NP–OH, B_NP@PDA nanoparticles and (b) B_NP@PDA/PLA films.

Table 3.1: Physico-chemical properties of Ingeo™ Biopolymer 6201D.

Specific Gravity	Relative Viscosity	Glass Transition Temperature (°C)	Crystalline Melt Temperature (°C)	Average molecular weight (kDa)	D-isomer units (mol.%)
1.24	3.1	55–60	155–170	160–170	1.2–1.6

PLA-based nanocomposite films were elaborated by the solution casting method using the volume fractions 3, 6, 10, 15 and 20 vol% of B_NP or B_NP@PDA nanoparticles. In this study, the volume fraction of the fillers was set less than or equal to 20 vol% because of both the deterioration of the mechanical properties at high loading and the spherical packing limitations. For this purpose, an adequate amount of PLA was solubilized in dichloromethane with magnetic stirring for 2 hours. Then, an appropriate mass of the B_NP or B_NP@PDA was dispersed therein, by ultrasound for 15 min, then homogenized by magnetic stirring for another 2 hours. The slurry was cast in a Teflon mold and then dried at room temperature to obtain a flexible composite film, then dried in vacuum at 40 °C for 12 h to remove the solvent. The thickness of the films was found to be between 5 and 15 microns.

Fig. 3.4 shows the morphological characteristics of B_NP/PLA and B_NP@PDA/PLA films at the surface and at the cross-section using 20 vol% of nanofillers. The black region corresponds to the PLA and the white spots represent the BCZT load. It was observed that the both B_NP and B_NP@PDA nanofillers were correctly dispersed in the PLA

matrix, indicating the excellent compatibility between PLA and BCZT nanoparticles. To have an insight on the compatibility between BCZT nanofillers and PLA matrix, Figs. 3.4c, d give an idea about the distribution of B_NP and B_NP@PDA inside the PLA matrix *via* a cross-section view. The nanofillers show a good dispersion in the PLA matrix and a large number of BCZT nanoparticles are covered with PLA matrix. This suggests the good compatibility between BCZT nanofillers and PLA matrix. It is worthy to mention that B_NP@PDA formed acicular paths in PLA matrix, leading to the formation of well-connected ellipsoidal agglomeration of B_NP@PDA particles. Figs. 3.5a, b illustrate schematic presentations of the dispersion of B_NP and B_NP@PDA inside the PLA matrix. Moreover, Fig. 3.5b provides an insight in the ellipsoidal agglomeration of B_NP@PDA nanofillers observed in B_NP@PDA/PLA nanocomposite film.

3.2.3 Dielectric properties of nanocomposite films

3.2.3.1 Effects of frequency, volume fraction of fillers and functionalization: qualitative analysis

High ε_r and low $\tan\delta$ are desired in energy storage materials. The frequency-dependence of the ε_r and $\tan\delta$ of B_NP/PLA and B_NP@PDA/PLA nanocomposites obtained at room temperature are shown in Fig. 3.6. Not surprisingly, an enhancement of ε_r and an increase of $\tan\delta$ were highlighted for all the nanocomposites in comparison to the pure PLA. The values of ε_r decrease gradually with increasing frequency. This effect, even stronger than the volume fraction of charges is large, can be explained by interfacial polarization, i.e., by Maxwell-Wagner-Sillars (MWS) effect [278]. At low frequency, B_NP or B_NP@PDA exhibit well defined conducting grains separated by thin insulating grain boundaries, which causes accumulation of charges under the influence of the electric field and thus increasing the interfacial polarization resulting in a higher dielectric constant. However, at higher frequencies, the charge carriers cannot align themselves in the direction of the electric field resulting in a reduced interfacial polarization and leading in a lower dielectric constant at high frequencies [279]. The charges stored within the nanocomposites

3.2. THE NEAR-SPHERICAL BCZT (B_NP)/PLA COMPOSITE AS A REFERENCE

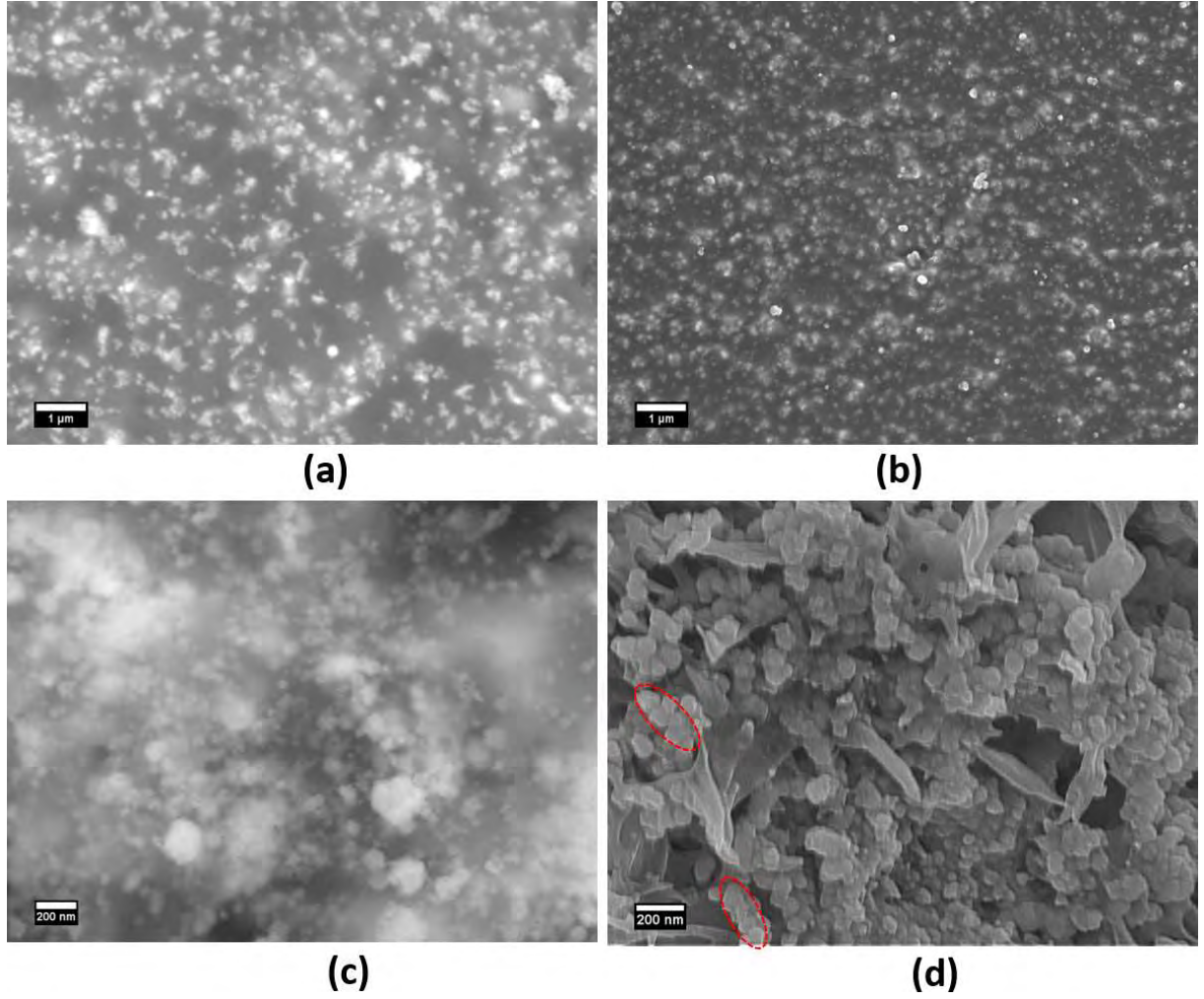


Figure 3.4: FESEM images of the (a, b) surface and the (c, d) cross-section of 20 vol% B_NP/PLA and 20 vol% B_NP@PDA/PLA nanocomposite films, respectively.

would possibly be delocalized either by tunneling or by ohmic conduction leading to fairly high loss factors [280]. The behavior of $\tan\delta$ is different. A decrease of $\tan\delta$, due to interfacial polarization, was observed up to a critical frequency (around 70 kHz), followed by a sharp increase attributed to the dipole polarization relaxation in PLA [281].

Fig. 3.7 compares the ε_r and $\tan\delta$ of the two PLA-based nanocomposite films at different volume fractions as measured at 1 kHz and room temperature. It can be seen that the dielectric properties of B_NP@PDA/PLA nanocomposites are systematically improved for all nanofiller concentrations in contrast to B_NP/PDA. At 20 vol%, the dielectric permittivity values of B_NP/PLA and B_NP@PDA/PLA nanocomposites are 9.11 and

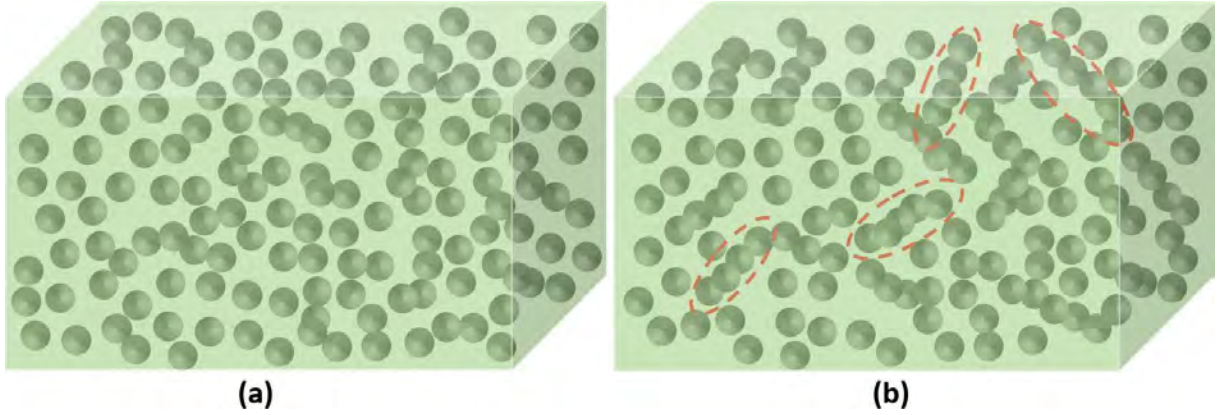


Figure 3.5: Schematic illustrations of the dispersion of (a) B_NP and (b) B_NP@PDA fillers inside the PLA matrix.

11.24, respectively, which are four times higher values than those of pure PLA (2.57 at 1 kHz). The increase of the permittivity of B_NP/PLA and B_NP@PDA/PLA composites was attended by an increase of dielectric losses. However, the maximum dielectric losses remain relatively weak in view of the maximum increase of permittivity.

Regarding the effects of functionalization, the improvement of the dielectric properties in B_NP@PDA/PLA films could be related to the improved interfacial compatibility between the nanoparticles and the PLA matrix, which suppresses the dipolar polarization loss of the PLA matrix. Furthermore, the surface water layer and other impurities may be removed during the introduction of PDA layer onto the B_NP nanoparticle's surface, which could result in reduced electrical conduction and/or interfacial polarization loss [268]. Moreover, the dielectric losses in B_NP@PDA/PLA are lower while it exhibits a higher permittivity than B_NP/PLA. Another important reason for the improvement of the dielectric properties in B_NP@PDA/PLA nanocomposite films could be the formation of well-connected ellipsoidal agglomeration of B_NP@PDA particles observed in Fig. 3.4d, which can affect both the 3D topology and the effective aspect ratio; the particles cannot longer be considered as spherical but rather as ellipsoidal. This point will be discussed further. It has however to be recognized that the functionalization has not a a very pronounced effect on dielectric properties of the nanocomposites.

3.2. THE NEAR-SPHERICAL BCZT (B_NP)/PLA COMPOSITE AS A REFERENCE

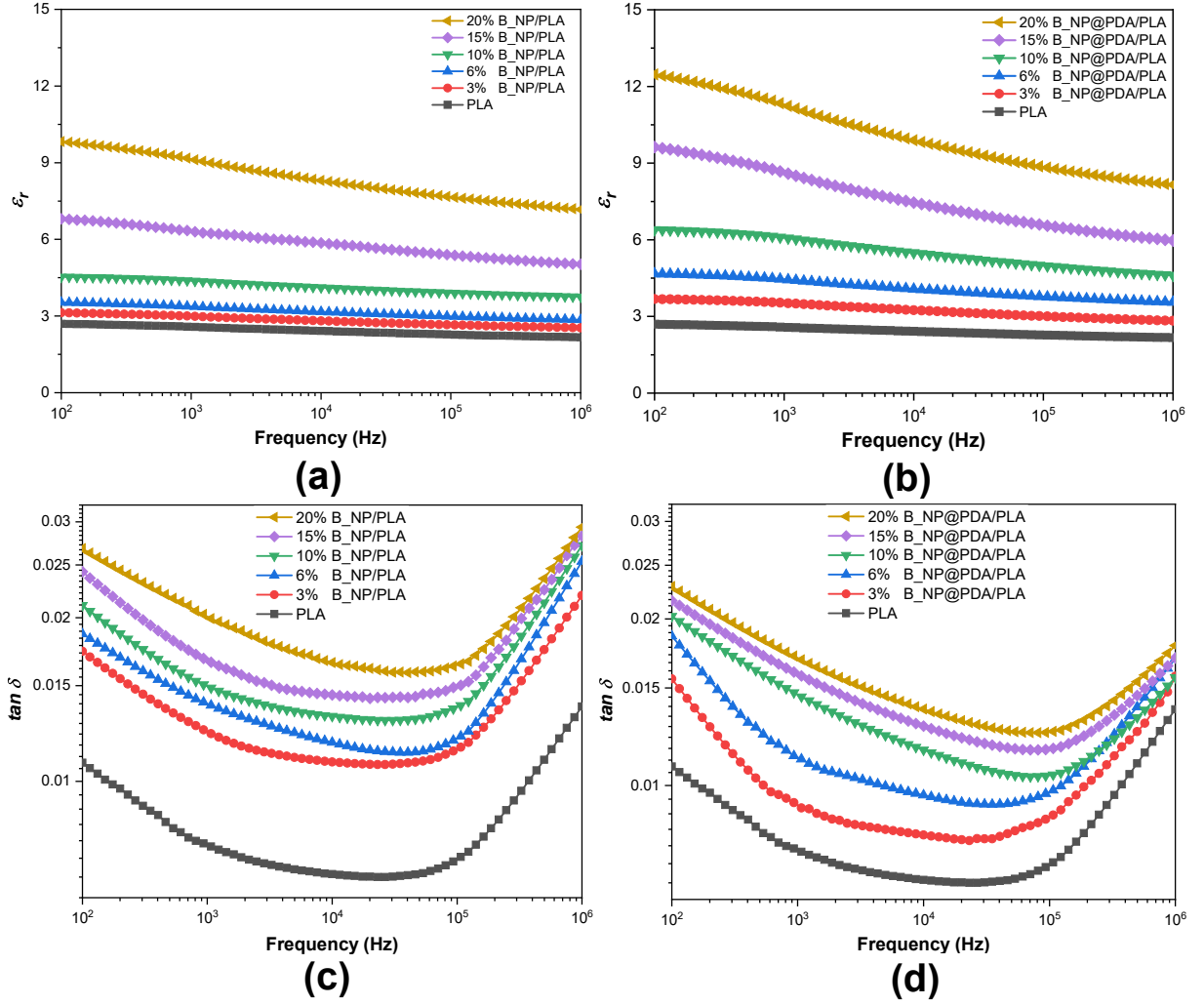


Figure 3.6: (a, b) ε_r and (c, d) $\tan \delta$ of B_NP/PLA and B_NP@PDA/PLA nanocomposites, respectively.

3.2.3.2 Effects of both volume fraction and aspect-ratio of fillers on the effective permittivity of the nanocomposite: quantitative analysis

The permittivity is a property that characterizes the electrical polarization of a material under the application of an external electric field. In our composites, the PLA polymer shows a low permittivity ($\varepsilon_r = 2.7$) while the B_NP ceramic exhibits a high permittivity as sintered. For the latter, the high dielectric constant reflects the spontaneous polarization of ferroelectrics; a small electric field is enough to create large polarization. In order to better understand the evolutions of the effective permittivity of the nanocomposites, the fundamental question that arises is how the introduction of B_NP ceramic as inclusions

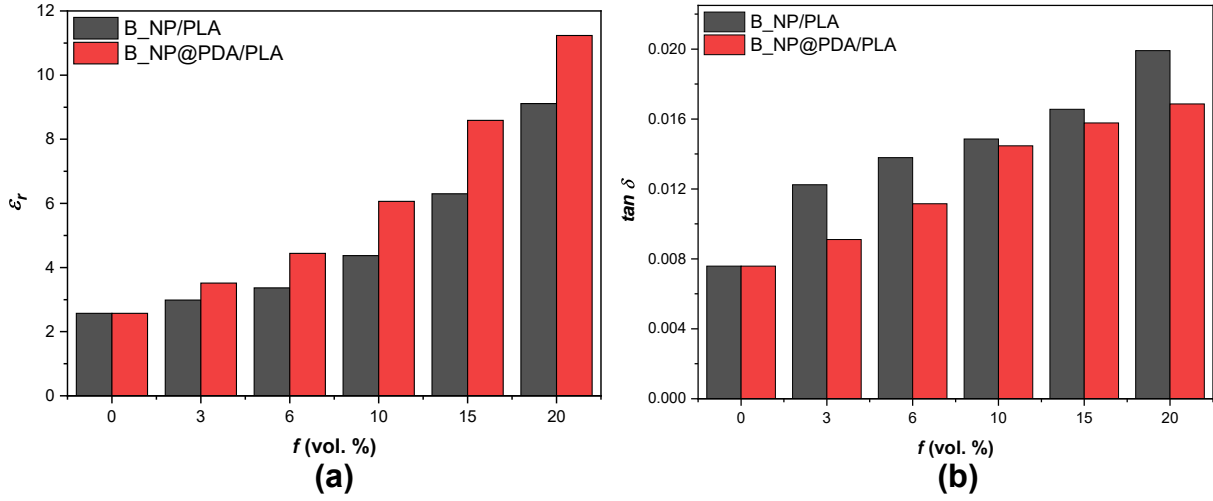


Figure 3.7: Effect of the volume fraction of B_NP and B_NP@PDA fillers on the (a) ϵ_r and (b) $\tan \delta$ of PLA-based nanocomposites.

into PLA polymer as host phase influences the polarization field. However, the reply to this question is not that simple for the reason that the latter depends on many factors such as morphology, 3D distribution and orientation of inclusions but also on the direction, the norm and the frequency of the external field applied, dielectric mismatch between the PLA polymer and the B_NP ceramic. From a general manner, the problem that has arisen is the determination of the effective permittivity of heterostructures. It is a complex problem that has long attracted attention, beginning with the pioneering work of Maxwell [282]. For possible answers to the previous question, it is prime of necessity to proceed step-by-step. First, Fig. 3.8 gives the comparison between the effective permittivities measured and those obtained from the so-called Wiener bounds as a function of B_NP volume fraction and for different values of B_NP permittivity (100, 1000 and 10000) [283]. The lower-bound and the upper-bound are given by the following equations, and correspond to capacitors that are connected in parallel or series in a circuit.

$$(\epsilon_{eff})_{inf} = \frac{\epsilon_c \epsilon_p}{f_c \epsilon_c + (1 - f_c) \epsilon_p} \quad (3.1)$$

$$(\epsilon_{eff})_{sup} = f_c \epsilon_c + (1 - f_c) \epsilon_p \quad (3.2)$$

It can be seen that the Wiener bounds depend on the set of permittivity and the volume fraction but not directly on the exact geometry of the mixture. Also, these bounds are known to be less restrictive than others such as Hashin–Shtrickman bounds [284].

3.2. THE NEAR-SPHERICAL BCZT (B_{NP})/PLA COMPOSITE AS A REFERENCE

Whatever the value of B_{NP} permittivity considered; the effective permittivity of the mixture is located between the Wiener bounds. This is not surprising since these bounds can be considered as absolute limits. However, it is worth noting that the lower bound characterizes a system in which the presence of ceramic inclusions does not influence the effective permittivity of the mixture up to a very high-volume fraction of ceramic (of about 70%). In other words, the polarization induced by the presence of inclusions in the mixture can be considered as negligible. Our experimental data are located above the lower bound and show clearly an increase of effective permittivity from 2.6 to 8.6 for the B_{NP} /PLA (and 11.6 for the $B_{NP}@PDA$ /PLA) within the B_{NP} volume fraction range of 0% to 20%. This highlights a change in the macroscopic electrical field inside the medium as a function of B_{NP} volume fraction.

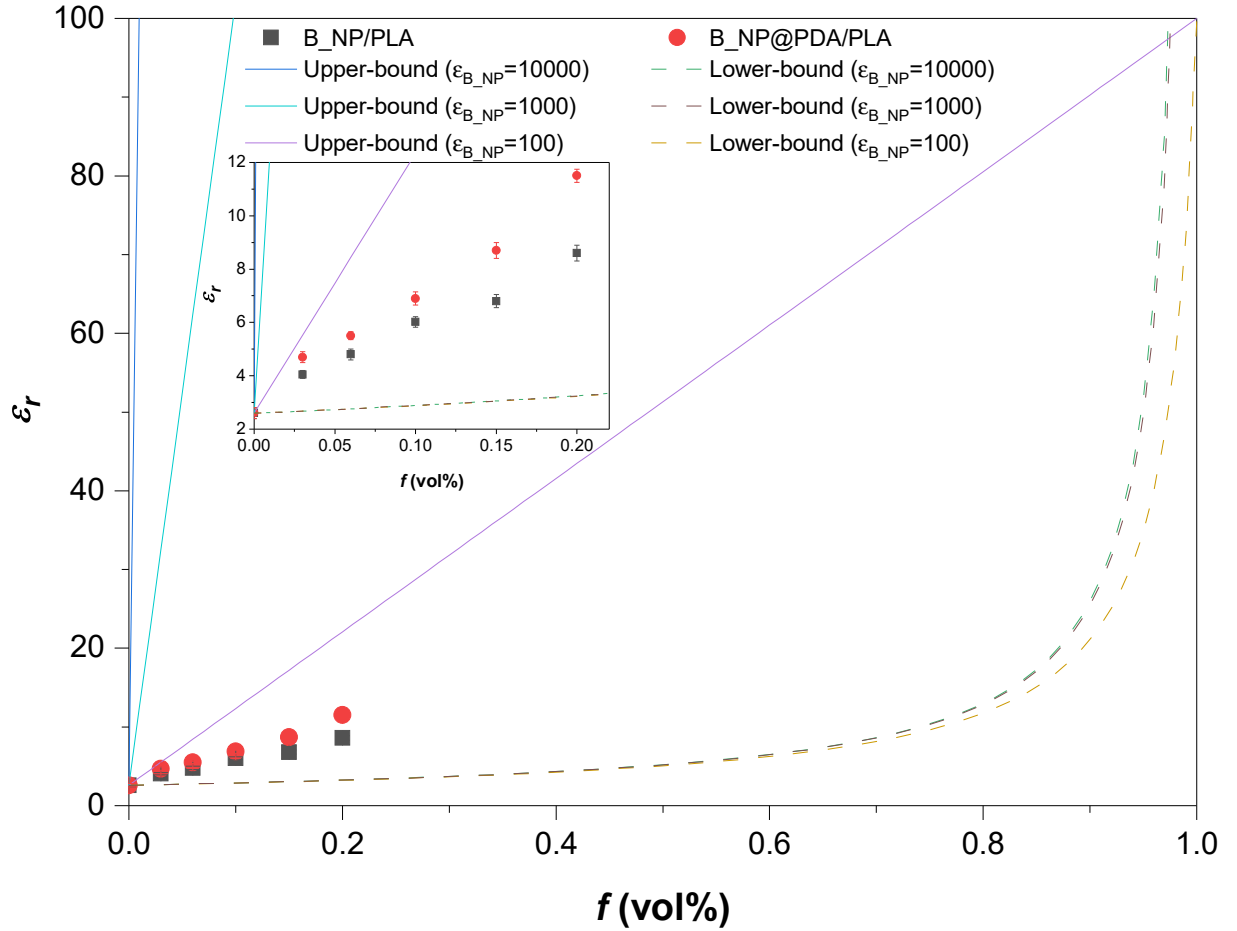


Figure 3.8: Evolution of the effective permittivity of the B_{NP}/PLA and $B_{NP}@PDA/PLA$ composites as a function of volume fraction of B_{NP} as inclusion. Comparison with the lower and upper Wiener bounds defined from different value of the B_{NP} permittivity.

Although the increase of the effective permittivity measured is relatively high (multiplied on average by 4 between 0 and 20% of B_NP in the composites), it remains weak in comparison with the expected high value of near-spherical B_NP permittivity. Furthermore, the effective permittivity of the composite evolves linearly between 0% and 20% of B_NP. This type of behavior was also highlighted in the case of (TiO₂/Epoxy composite for volume fractions of (TiO₂ below 35% [285]. An extrapolation of this trend to 100% of B_NP would give a permittivity of about 40 for the B_NP permittivity, a too low value when compared to the value of 12800 as sintered. As a result, a sharp increase of permittivity is expected from a critical volume fraction of B_NP. This behavior can be interpreted from the work of Cheng et al. and on the basis of a numerical three-dimensional “disordered model” [286]. It is based on finite element method (*FEM*) and takes into account the interconnection of inclusions when concentration of inclusions is increased. It is thus a powerful method to study the effects of both the permittivity contrast between ceramic as inclusion and polymer as matrix and the interconnection (or percolation) of ceramic particles into the polymer matrix. The dielectric properties obtained by the “disordered model” were compared to those of the periodic models and the classical analytical mixture rules. From this study, we can draw some important learning points. First, if the permittivity contrast is close to one, all the models are equivalents and the composite behaves as dilute mixture i.e. the effective permittivity evolves linearly with the volume fraction of the ceramic particles. Second, a deviation was observed when the permittivity contrast becomes larger. As it increases, the periodic and the Maxwell-Garnett models fail to describe the reliable effective permittivity [287]. The Maxwell rule is based on the assumption of spherical inclusions of mean distance much larger than their radius. In other words, it cannot be applied for high volume fraction of particles (>10%). The fact that periodic models fail show indirectly that arrangement of particles play a role in resulting effective permittivity; especially in the case of high permittivity contrast. Finally, in all cases and even for large contrast between inclusions and matrix, it is shown that below a critical volume fraction that depends on the model considered, the effective permittivity shows a linear dependence with the volume fraction of inclusions [286]. This can be simply explained by the fact that the domains are spatially separated and electrostatic interactions between each inclusion

3.2. THE NEAR-SPHERICAL BCZT (B_NP)/PLA COMPOSITE AS A REFERENCE

and its neighbors are relatively weak. For instance, the “disordered model” shows that the effective permittivity evolves linearly with the volume fraction of inclusions up to a critical volume fraction of around 20%; a value close to our observations. In order to go further, we have decided to apply the model developed by [288]. It has Maxwell-Garnett (MG) equation as a low volume filling ratio limit and Bruggeman Symmetrical (BS) equation as a high-volume filling ratio limit. When the volume fraction of inclusions increases, the local electric field acting on each inclusion approaches a similar field as in the BS mixing equation. This model was chosen since it was derived especially for composites with high electrical contrast between the inclusions and the background phase, inclusions are allowed to overlap and is valid for both spherical and ellipsoidal inclusions. The result is the following differential equation for the unknown effective permittivity and applicable for spherical shape of B_NP:

$$\frac{d\varepsilon_{eff}}{df} = \frac{\varepsilon_{PLA}(\varepsilon_{B_NP} - \varepsilon_{eff})}{\varepsilon_{B_NP} + 2\varepsilon_{eff} - 3f\varepsilon_{PLA}} \quad (3.3)$$

It was solved numerically and the effect of B_NP permittivity on the effective permittivity of the composite was calculated and compared to experimental results in Fig. 3.9.

Many interesting conclusions may be drawn. First, an abrupt change of the effective permittivity, even stronger than the electrical contrast between B_NP and PLA is high, was observed from a critical volume fraction of $\frac{1}{3}$. This value represents the depolarization factor in the case of spheres introduced into the model to describe how the polarization is affected by both the shape and the orientation of inclusions with respect to the applied field (see Eq. 3.7 and Eq. 3.11). It also corresponds to the percolation threshold (f_c) of spheres randomly distributed. Second, below the percolation threshold and as observed experimentally, the effective permittivity increases linearly with both increasing volume fraction and permittivity of B_NP. However, from a critical value of permittivity around 100 (that corresponds to a dielectric mismatch of $\frac{100}{2.7} = 37$), the effective permittivity no longer evolves. In other terms, when spherical inclusions does not touch each other, there is a critical permittivity of B_NP from which the effective permittivity do not increase even for giant permittivities of B_NP ceramic. This can be explained by solving Laplace

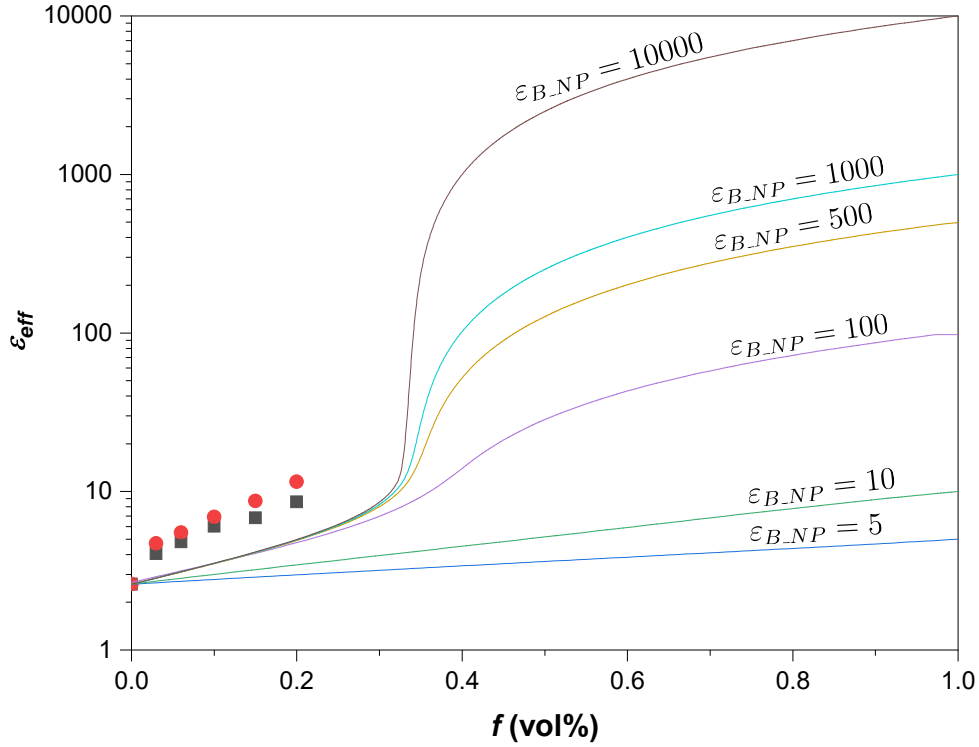


Figure 3.9: Evolution of the effective permittivity of the composite as a function of B_NP volume fraction for different values of B_NP permittivity. Comparison with the experimental data.

equation for a sphere embedded in an infinite host. Indeed, under these assumptions, the polarizability α and the depolarization field generated by the polarized matter inside the inclusion E_{dep} are given by the following equations [289]:

$$\alpha = a^3 \varepsilon_{PLA} \frac{\varepsilon_{B_NP} - \varepsilon_{PLA}}{\varepsilon_{B_NP} + 2\varepsilon_{PLA}} \quad (3.4)$$

$$E_{dep} = -E_{ext} \left(\frac{\varepsilon_{B_NP} - \varepsilon_{PLA}}{\varepsilon_{B_NP} + 2\varepsilon_{PLA}} \right) \quad (3.5)$$

where a is the mean radius of the B_NP inclusions, ε_{B_NP} and ε_{PLA} are the permittivity of B_NP ceramic and PLA polymer respectively and E_{ext} is the external field. The minus sign added indicates that the external field is counteracted by the depolarization field.

The internal field E_{int} inside the inclusions which is considered as uniform according to the weak Eshelby conjecture [290], can be rewritten from [289] as follow, since $E_{int} = E_{ext} + E_{dep}$ (where E_{dep} is the depolarization field).

$$E_{int} = E_{ext} \left(1 - \frac{\varepsilon_{B_NP} - \varepsilon_{PLA}}{\varepsilon_{B_NP} + 2\varepsilon_{PLA}} \right) \quad (3.6)$$

3.2. THE NEAR-SPHERICAL BCZT (B_NP)/PLA COMPOSITE AS A REFERENCE

It is thus interesting to plot $\frac{\alpha}{a^3}$ and $\frac{E_{int}}{E_{ext}}$ as a function of ε_{B_NP} for a value of $\varepsilon_{PLA} = 2.7$. The results obtained are given in Figs. 3.10a, b, respectively.

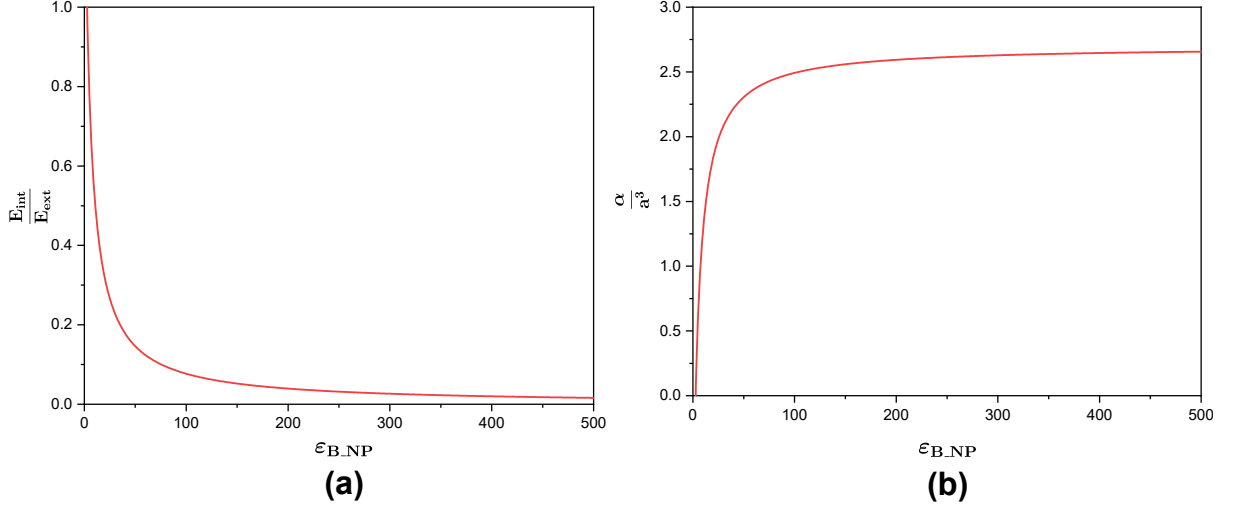


Figure 3.10: (a) Evolution of the internal field E_{int} (via the ratio $\frac{E_{int}}{E_{ext}}$) as a function of the B_NP permittivity. (b) Evolution of the polarizability α (via the ratio $\frac{\alpha}{a^3}$) as a function of the B_NP permittivity.

The primary lesson is that the polarizability α increases with increasing B_NP permittivity to reach a stagnant stage for a value of B_NP permittivity around 200. Another important conclusion is that the internal field inside inclusions decreases dramatically with increasing B_NP permittivity. This means that electrical field has difficulty in penetrating the disconnected B_NP inclusions when the electrical contrast between B_NP and PLA becomes high. There are the reasons why the effective permittivity of the composite is no longer increased beyond a critical permittivity of B_NP (evaluated around 200 in this work) for volume fractions of B_NP lower than the percolation threshold. The percolation threshold is thus a key parameter to control the resulting properties of the composites. When the shape of the inclusions is changed from the sphere and/or the distribution of the inclusions is not random, the percolation threshold is expected to decrease as it becomes more likely for the inclusions to touch each other. In our study, this is an interesting aspect since the morphology of dispersed B_NP is clearly not spherical in the B_NP@PDA/PLA composite and there is little chance that the distribution of B_NP into the composite is perfectly homogeneous. These are the probable reasons that would explain that the effective permittivities measured are located above the curves calculated (see Fig. 3.9).

3.2.3.3 Effects of the aspect-ratio of fillers on the effective permittivity of the nanocomposite: quantitative analysis

As explained before, the morphology of the dispersed B_NP ceramic can have an influence on the effective permittivity of the composites. In order to study this effect, we have decided to adapt the model developed to a mixture of randomly oriented ellipsoids of B_NP ceramic into PLA matrix. In that case, the differential equation used for spherical particles must be modified as follow [288]:

$$\frac{d\varepsilon_{eff}}{df} = \varepsilon_{PLA}(\varepsilon_{B_NP} - \varepsilon_{eff}) \frac{\sum_{j=x,y,z} (\varepsilon_{eff} + N_j(\varepsilon_{B_NP} - \varepsilon_{eff}))^{-1}}{3 - f_{B_NP} \sum_{j=x,y,z} (\varepsilon_{eff} + N_j(\varepsilon_{B_NP} - \varepsilon_{eff}))^{-1}} \quad (3.7)$$

where N_j are the depolarization factors in the three directions of space x , y and z , also known as the geometrical factors of electrostatics. More precisely, they represent the diagonal components of a tensor that can be interpreted as a generalized depolarizing dyadic of a particle. Assuming the spheroid z axis be the rotational axis, we have for prolate particles [291]:

$$N_z = \frac{1 - e^2}{e^3} (\operatorname{arctanh}(e) - e) \quad (3.8)$$

where e is the eccentricity. The prolate spheroid ranges from a needle ($e = 1$) to a sphere ($e = 0$). The hyperbolic arctan can be expressed as:

$$\operatorname{arctanh}(e) = \frac{1}{2} \ln \frac{1+e}{1-e} \quad (3.9)$$

For a prolate, the following expression must be used:

$$e = \sqrt{\frac{(\frac{c}{a})^2 - 1}{(\frac{c}{a})^2}} \quad (3.10)$$

where $\frac{c}{a}$ is the aspect ratio of particles.

The remaining depolarization factors N_x and N_y can be determined by using the sum rule: $N_x + N_y + N_z = 1$. We thus obtain the following relations:

$$\begin{cases} N_x = \frac{1}{2}(1 - N_z) \\ N_y = \frac{1}{2}(1 - N_z) \end{cases} \quad (3.11)$$

3.2. THE NEAR-SPHERICAL BCZT (B_NP)/PLA COMPOSITE AS A REFERENCE

Ultimately, the depolarization factors take into account that the polarizability induced by the presence of particles into composite is a function of the inclusion geometry and orientation with respect to the applied electrical field.

The Eq. 3.7 was solved numerically and the main results were given in Figs. 3.11 and 3.12. In Fig. 3.11, the effects of B_NP ceramic aspect ratio on the effective permittivity of the composite was highlighted. For a given permittivity of B_NP of 10000, increasing the aspect ratio of B_NP ceramic leads to an increase of the effective permittivity of the composite. The reason for this is that the induced polarizability is enhanced with the aspect ratio. Indeed, the average response of one ellipsoid is the sum of its three polarizability components [292]:

$$\alpha = \frac{1}{3} \sum_{j=x,y,z} \frac{\varepsilon_{B_NP} - 1}{1 + N_j(\varepsilon_c - 1)} \quad (3.12)$$

The polarizability induced by the major axis of the spheroid increases strongly with increasing eccentricity and aspect ratio.

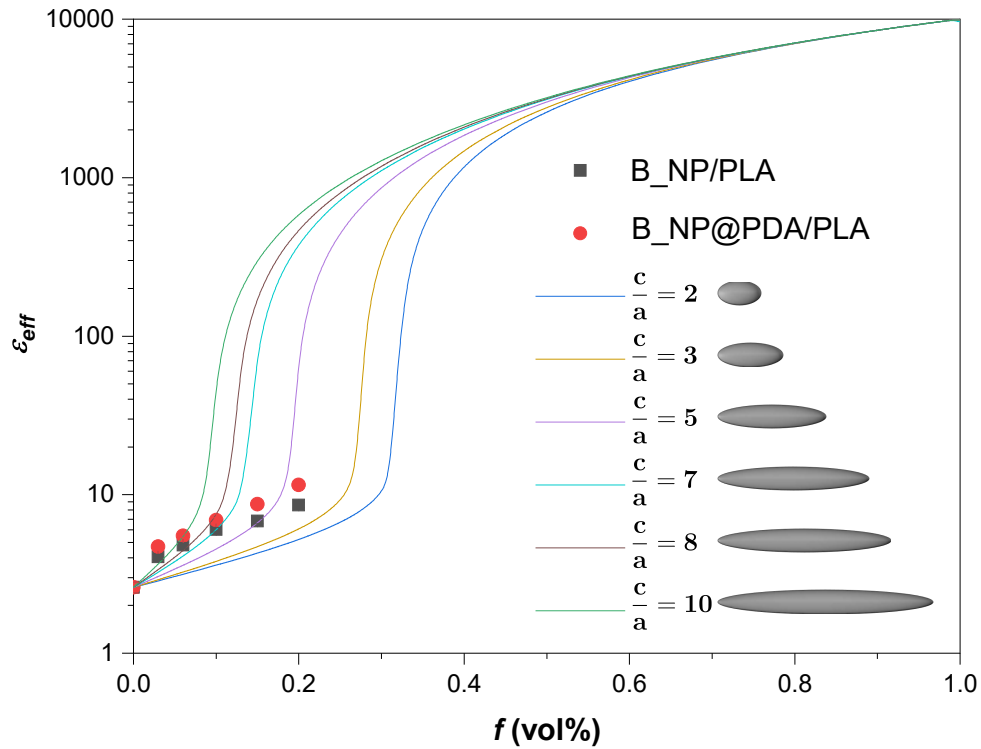


Figure 3.11: Evolution of the effective permittivity of the B_NP/PLA composite as a function the aspect ratio of the B_NP charge. For all calculations, the permittivity of the B_NP ceramic was considered equal to 10000.

Another possible and complementary way to think is to consider the effect of aspect ratio on the percolation threshold. Fig. 3.11 shows a rapid increase of effective permittivity at a given volume fraction of B_NP that depends on the aspect ratio. All happen as if the effective permittivity is strongly enhanced at a volume fraction that corresponds to the percolation threshold. In other word, the model developed reflect also the aspect ratio dependence of the percolation threshold (f_c) (see Fig. 3.12).

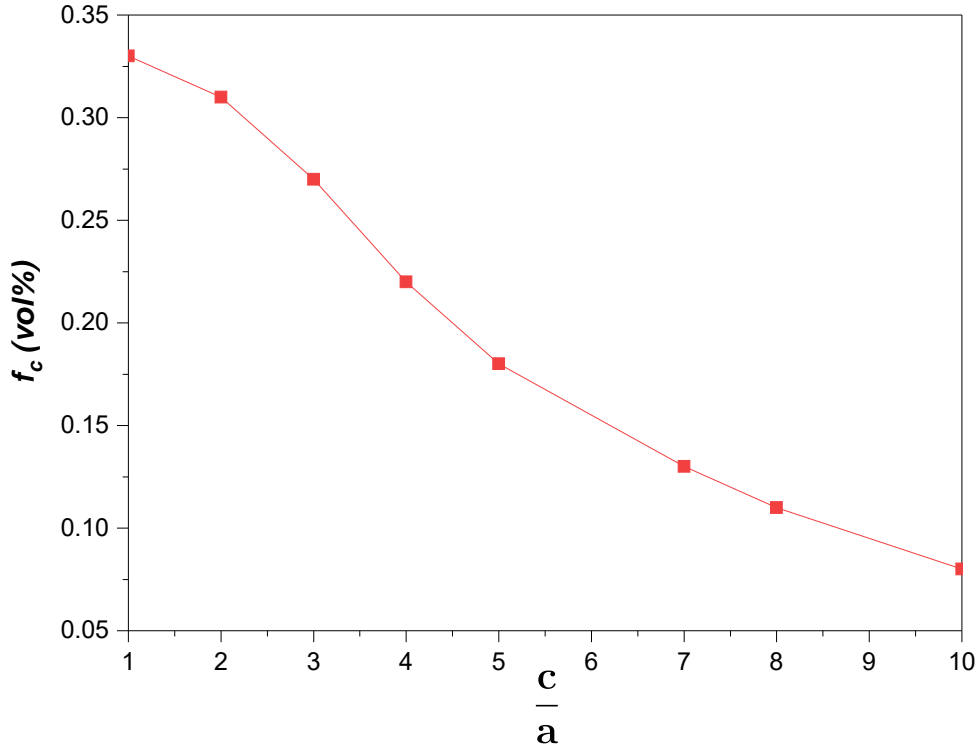


Figure 3.12: Calculation of the evolution of the percolation threshold of B_NP into PLA as a function the aspect ratio of B_NP.

The analysis performed show that both permittivity and aspect ratio of B_NP ceramic control the effective permittivity of the composite. Then, one might ask oneself what couples (ϵ_{B_NP} , $\frac{c}{a}$) might fit the experimental data. The calculations performed Fig. 3.13 evidence that the solution is not unique; there is exist an infinite.

Very interestingly, the experimental data can be fitted with very different values of B_NP permittivity but relatively close values of aspect ratio (see for example the couples ($\epsilon_{B_NP} = 10000$, $\frac{c}{a} = 3.9$) and ($\epsilon_{B_NP} = 200$, $\frac{c}{a} = 5.5$). We show here that a drastic decrease of the B_NP permittivity can be compensated by a relatively small increase of

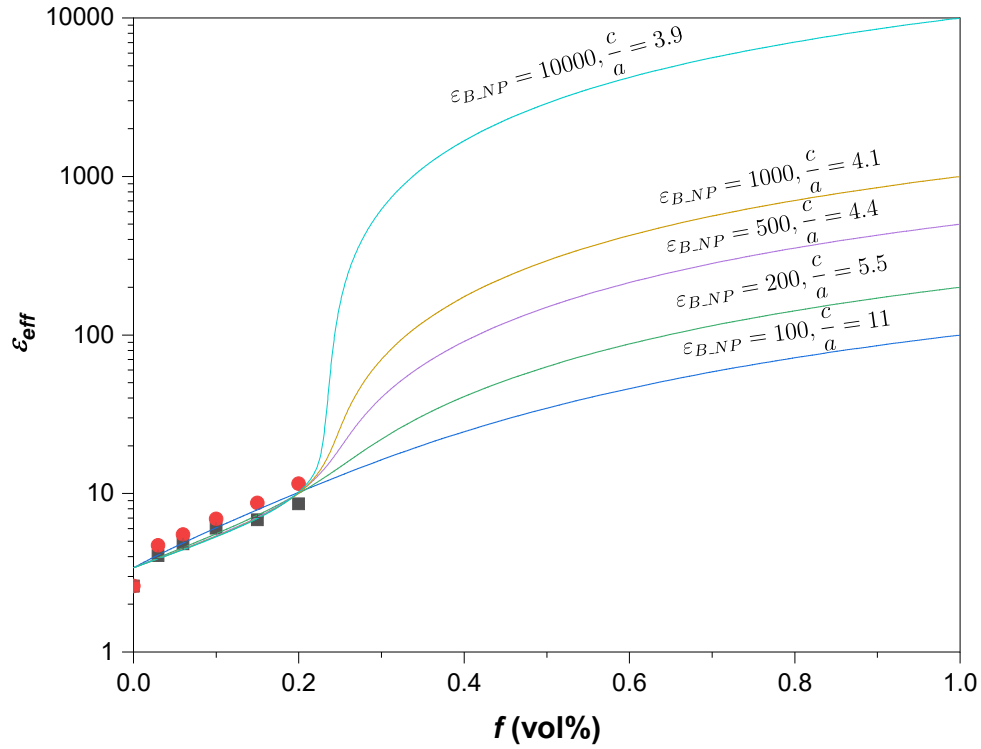


Figure 3.13: Calculation of the effective permittivity of the B_NP/PLA composite as a function of B_NP volume fraction for different couples $(\epsilon_{B_NP}, \frac{c}{a})$. Comparison with experimental data.

the aspect ratio of B_NP. This is a key point for improving the energy storage properties of the composite since the large difference between the dielectric permittivity of the inclusions and the matrix can lead to local electric field intensification and interfacial polarization. The study carried out previously introduces thus a paradigm we propose to study in the following section.

3.3 The permittivity *vs* the aspect ratio of the ceramic: a real paradigm?

3.3.1 Dielectric properties

Two main results were highlighted previously. For volume fractions of B_NP lower than the percolation threshold, the effective permittivity of the composite is no longer increased

Table 3.2: Comparison of the dielectric (at 1 kHz) and microstructure properties of B_NP, HZTO_NW and B_NR sintered ceramics at 1250 °C/10 h.

Ceramic	Shape	Aspect ratio	ε_m
B_NP	Near-spherical	1	12085
HZTO_NW	Nanowire	10	350
B_NR	Nanorod	50	11906

beyond a critical permittivity of B_NP (evaluated around 200 in this work) and a small increase of aspect ratio can compensate a large decrease of the B_NP permittivity. The development of ceramic/polymer composites is mainly motivated by the large difference of dielectric properties of the ceramic as filler and polymer as matrix. A paradigm emerges thus which can be summarized as follow: for improving properties of the composite, it is not necessary to use ceramics with high permittivity, we should rather control their geometry. We propose in this section to offer concrete answer to that question. To this end, two other different ceramics were selected for the preparation of ceramic/PLA composites. They are characterized by both different morphologies and permittivities than B_NP (see table 3.2). The average aspect ratios were calculated using the ratio of the average length and the average diameter of the particles from FESEM micrographs, and the ε_m corresponds to the maximum value of the dielectric constant.

In the same way as for B_NP, the HZTO_NW and B_NR ceramics were dispersed into PLA matrix. To have an insight on the morphological characteristics of high aspect ratio nanofillers in PLA matrix, Fig. 3.14 gives views of HZTO_NW/PLA nanocomposite films at the surface and at the cross-section using 3, 6 and 20 vol% of nanowires. It is observed that HZTO_NW are dispersed homogeneously in the PLA matrix, indicating the excellent compatibility between PLA and HZTO_NW. The nanowires show a good dispersion in the PLA matrix and a large number of HZTO_NW are covered with PLA matrix, and the majority of HZTO_NW are horizontally aligned in the PLA matrix. This suggests the good dispersion and the excellent compatibility between HZTO_NW and PLA. Besides, Fig. 3.15 provides surface and cross-section views of 3 vol% B_NR/PLA nanocomposite film. It is observed that the majority of B_NR are covered with PLA matrix, which evidences also the excellent compatibility between B_NR and PLA matrix.

3.3. THE PERMITTIVITY VS THE ASPECT RATIO OF THE CERAMIC: A REAL PARADIGM?

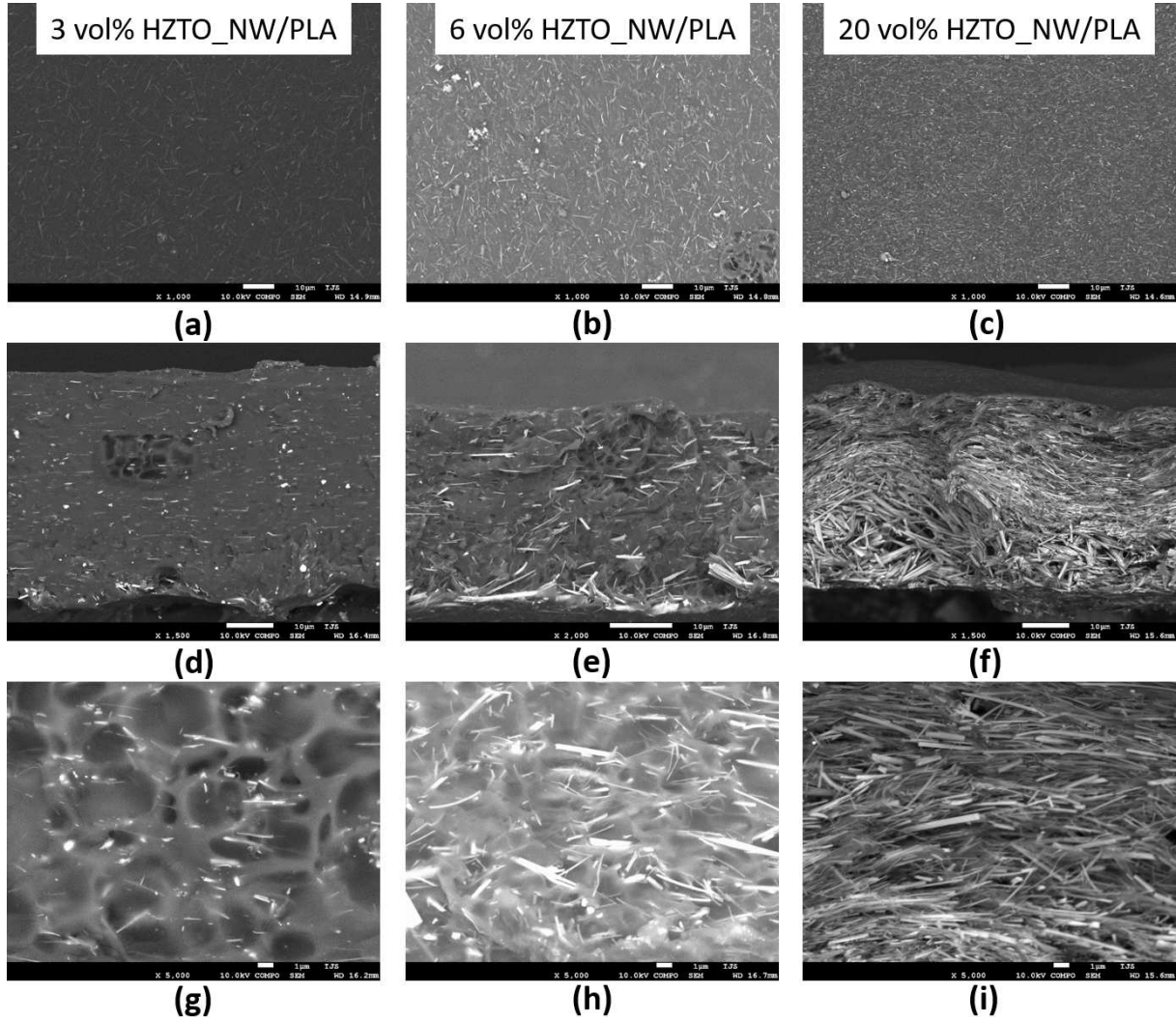


Figure 3.14: FESEM images of the (a-c) surface and the (d-i) cross-section of HZTO_NW/PLA nanocomposite films at various volume fractions.

The frequency-dependence of the ϵ_r and $\tan\delta$ of HZTO_NW/PLA and B_NR/PLA nanocomposites films with different volume fractions are measured under the frequency ranging from 100 Hz to 1 MHz at room temperature are shown in Fig. 3.16. All the nanocomposites have enhanced ϵ_r in comparison to the pure PLA (Figs. 3.16a, b). Compared to the nanocomposites with spherical inclusions (B_NP and B_NP@PDA), the nanocomposites loaded with high aspect ratio nanofiller (HZTO_NW and B_NR) possess a remarkably improved dielectric constant although the permittivities of HZTO_NW and B_NR is lower than the one of B_NP (see Table 1 for comparison). At 1 kHz and by using 20 vol% of nanofillers, the dielectric constants of the HZTO_NW/PLA and B_NR/PLA nanocomposites films reach 15.99 and 20.30, respectively, which are higher than those of

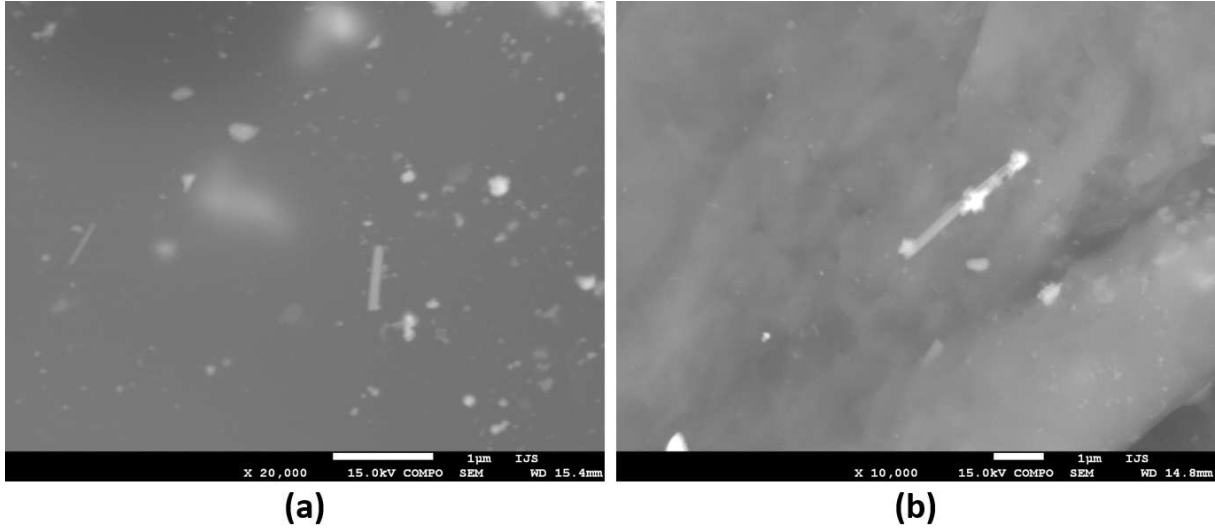


Figure 3.15: FESEM images of the (a) surface and the (b) cross-section of 3 vol% B_NR/PLA nanocomposite film.

B_NP/PLA ($\epsilon_r = 9.11$) and B_NP@PDA/PLA ($\epsilon_r = 11.24$). Meanwhile, Figs. 3.16c, d display that $\tan\delta$ of all nanocomposite films decreases at first and then increases with frequency. Around 100 Hz, the high $\tan\delta$ is due to the relaxation polarization loss caused by interfacial polarization. By increasing the nanofillers content, $\tan\delta$ of all nanocomposite films is inescapably amplified. It is worth noting that even at high nanofiller loads, the two types of nanocomposite films, do not show a high $\tan\delta$ at a wide frequency range.

To compare the dielectric properties of PLA-based nanocomposite films with different ceramic fillers, Fig. 3.17 recapitulates the values of ϵ_r and $\tan\delta$ at different volume fractions as measured at 1 kHz and room temperature of all nanocomposite films. It is clearly demonstrated that the nanocomposites with fillers with high aspect ratio (rods and nanowires) exhibit enhanced dielectric properties compared to those based on B_NP and B_NP@PDA. At 20 vol%, ϵ_r values of B_NP/PLA, B_NP@PDA/PLA, B_NR/PLA and HZTO_NW/PLA nanocomposite films are found to be 9.11, 11.24, 15.99 and 20.28, respectively. More interestingly, the dielectric loss is decreased in the nanocomposite based-on fillers with high aspect ratio. For instance, embedding PLA matrix with 20 vol% B_NR can enhance the dielectric permittivity more than twofold compared with B_NP with the same loading, while keeping low dielectric loss. The enhancement of the dielectric properties in fillers with high aspect ratio compared to near-spherical particles

3.3. THE PERMITTIVITY VS THE ASPECT RATIO OF THE CERAMIC: A REAL PARADIGM?

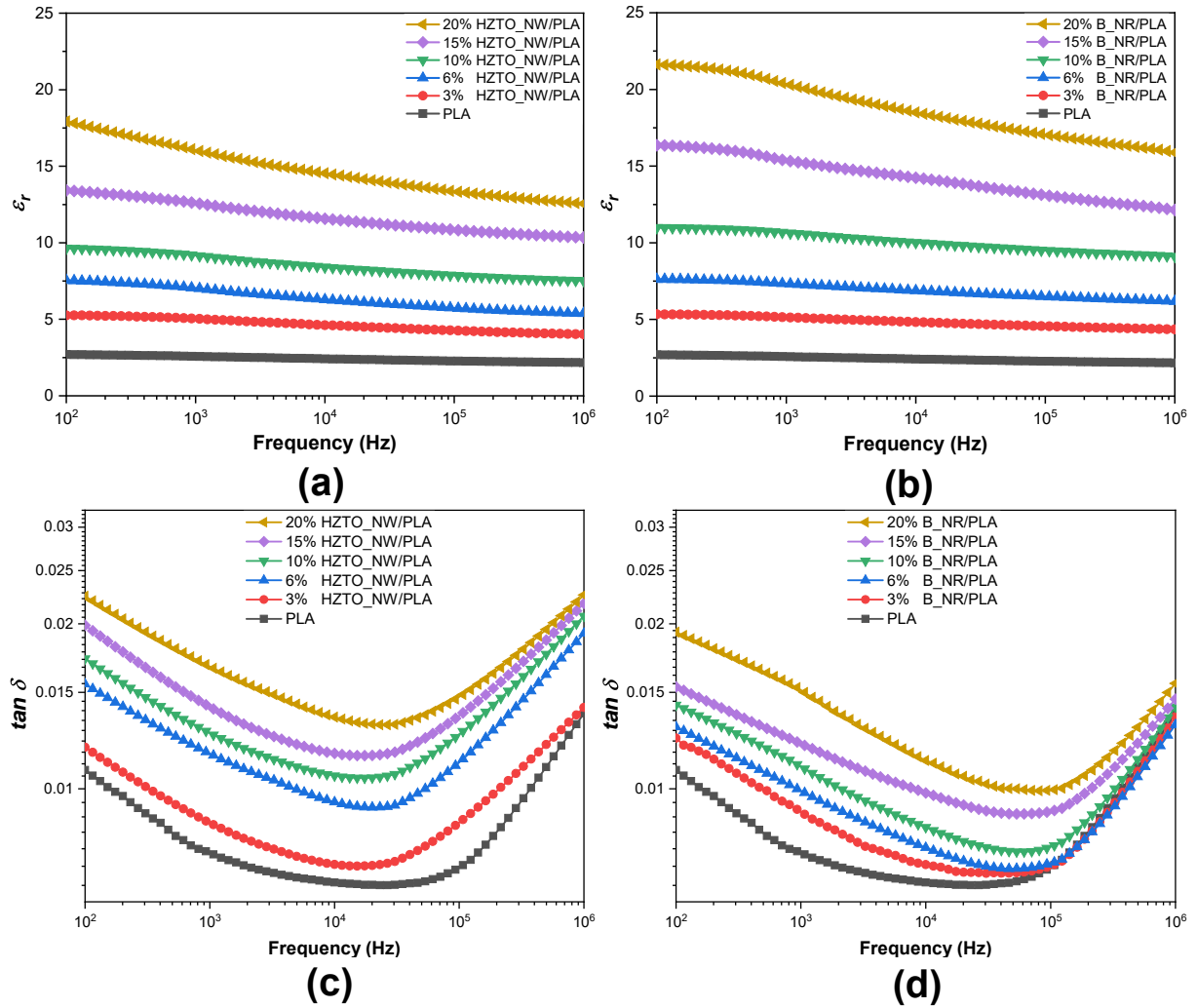


Figure 3.16: (a, b) ϵ_r and (c, d) $\tan\delta$ of HZTO_NW/PLA and B_NR/PLA nanocomposites, respectively.

are due to the percolation threshold of such fillers with high aspect ratio [293]. It was reported that the high aspect ratio fillers can improve the dielectric properties of the composites [253, 294, 295]. Theoretically, the high aspect ratio fillers reach the percolation threshold more easily than the low aspect ratio fillers, which allows connectivity or continuous path in the system and improves the dielectric properties of the composites. Moreover, the high aspect ratio can improve the dielectric constant of the composites due to the large dipole moment [253]. Besides, the high aspect ratio fillers have lower surface area than low aspect ratio fillers, which helps reduce the surface energy, thus preventing agglomeration and enhancing overall performance in the composites [296].

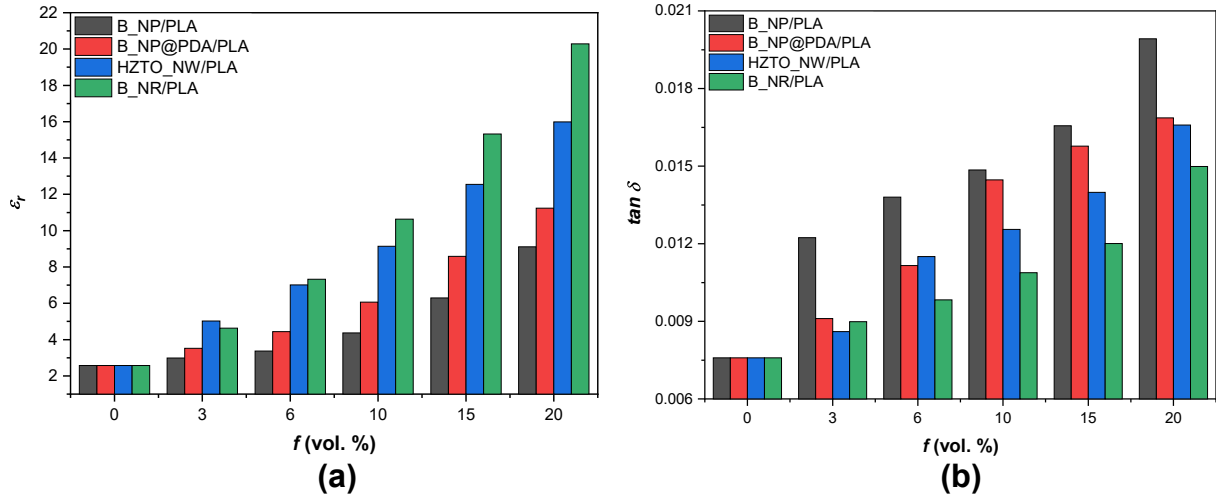


Figure 3.17: Effect of the volume fraction of B_NP, B_NP@PDA, HZTO_NW and B_NR fillers on the (a) ϵ_r and (b) $\tan \delta$ of PLA-based nanocomposites.

3.3.2 Energy storage performances

To have an insight on the energy storage of PLA-based nanocomposite films, Fig. 3.18 display the unipolar dielectric displacement–electric field ($D - E$) loops of B_NP/PLA, B_NP@PDA/PLA, HZTO_NW/PLA and B_NR/PLA nanocomposites measured at 100 Hz and an electric field of 1 MV/cm. The maximum displacement (D_{max}) and the remnant polarization (P_r) of each nanocomposite increase with increasing nanoparticle concentration. Furthermore, D and P_r of B_NR/PLA nanocomposites are found higher than those of HZTO_NW/PLA, B_NP@PDA/PLA and B_NP/PLA, which suggests that the use of high aspect ratio nanofiller has enhanced the ferroelectric properties of PLA-based nanocomposites. These results corroborate those obtained in the dielectric properties.

From the obtained $D - E$ loops, the total energy density (U_{tot}) of the nanocomposites can be estimated by means of the Eq. 3.13 [297], where E is the electric field, P_r is the remnant polarization and D_{max} is the maximum value of the observed dielectric displacement. U_{tot} was calculated *via* numerical integration by adding the area gathering the closed area of the $D - E$ hysteresis loops (U_{loss}) and the area between the polarization axis and the upper branch curve of the unipolar $D - E$ hysteresis loop (U_{rec}). The calculated values of the energy density at 1 MV/cm are presented in Fig. 3.19a. The total

3.3. THE PERMITTIVITY VS THE ASPECT RATIO OF THE CERAMIC: A REAL PARADIGM?

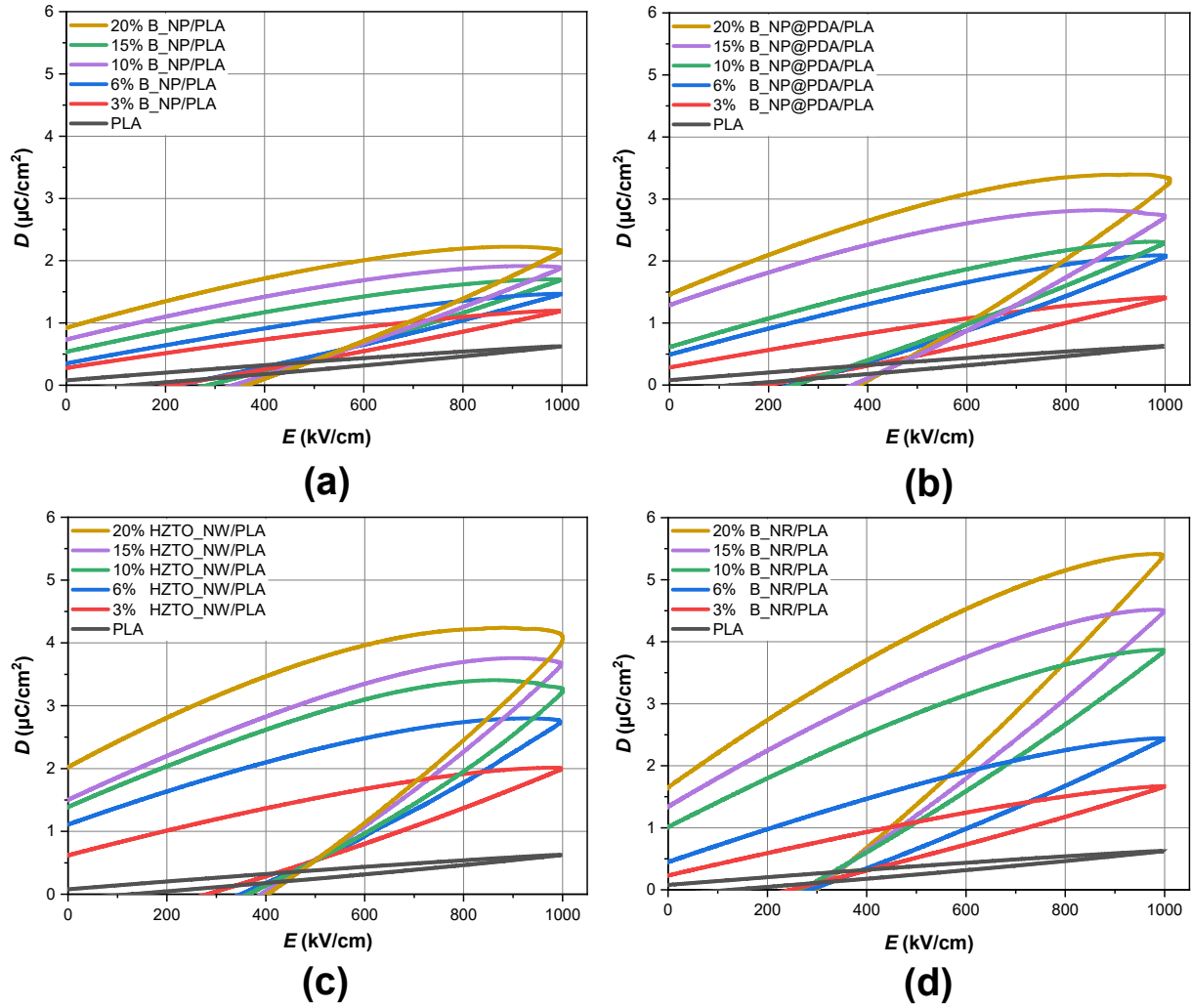


Figure 3.18: $D-E$ loops of (a) B_NP/PLA, (b) B_NP@PDA/PLA, (c) HZTO_NW/PLA and (d) B_NR/PLA nanocomposites.

stored energy density increases with increasing nanofiller concentration. It should be noted that the observed energy density values of B_NR/PLA nanocomposites are systematically higher than those of HZTO_NW/PLA, B_NP@PDA/PLA and B_NP/PLA, respectively. This is mainly due to the enhanced dielectric displacement in B_NR/PLA nanocomposites. At nanofiller concentration of 20 vol%, the total energy densities are 3.63, 3.13, 2.47 and 1.43 J/cm³ for B_NR/PLA, HZTO_NW/PLA, B_NP@PDA/PLA and B_NP/PLA, respectively.

$$U_{tot} = \int_0^{D_{max}} E \, dD \quad (3.13)$$

In order to measure the effective energy storage capability of a dielectric material, the recovered energy density was determined. As shown in Fig. 3.19b, the recovered energy density values of B_NR/PLA nanocomposites are systematically higher than those of HZTO_NW/PLA, B_NP@PDA/PLA and B_NP/PLA, respectively. This is due to the relatively slimmer hysteresis loops in B_NR/PLA. At nanofiller concentration of 20 vol%, the recovered energy densities, determined from Eq. 3.14 were found to be 1.80, 1.31, 1.11 and 0.55 J/cm³ for B_NR/PLA, HZTO_NW/PLA, B_NP@PDA/PLA and B_NP/PLA, respectively. The obtained energy performances are enhanced compared to those reported by Fan et al. in BaTiO₃/PLA nanocomposites [268]. This improvement could be attributed to the enhanced dielectric and ferroelectric properties in BCZT compared to BaTiO₃ ceramic, and the use of high aspect ratio fillers [170]. The energy storage efficiency (η) can be defined as the ratio of recovered energy density to the total stored energy density, as estimated in Eq. 3.15 [298]. As shown in Fig. 3.19c, at particle concentration of 20 vol%, the calculated values of η are 49.61, 41.66, 44.93 and 38.67% for B_NR/PLA, HZTO_NW/PLA, B_NP@PDA/PLA and B_NP/PLA, respectively. It is observed that the total stored energy density of the nanocomposite with 20 vol% of B_NR is ten time more than that of the pristine PLA polymer (0.365 J/cm³). Meanwhile, the recovered energy density of the nanocomposite with 20 vol% B_NR is more than six-fold of that of PLA polymer (0.365 J/cm³). It is worth noting that at $f = 3$ vol%, U_{tot} , U_{rec} and η of HZTO_NW are higher compared to the other PLA-nanocomposites, this could be due to the high dielectric constant and low dielectric loss observed in 3 vol% HZTO_NW/PLA nanocomposite. This behavior was observed by Wang et al., when comparing four kinds of nanowires (Na₂Ti₃O₇, TiO₂, BaTiO₃, and SrTiO₃) [72].

$$U_{rec} = \int_{D_r}^{D_{max}} E dD \quad (3.14)$$

$$\eta(\%) = \frac{U_{rec}}{U_{tot}} \times 100 = \frac{U_{rec}}{U_{rec} + U_{loss}} \times 100 \quad (3.15)$$

Many works have demonstrated that polydopamine is very promising to be utilized as a surface modifier to improve the inclusion of nanofillers inside polymer matrices, because of its exceptionally strong adhesion ability [98, 299, 300]. The reasons behind the

3.3. THE PERMITTIVITY VS THE ASPECT RATIO OF THE CERAMIC: A REAL PARADIGM?

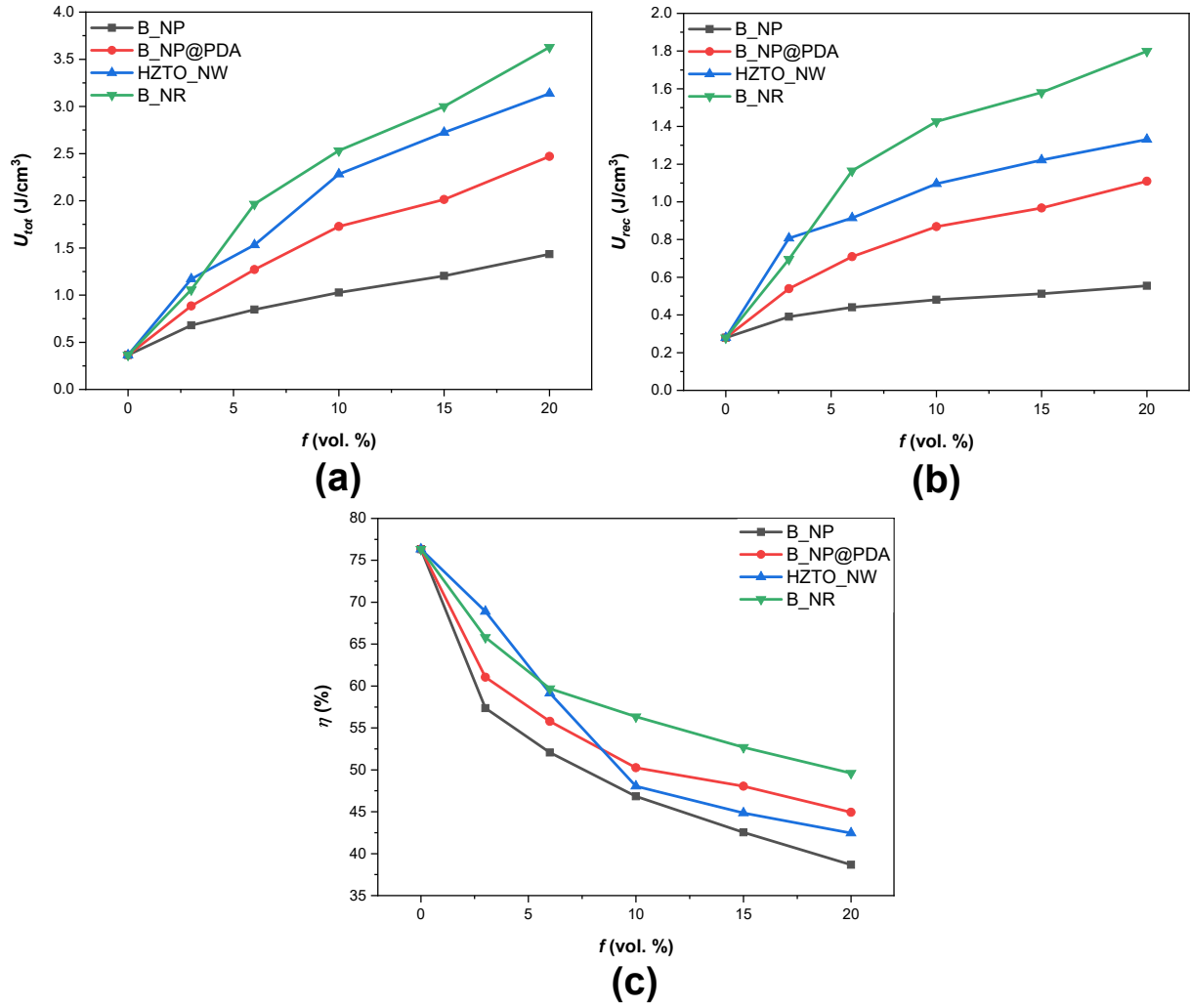


Figure 3.19: (a) The U_{tot} , (b) U_{rec} and (c) η of the PLA-based nanocomposite films.

improved energy storage performances in B_NP@PDA/PLA compared to B_NP/PLA nanocomposite films could be interpreted in two ways. (i) The polydopamine incorporation into the surface of B_NP improves the dispersion and compatibility of fillers in the PLA matrix. (ii) The polydopamine insulation layer enhances the insulation of the B_NP fillers and confines the accumulation and mobility of the filler-matrix space charge. Therefore, the B_NP@PDA introduction into the polymer matrix is more beneficial for improving energy density of nanocomposite films [301]. The main reason behind the enhanced energy storage performances in HZTO_NW/PLA and B_NR/PLA compared to B_NP/PLA and B_NP@PDA/PLA nanocomposite films, was attributed to the high aspect ratio of HZTO_NW and B_NR fillers embedded in PLA matrix. It was reported that 1D ceramic nanofillers with a high aspect ratio, can efficiently enhance the energy density of

nanocomposites when compared to their counterparts with spherical particles. This is due to the fact that the ceramic nanowires possess a large dipolar moment, and thus the dielectric constant of the nanocomposites can be increased at a low volume fraction of the ceramic component [72]. Therefore, these results suggest that the use of high aspect ratio nanofiller enhances the energy storage performance of PLA-based nanocomposites.

3.4 Conclusions

High- k nanocomposites based on biodegradable polymer matrix polylactic acid (PLA) and different inorganic nanofillers with various shapes (spherical, rod, and wire) and arrangements were successfully fabricated. The effects of both the permittivity and aspect ratio of the nanofiller and the core-shell structuration were explored by both an experimental and theoretical approach. The main results can be summarized as-follow:

- the increase of the effective permittivity of the B_NP/PLA and B_NP@PDA/PLA composites was attended by an increase of dielectric losses. However, the maximum dielectric losses remain relatively weak in view of the maximum increase of permittivity,
- although the increase of the effective permittivity measured is relatively high (multiplied on average by 4 between 0 and 20% of B_NP in the composites), it remains weak in comparison with the expected high value of the near-spherical B_NP permittivity,
- very surprisingly, the functionalization has not a very pronounced effect of the dielectric properties of the nanocomposites (effective permittivity and dielectric loss) but have a significant effect on both the total and recovered energy densities,
- the measured effective permittivities show a linear dependence with the volume fraction of BCZT. This can be simply explained by the fact that the domains are spatially separated and electrostatic interactions between each inclusion and its neighbors are relatively weak when volume fraction of fillers are below the percolation threshold,

- when spherical inclusions do not touch each other, there is a critical permittivity of ceramic from which the effective permittivity does not increase even for giant permittivities of ceramic. This was attributed to the fact that the electrical field has difficulty in penetrating the disconnected inclusions when the electrical contrast between B_NP and PLA becomes high,
- when the shape of the inclusions is changed from the sphere and/or the distribution of the inclusions is not random, the percolation threshold is expected to decrease as it becomes more likely for the inclusions to touch each other. The effect of aspect-ratio was thus studied. Very interestingly, the experimental data can be fitted with very different values of B_NP permittivity but relatively close values of aspect ratio (see for example the couples $(\varepsilon_{B_NP} = 10000, \frac{c}{a} = 3.9)$ and $(\varepsilon_{B_NP} = 200, \frac{c}{a} = 5.5)$). We show here that a drastic decrease of the B_NP permittivity can be compensated by a relatively small increase of the aspect ratio of B_NP,
- a paradigm emerges thus since the development of ceramic/polymer composites is mainly motivated by the large difference of dielectric properties of the ceramic as filler and polymer as matrix. To address this issue, two type of ceramic fillers owning adverse properties, i.e. B_NR with high dielectric constant and high aspect ratio and HZTO_NW with low dielectric constant and very high aspect ratio, were embedded in PLA matrix. The enhancement of the dielectric properties in fillers with high aspect ratio compared to near-spherical particles were due to the low the percolation threshold of such fillers with high aspect ratio. The energy storage performances of PLA-based nanocomposites were evaluated by $D - E$ loops using spherical, rod, and wire shaped particles. High-energy storage density and recovered energy density of 3.63 and 1.80 J/cm³, respectively, were obtained in nanocomposites based on rod-like fillers. Therefore, the use of high-aspect ratio nanofiller with high dielectric constant enhances the energy storage performance of PLA-based nanocomposites. Accordingly, this study reveals a paradigm between the dielectric constant and the aspect ratio of the ceramic filler, and the resulting dielectric properties and energy storage performances in ceramic/polymer nanocomposite were based on a compromise between the dielectric constant and the aspect ratio of the ceramic filler.

CHAPTER

4

Lead-free Nanocomposite Piezoelectric Nanogenerator Film for Biomechanical Energy Harvesting

Contents

4.1	Context of the study	129
4.2	Fabrication of the BF-PNG	130
4.3	Local piezoelectric properties	131
4.4	Mechanical energy harvesting	133
4.5	Conclusions	142

4.1 Context of the study

Because of their robustness and their enhanced output performances, the ceramic/polymer nanocomposite piezoelectric nanogenerators (PNGs) using piezoelectric materials at the nanoscale are in central focus in development of the new generation of mechanical energy-harvesting sources [106, 124–126]. These PNGs could drive self-powered and wireless healthcare systems such as heart monitor, pacemaker energizer, blood flow monitor, and real-time biomedical monitor [11, 131–133, 302]. However, the market of piezoelectric devices is dominated mainly by lead-based piezoceramics like $\text{PbZr}_x\text{Ti}_{1-x}\text{O}_3$ (PZT) and $(1-x)\text{Pb}(\text{Mg}_{1/3}\text{Nb}_{2/3})\text{O}_3-x\text{PbTiO}_3$ (PMN–PT) systems because of their excellent piezoelectric properties [11, 303, 304]. Nevertheless, lead is toxic and harmful to the environment and our health [152, 305, 306]. Hence, the replacement of PZT by the homologs with comparable piezoelectric properties but without lead is an urgent task [57, 121, 307, 308]. In this regard, lead-free $\text{Ba}_{0.85}\text{Ca}_{0.15}\text{Zr}_{0.1}\text{Ti}_{0.9}\text{O}_3$ (BCZT), which is a bioceramic with excellent dielectric, ferroelectric and piezoelectric properties, is a potential candidate to substitute lead-based materials [159, 176, 247, 309].

In chapter 2, we demonstrated that the synthesis temperature of BCZT powders could be decreased to a low temperature of 160 °C while still preserving enhanced dielectric and ferroelectric properties. Another important factor in BCZT ceramics is the biocompatibility nature [194–196], as reported in chapter 1. Furthermore, from an ecological point of view, all-ecological energy harvesting systems are currently experiencing a great deal of enthusiasm and attracting much attention due to the environmental constraints and considerations [127, 310]. As for polylactic acid (PLA), as conclusively shown in chapter 1, it is a low cost, biodegradable, and biocompatible polymer with excellent mechanical properties, chemical and electrical resistance, and it is amenable to a variety of processing techniques [311, 312]. PLA is becoming a promising candidate for energy harvesting applications owing to its high piezoelectric properties, which could outspread the applications of PNGs to several energy-related systems, namely in the biomedical field [112, 205, 313]. The carbonyl groups present in PLA structure induce polarity, and it shows a piezoelectric coefficient d_{14} value of 10 pC/N without additional poling step in its

crystalline structure [207].

In this chapter, an eco-friendly and bio-flexible piezoelectric nanogenerator (BF-PNG) combining the near-spherical BCZT nanoparticles (B_NP) functionalized with poly-dopamine (PDA) via core-shell structuration (B_NP@PDA) as illustrated in chapter 3, and PLA biopolymer was designed without any poling process. The outputs performances under different human body motions were tested, alongside with the feasibility of the BF-PNG to drive commercial electronics (charging capacitors and glowing a light-emitting diode (LED)).

4.2 Fabrication of the BF-PNG

The bio-flexible nanocomposite generator device (BF-PNG) was designed using the previously elaborated 20 vol% B_NP@PDA/PLA nanocomposite film. This later with 17 μm of thickness was sandwiched between two copper foils of $1.5 \times 1.3 \text{ cm}^2$ serving as top and bottom electrodes. For external connections, two copper wires were attached to the top and bottom electrodes to measure the open-circuit voltage (V_{oc}) and short-circuit current (I_{sc}). Then, the BF-PNG was additionally sandwiched by using the Kapton tape. This encapsulation prevented damage of the BF-PNG by repeated mechanical excitations and made it water- and dustproof. The schematic illustration and the photo of the flexible BF-PNG generator device are shown in Figs. 4.1a and 4.1b, respectively.

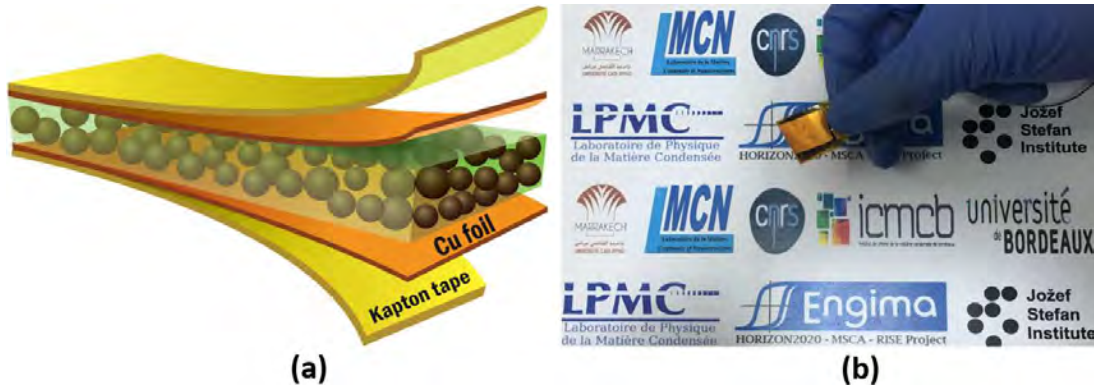


Figure 4.1: (a) Schematic illustration of the prepared composite generator and (b) a photograph of the flexible nanocomposite generator device (BF-PNG).

4.3 Local piezoelectric properties

Because the piezoelectric response is the key property in PNGs, it was carefully checked before and after embedding B_NP@PDA nanoparticles in the PLA matrix by piezoresponse force microscopy (PFM). PFM is based on the detection of a local electromechanical response of the ferroelectric material through the converse piezoelectric effect. Fig. 4.2 shows the schematics of the PFM setup and 20 vol% B_NP@PDA/PLA nanocomposite film. Detailed experimental setup can be found in Appendix H.

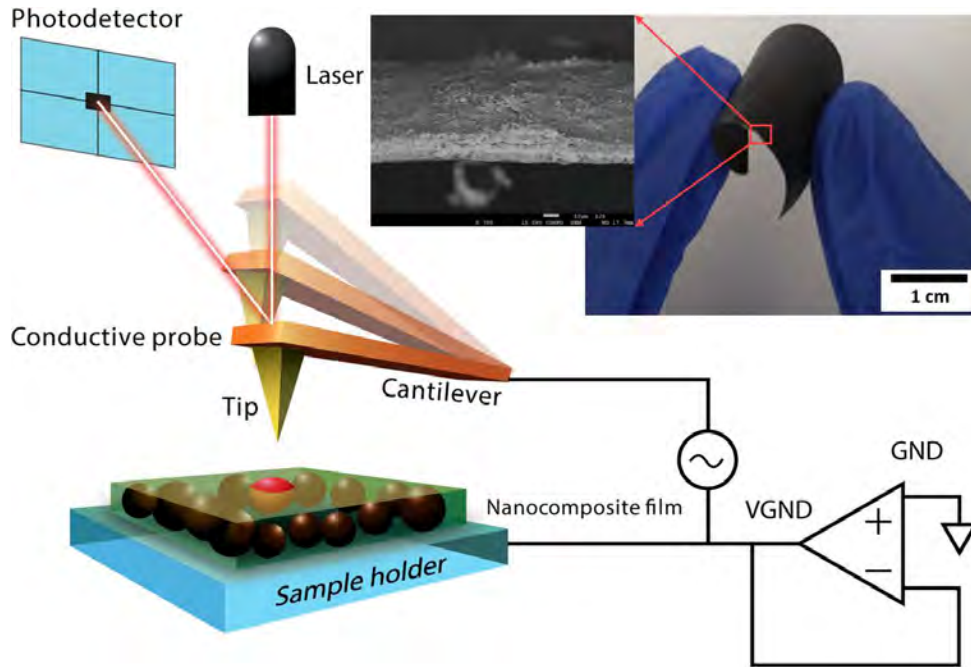


Figure 4.2: The operating PFM setup used to measure the piezoelectric response in 20 vol% B_NP@PDA/PLA nanocomposite film schematically shown in the upper right corner (zoomed inset displays field-emission scanning electron microscope (FESEM) image of the nanocomposite film).

Before the incorporation of B_NP@PDA nanofillers in the PLA matrix, the topographic and the out-of-plane amplitude PFM images are shown in Figs. 4.3a-h. The single particles can be clearly distinguished in topography (a) height and (b) deflection images. PFM amplitude and phase images show that the B_NP@PDA particles are piezoelectrically active (Figs. 4.3c, d, g, h). A closer look (Figs. 4.3e-h) reveals inside the particle's regions of different piezoelectric activity (white arrows mark some examples). To further investigate piezoelectric/ferroelectric responses, PFM switching spectroscopy

experiment was performed. The local phase and amplitude hysteresis loops typical for piezoelectric/ferroelectric material were measured, as shown in Figs. 4.3i, j.

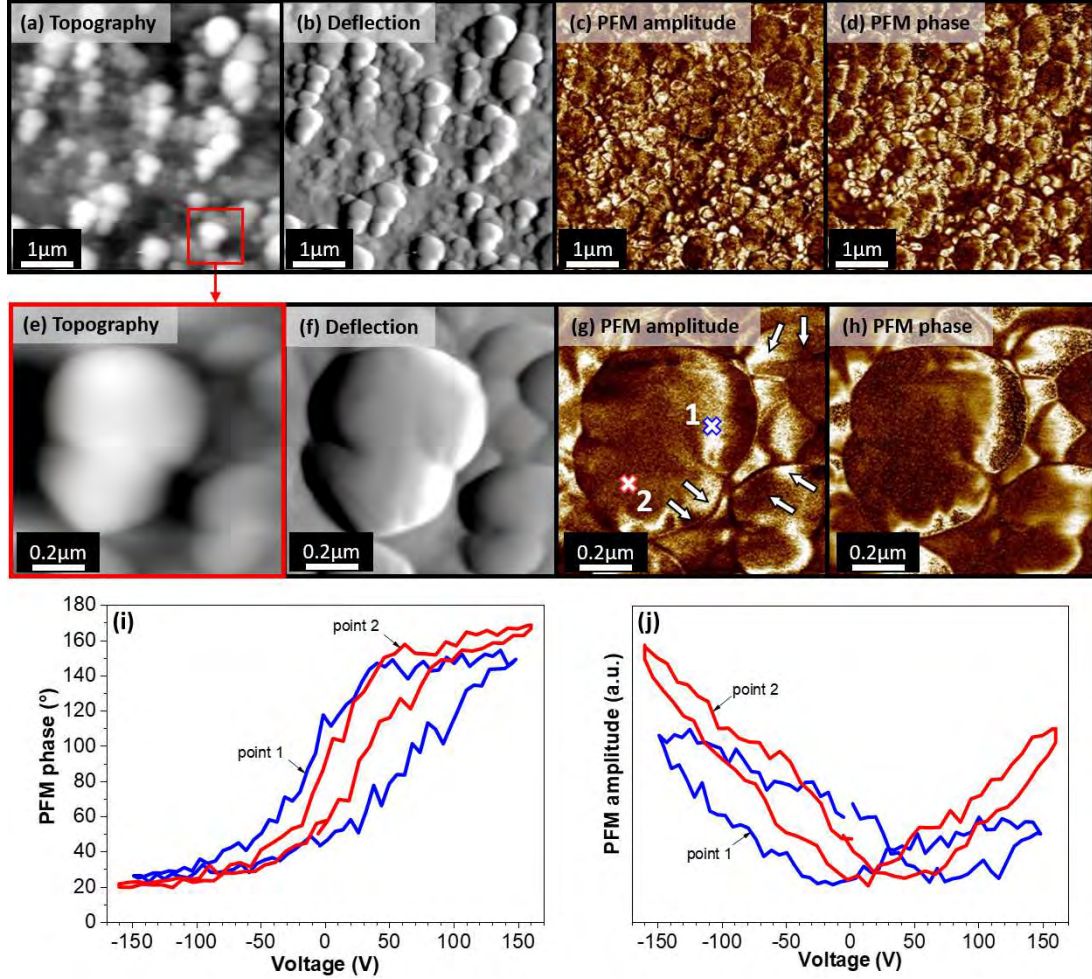


Figure 4.3: The topography (a, e) height, (b, f) deflection and out-of-plane PFM (c, g) amplitude, (d, h) phase images of B_NP@PDA nanoparticles. The PFM (i) phase and (j) amplitude local hysteresis loops measured in the two points 1 and 2 marked by crosses in panel (g). In both panels (i and j), a second cycle is shown.

Likewise, the local piezoelectric response and local domain switching properties of B_NP@PDA powder inserted in the PLA polymer matrix forming 20 vol% B_NP@PDA/PLA nanocomposite film were investigated by using the PFM (see Figs. 4.4a-g). The topography, out-of-plane amplitude and phase signals were analyzed (see Figs. 4.4a-d). By comparing the topography and amplitude PFM images, we can conclude that the enhancements in the PFM signal (bright regions) are observed at the positions of the B_NP@PDA powder is-

lands, indicating their piezoelectric activity. Additionally, the PFM switching spectroscopy experiment was performed on the B_NP@PDA powder island in two points (see Fig. 4.4e). The local PFM phase and amplitude hysteresis loops typical for piezoelectric/ferroelectric material are shown in Figs. 4.4f, g. Hence, the local piezoelectric response of 20 vol% B_NP@PDA/PLA nanocomposite film was evidenced.

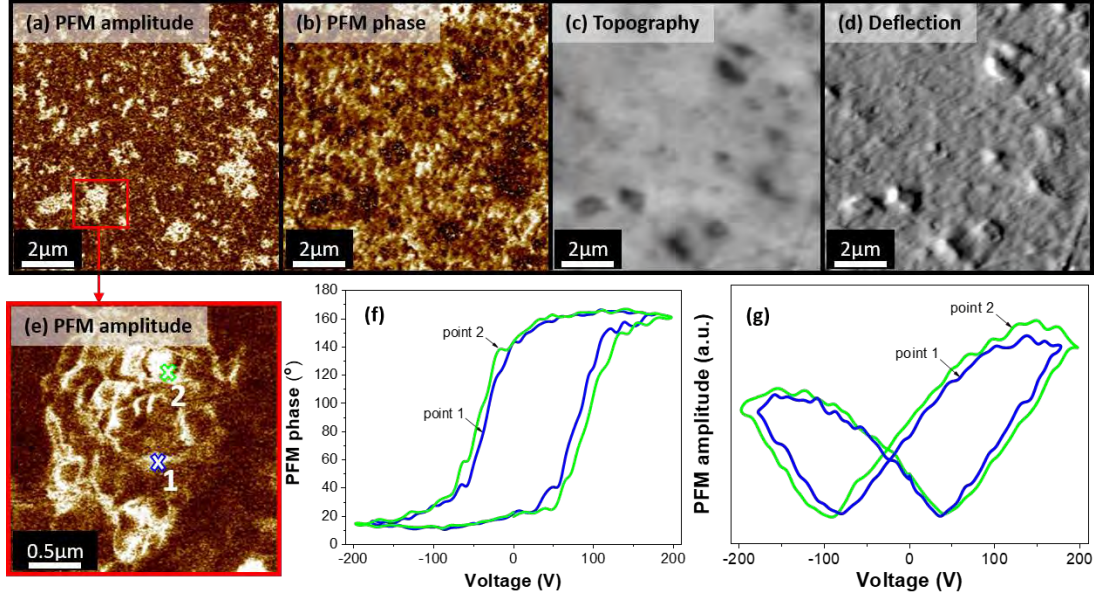


Figure 4.4: Out-of-plane PFM (a) amplitude, (b) phase images with the topography (c) height and (d) deflection of 20 vol% B_NP@PDA/PLA film. In the panel (a), the bright regions are the B_NP@PDA powder islands embedded in the darker PLA matrix. The large magnification of such an island is shown in panel (e). The panels (f) and (g) show phase and amplitude of local hysteresis loops, respectively, measured by PFM in the two points, marked by crosses 1 and 2 in the panel (e). In both panels (f and g), a second cycle is shown.

4.4 Mechanical energy harvesting

4.4.1 Input mechanical forces measurement

Generally, PNGs are used to harvest mechanical energy in a relatively low-frequency range (e.g., human activities, mechanical vibration, etc.). Here, the stress field (σ) plays a vital role in the generation of output voltage as the deformation of the crystal structure

depends on applied mechanical stress. In this study, two types of human impartations were investigated: the finger tapping and hand slapping under fixed frequency. The approximate contact force was evaluated experimentally by using a dual column mechanical testing system. The average contact forces (F) were estimated at 2.0 N and 27.9 N for the finger tapping and hand slapping, respectively, and the results are shown in Figs. 4.5a, b. The resulting input stress (σ) under finger tapping and hand slapping is estimated using the equation $\sigma = \frac{F}{area}$, and found to be 9.1 kPa (contact area $\approx 2.2 \text{ cm}^2$) and 18.5 kPa (contact area $\approx 15.1 \text{ cm}^2$), respectively. A demonstration for the contact force measurement under finger tapping is depicted in Fig. I.2 in Appendix I.

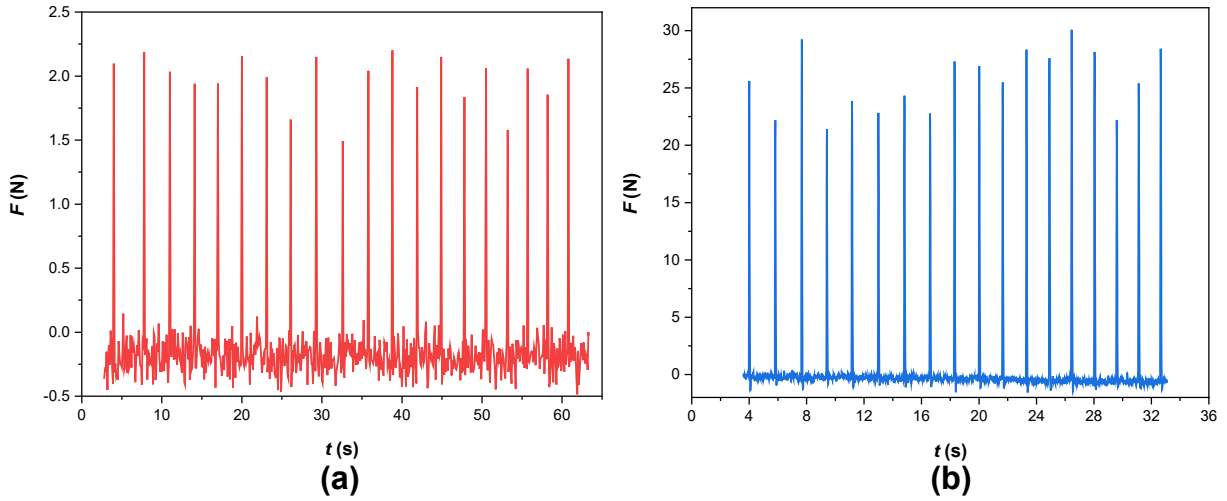


Figure 4.5: The measured contact force under (a) finger tapping and (b) hand slapping.

4.4.2 Output electrical properties

To have an insight into the mechanical energy harvesting performances of 20 vol% B_NP@PDA/PLA piezocomposite film from the energy available in the ambient environment (human body motions), a bio-flexible piezoelectric nanogenerator (BF-PNG) was designed as described in the fabrication section. In this regard, the open-circuit voltage (V_{oc}) and the corresponding short-circuit current (I_{sc}) of the BF-PNG were measured. Figs. 4.6a, b show the V_{oc} and the I_{sc} , respectively, of the BF-PNG subjected to a series of gentle finger tapping. By finger tapping, the V_{oc} and I_{sc} of the BF-PNG can reach values up to 14.40 V and 0.55 μA , respectively (Please see Fig. I.2 in Appendix I.). The slight variation

in the amplitude of each pulse could be attributed to the manual stress variation during the tapping sequence. It should be noted that these values are comparable to those found in PNGs containing other types of piezoelectric materials [119,314–316]. It is worth noting that contrary to polyvinylidene fluoride (PVDF) or polydimethylsiloxane (PDMS) based PNGs, no poling process is required before testing the PNG as the BF-PNG is a self-poled device. It benefits from the natural piezoelectricity developed in PLA after application of mechanical stress and the surface-charge induced polarization without applying any external electric field [112,317,318]. Hence, in BF-PNG, the traditional and necessary electrical poling process used in piezoelectric and ferroelectric materials-based energy harvesting devices is not required.

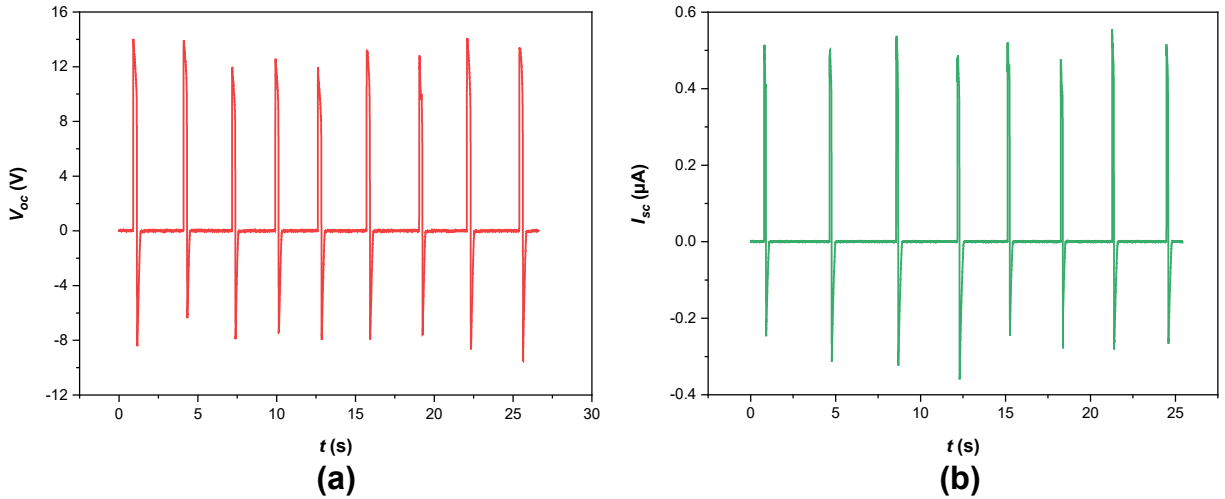


Figure 4.6: The generated (a) V_{oc} and (b) I_{sc} of the BF-PNG under finger tapping.

The BF-PNG working mechanism is as follows. The upper and lower surfaces of the BF-PNG are charged by the opposite charges, as shown in Fig. 4.7a. An external force applied to the BF-PNG surface deflects the dipoles in the B_NP@PDA and leads to a weakening of the internal electric depolarization field. Consequently, free BF-PNG surface absorbed charges move from the one electrode to the opposite electrode, during which a peak (positive signal in Fig. 4.7b) can be detected. When the stress is removed, the free charges flow in the opposite direction, leading to an inverse signal (negative signal in Fig. 4.7c).

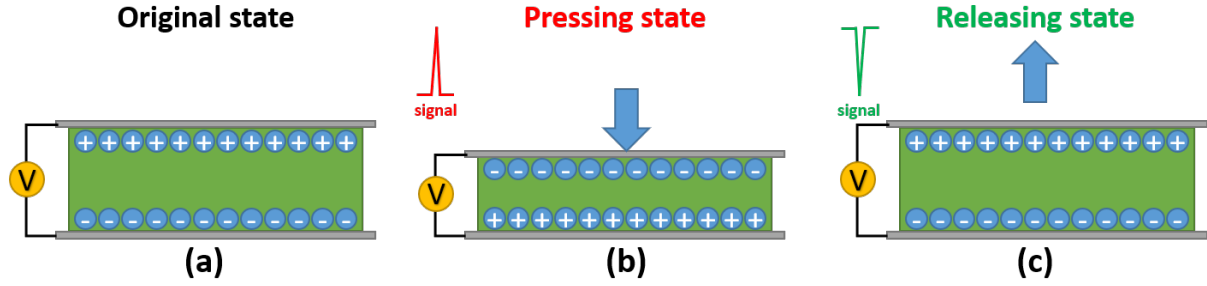


Figure 4.7: Schematic illustration of the BF-PNG in an (a) original state, (b) when the stress is applied and (c) stress is released.

4.4.3 Stability of the output voltage

The voltage-stability test of the fabricated BF-PNG was performed under gentle finger tapping at a driving frequency of 0.3 Hz for 115 s (Fig. 4.8a), and under 14000 tapping cycles by using a sewing machine at tapping frequency of 23 Hz for 625 s (Fig. 4.8b). The sewing machine was used as a constant and accurate stress source compared to finger tapping and hand slapping. Here, the sewing machine needle was substituted by a cylindrical plastic piece with a tapping area close to that of a human finger. In this case, the BF-PNG was exposed to the direct stress tapping indicating its high mechanical stability. It is worth noting that neither performance degradation nor mechanical damage after 14000 cycles at a frequency of 23 Hz was observed. The mechanical robustness and the excellent stability of the BF-PNG signal without a significant drop in V_{oc} prove its applicability as a capable energy harvesting device of irregular and regular excitations present in our living environment and as a powering device for small portable electronic applications and flexible high energy density capacitors. A demonstration for the output voltage stability under sewing machine is illustrated in Fig. I.3 in Appendix I. Various tests were devoted to verify the potential use of the BF-PNG for operating commercial electronic devices.

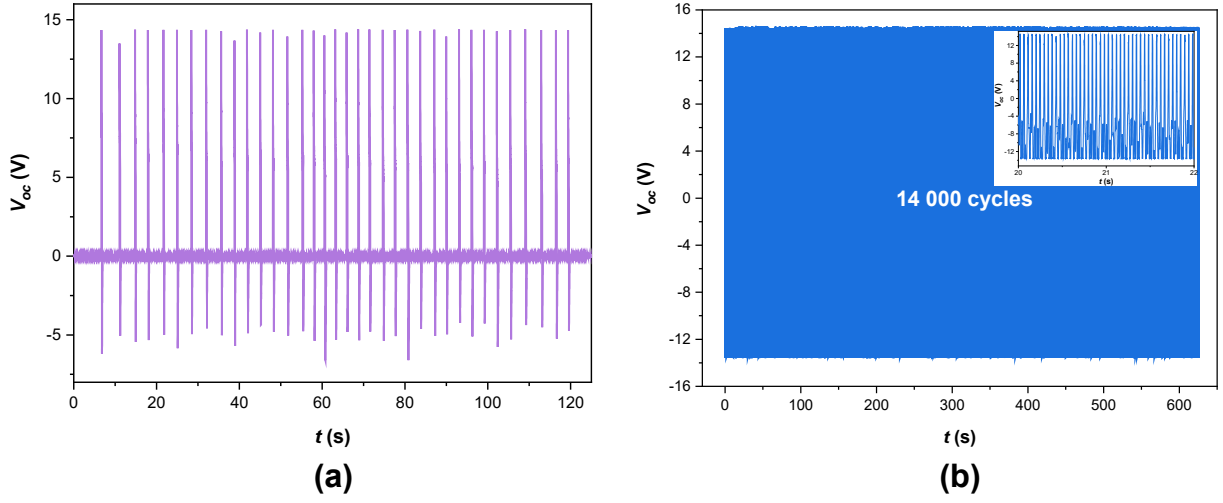


Figure 4.8: The output voltage stability tests of the BF-PNG device under (a) finger tapping and (b) under 14000 tapping cycles using a sewing machine (inset shows a magnified view of the voltage stability).

4.4.4 Charge-storage capability

The power and accumulation tests checked the feasibility of the BF-PNG device for energy applications. To evaluate the energy storage capability of the BF-PNG device, one cycle of charging and discharging was performed on a commercial capacitor ($1 \mu\text{F}$) under finger tapping and hand slapping with a frequency of 4 Hz as shown in Fig. 4.9a. Besides, real-time pictures of the accumulated voltage across the capacitor under finger tapping and hand slapping is presented in Figs. I.4 and I.4, respectively in Appendix I.. The inset of Fig. 4.9b illustrates the schematic circuit diagram for the following of the accumulated voltage during capacitor charging, which includes a full-wave bridge rectifier, capacitor, and BF-PNG. The AC output generated by the BF-PNG was first converted into DC power through the rectifier, then the generated dc power was used to charge the capacitor. The enlarged plot of accumulated voltage-time charging curves under (inset of Fig. 4.9a) shows stepwise charging of the capacitor under both human body motions. In the case of finger tapping and hand slapping, the BF-PNG could charge the capacitor up to 2.27 and 4.94 V, respectively, which correspond according to $W = \frac{1}{2}CV^2$, to a stored energy of 2.57 and 12.20 μJ , respectively (Fig. 4.9b). Here W , C , and V correspond to the stored electric density, capacitor capacity, and the generated voltage, respectively. The equivalent energy density using finger tapping and hand slapping reached 0.775 and 3.68

mJ/cm^3 , respectively. This latter is 1.7 times higher than that found by Shin et al. in BZT–BCT/PVDF composite film. A demonstration for the contact force measurement under finger tapping is depicted in Fig. I.1 in Appendix I. [319].

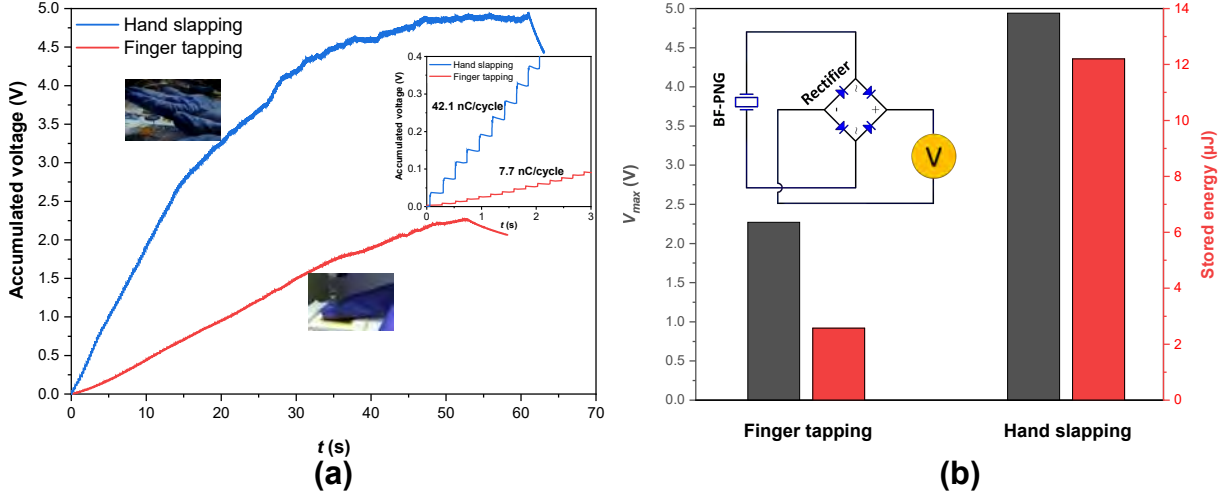


Figure 4.9: (a) The accumulated voltage across a single capacitor of $1 \mu\text{F}$ charged by the BF-PNG at 4 Hz of imparting frequency under finger tapping and hand slapping, (b) the maximal output voltage and the equivalent stored energy (inset schematic circuit diagram of capacitor charging).

To characterize the output performance of PNGs, the output charge density is an important parameter, though, most works about PNGs do not report the output charge density. The corresponding average charging rate is 7.7 and 42.2 nC per cycle, equivalent to 39.5 and $215.8 \mu\text{C}/\text{m}^2$, for finger tapping and hand slapping, respectively. The output charge density and the generated energy in the case of hand slapping are more significant due to the higher input stress ($\sigma = 18.5 \text{ kPa}$). The obtained value of the output charge density in the case of hand slapping is higher than that found by Gu et al. ($193 \mu\text{C}/\text{m}^2$) in PNG based on 2.5% mol Sm-doped PMN-0.31PT NWs, with a three-dimensional intercalation electrode (IENG) using foot stepping [320]. Moreover, our BF-PNG demonstrated higher output charge density compared to some reported triboelectric nanogenerators (TENGs) [321–323]. It is worthy to note that the unsmooth charging curves, especially, during hand slapping is originated from the inhomogeneous motions. To overcome this drawback, the sewing machine was used as a nearly constant stress source compared to a human finger. The charging capability of the BF-PNG under constant stress source was tested by storing a

rectified electrical output from the BF-PNG in two commercial capacitors of $1\ \mu\text{F}$ and $2.2\ \mu\text{F}$. Three charge-discharge cycles were performed to prove the performance reproducibility of the BF-PNG. The charging and discharging behavior of the capacitors $1\ \mu\text{F}$ (Fig. 4.10a) and $2.2\ \mu\text{F}$ (Fig. 4.10b) at a constant frequency of 23 Hz are shown in Fig. 4.10a and Fig. 4.10b, respectively. The insets of Figs. 4.10a, b display the enlarged views of the charging behaviors of the capacitors. The typical stepwise charging and the discharging response of the capacitor signify the high energy storage capacity. The BF-PNG could charge the $1\ \mu\text{F}$ -capacitor up to 6.36 V within 18.4 s only, which corresponds to stored energy of 20.22 μJ . The discharging process requires more time than the charging one. Hence, three discharging cycles were performed for discharging down to 3 V. This implies that the fabricated BF-PNG device could be used to recharge discharged batteries. Furthermore, it can also be seen that the fabricated device can charge the capacitor several times, which proves the reproducibility of the BF-PNG under cyclic charging and discharging conditions. The charging and discharging behavior of a commercial capacitor of $2.2\ \mu\text{F}$ are shown in Fig. 4.10b. After 52 s of impartation, the $2.2\ \mu\text{F}$ capacitor reached a voltage of 3.38 V, which corresponds to the stored energy of 12.56 μJ . The charging and discharging experiment were carried three times wherein each step the maximum voltage of the capacitor reached up to 3.52 V, which also proves the reproducibility of the BF-PNG. From these results, we can conclude that the capacitors of different capacitance can be charged up by the BF-PNG to a certain voltage under specific time and with high stored energy, which will be useful for further utilization.

4.4.5 Energy harvesting performances

For a practical use of the harvested energy, the device cannot operate in open circuit, but instead must be connected to a load [324]. To examine the energy performances of BF-PNG, the output voltage characteristic was measured at various external resistive loads, as shown in the schematic circuit diagram in the inset of Fig. 4.11. It is observed that the generated output voltage from the BF-PNG across a load resistor gradually increases with increasing resistance to reach a maximum then decreases (Fig. 4.11). The variation of

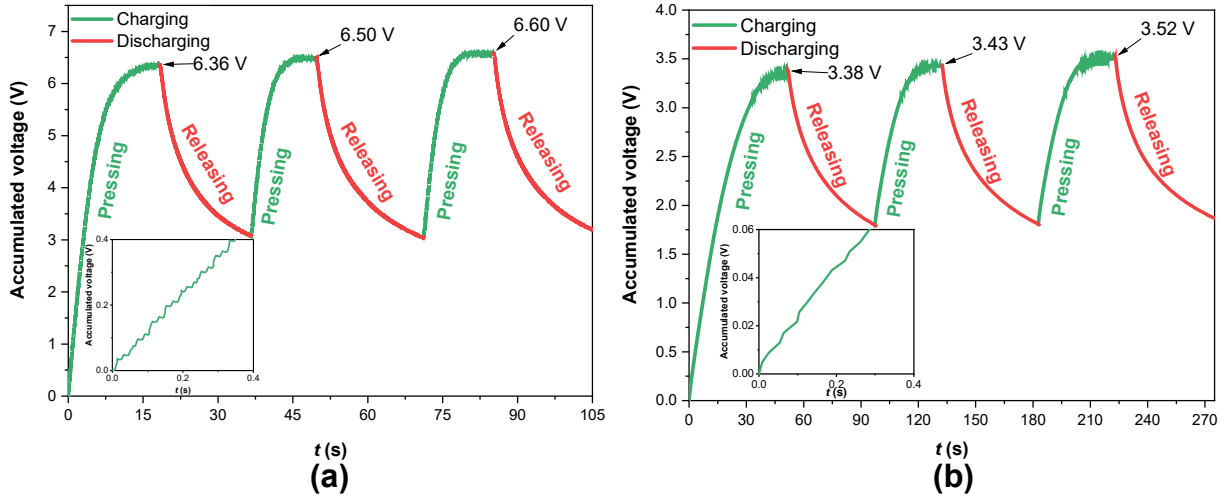


Figure 4.10: Repeated charging and discharging shown for the (a) $1 \mu\text{F}$ and (b) $2.2 \mu\text{F}$ commercial capacitors charged by the BF-PNG at 23 Hz of sewing machine tapping frequency (insets show the zoomed portion of a charging curve).

the power (P) related to the external resistance is also depicted in Fig. 4.11. P increases with the increasing resistance up to reach a maximum value and then decreases by further increasing the resistance. The maximal power $P_{max} = \frac{V^2}{R_L}$ of $25 \mu\text{W}$ was reached at the resistive load $R_L = 3.5 \text{ M}\Omega$. It occurs when the value of the resistive load is equal to the impedance of the BF-PNG piezoelectric capacitor. The obtained P_{max} is more than three-fold higher than that obtained, by Baek et al. in a piezoelectric nanogenerator based on encapsulated BCZT nanoparticles and Ag nanowires in the PDMS matrix at the resistive load $R_L = 100 \text{ M}\Omega$ [325]. Moreover, such low R_L is also enabling the BF-PNG as a high output power source, compared to previously reported PNGs in Table 1. This value is quite similar to that reported by Karan et al. [326]. The area power density $P_{max}^s = 12.82 \mu\text{W}/\text{cm}^2$ and volumetric power density $P_{max}^v = 7.54 \text{ mW}/\text{cm}^3$ were estimated by using the Eqs. 4.1 and 4.2,

$$P_{max}^s = \frac{V^2}{R_L \times \text{area}} \quad (4.1)$$

$$P_{max}^v = \frac{V^2}{R_L \times \text{volume}} \quad (4.2)$$

Here, the active volume of $1.5 \text{ cm} \times 1.3 \text{ cm} \times 17 \mu\text{m}$ of the BF-PNG was used.

Table 1 compares the energy harvesting performance of BF-PNG with other PNGs reported in the literature. The V_{oc} and I_{sc} of our BF-PNG are higher than that reported in

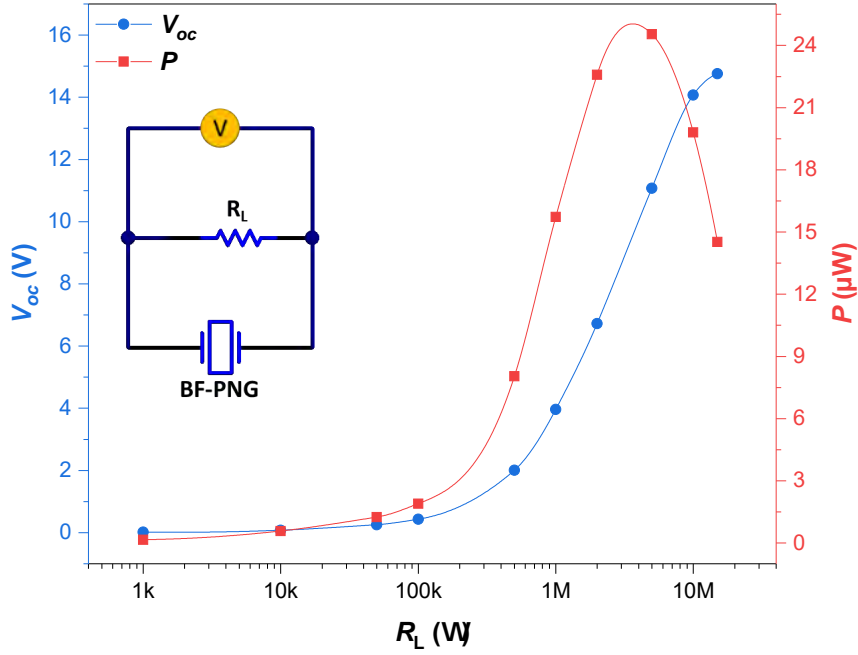


Figure 4.11: The output voltage and power density generated by the BF-PNG across various resistors (inset shows the schematic circuit diagram of the harvested output voltage).

[118, 316, 327–336] and lower than stated in refs [303, 319, 326, 335, 336]. The obtained power density in the BF-PNG is much higher than that reported in refs [303, 319, 326, 335, 336]. This is mainly due to the thinner nanocomposite film that was used to design our BF-PNG. As stated before, the biodegradable PLA leads to natural piezoelectricity that makes the BF-PNG a self-poled device. This eliminates the need for high electric fields, in contrast to the majority of PVDF or PDMS-based PNGs, which request a high electric field, high temperature and additional time during the poling process [303, 319, 331–334].

4.4.6 Feasibility demonstration

To support the analysis above and demonstrate the output performance of our BF-PNG to power commercial electronics, a visual and realistic application was devoted. The electrical energy harvested from the finger tapping of the BF-PNG was successfully used to drive commercial red LED (light-emitting diode) connected to a $1 \mu\text{F}$ capacitor (Fig. 4.12a). The schematic circuit diagram for the LED lighting is depicted in Fig. 4.12b. This capacitor could be charged up to 2.8 V in 115 s under successive finger tapping at a frequency of

Table 4.1: Comparison of the energy harvesting performances of BF-PNG with other PNGs reported in the literature.

Piezoelectric nanogenerator	Poling conditions	R_L ($M\Omega$)	V_{oc} (V)	I_{sc} (μA)	P_{max}^v ($\mu W/cm^3$)	Ref.
20 vol% B_NP@PDA/PLA (BF-PNG)	No poling	3.5	14.4	0.55	7540	This work
BZT-BCT/PVDF	35 kV/cm, 10 h, 130 °C	-	20.61	2.0	3450	[319]
Cu-BZT-BCT/PVDF	35 kV/cm, 10 h, 130 °C	-	18.8	1.84	4120	[319]
BCZT nanofibers/PVDFHFP composite	20 kV/cm, 2 h, 50 °C	5.5	10	0.75	2.91	[334]
BaTiO ₃ thin film	200 kV/cm, 15 h, 150 °C	-	1	0.026	7000	[327]
Oriented BaTiO ₃ film	30 kV/cm, RT	80	6.5	0.14	105	[328]
BCZT nanowires	15 kV/cm, 2 h, 90 °C	-	3.25	0.055	338	[329]
ZnO nanowires	Not supplied	-	2.03	0.107	11000	[330]
PZT thin film	100 kV/cm, 3 h, 120 °C	200	200	1.5	1750	[335]
PZT/PVDF-HFP	250 kV/cm, 1 h, 150 °C	-	65.0	1.0	81.25	[303]
PZT/PET	40 kV/cm, 15 min, 130 °C	100	6.0	0.045	200	[118]
KNNS-BNKZ nanofibers	50 kV/cm, 150 °C, RT	100	10	-	4508	[316]
KNbO ₃ nanowires/PDMS	50 kV/cm, 1 h, RT	10	10.5	1.3	42	[331]
BaTiO ₃ nanotubes/PDMS	80 kV/cm, 12 h, RT	-	5.5	0.35	64	[332]
KNbO ₃ nanorods/PDMS	150 kV/cm, 1 h, RT	-	3.2	0.0675	11.9	[333]
Chitin nanofiber/PDMS	Not supplied	-	22.0	0.12	97	[336]
Chitin nanofiber/PVDF/PDMS	Not supplied	-	49.0	1.9	6600	[336]
Eggshell membrane/PDMS	2 kV, 48 h	15	26.4	1.45	238.17	[326]

4 Hz, which corresponds to a stored energy of 3.92 μJ . A real-time picture for the LED lighting is depicted in Fig. I.6 in Appendix I.. Hence, the combination of BF-PNG and energy storage device could cover a potential solution to the frequent replacement of the discharged batteries. In addition, it can be of great potential for effective power generation and energy harvesting from human movements to power small portable electronics [310]. As reported by Hwang et al. in the case of healthy animals, the minimum external electric energy needed to trigger the action potential required to contract the heart artificially is 1.1 μJ [131]. Hence, the BF-PNG could be applicable for biomedical sensors and actuators such as pacemakers. Moreover, the choice of biodegradable polymer (PLA) [200, 337, 338] that is extensively used in medicine and lead-free biocompatible ceramic (BCZT) [194–196] are encouraging for such applications.

4.5 Conclusions

All-ecological piezoelectric nanogenerator was designed *via* core-shell structuration of near-spherical BCZT filler (B_NP) with PDA layer and a biodegradable PLA matrix. The piezoelectricity of B_NP@PDA nanoparticles before and after embedding in the

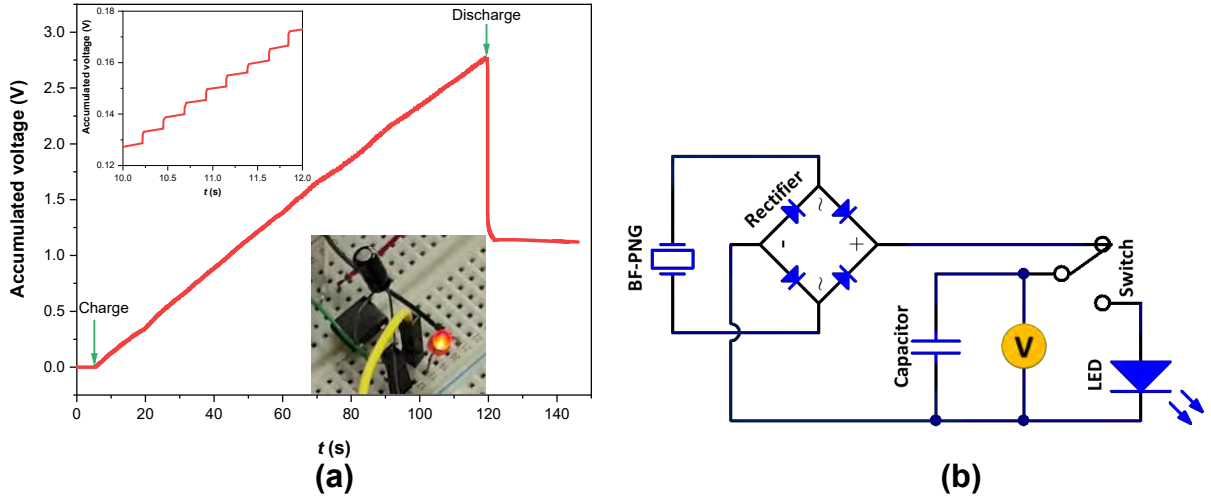


Figure 4.12: The output voltage charging curve of a $1 \mu\text{F}$ commercial capacitor by the BF-PNG under finger tapping at a frequency of 4 Hz. The upper inset shows an enlarged plot of voltage steps during capacitor charging. The lower inset depicts a digital photograph of a glowing red LED powered by the charged capacitor. (b) Schematic circuit diagram for the measurement of the accumulated voltage across the capacitor and for the LED lighting.

PLA matrix was checked *via* measurements of the piezoelectric hysteresis loops by PFM. The designed BF-PNG could generate open-circuit voltage and short-circuit current of 14.4 V and $0.55 \mu\text{A}$, respectively, under gentle finger tapping. Moreover, the BF-PNG demonstrated outstanding durability, high mechanical robustness and stable output voltage even after 14000 cycles of high-frequency impartations. The maximum power density achieved was around $7.54 \text{ mW}/\text{cm}^3$ at a low resistive load of $3.5 \text{ M}\Omega$. The feasibility of the BF-PNG was verified by triggering commercial electronics (charging capacitors and lighting an LED). The BF-PNG could drive a $1 \mu\text{F}$ capacitor to store energy of $3.92 \mu\text{J}$ within 115 s under gentle finger tapping. This research demonstrates that a lead-free piezoceramic in combination with a biodegradable piezopolymer can lead to a design of bio-flexible piezoelectric nanogenerators with outstanding performances and in particular useful in self-powered medical devices.

Conclusions and suggested directions for future work

Contents

I .	Conclusions	145
II .	Suggested directions for future work	146

I . Conclusions

Energy storage and harvesting technologies suffer from the moderate performances, low flexibility and the use of non-environmental compounds. This work focuses on designing multifunctional ceramic/polymer nanocomposites for these applications. The controlled syntheses of nanostructured BCZT ferroelectric materials with different sizes, size distributions and shapes were discussed. BCZT spherical nanoparticles were synthesized using two strategies: (i) surfactant-assisted solvothermal and (ii) low-temperature sol-gel-hydrothermal routes. The first one involves the use of surfactants to better control the grain size of BCZT powders, however, it requires a calcination step to obtain pure and crystalline BCZT powders. To overcome this problem, the second strategy was designed basing on sol-gel followed by a hydrothermal reaction, and for the first time, BCZT nanocrystalline powders were found at very-low temperature including room-temperature. Next, BCZT nanorods were designed by surfactant assisted solvothermal processing using higher surfactant (CTAB) concentration. Then, lead-free BCZT nanostructured multipods were elaborated using two-steps hydrothermal processing, the effect of A-site precursor's concentrations and the morphogenesis mechanism of BCZT multipods were investigated. Later, the dielectric and ferroelectric properties of BCZT sintered ceramics were examined for each powder (spherical nanoparticles, nanorods and anisotropic morphologies). The effects of grain size and grain shape of BCZT ceramics on the dielectric properties were discussed. We found that the BCZT ceramic with near-spherical particles issued from strategy N°2 and elaborated at 160 °C revealed enhanced dielectric and ferroelectric properties compared to the other BCZT ceramics.

Subsequently, BCZT near-spherical particles BCZT nanorods and HZTO nanowires were embedded in the biodegradable PLA polymer matrix. The effect of the ceramic shape, arrangement, dielectric constant and aspect ratio were explored using the effective dielectric constant of the nanocomposite models. The paradigm dielectric constant vs aspect ratio was disclosed through the embedding of BCZT nanorods with high dielectric constant and high aspect ratio, and HZTO nanowires with ultrahigh aspect ratio and low dielectric constant. It was found that for improving the dielectric properties of the

composite, it is not necessary to use ceramic fillers with high permittivity; indeed, a better control of their geometry could be appreciated. Afterwards, the energy storage performances (total energy density, recovered energy density and energy efficiency) of PLA-based nanocomposites were evaluated by $D - E$ hysteresis loops. High-energy storage density and recovered energy density of 3.63 and 1.80 J/cm³, respectively, were obtained in nanocomposites based on rod-like fillers.

The energy harvesting aspect was investigated using the concept of piezoelectric nanogenerators to convert the ambient mechanical energy to electrical energy. For this purpose, a bio-flexible piezoelectric nanogenerator (BF-PNG) based on 20 vol% BCZT@PDA/PLA nanocomposite film was designed. The BF-PNG could generate open-circuit voltage and short-circuit current of 14.4 V and 0.55 μ A, respectively, under gentle finger tapping. Besides, outstanding durability, high mechanical robustness and stable output voltage even after 14000 cycles of high-frequency impartations were demonstrated in the BF-PNG. Moreover, an outstanding maximum power density of 7.54 mW/cm³ at a low resistive load of 3.5 M Ω was obtained in the BF-PNG compared to other ceramic/polymer composites. The feasibility of the BF-PNG was tested by driving commercial electronics (charging capacitors and lighting an LED). More interestingly, the BF-PNG could drive a 1 μ F capacitor to store energy of 3.92 μ J within 115 s under gentle finger tapping, which make it applicable for biomedical sensors and actuators such as pacemakers. Accordingly, this work demonstrates that BCZT lead-free piezoceramic in combination with PLA biodegradable piezopolymer can lead to a design of bio-flexible nanocomposite with outstanding energy storage and energy harvesting performances for application in self-powered medical devices.

II . Suggested directions for future work

This research work mostly emphasizes on the experimental trials to seek the relationship between size, size distribution, shape, arrangement, aspect ratio, the dielectric and ferroelectric properties of the nanocomposites. There are numerous topics of future work which may extend to improve the performance of BCZT/PLA nanocomposites for embedded

CONCLUSIONS AND SUGGESTED DIRECTIONS FOR FUTURE WORK

capacitor and piezoelectric nanogenerator applications. The following points, which can be taken up as the future study:

1. Investigation of the direct and indirect piezoelectric effect of BCZT ceramics and the study of the temperature dependence of the piezoelectric properties.
2. Design of an elaboration procedure to obtain BCZT nanowires (BCZT_NW) with high aspect ratio, study of the dielectric and ferroelectric properties of sintered ceramic, fabricate BCZT_NW/PLA nanocomposite and investigate their dielectric and energy storage properties.
3. It was reported that the orientation of the ceramic filler inside the polymer matrix highly affect the energy storage performances. Hence, it will be appreciated to study the effects of B_NR and HZTO_NW orientations in PLA matrix on the energy storage performances.
4. For practical application of energy storage capacitors, the temperature stability of the recovered energy storage of PLA-based nanocomposites could be interesting to study, alongside with the power density of these nanocomposites.
5. It is interesting to test the biodegradability and biocompatibility of PLA-based nanocomposites for *in vivo* applications.
6. Study of the effect of the filler's aspect ratio on the output performances in the piezoelectric nanogenerators for energy harvesting applications.
7. Numerical modeling and optimizing the architecture of the piezoelectric nanogenerator for better mechanical energy conversion.
8. *in vitro* and *in vivo* energy generation and internal charging by the natural body activity and physiological environment for self-powered implantable devices.

Bibliography

- [1] L. B. Kong, H. Huang, and S. Li, “Fundamentals of Ferroelectric Materials,” in *Ferroelectric Materials for Energy Applications*, pp. 1–31, Weinheim, Germany: Wiley-VCH Verlag GmbH & Co. KGaA, sep 2018.
- [2] E. Schrödinger, “Studien über Kinetik der Dielektrika, den Schmelzpunkt, Pyro- und Piezoelektrizität,” *Sitzungsberichten der kaiserl. Akademie der Wissenschaften in Wien.*, vol. 121, pp. 1937–1972, 1912.
- [3] J. Valasek, “Piezo-electric and allied phenomena in Rochelle salt,” *Physical Review*, vol. 17, pp. 475–481, apr 1921.
- [4] J. Varghese, R. W. Whatmore, and J. D. Holmes, “Ferroelectric nanoparticles, wires and tubes: Synthesis, characterisation and applications,” *Journal of Materials Chemistry C*, vol. 1, no. 15, pp. 2618–2638, 2013.
- [5] H. Thurnaurer and J. Deaderick, “U.S. Patent No. 2,429,588,” 1947.
- [6] B. Wul and J. M. Goldman, “Ferroelectric switching in BaTiO₃ ceramics,” *CR Acad Sci URSS*, vol. 51, p. 21, 1946.
- [7] M. E. Lines and A. M. Glass, *Principles and Applications of Ferroelectrics and Related Materials*. Oxford University Press, feb 2010.
- [8] S. Xu, Y. Qin, C. Xu, Y. Wei, R. Yang, and Z. L. Wang, “Self-powered nanowire devices,” *Nature Nanotechnology*, vol. 5, pp. 366–373, may 2010.

- [9] S. B. Cho, M. Oledzka, and R. E. Riman, “Hydrothermal synthesis of acicular lead zirconate titanate (PZT),” *Journal of Crystal Growth*, vol. 226, no. 2-3, pp. 313–326, 2001.
- [10] G. Liu, S. Zhang, W. Jiang, and W. Cao, “Losses in ferroelectric materials,” 2015.
- [11] H. Feng, C. Zhao, P. Tan, R. Liu, X. Chen, and Z. Li, “Nanogenerator for Biomedical Applications,” *Advanced Healthcare Materials*, vol. 7, no. 10, pp. 1–18, 2018.
- [12] M. H. Seo, J. Y. Yoo, S. Y. Choi, J. S. Lee, K. W. Choi, C. K. Jeong, K. J. Lee, and J. B. Yoon, “Versatile Transfer of an Ultralong and Seamless Nanowire Array Crystallized at High Temperature for Use in High-Performance Flexible Devices,” *ACS Nano*, vol. 11, no. 2, pp. 1520–1529, 2017.
- [13] E. J. Curry, K. Ke, M. T. Chorsi, K. S. Wrobel, A. N. Miller, A. Patel, I. Kim, J. Feng, L. Yue, Q. Wu, C. L. Kuo, K. W. Lo, C. T. Laurencin, H. Ilies, P. K. Purohit, and T. D. Nguyen, “Biodegradable piezoelectric force sensor,” *Proceedings of the National Academy of Sciences of the United States of America*, vol. 115, pp. 909–914, jan 2018.
- [14] V. M. Goldschmidt and Others, “Skifter Norske Videnskaps-Akad. Oslo, I,” *Mat.-Naturv. Kl*, no. 8, 1926.
- [15] H. D. Megaw, “Temperature changes in the crystal structure of barium titanium oxide,” *Proceedings of the Royal Society of London. Series A. Mathematical and Physical Sciences*, vol. 189, pp. 261–283, apr 1947.
- [16] A. Devonshire, “XCVI. Theory of barium titanate,” *The London, Edinburgh, and Dublin Philosophical Magazine and Journal of Science*, vol. 40, pp. 1040–1063, oct 1949.
- [17] B. T. Matthias, “New Ferroelectric Crystals,” *Physical Review*, vol. 75, p. 1771, jun 1949.
- [18] A. F. Devonshire, “Theory of ferroelectrics,” *Advances in Physics*, vol. 3, pp. 85–130, apr 1954.

- [19] H. D. Megaw, “Origin of ferroelectricity in barium titanate and other perovskite-type crystals,” *Acta Crystallographica*, vol. 5, pp. 739–749, nov 1952.
- [20] A. von Hippel, R. G. Breckenridge, F. G. Chesley, and L. Tisza, “High dielectric constant ceramics,” *Industrial & Engineering Chemistry*, vol. 38, pp. 1097–1109, nov 1946.
- [21] E. Wainer, “High Titania Dielectrics,” *Transactions of The Electrochemical Society*, vol. 89, no. 1, p. 331, 1946.
- [22] A. Von Hippel, “Ferroelectricity, domain structure, and phase transitions of barium titanate,” *Reviews of Modern Physics*, vol. 22, pp. 221–237, jul 1950.
- [23] L. A. L. E. Landau and E. Lifshitz, “On the theory of the dispersion of magnetic permeability in ferromagnetic bodies,” *Phys. Z. Sowjetunion*, vol. 101, no. 8, 1935.
- [24] V. L. Ginzburg, “On the Dielectric Properties of Ferroelectric (Segnetoelectric Crystals and Barium Titanate),” *Journal of Experimental and Theoretical Physics*, vol. 1945, no. 15, 1945.
- [25] G. H. Haertling, “Ferroelectric ceramics: History and technology,” *Journal of the American Ceramic Society*, vol. 82, pp. 797–818, apr 1999.
- [26] H. Warlimont and W. Martienssen, *Springer Handbook of Materials Data*. Springer Handbooks, Cham: Springer International Publishing, 2018.
- [27] M. Rabuffi and G. Picci, “Status quo and future prospects for metallized polypropylene energy storage capacitors,” *IEEE Transactions on Plasma Science*, vol. 30, pp. 1939–1942, oct 2002.
- [28] A. Feteira, D. C. Sinclair, K. Z. Rajab, and M. T. Lanagan, “Crystal structure and microwave dielectric properties of alkaline-earth hafnates, AHfO_3 ($\text{A}=\text{Ba}$, Sr , Ca),” *Journal of the American Ceramic Society*, vol. 91, pp. 893–901, mar 2008.
- [29] H. Lee, J. R. Kim, M. J. Lanagan, S. Trolier-Mckinstry, and C. A. Randall, “High-energy density dielectrics and capacitors for elevated temperatures: $\text{Ca}(\text{Zr}, \text{Ti})\text{O}_3$,” *Journal of the American Ceramic Society*, vol. 96, pp. 1209–1213, apr 2013.

- [30] M. D. Nguyen, E. P. Houwman, M. Dekkers, C. T. Nguyen, H. N. Vu, and G. Rijnders, “Research Update: Enhanced energy storage density and energy efficiency of epitaxial $\text{Pb}_{0.9}\text{La}_{0.1}(\text{Zr}_{0.52}\text{Ti}_{0.48})\text{O}_3$ relaxor-ferroelectric thin-films deposited on silicon by pulsed laser deposition,” *APL Materials*, vol. 4, p. 080701, aug 2016.
- [31] Z. Hanani, D. Mezzane, M. Amjoud, A. G. G. Razumnaya, S. Fourcade, Y. Gagou, K. Hoummada, M. El Marssi, and M. Gouné, “Phase transitions, energy storage performances and electrocaloric effect of the lead-free $\text{Ba}_{0.85}\text{Ca}_{0.15}\text{Zr}_{0.10}\text{Ti}_{0.90}\text{O}_3$ ceramic relaxor,” *Journal of Materials Science: Materials in Electronics*, vol. 30, pp. 6430–6438, apr 2019.
- [32] S. Patel, A. Chauhan, and R. Vaish, “Enhancing electrical energy storage density in antiferroelectric ceramics using ferroelastic domain switching,” *Materials Research Express*, vol. 1, p. 045502, oct 2015.
- [33] Z. Sun, Z. Wang, Y. Tian, G. Wang, W. Wang, M. Yang, X. Wang, F. Zhang, and Y. Pu, “Progress, Outlook, and Challenges in Lead-Free Energy-Storage Ferroelectrics,” *Advanced Electronic Materials*, vol. 6, p. 1900698, jan 2020.
- [34] H. Palneedi, M. Peddigari, G. T. Hwang, D. Y. Jeong, and J. Ryu, “High-Performance Dielectric Ceramic Films for Energy Storage Capacitors: Progress and Outlook,” *Advanced Functional Materials*, vol. 28, p. 1803665, oct 2018.
- [35] C. B. Sawyer and C. H. Tower, “Rochelle salt as a dielectric,” *Physical Review*, vol. 35, pp. 269–273, feb 1930.
- [36] T. Yoshimura and N. Fujimura, “Polarization hysteresis loops of ferroelectric gate capacitors measured by Sawyer-Tower circuit,” *Japanese Journal of Applied Physics, Part 1: Regular Papers and Short Notes and Review Papers*, vol. 42, pp. 6011–6014, sep 2003.
- [37] X. Zhou, H. Qi, Z. Yan, G. Xue, H. Luo, and D. Zhang, “Large energy density with excellent stability in fine-grained $(\text{Bi}_{0.5}\text{Na}_{0.5})\text{TiO}_3$ -based lead-free ceramics,” *Journal of the European Ceramic Society*, vol. 39, pp. 4053–4059, nov 2019.

- [38] H. Yang, H. Qi, and R. Zuo, “Enhanced breakdown strength and energy storage density in a new BiFeO₃ -based ternary lead-free relaxor ferroelectric ceramic,” *Journal of the European Ceramic Society*, vol. 39, pp. 2673–2679, jul 2019.
- [39] F. Wang, W. Li, H. Jiang, M. Xue, J. Lu, and J. Yao, “Preparation and dielectric properties of Ba_{0.95}Ca_{0.05}Ti_{0.8}Zr_{0.2}O₃ -polyethersulfone composites,” *Journal of Applied Physics*, vol. 107, p. 043528, feb 2010.
- [40] K. Uchino and S. Nomura, “Critical exponents of the dielectric constants in diffused-phase-transition crystals,” *Ferroelectrics Letters Section*, vol. 44, pp. 55–61, apr 1982.
- [41] X. Nie, S. Yan, S. Guo, F. Cao, C. Yao, C. Mao, X. Dong, and G. Wang, “The influence of phase transition on electrocaloric effect in lead-free (Ba_{0.9}Ca_{0.1})(Ti_{1-x}Zr_x)O₃ ceramics,” *Journal of the American Ceramic Society*, vol. 100, pp. 5202–5210, nov 2017.
- [42] J. Wu, “BaTiO₃-Based Piezoelectric Materials,” in *Advances in Lead-Free Piezoelectric Materials*, pp. 247–299, Singapore: Springer Singapore, 2018.
- [43] G. A. Smolenskii and V. A. Isupov, “Segnetoelektricheskie svoistva tverdykh rastvorov stannata bariya v titanate bariya,” *ZHURNAL TEKHNIČESKOI FIZIKI*, vol. 24, no. 8, pp. 1375–1386, 1954.
- [44] V. V. Shvartsman and D. C. Lupascu, “Lead-free relaxor ferroelectrics,” *Journal of the American Ceramic Society*, vol. 95, pp. 1–26, jan 2012.
- [45] G. A. Smolenskii, “Physical phenomena in ferroelectrics with diffused phase transition,” *Journal of the physical society of Japan (Supplement)*, vol. 28, no. 1, pp. 26–37, 1970.
- [46] Y. Lin, D. Li, M. Zhang, S. Zhan, Y. Yang, H. Yang, and Q. Yuan, “Excellent Energy-Storage Properties Achieved in BaTiO₃-Based Lead-Free Relaxor Ferroelectric Ceramics via Domain Engineering on the Nanoscale,” *ACS Applied Materials and Interfaces*, vol. 11, pp. 36824–36830, oct 2019.

- [47] J. Shi, X. Liu, and W. Tian, “High energy-storage properties of $\text{Bi}_{0.5}\text{Na}_{0.5}\text{TiO}_3\text{-BaTiO}_3\text{-SrTi}_{0.875}\text{Nb}_{0.1}\text{O}_3$ lead-free relaxor ferroelectrics,” *Journal of Materials Science and Technology*, vol. 34, no. 12, pp. 2371–2374, 2018.
- [48] V. V. Shvartsman, J. Zhai, and W. Kleemann, “The dielectric relaxation in solid solutions $\text{BaTi}_{1-x}\text{Zr}_x\text{O}_3$,” *Ferroelectrics*, vol. 379, pp. 77–85, may 2009.
- [49] F. Li, S. Zhang, T. Yang, Z. Xu, N. Zhang, G. Liu, J. Wang, J. Wang, Z. Cheng, Z. G. Ye, J. Luo, T. R. Shrout, and L. Q. Chen, “The origin of ultrahigh piezoelectricity in relaxor-ferroelectric solid solution crystals,” *Nature Communications*, vol. 7, p. 13807, dec 2016.
- [50] W. Krauss, D. Schütz, F. A. Mautner, A. Feteira, and K. Reichmann, “Piezoelectric properties and phase transition temperatures of the solid solution of $(1-x)(\text{Bi}_{0.5}\text{Na}_{0.5})\text{TiO}_3\text{-xSrTiO}_3$,” *Journal of the European Ceramic Society*, vol. 30, pp. 1827–1832, jun 2010.
- [51] Y. Zhao, J. Xu, L. Yang, C. Zhou, X. Lu, C. Yuan, Q. Li, G. Chen, and H. Wang, “High energy storage property and breakdown strength of $\text{Bi}_{0.5}(\text{Na}_{0.82}\text{K}_{0.18})_{0.5}\text{TiO}_3$ ceramics modified by $(\text{Al}_{0.5}\text{Nb}_{0.5})_{4+}$ complex-ion,” *Journal of Alloys and Compounds*, vol. 666, pp. 209–216, may 2016.
- [52] J. Wu, A. Mahajan, L. Riekehr, H. Zhang, B. Yang, N. Meng, Z. Zhang, and H. Yan, “Perovskite $\text{Sr}_x(\text{Bi}_{1-x}\text{Na}_{0.97-x}\text{Li}_{0.03})_{0.5}\text{TiO}_3$ ceramics with polar nano regions for high power energy storage,” *Nano Energy*, vol. 50, pp. 723–732, aug 2018.
- [53] F. Yan, X. Zhou, X. He, H. Bai, S. Wu, B. Shen, and J. Zhai, “Superior energy storage properties and excellent stability achieved in environment-friendly ferroelectrics via composition design strategy,” *Nano Energy*, p. 105012, may 2020.
- [54] G. Burns and F. H. Dacol, “Glassy polarization behavior in ferroelectric compounds $\text{Pb}(\text{Mg}_{1/3}\text{Nb}_{2/3})\text{O}_3$ and $\text{Pb}(\text{Zn}_{1/3}\text{Nb}_{2/3})\text{O}_3$,” *Solid State Communications*, vol. 48, pp. 853–856, dec 1983.

- [55] J. Rödel, W. Jo, K. T. Seifert, E. M. Anton, T. Granzow, and D. Damjanovic, “Perspective on the development of lead-free piezoceramics,” *Journal of the American Ceramic Society*, vol. 92, pp. 1153–1177, jun 2009.
- [56] T. R. Shrout and S. J. Zhang, “Lead-free piezoelectric ceramics: Alternatives for PZT?,” *Journal of Electroceramics*, vol. 19, pp. 111–124, sep 2007.
- [57] P. K. Panda and B. Sahoo, “PZT to lead free piezo ceramics: A review,” *Ferroelectrics*, vol. 474, pp. 128–143, jan 2015.
- [58] J. Gao, D. Xue, W. Liu, C. Zhou, and X. Ren, “Recent Progress on BaTiO₃-Based Piezoelectric Ceramics for Actuator Applications,” *Actuators*, vol. 6, p. 24, jul 2017.
- [59] C. H. Hong, H. P. Kim, B. Y. Choi, H. S. Han, J. S. Son, C. W. Ahn, and W. Jo, “Lead-free piezoceramics – Where to move on?,” *Journal of Materiomics*, vol. 2, pp. 1–24, mar 2016.
- [60] J. Koruza, A. J. Bell, T. Frömling, K. G. Webber, K. Wang, and J. Rödel, “Requirements for the transfer of lead-free piezoceramics into application,” *Journal of Materiomics*, vol. 4, pp. 13–26, mar 2018.
- [61] H. Ogihara, C. A. Randall, and S. Trolier-Mckinstry, “High-energy density capacitors utilizing 0.7 baTiO₃-0.3 BiScO₃ ceramics,” *Journal of the American Ceramic Society*, vol. 92, pp. 1719–1724, aug 2009.
- [62] J. B. Lim, S. Zhang, N. Kim, and T. R. Shrout, “High-temperature dielectrics in the BiScO₃-BaTiO₃-(K₁/2Bi₁/2)TiO₃ ternary system,” *Journal of the American Ceramic Society*, vol. 92, pp. 679–682, mar 2009.
- [63] T. Wang, L. Jin, C. Li, Q. Hu, and X. Wei, “Relaxor ferroelectric BaTiO₃-Bi(Mg₂/3Nb₁/3)O₃ ceramics for energy storage application,” *Journal of the American Ceramic Society*, vol. 98, pp. 559–566, feb 2014.
- [64] V. S. Puli, D. K. Pradhan, I. Coondoo, N. Panwar, S. Adireddy, S. Luo, R. S. Katiyar, and D. B. Chrisey, “Observation of large enhancement in energy-storage properties

- of lead-free polycrystalline $0.5\text{BaZr}_{0.2}\text{Ti}_{0.8}\text{O}_3$ - $0.5\text{Ba}_{0.7}\text{Ca}_{0.3}\text{TiO}_3$ ferroelectric thin films,” *Journal of Physics D: Applied Physics*, vol. 52, p. 255304, apr 2019.
- [65] W. R. Buessem, L. E. Cross, and A. K. Goswami, “Phenomenological Theory of High Permittivity in Fine-Grained Barium Titanate,” *Journal of the American Ceramic Society*, vol. 49, pp. 33–36, jan 1966.
- [66] B. Liu, X. Wang, R. Zhang, and L. Li, “Grain size effect and microstructure influence on the energy storage properties of fine-grained BaTiO_3 -based ceramics,” *Journal of the American Ceramic Society*, vol. 100, pp. 3599–3607, aug 2017.
- [67] T. Tunkasiri and G. Rujijanagul, “Dielectric strength of fine grained barium titanate ceramics,” *Journal of Materials Science Letters*, vol. 15, no. 20, pp. 1767–1769, 1996.
- [68] L. Yang, X. Kong, F. Li, H. Hao, Z. Cheng, H. Liu, J. F. Li, and S. Zhang, “Perovskite lead-free dielectrics for energy storage applications,” *Progress in Materials Science*, vol. 102, pp. 72–108, 2019.
- [69] R. Dorey, “Microstructure–property relationships,” in *Ceramic Thick Films for MEMS and Microdevices*, pp. 85–112, Elsevier, 2012.
- [70] S. Gopi, A. Pius, and S. Thomas, “Synthesis, microstructure, and properties of high-strength porous ceramics,” in *Fundamental Biomaterials: Ceramics*, pp. 265–271, Elsevier, 2018.
- [71] Y. Wang and Z. Peng, “Performance of $\text{Ba}_{0.95}\text{Ca}_{0.05}\text{Zr}_{0.15}\text{Ti}_{0.85}\text{O}_3$ /PVDF composite flexible films,” *Journal of the Ceramic Society of Japan*, vol. 122, no. 1428, pp. 719–724, 2014.
- [72] G. Wang, X. Huang, and P. Jiang, “Tailoring Dielectric Properties and Energy Density of Ferroelectric Polymer Nanocomposites by High-k Nanowires,” *ACS Applied Materials and Interfaces*, vol. 7, no. 32, pp. 18017–18027, 2015.
- [73] Y. Huang and X. Huang, “Dielectric loss of polymer nanocomposites and how to keep the dielectric loss low,” in *Polymer Nanocomposites: Electrical and Thermal Properties*, pp. 29–50, Cham: Springer International Publishing, 2016.

- [74] K. Yang, X. Huang, M. Zhu, L. Xie, T. Tanaka, and P. Jiang, "Combining RAFT polymerization and thiol-ene click reaction for core-shell structured polymer@BaTiO₃ nanodielectrics with high dielectric constant, low dielectric loss, and high energy storage capability," *ACS Applied Materials and Interfaces*, vol. 6, no. 3, pp. 1812–1822, 2014.
- [75] Q. Li, L. Q. L. Chen, M. R. Gadinski, S. Zhang, G. Zhang, H. Li, A. Haque, L. Q. L. Chen, T. Jackson, and Q. Wang, "Flexible higherature dielectric materials from polymer nanocomposites," *Nature*, vol. 523, pp. 576–579, jul 2015.
- [76] S. Luo, J. Yu, S. Yu, R. Sun, L. Cao, W. H. Liao, and C. P. Wong, "Significantly Enhanced Electrostatic Energy Storage Performance of Flexible Polymer Composites by Introducing Highly Insulating-Ferroelectric Microhybrids as Fillers," *Advanced Energy Materials*, vol. 9, no. 5, 2019.
- [77] X. Huang, B. Sun, Y. Zhu, S. Li, and P. Jiang, "High-k polymer nanocomposites with 1D filler for dielectric and energy storage applications," *Progress in Materials Science*, vol. 100, pp. 187–225, feb 2019.
- [78] Y. Qiao, X. Yin, T. Zhu, H. Li, and C. Tang, "Dielectric polymers with novel chemistry, compositions and architectures," *Progress in Polymer Science*, vol. 80, pp. 153–162, may 2018.
- [79] S. Ray, *An introduction to high voltage engineering*. 2 ed., 2013.
- [80] X. Huang and P. Jiang, "Core-shell structured high-k polymer nanocomposites for energy storage and dielectric applications," *Advanced Materials*, vol. 27, pp. 546–554, jan 2015.
- [81] S. Liu, S. Xue, W. Zhang, J. Zhai, and G. Chen, "Significantly enhanced dielectric property in PVDF nanocomposites flexible films through a small loading of surface-hydroxylated Ba_{0.6} Sr_{0.4} TiO₃ nanotubes," *Journal of Materials Chemistry A*, vol. 2, pp. 18040–18046, sep 2014.

- [82] P. Kim, N. M. Doss, J. P. Tillotson, P. J. Hotchkiss, M. J. Pan, S. R. Marder, J. Li, J. P. Calame, and J. W. Perry, “High energy density nanocomposites based on surface-modified BaTiO₃ and a ferroelectric polymer,” *ACS Nano*, vol. 3, pp. 2581–2592, sep 2009.
- [83] T. Hanemann and D. V. Szabó, “Polymer-nanoparticle composites: From synthesis to modern applications,” *Materials*, vol. 3, pp. 3468–3517, may 2010.
- [84] M. Z. Rong, M. Q. Zhang, and W. H. Ruan, “Surface modification of nanoscale fillers for improving properties of polymer nanocomposites: A review,” *Materials Science and Technology*, vol. 22, pp. 787–796, jul 2006.
- [85] P. Kim, S. C. Jones, P. J. Hotchkiss, J. N. Haddock, B. Kippelen, S. R. Marder, and J. W. Perry, “Phosphonic acid-modified barium titanate polymer nanocomposites with high permittivity and dielectric strength,” *Advanced Materials*, vol. 19, pp. 1001–1005, apr 2007.
- [86] S. J. Chang, W. S. Liao, C. J. Ciou, J. T. Lee, and C. C. Li, “An efficient approach to derive hydroxyl groups on the surface of barium titanate nanoparticles to improve its chemical modification ability,” *Journal of Colloid and Interface Science*, vol. 329, pp. 300–305, jan 2009.
- [87] M. N. Almadhoun, U. S. Bhansali, and H. N. Alshareef, “Nanocomposites of ferroelectric polymers with surface-hydroxylated BaTiO₃ nanoparticles for energy storage applications,” *Journal of Materials Chemistry*, vol. 22, no. 22, p. 11196, 2012.
- [88] S. Liu, S. Xiu, B. Shen, J. Zhai, and L. B. Kong, “Dielectric properties and energy storage densities of poly(vinylidene fluoride) nanocomposite with surface hydroxylated cube shaped Ba_{0.6}Sr_{0.4}TiO₃ nanoparticles,” *Polymers*, vol. 8, p. 45, feb 2016.
- [89] T. Zhou, J. W. Zha, R. Y. Cui, B. H. Fan, J. K. Yuan, and Z. M. Dang, “Improving dielectric properties of BaTiO₃/ferroelectric polymer composites by employing surface hydroxylated BaTiO₃ nanoparticles,” *ACS Applied Materials and Interfaces*, vol. 3, pp. 2184–2188, jul 2011.

- [90] L. Shaohui, Z. Jiwei, W. Jinwen, X. Shuangxi, and Z. Wenqin, “Enhanced energy storage density in poly(vinylidene fluoride) nanocomposites by a small loading of surface-hydroxylated Ba_{0.6}Sr_{0.4}TiO₃ nanofibers,” *ACS Applied Materials and Interfaces*, vol. 6, pp. 1533–1540, feb 2014.
- [91] Y. Fan, G. Wang, X. Huang, J. Bu, X. Sun, and P. Jiang, “Molecular structures of (3-aminopropyl)trialkoxysilane on hydroxylated barium titanate nanoparticle surfaces induced by different solvents and their effect on electrical properties of barium titanate based polymer nanocomposites,” *Applied Surface Science*, vol. 364, pp. 798–807, feb 2016.
- [92] H. Luo, C. Ma, X. Zhou, S. Chen, and D. Zhang, “Interfacial Design in Dielectric Nanocomposite Using Liquid-Crystalline Polymers,” *Macromolecules*, vol. 50, pp. 5132–5137, jul 2017.
- [93] K. Yu, Y. Niu, F. Xiang, Y. Zhou, Y. Bai, and H. Wang, “Enhanced electric breakdown strength and high energy density of barium titanate filled polymer nanocomposites,” *Journal of Applied Physics*, vol. 114, p. 174107, nov 2013.
- [94] K. Yu, H. Wang, Y. Zhou, Y. Bai, and Y. Niu, “Enhanced dielectric properties of BaTiO₃/poly(vinylidene fluoride) nanocomposites for energy storage applications,” *Journal of Applied Physics*, vol. 113, p. 034105, jan 2013.
- [95] B. Xie, Y. Zhu, M. A. Marwat, S. Zhang, L. Zhang, and H. Zhang, “Tailoring the energy storage performance of polymer nanocomposites with aspect ratio optimized 1D nanofillers,” *Journal of Materials Chemistry A*, vol. 6, no. 41, pp. 20356–20364, 2018.
- [96] Z. H. Shen, J. J. Wang, Y. Lin, C. W. Nan, L. Q. Chen, and Y. Shen, “High-Throughput Phase-Field Design of High-Energy-Density Polymer Nanocomposites,” *Advanced Materials*, vol. 30, p. 1704380, jan 2018.
- [97] X. Zhang, J. Jiang, Z. Shen, Z. Dan, M. Li, Y. Lin, C. W. Nan, L. Chen, and Y. Shen, “Polymer Nanocomposites with Ultrahigh Energy Density and High Dis-

- charge Efficiency by Modulating their Nanostructures in Three Dimensions,” *Advanced Materials*, vol. 30, no. 16, 2018.
- [98] H. Luo, X. Zhou, C. Ellingford, Y. Zhang, S. Chen, K. Zhou, D. Zhang, C. R. Bowen, and C. Wan, “Interface design for high energy density polymer nanocomposites,” 2019.
- [99] Z. M. Dang, J. K. Yuan, S. H. Yao, and R. J. Liao, “Flexible nanodielectric materials with high permittivity for power energy storage,” 2013.
- [100] M. Arbatti, X. Shan, and Z. Cheng, “Ceramic-polymer composites with high dielectric constant,” *Advanced Materials*, vol. 19, pp. 1369–1372, may 2007.
- [101] A. Srivastava, K. K. Jana, P. Maiti, D. Kumar, and O. Parkash, “Investigations on Structural, Mechanical, and Dielectric Properties of PVDF/Ceramic Composites,” *Journal of Engineering (United Kingdom)*, vol. 2015, pp. 1–9, 2015.
- [102] B. Xie, Q. Zhang, H. Zhang, G. Zhang, S. Qiu, and S. Jiang, “Largely enhanced ferroelectric and energy storage performances of P(VDF-CTFE) nanocomposites at a lower electric field using BaTiO₃ nanowires by stirring hydrothermal method,” *Ceramics International*, vol. 42, pp. 19012–19018, dec 2016.
- [103] D. Zhang, X. Zhou, J. Roscow, K. Zhou, L. Wang, H. Luo, and C. R. Bowen, “Significantly Enhanced Energy Storage Density by Modulating the Aspect Ratio of BaTiO₃ Nanofibers,” *Scientific Reports*, vol. 7, p. 45179, may 2017.
- [104] Q. Chi, G. Liu, C. Zhang, Y. Cui, X. Wang, and Q. Lei, “Microstructure and dielectric properties of BZT-BCT/PVDF nanocomposites,” *Results in Physics*, vol. 8, pp. 391–396, mar 2018.
- [105] P. Muralt, “Stress Coupled Phenomena: Piezoelectric Effect,” in *Encyclopedia of Materials: Science and Technology*, pp. 8894–8897, Elsevier, jan 2001.
- [106] D. Hu, M. Yao, Y. Fan, C. Ma, M. Fan, and M. Liu, “Strategies to achieve high performance piezoelectric nanogenerators,” *Nano Energy*, vol. 55, pp. 288–304, jan 2019.

- [107] Z. L. Wang and J. Song, “Piezoelectric nanogenerators based on zinc oxide nanowire arrays,” *Science*, vol. 312, pp. 242–246, apr 2006.
- [108] X. Wang, J. Song, J. Liu, and L. W. Zhong, “Direct-current nanogenerator driven by ultrasonic waves,” *Science*, vol. 316, pp. 102–105, apr 2007.
- [109] G. Zhu, A. C. Wang, Y. Liu, Y. Zhou, and Z. L. Wang, “Functional electrical stimulation by nanogenerator with 58 V output voltage,” *Nano Letters*, vol. 12, no. 6, pp. 3086–3090, 2012.
- [110] S. Xu, Y. Wei, J. Liu, R. Yang, and Z. L. Wang, “Integrated multilayer nanogenerator fabricated using paired nanotip-to-nanowire brushes,” *Nano Letters*, vol. 8, pp. 4027–4032, nov 2008.
- [111] K.-I. Park, M. Lee, Y. Liu, S. Moon, G.-T. Hwang, G. Zhu, J. E. Kim, S. O. Kim, D. K. Kim, Z. L. Wang, and K. J. Lee, “Nanocomposite Generators: Flexible Nanocomposite Generator Made of BaTiO₃ Nanoparticles and Graphitic Carbons,” *Advanced Materials*, vol. 24, no. 22, pp. 2937–2937, 2012.
- [112] S. Mishra, L. Unnikrishnan, S. K. Nayak, and S. Mohanty, “Advances in Piezoelectric Polymer Composites for Energy Harvesting Applications: A Systematic Review,” *Macromolecular Materials and Engineering*, vol. 304, p. 1800463, jan 2019.
- [113] Z. L. Wang, T. Jiang, and L. Xu, “Toward the blue energy dream by triboelectric nanogenerator networks,” *Nano Energy*, vol. 39, pp. 9–23, sep 2017.
- [114] Z. L. Wang, “On Maxwell’s displacement current for energy and sensors: the origin of nanogenerators,” *Materials Today*, vol. 20, pp. 74–82, mar 2017.
- [115] B. Kumar and S. W. Kim, “Recent advances in power generation through piezoelectric nanogenerators,” *Journal of Materials Chemistry*, vol. 21, no. 47, pp. 18946–18958, 2011.
- [116] L. F. Chen, Y. P. Hong, X. J. Chen, Q. L. Wu, Q. J. Huang, and X. T. Luo, “Preparation and properties of polymer matrix piezoelectric composites containing

- aligned BaTiO₃ whiskers,” *Journal of Materials Science*, vol. 39, no. 9, pp. 2997–3001, 2004.
- [117] J. Kwon, W. Seung, B. K. Sharma, S. W. Kim, and J. H. Ahn, “A high performance PZT ribbon-based nanogenerator using graphene transparent electrodes,” *Energy and Environmental Science*, vol. 5, no. 10, pp. 8970–8975, 2012.
- [118] W. Wu, S. Bai, M. Yuan, Y. Qin, Z. L. Wang, and T. Jing, “Lead zirconate titanate nanowire textile nanogenerator for wearable energy-harvesting and self-powered devices,” *ACS Nano*, vol. 6, pp. 6231–6235, jul 2012.
- [119] X. Ni, F. Wang, A. Lin, Q. Xu, Z. Yang, and Y. Qin, “Flexible nanogenerator based on single BaTiO₃ nanowire,” *Science of Advanced Materials*, vol. 5, pp. 1781–1787, nov 2013.
- [120] C. Baek, J. H. Yun, H. S. Wang, J. E. Wang, H. Park, K. I. Park, and D. K. Kim, “Enhanced output performance of a lead-free nanocomposite generator using BaTiO₃ nanoparticles and nanowires filler,” *Applied Surface Science*, vol. 429, pp. 164–170, 2018.
- [121] L.-Q. Cheng and J.-F. Li, “A review on one dimensional perovskite nanocrystals for piezoelectric applications,” *Journal of Materiomics*, vol. 2, no. 1, pp. 25–36, 2016.
- [122] J. Shi, R. Zhu, X. Liu, B. Fang, N. Yuan, J. Ding, and H. Luo, “Large electrocaloric effect in lead-free(Ba_{0.85}Ca_{0.15})(Zr_{0.1}Ti_{0.9})O₃ ceramics prepared via citrate route,” *Materials*, vol. 10, p. 1093, sep 2017.
- [123] W. Li, Z. Xu, R. Chu, P. Fu, and P. An, “Effect of Ho doping on piezoelectric properties of BCZT ceramics,” *Ceramics International*, vol. 38, pp. 4353–4355, jul 2012.
- [124] M. A. Parvez Mahmud, N. Huda, S. H. Farjana, M. Asadnia, and C. Lang, “Recent Advances in Nanogenerator-Driven Self-Powered Implantable Biomedical Devices,” *Advanced Energy Materials*, vol. 8, no. 2, pp. 1–25, 2018.

- [125] Y. Zhang, M. Wu, Q. Zhu, F. Wang, H. Su, H. Li, C. Diao, H. Zheng, Y. Wu, and Z. L. Wang, "Performance Enhancement of Flexible Piezoelectric Nanogenerator via Doping and Rational 3D Structure Design For Self-Powered Mechanosensational System," *Advanced Functional Materials*, vol. 29, p. 1904259, oct 2019.
- [126] Z. Zhou, Z. Zhang, Q. Zhang, H. Yang, Y. Zhu, Y. Wang, and L. Chen, "Controllable Core-Shell BaTiO₃@Carbon Nanoparticle-Enabled P(VDF-TrFE) Composites: A Cost-Effective Approach to High-Performance Piezoelectric Nanogenerators," *ACS Applied Materials and Interfaces*, vol. 12, pp. 1567–1576, jan 2020.
- [127] N. R. Alluri, A. Chandrasekhar, V. Vivekananthan, Y. Purusothaman, S. Selvarajan, J. H. Jeong, and S. J. Kim, "Scavenging Biomechanical Energy Using High-Performance, Flexible BaTiO₃ Nanocube/PDMS Composite Films," *ACS Sustainable Chemistry and Engineering*, vol. 5, pp. 4730–4738, jun 2017.
- [128] J. Lim, H. Jung, C. Baek, G. T. Hwang, J. Ryu, D. Yoon, J. Yoo, K. I. Park, and J. H. Kim, "All-inkjet-printed flexible piezoelectric generator made of solvent evaporation assisted BaTiO₃ hybrid material," *Nano Energy*, vol. 41, pp. 337–343, 2017.
- [129] Y. Hu, C. Xu, Y. Zhang, L. Lin, R. L. Snyder, and Z. L. Wang, "A nanogenerator for energy harvesting from a rotating tire and its application as a self-powered pressure/speed sensor," *Advanced Materials*, vol. 23, no. 35, pp. 4068–4071, 2011.
- [130] M. Zhang, T. Gao, J. Wang, J. Liao, Y. Qiu, Q. Yang, H. Xue, Z. Shi, Y. Zhao, Z. Xiong, and L. Chen, "A hybrid fibers based wearable fabric piezoelectric nanogenerator for energy harvesting application," *Nano Energy*, vol. 13, pp. 298–305, 2015.
- [131] G. T. Hwang, H. Park, J. H. Lee, S. Oh, K. I. Park, M. Byun, H. Park, G. Ahn, C. K. Jeong, K. No, H. Kwon, S. G. Lee, B. Joung, and K. J. Lee, "Self-powered cardiac pacemaker enabled by flexible single crystalline PMN-PT piezoelectric energy harvester," *Advanced Materials*, vol. 26, pp. 4880–4887, jul 2014.

- [132] F. W. Horlbeck, F. Mellert, J. Kreuz, G. Nickenig, and J. O. Schwab, “Real-world data on the lifespan of implantable cardioverter-defibrillators depending on manufacturers and the amount of ventricular pacing,” *Journal of Cardiovascular Electrophysiology*, vol. 23, pp. 1336–1342, dec 2012.
- [133] Z. Li, G. Zhu, R. Yang, A. C. Wang, and Z. L. Wang, “Muscle-driven in vivo nanogenerator,” *Advanced Materials*, vol. 22, pp. 2534–2537, may 2010.
- [134] S. Priya and S. Nahm, *Lead-free piezoelectrics*, vol. 9781441995. New York, NY: Springer New York, 2013.
- [135] D. S. Keeble, F. Benabdallah, P. A. Thomas, M. Maglione, and J. Kreisel, “Revised structural phase diagram of $(\text{Ba}_{0.7}\text{Ca}_{0.3}\text{TiO}_3)$ - $(\text{BaZr}_{0.2}\text{Ti}_{0.8}\text{O}_3)$,” *Applied Physics Letters*, vol. 102, no. 9, p. 092903, 2013.
- [136] P. Bharathi and K. B. Varma, “Grain and the concomitant ferroelectric domain size dependent physical properties of $\text{Ba}_{0.85}\text{Ca}_{0.15}\text{Zr}_{0.1}\text{Ti}_{0.9}\text{O}_3$ ceramics fabricated using powders derived from oxalate precursor route,” *Journal of Applied Physics*, vol. 116, p. 164107, oct 2014.
- [137] M. Zakhosheva, L. A. Schmitt, M. Acosta, H. Guo, W. Jo, R. Schierholz, H. J. Kleebe, and X. Tan, “Wide compositional range in situ electric field investigations on lead-free $\text{Ba}(\text{Zr}_{0.2}\text{Ti}_{0.8})\text{O}_{3-x}(\text{Ba}_{0.7}\text{Ca}_{0.3})\text{TiO}_3$ piezoceramics,” *Physical Review Applied*, vol. 3, p. 064018, jun 2015.
- [138] J. P. Praveen, T. Karthik, A. R. James, E. Chandrakala, S. Asthana, and D. Das, “Effect of poling process on piezoelectric properties of sol-gel derived BZT-BCT ceramics,” *Journal of the European Ceramic Society*, vol. 35, no. 6, pp. 1785–1798, 2015.
- [139] V. S. Puli, D. K. Pradhan, D. B. Chrissey, M. Tomozawa, G. L. Sharma, J. F. Scott, and R. S. Katiyar, “Structure, dielectric, ferroelectric, and energy density properties of $(1-x)\text{BZT}-x\text{BCT}$ ceramic capacitors for energy storage applications,” *Journal of Materials Science*, vol. 48, pp. 2151–2157, mar 2013.

- [140] B. Asbani, J. L. Dellis, A. Lahmar, M. Courty, M. Amjoud, Y. Gagou, K. Djellab, D. Mezzane, Z. Kutnjak, and M. El Marssi, “Lead-free $\text{Ba}_{0.8}\text{Ca}_{0.2}(\text{Zr}_x\text{Ti}_{1-x})\text{O}_3$ ceramics with large electrocaloric effect,” *Applied Physics Letters*, vol. 106, p. 42902, jan 2015.
- [141] I. Coondoo, N. Panwar, H. Amorín, M. Alguero, and A. L. Kholkin, “Synthesis and characterization of lead-free $0.5\text{Ba}(\text{Zr}_{0.2}\text{Ti}_{0.8})\text{O}_3$ - $0.5(\text{Ba}_{0.7}\text{Ca}_{0.3})\text{TiO}_3$ ceramic,” *Journal of Applied Physics*, vol. 113, no. 21, p. 214107, 2013.
- [142] J. Gao, X. Hu, Y. Wang, Y. Liu, L. Zhang, X. Ke, L. Zhong, H. Zhao, and X. Ren, “Understanding the mechanism of large dielectric response in Pb-free $(1-x)\text{Ba}(\text{Zr}_{0.2}\text{Ti}_{0.8})\text{O}_3$ - $x(\text{Ba}_{0.7}\text{Ca}_{0.3})\text{TiO}_3$ ferroelectric ceramics,” *Acta Materialia*, vol. 125, pp. 177–186, 2017.
- [143] S. Patel, P. Sharma, and R. Vaish, “Enhanced electrocaloric effect in $\text{Ba}_{0.85}\text{Ca}_{0.15}\text{Zr}_{0.1}\text{Ti}_{0.9-x}\text{Sn}_x\text{O}_3$ ferroelectric ceramics,” *Phase Transitions*, vol. 89, pp. 1062–1073, mar 2016.
- [144] T. Mitsui and W. B. Westphal, “Dielectric and X-ray studies of $\text{Ca}_x\text{Ba}_{1-x}\text{TiO}_3$ and $\text{Ca}_x\text{Sr}_{1-x}\text{TiO}_3$,” *Physical Review*, vol. 124, pp. 1354–1359, dec 1961.
- [145] N. Pisitpipathsin, P. Kantha, K. Pengpat, and G. Rujijanagul, “Influence of Ca substitution on microstructure and electrical properties of $\text{Ba}(\text{Zr},\text{Ti})\text{O}_3$ ceramics,” in *Ceramics International*, vol. 39, pp. S35–S39, Elsevier, may 2013.
- [146] R. C. Pullar, Y. Zhang, L. Chen, S. Yang, J. R. G. Evans, A. N. Salak, D. A. Kiselev, A. L. Kholkin, V. M. Ferreira, and N. M. Alford, “Dielectric measurements on a novel $\text{Ba}_{1-x}\text{Ca}_x\text{TiO}_3$ (BCT) bulk ceramic combinatorial library,” *Journal of Electroceramics*, vol. 22, pp. 245–251, feb 2009.
- [147] I. Szafraniak-Wiza, L. Kozielski, and T. Sebastian, “Preparation and properties of $\text{Ba}_{1-x}\text{Ca}_x\text{TiO}_3$ nanopowders obtained by mechanochemical synthesis,” *Phase Transitions*, vol. 89, pp. 803–807, aug 2016.

-
- [148] A. Purwanto, D. Hidayat, Y. Terashi, and K. Okuyama, "Synthesis of monophasic $\text{Ca}_x\text{Ba}_{(1-x)}\text{TiO}_3$ nanoparticles with high Ca content ($x > 23\%$) and their photoluminescence properties," *Chemistry of Materials*, vol. 20, pp. 7440–7446, dec 2008.
- [149] W. Li, Z. Xu, R. Chu, P. Fu, and G. Zang, "High piezoelectric d_{33} coefficient in $(\text{Ba}_{1-x}\text{Ca}_x)(\text{Ti}_{0.98}\text{Zr}_{0.02})\text{O}_3$ lead-free ceramics with relative high Curie temperature," *Materials Letters*, vol. 64, pp. 2325–2327, nov 2010.
- [150] B. Asbani, Y. Gagou, J. L. Dellis, A. Lahmar, M. Amjoud, D. Mezzane, Z. Kutnjak, and M. El Marssi, "Structural, dielectric and electrocaloric properties in lead-free Zr-doped $\text{Ba}_{0.8}\text{Ca}_{0.2}\text{TiO}_3$ solid solution," *Solid State Communications*, vol. 237-238, pp. 49–54, 2016.
- [151] H. Kaddoussi, A. Lahmar, Y. Gagou, B. Manoun, J. N. Chotard, J. L. Dellis, Z. Kutnjak, H. Khemakhem, B. Elouadi, and M. El Marssi, "Sequence of structural transitions and electrocaloric properties in $(\text{Ba}_{1-x}\text{Ca}_x)(\text{Zr}_{0.1}\text{Ti}_{0.9})\text{O}_3$ ceramics," *Journal of Alloys and Compounds*, vol. 713, pp. 164–179, aug 2017.
- [152] Z. Hanani, D. Mezzane, M. Amjoud, S. Fourcade, A. G. Razumnaya, I. A. Luk'yanchuk, and M. Gouné, "Enhancement of dielectric properties of lead-free BCZT ferroelectric ceramics by grain size engineering," *Superlattices and Microstructures*, vol. 127, pp. 109–117, mar 2019.
- [153] W. Li, Z. Xu, R. Chu, P. Fu, and G. Zang, "Piezoelectric and dielectric properties of $(\text{Ba}_{1-x}\text{Ca}_x)(\text{Ti}_{0.95}\text{Zr}_{0.05})\text{O}_3$ lead-free ceramics," *Journal of the American Ceramic Society*, vol. 93, pp. 2942–2944, oct 2010.
- [154] V. Buscaglia, S. Tripathi, V. Petkov, M. Dapiaggi, M. Deluca, A. Gajović, and Y. Ren, "Average and local atomic-scale structure in $\text{BaZr}_x\text{Ti}_{1-x}\text{O}_3$ ($x = 0.10, 0.20, 0.40$) ceramics by high-energy x-ray diffraction and Raman spectroscopy," *Journal of Physics Condensed Matter*, vol. 26, p. 065901, feb 2014.

- [155] H. Bao, C. Zhou, D. Xue, J. Gao, and X. Ren, “A modified lead-free piezoelectric BZT-xBCT system with higher T_c ,” *Journal of Physics D: Applied Physics*, vol. 43, p. 465401, nov 2010.
- [156] Z. Yu, C. Ang, R. Guo, and A. S. Bhalla, “Piezoelectric and strain properties of $\text{Ba}(\text{Ti}_{1-x}\text{Zr}_x)\text{O}_3$ ceramics,” *Journal of Applied Physics*, vol. 92, pp. 1489–1493, aug 2002.
- [157] Y. Bai, A. Matousek, P. Tofel, V. Bijalwan, B. Nan, H. Hughes, and T. W. W. Button, “ $(\text{Ba,Ca})(\text{Zr,Ti})\text{O}_3$ lead-free piezoelectric ceramics-The critical role of processing on properties,” *Journal of the European Ceramic Society*, vol. 35, pp. 3445–3456, nov 2015.
- [158] J. Wu, D. Xiao, W. Wu, Q. Chen, J. Zhu, Z. Yang, and J. Wang, “Composition and poling condition-induced electrical behavior of $(\text{Ba}_{0.85}\text{Ca}_{0.15})(\text{Ti}_{1-x}\text{Zr}_x)\text{O}_3$ lead-free piezoelectric ceramics,” *Journal of the European Ceramic Society*, vol. 32, no. 4, pp. 891–898, 2012.
- [159] W. Liu and X. Ren, “Large piezoelectric effect in Pb-free ceramics,” *Physical Review Letters*, vol. 103, p. 257602, dec 2009.
- [160] D. Fu, Y. Kamai, N. Sakamoto, N. Wakiya, H. Suzuki, and M. Itoh, “Phase diagram and piezoelectric response of $(\text{Ba}_{1-x}\text{Ca}_x)(\text{Zr}_{0.1}\text{Ti}_{0.9})\text{O}_3$ solid solution,” *Journal of Physics Condensed Matter*, vol. 25, oct 2013.
- [161] Z. Wang, J. Wang, X. Chao, L. Wei, B. Yang, D. Wang, and Z. Yang, “Synthesis, structure, dielectric, piezoelectric, and energy storage performance of $(\text{Ba}_{0.85}\text{Ca}_{0.15})(\text{Ti}_{0.9}\text{Zr}_{0.1})\text{O}_3$ ceramics prepared by different methods,” *Journal of Materials Science: Materials in Electronics*, vol. 27, pp. 5047–5058, may 2016.
- [162] M. A. Rafiq, M. N. Rafiq, and K. Venkata Saravanan, “Dielectric and impedance spectroscopic studies of lead-free barium-calcium-zirconium-titanium oxide ceramics,” *Ceramics International*, vol. 41, no. 9PartA, pp. 11436–11444, 2015.

- [163] M. ben Abdessalem, I. Kriaa, A. Aydi, N. Abdelmoula, M. ben Abdessalem, I. Kriaa, A. Aydi, and N. Abdelmoula, “Large electrocaloric effect in lead-free $\text{Ba}_{1-x}\text{Ca}_x\text{Ti}_{1-y}\text{Zr}_y\text{O}_3$ ceramics under strong electric field at room-temperature,” *Ceramics International*, vol. 44, no. 12, pp. 13595–13601, 2018.
- [164] S. Patel, D. Sharma, A. Singh, and R. Vaish, “Enhanced thermal energy conversion and dynamic hysteresis behavior of Sr-added $\text{Ba}_{0.85}\text{Ca}_{0.15}\text{Ti}_{0.9}\text{Zr}_{0.1}\text{O}_3$ ferroelectric ceramics,” *Journal of Materiomics*, vol. 2, pp. 75–86, mar 2016.
- [165] S. Hunpratub, S. Maensiri, and P. Chindaprasirt, “Synthesis and characterization of $\text{Ba}_{0.85}\text{Ca}_{0.15}\text{Ti}_{0.9}\text{Zr}_{0.1}\text{O}_3$ ceramics by hydrothermal method,” *Ceramics International*, vol. 40, no. 8 PART B, pp. 13025–13031, 2014.
- [166] T. H. Hsieh, S. C. Yen, and D. T. Ray, “A study on the synthesis of $(\text{Ba,Ca})(\text{Ti,Zr})\text{O}_3$ nano powders using Pechini polymeric precursor method,” *Ceramics International*, vol. 38, pp. 755–759, jan 2012.
- [167] D. Zhan, Q. Xu, D. P. Huang, H. X. Liu, W. Chen, and F. Zhang, “Dielectric nonlinearity and electric breakdown behaviors of $\text{Ba}_{0.95}\text{Ca}_{0.05}\text{Zr}_{0.3}\text{Ti}_{0.7}\text{O}_3$ ceramics for energy storage utilizations,” *Journal of Alloys and Compounds*, vol. 682, pp. 594–600, oct 2016.
- [168] P. Jaimeewong, M. Promsawat, A. Watcharapasorn, and S. Jiansirisomboon, “Comparative study of properties of BCZT ceramics prepared from conventional and sol-gel auto combustion powders,” *Integrated Ferroelectrics*, vol. 175, pp. 25–32, oct 2016.
- [169] L. Yao, Z. Pan, J. Zhai, and H. H. D. D. Chen, “Novel design of highly $[110]$ -oriented barium titanate nanorod array and its application in nanocomposite capacitors,” *Nanoscale*, vol. 9, no. 12, pp. 4255–4264, 2017.
- [170] Z. Zhou, C. C. Bowland, M. H. Malakooti, H. Tang, and H. A. Sodano, “Lead-free $0.5\text{Ba}(\text{Zr}_{0.2}\text{Ti}_{0.8})\text{O}_3$ - $0.5(\text{Ba}_{0.7}\text{Ca}_{0.3})\text{TiO}_3$ nanowires for energy harvesting,” *Nanoscale*, vol. 8, no. 9, pp. 5098–5105, 2016.

- [171] A. Koka, Z. Zhou, and H. A. Sodano, “Vertically aligned BaTiO₃ nanowire arrays for energy harvesting,” *Energy and Environmental Science*, vol. 7, no. 1, pp. 288–296, 2014.
- [172] Z. Zhou, H. Tang, and H. A. Sodano, “Vertically aligned arrays of BaTiO₃ Nanowires,” *ACS Applied Materials and Interfaces*, vol. 5, no. 22, pp. 11894–11899, 2013.
- [173] Y. Deng, J. L. Wang, K. R. Zhu, M. S. Zhang, J. M. Hong, Q. R. Gu, and Z. Yin, “Synthesis and characterization of single-crystal PbTiO₃ nanorods,” *Materials Letters*, vol. 59, no. 26, pp. 3272–3275, 2005.
- [174] M. Alexe and D. Hesse, “One-dimensional ferroelectrics: Nanowires and nanotubes,” *Ferroelectrics*, vol. 433, no. 1, pp. 53–64, 2012.
- [175] N. Bao, L. Shen, G. Srinivasan, K. Yanagisawa, and A. Gupta, “Shape-controlled monocrystalline ferroelectric barium titanate nanostructures: From nanotubes and nanowires to ordered nanostructures,” *Journal of Physical Chemistry C*, vol. 112, no. 23, pp. 8634–8642, 2008.
- [176] X. Ji, C. Wang, S. Zhang, R. Tu, Q. Shen, J. Shi, and L. Zhang, “Structural and electrical properties of BCZT ceramics synthesized by sol–gel-hydrothermal process at low temperature,” *Journal of Materials Science: Materials in Electronics*, vol. 30, pp. 12197–12203, jul 2019.
- [177] C. Baek, J. E. Wang, S. Ryu, J. H. Kim, C. K. Jeong, K. I. Park, and D. K. Kim, “Facile hydrothermal synthesis of BaZr_xTi_{1-x}O₃ nanoparticles and their application to a lead-free nanocomposite generator,” *RSC Advances*, vol. 7, no. 5, pp. 2851–2856, 2017.
- [178] T. Maiti, R. Guo, and A. S. Bhalla, “The evolution of relaxor behavior in Ti⁴⁺-doped BaZrO₃ ceramics,” *Journal of Applied Physics*, vol. 100, no. 11, p. 114109, 2006.
- [179] X. Gao, M. Zheng, X. Yan, J. Fu, M. Zhu, and Y. Hou, “The alignment of BCZT particles in PDMS boosts the sensitivity and cycling reliability of a flexible piezo-

- electric touch sensor,” *Journal of Materials Chemistry C*, vol. 7, no. 4, pp. 961–967, 2019.
- [180] Z. Pan, L. Yao, J. Zhai, H. Wang, and B. Shen, “Ultrafast Discharge and Enhanced Energy Density of Polymer Nanocomposites Loaded with $0.5(\text{Ba}_{0.7}\text{Ca}_{0.3})\text{TiO}_3\text{-}0.5\text{Ba}(\text{Zr}_{0.2}\text{Ti}_{0.8})\text{O}_3$ One-Dimensional Nanofibers,” *ACS Applied Materials and Interfaces*, vol. 9, pp. 14337–14346, apr 2017.
- [181] C. C. Jin, X. C. Liu, C. H. Liu, Y. Wang, H. L. Hwang, and Q. Wang, “High-performance BCTZ nanowires-based energy harvesting device and self-powered bio-compatible flexion sensor,” *Materials and Design*, vol. 144, pp. 55–63, apr 2018.
- [182] K. S. Chary, H. S. Panda, and C. D. Prasad, “Fabrication of Large Aspect Ratio $\text{Ba}_{0.85}\text{Ca}_{0.15}\text{Zr}_{0.1}\text{Ti}_{0.9}\text{O}_3$ Superfine Fibers-Based Flexible Nanogenerator Device: Synergistic Effect on Curie Temperature, Harvested Voltage, and Power,” *Industrial and Engineering Chemistry Research*, vol. 56, no. 37, pp. 10335–10342, 2017.
- [183] K. Castkova, K. Maca, J. Cihlar, H. Hughes, A. Matousek, P. Tofel, Y. Bai, and T. W. Button, “Chemical Synthesis, Sintering and Piezoelectric Properties of $\text{Ba}_{0.85}\text{Ca}_{0.15}\text{Zr}_{0.1}\text{Ti}_{0.9}\text{O}_3$ Lead-Free Ceramics,” *Journal of the American Ceramic Society*, vol. 98, pp. 2373–2380, aug 2015.
- [184] Y. Tian, X. Chao, L. Wei, P. Liang, and Z. Yang, “Phase transition behavior and electrical properties of lead-free $(\text{Ba}_{1-x}\text{Ca}_x)(\text{Zr}_{0.1}\text{Ti}_{0.9})\text{O}_3$ piezoelectric ceramics,” *Journal of Applied Physics*, vol. 113, p. 184107, may 2013.
- [185] Z. Wang, X. Chen, X. Chao, J. Wang, P. Liang, and Z. Yang, “Low temperature sintering and dielectric properties of $(\text{Ba}_{0.85}\text{Ca}_{0.15})(\text{Ti}_{0.9}\text{Zr}_{0.1})\text{O}_3\text{-xCu}^{2+}$ ceramics obtained by the sol-gel technique,” *Ceramics International*, vol. 42, no. 16, pp. 18037–18044, 2016.
- [186] P. Mishra, Sonia, and P. Kumar, “Enhanced dielectric and piezoelectric properties of BZT-BCT system near MPB,” *Ceramics International*, vol. 40, no. 9 PART A, pp. 14149–14157, 2014.

- [187] D. Xue, Y. Zhou, H. Bao, J. Gao, C. Zhou, and X. Ren, “Large piezoelectric effect in Pb-free Ba(Ti,Sn)O₃-x(Ba,Ca) TiO₃ ceramics,” *Applied Physics Letters*, vol. 99, p. 122901, sep 2011.
- [188] X. Liu, Z. Chen, B. Fang, J. Ding, X. Zhao, H. Xu, and H. Luo, “Enhancing piezoelectric properties of BCZT ceramics by Sr and Sn co-doping,” *Journal of Alloys and Compounds*, vol. 640, pp. 128–133, aug 2015.
- [189] X.-G. Tang and H. L.-W. Chan, “Effect of grain size on the electrical properties of (Ba,Ca)(Zr,Ti)O₃ relaxor ferroelectric ceramics,” *Journal of Applied Physics*, vol. 97, no. 3, p. 034109, 2005.
- [190] J. Wu, D. Xiao, W. Wu, Q. Chen, J. Zhu, Z. Yang, and J. Wang, “Role of room-temperature phase transition in the electrical properties of (Ba, Ca)(Ti, Zr)O₃ ceramics,” *Scripta Materialia*, vol. 65, pp. 771–774, nov 2011.
- [191] P. Jaimeewong, S. Sittinon, S. Buntham, P. Bomlai, O. Namsar, S. Pojprapai, and A. Watcharapasorn, “Ferroelectric, Piezoelectric and Dielectric Behaviors of CoO- and Fe₂O₃-Doped BCZT Ceramics,” *Physica Status Solidi (A) Applications and Materials Science*, vol. 215, p. 1701023, oct 2018.
- [192] T. M. Correia, M. McMillen, M. K. Rokosz, P. M. Weaver, J. M. Gregg, G. Viola, and M. G. Cain, “A lead-free and high-energy density ceramic for energy storage applications,” *Journal of the American Ceramic Society*, vol. 96, pp. 2699–2702, sep 2013.
- [193] M. Maraj, W. Wei, B. Peng, and W. Sun, “Dielectric and energy storage properties of Ba(1-x)Ca_xZr_yTi(1-y)O₃ (BCZT): A review,” *Materials*, vol. 12, p. 3641, nov 2019.
- [194] C. S. Manohar, B. S. Kumar, S. P. P. Sadhu, S. K. Srimadh, V. S. Muthukumar, S. Venketesh, and K. B. Varma, “Novel Lead-free biocompatible piezoelectric Hydroxyapatite (HA)-BCZT (Ba_{0.85}Ca_{0.15}Zr_{0.1}Ti_{0.9}O₃) nanocrystal composites for bone regeneration,” *Nanotechnology Reviews*, vol. 8, pp. 61–78, may 2019.

- [195] K. K. Poon, M. C. Wurm, D. M. Evans, M. A. Einarsrud, R. Lutz, and J. Glaum, “Biocompatibility of (Ba,Ca)(Zr,Ti)O₃ piezoelectric ceramics for bone replacement materials,” *Journal of Biomedical Materials Research - Part B Applied Biomaterials*, vol. 108, pp. 1295–1303, may 2019.
- [196] N. D. Scarisoreanu, F. Craciun, V. Ion, R. Birjega, A. Bercea, V. Dinca, M. Dinescu, L. E. Sima, M. Icriverzi, A. Roseanu, L. Gruionu, and G. Gruionu, “Lead-Free Piezoelectric (Ba,Ca)(Zr,Ti)O₃ Thin Films for Biocompatible and Flexible Devices,” *ACS applied materials & interfaces*, vol. 9, pp. 266–278, jan 2017.
- [197] M. Cruz-Romero, “Crop-based biodegradable packaging and its environmental implications,” *CAB Reviews: Perspectives in Agriculture, Veterinary Science, Nutrition and Natural Resources*, vol. 3, jan 2008.
- [198] M. Zenkiewicz, J. Richert, P. Rytlewski, K. Moraczewski, M. Stepczyńska, and T. Karasiewicz, “Characterisation of multi-extruded poly(lactic acid),” *Polymer Testing*, vol. 28, pp. 412–418, jun 2009.
- [199] Z. Li, B. H. Tan, T. Lin, and C. He, “Recent advances in stereocomplexation of enantiomeric PLA-based copolymers and applications,” *Progress in Polymer Science*, vol. 62, pp. 22–72, nov 2016.
- [200] A. J. Lasprilla, G. A. Martinez, B. H. Lunelli, A. L. Jardini, and R. M. Filho, “Polylactic acid synthesis for application in biomedical devices - A review,” *Biotechnology Advances*, vol. 30, pp. 321–328, jan 2012.
- [201] M. Niaounakis, “Adhesive Compositions,” in *Biopolymers: Processing and Products*, pp. 459–480, Elsevier, 2015.
- [202] S. Corneillie and M. Smet, “PLA architectures: The role of branching,” *Polymer Chemistry*, vol. 6, no. 6, pp. 850–867, 2015.
- [203] V. Hegde, *Dielectric study of biodegradable and/or bio-based polymeric materials*. PhD thesis, jul 2017.

- [204] Y. Ohki and N. Hirai, “Dielectric properties of biodegradable polymers,” in *Annual Report - Conference on Electrical Insulation and Dielectric Phenomena, CEIDP*, pp. 668–671, 2006.
- [205] X. Li, S. Chen, X. Zhang, J. Li, H. Liu, N. Han, and X. Zhang, “Poly-l-Lactic Acid/Graphene Electrospun Composite Nanofibers for Wearable Sensors,” *Energy Technology*, vol. 8, p. 1901252, may 2020.
- [206] M. Varga, J. Morvan, N. Diorio, E. Buyuktanir, J. Harden, J. L. West, and A. Jákli, “Direct piezoelectric responses of soft composite fiber mats,” *Applied Physics Letters*, vol. 102, p. 153903, apr 2013.
- [207] M. Ando, S. Takeshima, Y. Ishiura, K. Ando, and O. Onishi, “Piezoelectric antibacterial fabric comprised of poly(L-lactic acid) yarn,” *Japanese Journal of Applied Physics*, vol. 56, p. 10PG01, oct 2017.
- [208] M. Smith, Y. Calahorra, Q. Jing, and S. Kar-Narayan, “Direct observation of shear piezoelectricity in poly-l-lactic acid nanowires,” *APL Materials*, vol. 5, p. 074105, jul 2017.
- [209] V. Sencadas, C. Ribeiro, A. Heredia, I. K. Bdikin, A. L. Kholkin, and S. Lanceros-Mendez, “Local piezoelectric activity of single poly(L-lactic acid) (PLLA) microfibers,” *Applied Physics A: Materials Science and Processing*, vol. 109, pp. 51–55, oct 2012.
- [210] P. Mishra, Sonia, and P. Kumar, “Effect of sintering temperature on dielectric, piezoelectric and ferroelectric properties of BZT-BCT 50/50 ceramics,” *Journal of Alloys and Compounds*, vol. 545, pp. 210–215, dec 2012.
- [211] A. Frattini, A. Di Loreto, O. de Sanctis, and E. Benavidez, “BCZT Ceramics Prepared from Activated Powders,” *Procedia Materials Science*, vol. 1, pp. 359–365, 2012.
- [212] Z. M. Wang, K. Zhao, X. L. Guo, W. Sun, H. L. Jiang, X. Q. Han, X. T. Tao, Z. X. Cheng, H. Y. Zhao, H. Kimura, G. L. Yuan, J. Yin, and Z. G. Liu, “Crystallization,

- phase evolution and ferroelectric properties of sol-gel-synthesized $\text{Ba}(\text{Ti}_{0.8}\text{Zr}_{0.2})\text{O}_{3-x}(\text{Ba}_{0.7}\text{Ca}_{0.3})\text{TiO}_3$ thin films,” *Journal of Materials Chemistry C*, vol. 1, no. 3, pp. 522–530, 2013.
- [213] Y. Tian, L. Wei, X. Chao, Z. Liu, and Z. Yang, “Phase transition behavior and large piezoelectricity near the morphotropic phase boundary of lead-free $(\text{Ba}_{0.85}\text{Ca}_{0.15})(\text{Zr}_{0.1}\text{Ti}_{0.9})\text{O}_3$ ceramics,” *Journal of the American Ceramic Society*, vol. 96, pp. 496–502, nov 2013.
- [214] G. K. Sahoo and R. Mazumder, “Low temperature synthesis of $\text{Ba}(\text{Zr}_{0.2}\text{Ti}_{0.8})\text{O}_{3-0.5}(\text{Ba}_{0.7}\text{Ca}_{0.3})\text{TiO}_3$ nanopowders by solution based auto combustion method,” *Journal of Materials Science: Materials in Electronics*, vol. 25, pp. 3515–3519, aug 2014.
- [215] C. Chen, Y. Wei, X. Jiao, and D. Chen, “Hydrothermal synthesis of BaTiO_3 : Crystal phase and the Ba^{2+} ions leaching behavior in aqueous medium,” *Materials Chemistry and Physics*, vol. 110, pp. 186–191, jul 2008.
- [216] Z. hui Chen, Z. wei Li, J. hua Qiu, T. xiang Zhao, J. ning Ding, X. guang Jia, W. qin Zhu, J. jun Xu, Z. hui Chen, Z. wei Li, J. hua Qiu, T. xiang Zhao, J. ning Ding, X. guang Jia, W. qin Zhu, and J. jun Xu, “ Y_2O_3 doped $\text{Ba}_{0.9}\text{Ca}_{0.1}\text{Ti}_{0.9}\text{Sn}_{0.1}\text{O}_3$ ceramics with improved piezoelectric properties,” *Journal of the European Ceramic Society*, vol. 38, pp. 1349–1355, oct 2018.
- [217] W. Wang, L. Cao, W. Liu, G. Su, and W. Zhang, “Low-temperature synthesis of BaTiO_3 powders by the sol-gel-hydrothermal method,” *Ceramics International*, vol. 39, pp. 7127–7134, aug 2013.
- [218] J. O. Eckert, C. C. Hung-Houston, B. L. Gersten, M. M. Lencka, and R. E. Riman, “Kinetics and mechanisms of hydrothermal synthesis of barium titanate,” nov 1996.
- [219] H. A. Ávila, L. A. Ramajo, M. M. Reboredo, M. S. Castro, and R. Parra, “Hydrothermal synthesis of BaTiO_3 from different Ti-precursors and microstructural and electrical properties of sintered samples with submicrometric grain size,” *Ceramics International*, vol. 37, pp. 2383–2390, sep 2011.

- [220] S. Roy, R. Maharana, S. R. Reddy, S. Singh, P. Kumar, T. Karthik, S. Asthana, V. V. Bhanu Prasad, and S. V. Kamat, "Structural, ferroelectric and piezoelectric properties of chemically processed, low temperature sintered piezoelectric BZT-BCT ceramics," *Materials Research Express*, vol. 3, p. 035702, mar 2016.
- [221] H. Xu, L. Gao, and J. Guo, "Preparation and characterizations of tetragonal barium titanate powders by hydrothermal method," *Journal of the European Ceramic Society*, vol. 22, no. 7, pp. 1163–1170, 2002.
- [222] I. K. Jeong and J. S. Ahn, "The atomic structure of lead-free $\text{Ba}(\text{Zr}_{0.2}\text{Ti}_{0.8})\text{O}_3$ - $(\text{Ba}_{0.7}\text{Ca}_{0.3})\text{TiO}_3$ by using neutron total scattering analysis," *Applied Physics Letters*, vol. 101, no. 24, p. 242901, 2012.
- [223] M. Salarian, M. Solati-Hashjin, S. Sara Shafiei, A. Goudarzi, R. Salarian, and A. Nemati, "Surfactant-assisted synthesis and characterization of hydroxyapatite nanorods under hydrothermal conditions," *Materials Science- Poland*, vol. 27, no. 4, pp. 961–971, 2009.
- [224] Y. Liu, D. Hou, and G. Wang, "A simple wet chemical synthesis and characterization of hydroxyapatite nanorods," *Materials Chemistry and Physics*, vol. 86, no. 1, pp. 69–73, 2004.
- [225] P. Zhao, L. Wang, L. Bian, J. Xu, A. Chang, X. Xiong, F. Xu, and J. Zhang, "Growth Mechanism, Modified Morphology and Optical Properties of Coral-like BaTiO_3 Architecture through CTAB Assisted Synthesis," *Journal of Materials Science & Technology*, vol. 31, pp. 223–228, feb 2015.
- [226] O. Yayapao, T. Thongtem, A. Phuruangrat, and S. Thongtem, "CTAB-assisted hydrothermal synthesis of tungsten oxide microflowers," *Journal of Alloys and Compounds*, vol. 509, no. 5, pp. 2294–2299, 2011.
- [227] A. Chaudhuri, S. Haldar, and A. Chattopadhyay, "Structural transition in micelles: Novel insight into microenvironmental changes in polarity and dynamics," in *Chemistry and Physics of Lipids*, vol. 165, pp. 497–504, 2012.

- [228] V. Kalyani, B. S. Vasile, A. Ianculescu, M. T. Buscaglia, V. Buscaglia, and P. Nanni, “Hydrothermal synthesis of SrTiO₃ mesocrystals: Single crystal to mesocrystal transformation induced by topochemical reactions,” *Crystal Growth and Design*, vol. 12, pp. 4450–4456, sep 2012.
- [229] V. Kalyani, B. S. Vasile, A. Ianculescu, A. Testino, A. Carino, M. T. Buscaglia, V. Buscaglia, and P. Nanni, “Hydrothermal Synthesis of SrTiO₃: Role of Interfaces,” *Crystal Growth and Design*, vol. 15, pp. 5712–5725, dec 2015.
- [230] D. Spagnoli, J. F. Banfield, and S. C. Parker, “Free Energy Change of Aggregation of Nanoparticles,” *The Journal of Physical Chemistry C*, vol. 112, pp. 14731–14736, sep 2008.
- [231] R. L. Penn and J. F. Banfield, “Morphology development and crystal growth in nanocrystalline aggregates under hydrothermal conditions: Insights from titania,” *Geochimica et Cosmochimica Acta*, vol. 63, pp. 1549–1557, may 1999.
- [232] C. Dong, Y. Zhou, N. Ta, and W. Shen, “Formation mechanism and size control of ceria nanocubes,” *CrystEngComm*, vol. 22, no. 17, pp. 3033–3041, 2020.
- [233] Z. L. Wang, “Transmission electron microscopy of shape-controlled nanocrystals and their assemblies,” *Journal of Physical Chemistry B*, vol. 104, pp. 1153–1175, feb 2000.
- [234] X. Lan, J. Zhang, H. Gao, and T. Wang, “Morphology-controlled hydrothermal synthesis and growth mechanism of microcrystal Cu₂O,” *CrystEngComm*, vol. 13, no. 2, pp. 633–636, 2011.
- [235] L. Li, L. Tian, Y. Liu, D. Liu, C. Li, M. Liu, and C. Wang, “A self-defined intermediate product captured from the evolution process from a six-pod to an octahedral PbS sub-micrometer particle,” *CrystEngComm*, vol. 19, no. 16, pp. 2195–2201, 2017.
- [236] Z. Zhang, L. Miao, M. Yao, L. Li, F. Zhao, H. Gu, Y. Han, G. A. Sewvandi, Q. Feng, D. Yang, X. Wang, and D. Hu, “Rod-like incipient ferroelectric SrTiO₃ polycrystal

- with crystal-axis orientation,” *Ceramics International*, vol. 46, pp. 3675–3687, feb 2020.
- [237] Y. Li, X. P. Gao, G. L. Pan, T. Y. Yan, and H. Y. Zhu, “Titanate nanofiber reactivity: Fabrication of MTiO₃ (M = Ca, Sr, and Ba) perovskite oxides,” *Journal of Physical Chemistry C*, vol. 113, pp. 4386–4394, mar 2009.
- [238] P. Kumar, C. Prakash, O. P. Thakur, R. Chatterjee, and T. C. Goel, “Dielectric, ferroelectric and pyroelectric properties of PMNT ceramics,” *Physica B: Condensed Matter*, vol. 371, no. 2, pp. 313–316, 2006.
- [239] A. A. Bokov and Z. G. Ye, “Recent progress in relaxor ferroelectrics with perovskite structure,” in *Frontiers of Ferroelectricity: A Special Issue of the Journal of Materials Science*, pp. 31–52, Boston: Springer US, 2007.
- [240] Y. Liu, Y. Pu, and Z. Sun, “Enhanced relaxor ferroelectric behavior of BCZT lead-free ceramics prepared by hydrothermal method,” *Materials Letters*, vol. 137, pp. 128–131, 2014.
- [241] H. Ghayour and M. Abdellahi, “A brief review of the effect of grain size variation on the electrical properties of BaTiO₃-based ceramics,” 2016.
- [242] H. L. Sun, Q. J. Zheng, Y. Wan, Y. Chen, X. Wu, K. W. Kwok, H. L. Chan, and D. M. Lin, “Correlation of grain size, phase transition and piezoelectric properties in Ba_{0.85}Ca_{0.15}Ti_{0.90}Zr_{0.10}O₃ ceramics,” *Journal of Materials Science: Materials in Electronics*, vol. 26, pp. 5270–5278, jul 2015.
- [243] Y. Tan, J. Zhang, Y. Wu, C. Wang, V. Koval, B. Shi, H. Ye, R. McKinnon, G. Viola, and H. Yan, “Unfolding grain size effects in barium titanate ferroelectric ceramics,” *Scientific Reports*, vol. 5, p. 9953, sep 2015.
- [244] Y. Zhen and J. F. Li, “Normal sintering of (K,Na)NbO₃-based ceramics: Influence of sintering temperature on densification, microstructure, and electrical properties,” *Journal of the American Ceramic Society*, vol. 89, pp. 3669–3675, dec 2006.

- [245] C. G. Stenger and A. J. Burggraaf, “Study of phase transitions and properties of tetragonal (Pb,La)(Zr,Ti)O₃ ceramics-I. Phase diagram and β -phase,” *Journal of Physics and Chemistry of Solids*, vol. 41, pp. 17–23, jan 1980.
- [246] K. M. Sangwan, N. Ahlawat, R. S. Kundu, S. Rani, S. Rani, N. Ahlawat, and S. Murugavel, “Improved dielectric and ferroelectric properties of Mn doped barium zirconium titanate (BZT) ceramics for energy storage applications,” *Journal of Physics and Chemistry of Solids*, vol. 117, pp. 158–166, jun 2018.
- [247] Z. Hanani, S. Merselmiz, A. Danine, N. Stein, D. Mezzane, M. Amjoud, M. Lahcini, Y. Gagou, M. Spreitzer, D. Vengust, Z. Kutnjak, M. El Marssi, I. A. Luk’yanchuk, and M. Gouné, “Enhanced dielectric and electrocaloric properties in lead-free rod-like BCZT ceramics,” *Journal of Advanced Ceramics*, vol. 9, pp. 210–219, apr 2020.
- [248] W. Cai, Y. Fan, J. Gao, C. Fu, and X. Deng, “Microstructure, dielectric properties and diffuse phase transition of barium stannate titanate ceramics,” *Journal of Materials Science: Materials in Electronics*, vol. 22, pp. 265–272, mar 2011.
- [249] J. Zhai, X. Yao, J. Shen, L. Zhang, and H. Chen, “Structural and dielectric properties of Ba(Zr_xTi_{1-x})O₃ thin films prepared by the sol-gel process,” *Journal of Physics D: Applied Physics*, vol. 37, pp. 748–752, mar 2004.
- [250] C. Zhang, F. Chen, X. Zhong, Z. Ling, Z. Tang, and G. Jian, “Enhanced ferroelectric relaxor behavior of Ho₂O₃-modified barium zirconate titanate ceramics,” *Journal of Materials Science: Materials in Electronics*, vol. 29, pp. 16730–16739, oct 2018.
- [251] W. Bai, D. Chen, J. Zhang, J. Zhong, M. Ding, B. Shen, J. Zhai, and Z. Ji, “Phase transition behavior and enhanced electromechanical properties in (Ba_{0.85}Ca_{0.15})(Zr_xTi_{1-x})O₃ lead-free piezoceramics,” *Ceramics International*, vol. 42, pp. 3598–3608, feb 2016.
- [252] E. Venkata Ramana, A. Mahajan, M. P. Graça, S. K. Mendiratta, J. M. Monteiro, and M. A. Valente, “Structure and ferroelectric studies of (Ba_{0.85}Ca_{0.15})(Ti_{0.9}Zr_{0.1})O₃ piezoelectric ceramics,” *Materials Research Bulletin*, vol. 48, no. 10, pp. 4395–4401, 2013.

- [253] H. Tang, Z. Zhou, and H. A. Sodano, “Relationship between BaTiO₃ nanowire aspect ratio and the dielectric permittivity of nanocomposites,” *ACS Applied Materials and Interfaces*, vol. 6, pp. 5450–5455, apr 2014.
- [254] N. Sriharan, N. Muthukumarasamy, and T. S. Senthil, “Preparation and Characterization of Al₂O₃ Doped TiO₂ Nanocomposites Prepared from Simple Sol-Gel Method,” *Zeitschrift fur Physikalische Chemie*, vol. 230, pp. 1745–1758, jan 2016.
- [255] M. Stewart, M. G. Cain, and P. Weaver, “Electrical Measurement of Ferroelectric Properties,” pp. 1–14, 2014.
- [256] B. Lu, P. Li, Z. Tang, Y. Yao, X. Gao, W. Kleemann, and S. G. Lu, “Large Electrocaloric Effect in Relaxor Ferroelectric and Antiferroelectric Lanthanum Doped Lead Zirconate Titanate Ceramics,” *Scientific Reports*, vol. 7, p. 45335, may 2017.
- [257] X. Li, L. Yang, C. F. Li, M. F. Liu, Z. Fan, Y. L. Xie, C. L. Lu, L. Lin, Z. B. Yan, Z. Zhang, J. Y. Dai, J. M. Liu, and S. W. Cheong, “Ultra-low coercive field of improper ferroelectric Ca₃Ti₂O₇ epitaxial thin films,” *Applied Physics Letters*, vol. 110, p. 042901, jan 2017.
- [258] Z. Z. Hu, J. J. Lu, B. H. Chen, T. T. Gao, X. Q. Liu, W. Wen, and X. M. Chen, “First-order phase transition and unexpected rigid rotation mode in hybrid improper ferroelectric (La, Al) co-substituted Ca₃Ti₂O₇ ceramics,” *Journal of Materiomics*, vol. 5, pp. 618–625, dec 2019.
- [259] Y. Huang, F. Li, H. Hao, F. Xia, H. Liu, and S. Zhang, “(Bi_{0.51} Na_{0.47})TiO₃ based lead free ceramics with high energy density and efficiency,” *Journal of Materiomics*, vol. 5, pp. 385–393, sep 2019.
- [260] X. Ji, C. Wang, S. Li, S. Zhang, R. Tu, Q. Shen, J. Shi, and L. Zhang, “Structural and electrical properties of BCZT ceramics synthesized by sol–gel process,” *Journal of Materials Science: Materials in Electronics*, vol. 29, pp. 7592–7599, may 2018.
- [261] E. Chandrakala, J. Paul Praveen, B. K. Hazra, and D. Das, “Effect of sintering temperature on structural, dielectric, piezoelectric and ferroelectric properties of

- sol-gel derived BZT-BCT ceramics,” *Ceramics International*, vol. 42, pp. 4964–4977, mar 2016.
- [262] K. Xu, P. Yang, W. Peng, and L. Li, “Temperature-stable MgO-doped BCZT lead-free ceramics with ultra-high energy storage efficiency,” *Journal of Alloys and Compounds*, vol. 829, p. 154516, jul 2020.
- [263] X. Wang, P. Liang, X. Chao, and Z. Yang, “Dielectric Properties and Impedance Spectroscopy of MnCO₃-Modified (Ba_{0.85}Ca_{0.15})(Zr_{0.1}Ti_{0.9})O₃ Lead-Free Ceramics,” *Journal of the American Ceramic Society*, vol. 98, pp. 1506–1514, may 2015.
- [264] L. Zhu, “Exploring strategies for high dielectric constant and low loss polymer dielectrics,” 2014.
- [265] C. Wu, X. Huang, L. Lv, G. Chen, J. Yu, L. Xie, and P. Jiang, “High-permittivity and low-dielectric-loss polymer composites based on TiO₂-nanorod functionalized carbon nanotubes,” in *Proceedings of 2012 IEEE International Conference on Condition Monitoring and Diagnosis, CMD 2012*, pp. 347–349, IEEE, sep 2012.
- [266] T. Tanaka, “Dielectric breakdown in polymer nanocomposites,” in *Polymer Nanocomposites: Electrical and Thermal Properties*, pp. 113–137, Cham: Springer International Publishing, 2016.
- [267] P. Barber, S. Balasubramanian, Y. Anguchamy, S. Gong, A. Wibowo, H. Gao, H. J. Ploehn, and H. C. Z. Loye, “Polymer composite and nanocomposite dielectric materials for pulse power energy storage,” *Materials*, vol. 2, pp. 1697–1733, oct 2009.
- [268] Y. Fan, X. Huang, G. Wang, and P. Jiang, “Core-Shell Structured Biopolymer@BaTiO₃ Nanoparticles for Biopolymer Nanocomposites with Significantly Enhanced Dielectric Properties and Energy Storage Capability,” *Journal of Physical Chemistry C*, vol. 119, no. 49, pp. 27330–27339, 2015.
- [269] M. Ejaz, V. S. Puli, R. Elupula, S. Adireddy, B. C. Riggs, D. B. Chrisey, and S. M. Grayson, “Core-shell structured poly(glycidyl methacrylate)/BaTiO₃ nanocomposites prepared by surface-initiated atom transfer radical polymerization: A novel

- material for high energy density dielectric storage,” *Journal of Polymer Science, Part A: Polymer Chemistry*, vol. 53, pp. 719–728, mar 2015.
- [270] K. Bi, M. Bi, Y. Hao, W. Luo, Z. Cai, X. Wang, and Y. Huang, “Ultrafine core-shell BaTiO₃@SiO₂ structures for nanocomposite capacitors with high energy density,” *Nano Energy*, vol. 51, pp. 513–523, sep 2018.
- [271] Z. Pan, L. Yao, J. Liu, X. Liu, F. Pi, J. Chen, B. Shen, and J. Zhai, “Superior discharge energy density and efficiency in polymer nanocomposites induced by linear dielectric core-shell nanofibers,” *Journal of Materials Chemistry C*, vol. 7, no. 2, pp. 405–413, 2019.
- [272] C. C. Li, S. J. Chang, J. T. Lee, and W. S. Liao, “Efficient hydroxylation of BaTiO₃ nanoparticles by using hydrogen peroxide,” *Colloids and Surfaces A: Physicochemical and Engineering Aspects*, vol. 361, no. 1-3, pp. 143–149, 2010.
- [273] Z. Hanani, E. H. Ablouh, M. b. Amjoud, D. Mezzane, S. Fourcade, and M. Gouné, “Very-low temperature synthesis of pure and crystalline lead-free Ba_{0.85}Ca_{0.15}Zr_{0.1}Ti_{0.9}O₃ ceramic,” *Ceramics International*, vol. 44, pp. 10997–11000, jun 2018.
- [274] W. Xia, Y. Yin, J. Xing, and Z. Xu, “The effects of double-shell organic interfaces on the dielectric and energy storage properties of the P(VDF-CTFE)/BT@HBP@PDA-Ag nanocomposite films,” *Results in Physics*, vol. 11, pp. 877–884, dec 2018.
- [275] K. Wang, J. Fu, S. Wang, M. Gao, J. Zhu, Z. Wang, and Q. Xu, “Polydopamine-coated magnetic nanochains as efficient dye adsorbent with good recyclability and magnetic separability,” *Journal of Colloid and Interface Science*, vol. 516, pp. 263–273, apr 2018.
- [276] S. K. Singh, P. Anthony, and A. Chowdhury, “High molecular weight poly(lactic acid) synthesized with apposite catalytic combination and longer time,” *Oriental Journal of Chemistry*, vol. 34, pp. 1984–1990, aug 2018.

- [277] L. Zhang, S. Lv, C. Sun, L. Wan, H. Tan, and Y. Zhang, “Effect of MAH-g-PLA on the Properties of Wood Fiber/Polylactic Acid Composites,” *Polymers*, vol. 9, p. 591, nov 2017.
- [278] S. Jiang, L. Jin, H. Hou, and L. Zhang, “Polymer-based nanocomposites with high dielectric permittivity,” in *Polymer-Based Multifunctional Nanocomposites and Their Applications*, pp. 201–243, Elsevier, jan 2018.
- [279] K. Deshmukh, M. Basheer Ahamed, R. R. Deshmukh, S. K. Khadheer Pasha, P. R. Bhagat, and K. Chidambaram, “Biopolymer Composites with High Dielectric Performance: Interface Engineering,” in *Biopolymer Composites in Electronics*, pp. 27–128, Elsevier, jan 2017.
- [280] T. F. Zhang, X. G. Tang, Q. X. Liu, Y. P. Jiang, X. X. Huang, and Q. F. Zhou, “Energy-storage properties and high-temperature dielectric relaxation behaviors of relaxor ferroelectric $\text{Pb}(\text{Mg}_{1/3}\text{Nb}_{2/3})\text{O}_3\text{-PbTiO}_3$ ceramics,” *Journal of Physics D: Applied Physics*, vol. 49, p. 095302, mar 2016.
- [281] Z. Wang, T. Wang, C. Wang, and Y. Xiao, “The effect of interfacial interaction-induced soft percolation regime on dielectric properties in $\text{Ba}(\text{Fe}_{0.5}\text{Nb}_{0.5})\text{O}_3/\text{P}(\text{VDF-TrFE})$ nanocomposites,” *Journal of Materials Science*, vol. 52, pp. 11496–11505, oct 2017.
- [282] J. C. Maxwell, *A Treatise on Electricity and Magnetism*. Cambridge: Cambridge University Press, 2010.
- [283] O. Wiener, *Zur theorie der refraktionskonstanten*. Leipzig Ber., 1910.
- [284] K. Golden, “Bounds on the complex permittivity of a multicomponent material,” *Journal of the Mechanics and Physics of Solids*, vol. 34, pp. 333–358, jan 1986.
- [285] L. Jylhä, J. Honkamo, H. Jantunen, and A. Sihvola, “Microstructure-based numerical modeling method for effective permittivity of ceramic/polymer composites,” *Journal of Applied Physics*, vol. 97, p. 104104, may 2005.

- [286] Y. Cheng, X. Chen, K. Wu, S. Wu, Y. Chen, and Y. Meng, “Modeling and simulation for effective permittivity of two-phase disordered composites,” *Journal of Applied Physics*, vol. 103, p. 034111, feb 2008.
- [287] J. C. Maxwell Garnett, “XII. Colours in metal glasses and in metallic films,” *Philosophical Transactions of the Royal Society of London. Series A, Containing Papers of a Mathematical or Physical Character*, vol. 203, pp. 385–420, jan 1904.
- [288] L. Jylhä and A. Sihvola, “Equation for the effective permittivity of particle-filled composites for material design applications,” *Journal of Physics D: Applied Physics*, vol. 40, pp. 4966–4973, aug 2007.
- [289] V. A. Markel, “Introduction to the Maxwell Garnett approximation: tutorial,” *Journal of the Optical Society of America A*, vol. 33, p. 1244, jul 2016.
- [290] H. Kang and G. W. Milton, “Solutions to the pólya-szegő conjecture and the weak eshelby conjecture,” *Archive for Rational Mechanics and Analysis*, vol. 188, pp. 93–116, apr 2008.
- [291] A. Moroz, “Depolarization field of spheroidal particles,” *Journal of the Optical Society of America B*, vol. 26, p. 517, mar 2009.
- [292] A. Sihvola, “Dielectric polarization and particle shape effects,” *Journal of Nanomaterials*, vol. 2007, pp. 1–9, 2007.
- [293] A. B. Da Silva, M. Arjmand, U. Sundararaj, and R. E. S. Bretas, “Novel composites of copper nanowire/PVDF with superior dielectric properties,” *Polymer*, vol. 55, pp. 226–234, jan 2014.
- [294] M. C. Araújo, C. M. Costa, and S. Lanceros-Méndez, “Evaluation of dielectric models for ceramic/polymer composites: Effect of filler size and concentration,” *Journal of Non-Crystalline Solids*, vol. 387, pp. 6–15, mar 2014.
- [295] H. Tang, M. H. Malakooti, and H. A. Sodano, “Relationship between orientation factor of lead zirconate titanate nanowires and dielectric permittivity of nanocomposites,” *Applied Physics Letters*, vol. 103, p. 222901, nov 2013.

- [296] Y. Feng, W. L. Li, Y. F. Hou, Y. Yu, W. P. Cao, T. D. Zhang, and W. D. Fei, “Enhanced dielectric properties of PVDF-HFP/BaTiO₃-nanowire composites induced by interfacial polarization and wire-shape,” *Journal of Materials Chemistry C*, vol. 3, no. 6, pp. 1250–1260, 2015.
- [297] M. A. Marwat, B. Xie, Y. Zhu, P. Fan, W. Ma, H. Liu, M. Ashtar, J. Xiao, D. Salamon, C. Samart, and H. Zhang, “Largely enhanced discharge energy density in linear polymer nanocomposites by designing a sandwich structure,” *Composites Part A: Applied Science and Manufacturing*, vol. 121, pp. 115–122, jun 2019.
- [298] Y. Sun, Y. Zhou, Q. Lu, and S. Zhao, “High Energy Storage Efficiency with Fatigue Resistance and Thermal Stability in Lead-Free Na_{0.5}K_{0.5}NbO₃/BiMnO₃ Solid-Solution Films,” *Physica Status Solidi - Rapid Research Letters*, vol. 12, p. 1700364, feb 2018.
- [299] Q. Chi, T. Ma, Y. Zhang, Y. Cui, C. Zhang, J. Lin, X. Wang, and Q. Lei, “Significantly enhanced energy storage density for poly(vinylidene fluoride) composites by induced PDA-coated 0.5Ba(Zr_{0.2}Ti_{0.8})O₃-0.5(Ba_{0.7}Ca_{0.3})TiO₃ nanofibers,” *Journal of Materials Chemistry A*, vol. 5, no. 32, pp. 16757–16766, 2017.
- [300] Z. Pan, L. Yao, G. Ge, B. Shen, and J. Zhai, “High-performance capacitors based on NaNbO₃ nanowires/poly(vinylidene fluoride) nanocomposites,” *Journal of Materials Chemistry A*, vol. 6, no. 30, pp. 14614–14622, 2018.
- [301] L. Yao, Z. Pan, J. Zhai, G. Zhang, Z. Liu, and Y. Liu, “High-energy-density with polymer nanocomposites containing of SrTiO₃ nanofibers for capacitor application,” *Composites Part A: Applied Science and Manufacturing*, vol. 109, pp. 48–54, jun 2018.
- [302] D. H. Kim, H. J. Shin, H. Lee, C. K. Jeong, H. Park, G. T. Hwang, H. Y. Lee, D. J. Joe, J. H. Han, S. H. Lee, J. Kim, B. Joung, and K. J. Lee, “In Vivo Self-Powered Wireless Transmission Using Biocompatible Flexible Energy Harvesters,” *Advanced Functional Materials*, vol. 27, p. 1700341, jul 2017.

- [303] X. Niu, W. Jia, S. Qian, J. Zhu, J. Zhang, X. Hou, J. Mu, W. Geng, J. Cho, J. He, and X. Chou, “High-Performance PZT-Based Stretchable Piezoelectric Nanogenerator,” *ACS Sustainable Chemistry and Engineering*, vol. 7, pp. 979–985, jan 2019.
- [304] Y. Liu, L. Zhao, L. Wang, H. Zheng, D. Li, R. Avila, K. W. Lai, Z. Wang, Z. Xie, Y. Zi, and X. Yu, “Skin-Integrated Graphene-Embedded Lead Zirconate Titanate Rubber for Energy Harvesting and Mechanical Sensing,” *Advanced Materials Technologies*, vol. 4, p. 1900744, dec 2019.
- [305] Binoy Bera, “Recent Advances In Piezoelectric Nano generators In Energy Harvesting Applications BinoyBera,” *Imperial Journal of Interdisciplinary Research*, vol. 2, no. 7, pp. 1274–1291, 2016.
- [306] J. Wu, “Historical Introduction,” in *Advances in Lead-Free Piezoelectric Materials*, pp. 1–40, Singapore: Springer Singapore, 2018.
- [307] Z. Hanani, D. Mezzane, M. Amjoud, A. G. G. Razumnaya, S. Fourcade, Y. Gagou, K. Hoummada, M. El Marssi, and M. Gouné, “Phase transitions, energy storage performances and electrocaloric effect of the lead-free Ba_{0.85}Ca_{0.15}Zr_{0.10}Ti_{0.90}O₃ ceramic relaxor,” *Journal of Materials Science: Materials in Electronics*, vol. 30, pp. 6430–6438, apr 2019.
- [308] S. Siddiqui, D. I. Kim, E. Roh, L. T. Duy, T. Q. Trung, M. T. Nguyen, and N. E. Lee, “A durable and stable piezoelectric nanogenerator with nanocomposite nanofibers embedded in an elastomer under high loading for a self-powered sensor system,” *Nano Energy*, vol. 30, pp. 434–442, dec 2016.
- [309] W. Cai, Q. Zhang, C. Zhou, R. Gao, S. Zhang, Z. Li, R. Xu, G. Chen, X. Deng, Z. Wang, and C. Fu, “Synergistic effect of grain size and phase boundary on energy storage performance and electric properties of BCZT ceramics,” *Journal of Materials Science: Materials in Electronics*, vol. 31, pp. 9167–9175, apr 2020.
- [310] S. K. Si, S. K. Karan, S. Paria, A. Maitra, A. K. Das, R. Bera, A. Bera, L. Halder, and B. B. Khatua, “A strategy to develop an efficient piezoelectric nanogenerator through ZTO assisted γ -phase nucleation of PVDF in ZTO/PVDF nanocomposite

- for harvesting bio-mechanical energy and energy storage application,” *Materials Chemistry and Physics*, vol. 213, pp. 525–537, jul 2018.
- [311] I. Navarro-Baena, V. Sessini, F. Dominici, L. Torre, J. M. Kenny, and L. Peponi, “Design of biodegradable blends based on PLA and PCL: From morphological, thermal and mechanical studies to shape memory behavior,” 2016.
- [312] S. Saravanamoorthy, M. Muneeswaran, N. V. Giridharan, and S. Velmathi, “Solvent-free ring opening polymerization of ϵ -caprolactone and electrical properties of polycaprolactone blended BiFeO₃ nanocomposites,” *RSC Advances*, vol. 5, no. 54, pp. 43897–43905, 2015.
- [313] S. Gong, B. Zhang, J. Zhang, Z. L. Wang, and K. Ren, “Biocompatible Poly(lactic acid)-Based Hybrid Piezoelectric and Electret Nanogenerator for Electronic Skin Applications,” *Advanced Functional Materials*, vol. 30, p. 1908724, apr 2020.
- [314] F. Wang, Y. W. Mai, D. Wang, R. Ding, and W. Shi, “High quality barium titanate nanofibers for flexible piezoelectric device applications,” *Sensors and Actuators, A: Physical*, vol. 233, pp. 195–201, 2015.
- [315] C. Hu, L. Cheng, Z. Wang, Y. Zheng, S. Bai, and Y. Qin, “A Transparent Antipeep Piezoelectric Nanogenerator to Harvest Tapping Energy on Screen,” *Small*, vol. 12, no. 10, pp. 1315–1321, 2016.
- [316] R. Zhu, J. Jiang, Z. Wang, Z. Cheng, and H. Kimura, “High output power density nanogenerator based on lead-free 0.96(K_{0.48}Na_{0.52})(Nb_{0.95}Sb_{0.05})O₃-0.04Bi_{0.5}(Na_{0.82}K_{0.18})_{0.5}ZrO₃ piezoelectric nanofibers,” *RSC Advances*, vol. 6, no. 71, pp. 66451–66456, 2016.
- [317] F. Bernard, L. Gimeno, B. Viala, B. Gusarov, and O. Cugat, “Direct Piezoelectric Coefficient Measurements of PVDF and PLLA under Controlled Strain and Stress,” *Proceedings*, vol. 1, p. 335, aug 2017.
- [318] C. Zhao, J. Zhang, Z. L. Wang, and K. Ren, “A Poly(l-Lactic Acid) Polymer-Based Thermally Stable Cantilever for Vibration Energy Harvesting Applications,” *Advanced Sustainable Systems*, vol. 1, p. 1700068, sep 2017.

- [319] D. J. Shin, J. H. Ji, J. Kim, G. H. Jo, S. J. Jeong, and J. H. Koh, “Enhanced flexible piezoelectric energy harvesters based on BaZrTiO₃–BaCaTiO₃ nanoparticles/PVDF composite films with Cu floating electrodes,” *Journal of Alloys and Compounds*, vol. 802, pp. 562–572, sep 2019.
- [320] L. Gu, J. Liu, N. Cui, Q. Xu, T. Du, L. Zhang, Z. Wang, C. Long, and Y. Qin, “Enhancing the current density of a piezoelectric nanogenerator using a three-dimensional intercalation electrode,” *Nature Communications*, vol. 11, p. 1030, dec 2020.
- [321] S. Wang, L. Lin, Y. Xie, Q. Jing, S. Niu, and Z. L. Wang, “Sliding-triboelectric nanogenerators based on in-plane charge-separation mechanism,” *Nano Letters*, vol. 13, pp. 2226–2233, may 2013.
- [322] S. Niu, Y. S. Zhou, S. Wang, Y. Liu, L. Lin, Y. Bando, and Z. L. Wang, “Simulation method for optimizing the performance of an integrated triboelectric nanogenerator energy harvesting system,” *Nano Energy*, vol. 8, pp. 150–156, sep 2014.
- [323] S. Niu, S. Wang, L. Lin, Y. Liu, Y. S. Zhou, Y. Hu, and Z. L. Wang, “Theoretical study of contact-mode triboelectric nanogenerators as an effective power source,” *Energy and Environmental Science*, vol. 6, no. 12, pp. 3576–3583, 2013.
- [324] J. Briscoe, N. Jalali, P. Woolliams, M. Stewart, P. M. Weaver, M. Cain, and S. Dunn, “Measurement techniques for piezoelectric nanogenerators,” *Energy and Environmental Science*, vol. 6, no. 10, pp. 3035–3045, 2013.
- [325] C. Baek, J. H. Yun, J. E. Wang, C. K. Jeong, K. J. Lee, K. I. Park, and D. K. Kim, “A flexible energy harvester based on a lead-free and piezoelectric BCTZ nanoparticle-polymer composite,” *Nanoscale*, vol. 8, no. 40, pp. 17632–17638, 2016.
- [326] S. K. Karan, S. Maiti, S. Paria, A. Maitra, S. K. Si, J. K. Kim, and B. B. Khatua, “A new insight towards eggshell membrane as high energy conversion efficient bio-piezoelectric energy harvester,” *Materials Today Energy*, vol. 9, pp. 114–125, sep 2018.

- [327] K. I. Park, S. Xu, Y. Liu, G. T. Hwang, S. J. L. Kang, Z. L. Wang, and K. J. Lee, “Piezoelectric BaTiO₃ thin film nanogenerator on plastic substrates,” *Nano Letters*, vol. 10, pp. 4939–4943, dec 2010.
- [328] T. Gao, J. Liao, J. Wang, Y. Qiu, Q. Yang, M. Zhang, Y. Zhao, L. Qin, H. Xue, Z. Xiong, L. Chen, and Q. M. Wang, “Highly oriented BaTiO₃ film self-assembled using an interfacial strategy and its application as a flexible piezoelectric generator for wind energy harvesting,” *Journal of Materials Chemistry A*, vol. 3, no. 18, pp. 9965–9971, 2015.
- [329] W. Wu, L. Cheng, S. Bai, W. Dou, Q. Xu, Z. Wei, and Y. Qin, “Electrospinning lead-free 0.5Ba(Zr_{0.2}Ti_{0.8})O₃-0.5(Ba_{0.7}Ca_{0.3})TiO₃ nanowires and their application in energy harvesting,” *Journal of Materials Chemistry A*, vol. 1, no. 25, pp. 7332–7338, 2013.
- [330] G. Zhu, R. Yang, S. Wang, and Z. L. Wang, “Flexible high-output nanogenerator based on lateral ZnO nanowire array,” *Nano Letters*, vol. 10, pp. 3151–3155, aug 2010.
- [331] M. R. Joung, H. Xu, I. T. Seo, D. H. Kim, J. Hur, S. Nahm, C. Y. Kang, S. J. Yoon, and H. M. Park, “Piezoelectric nanogenerators synthesized using KNbO₃ nanowires with various crystal structures,” *Journal of Materials Chemistry A*, vol. 2, pp. 18547–18553, oct 2014.
- [332] Z. H. Lin, Y. Yang, J. M. Wu, Y. Liu, F. Zhang, and Z. L. Wang, “BaTiO₃ nanotubes-based flexible and transparent nanogenerators,” *Journal of Physical Chemistry Letters*, vol. 3, pp. 3599–3604, dec 2012.
- [333] J. H. Jung, C. Y. Chen, B. K. Yun, N. Lee, Y. Zhou, W. Jo, L. J. Chou, and Z. L. Wang, “Lead-free KNbO₃ ferroelectric nanorod based flexible nanogenerators and capacitors,” *Nanotechnology*, vol. 23, p. 375401, sep 2012.
- [334] K. S. Chary, V. Kumar, C. D. Prasad, and H. S. Panda, “Dopamine-modified Ba_{0.85}Ca_{0.15}Zr_{0.1}Ti_{0.9}O₃ ultra-fine fibers/PVDF-HFP composite-based nanogen-

-
- erator: synergistic effect on output electric signal,” *Journal of the Australian Ceramic Society*, feb 2020.
- [335] K. I. Park, J. H. Son, G. T. Hwang, C. K. Jeong, J. Ryu, M. Koo, I. Choi, S. H. Lee, M. Byun, Z. L. Wang, and K. J. Lee, “Highly-efficient, flexible piezoelectric PZT thin film nanogenerator on plastic substrates,” *Advanced Materials*, vol. 26, pp. 2514–2520, apr 2014.
- [336] N. A. Hoque, P. Thakur, P. Biswas, M. M. Saikh, S. Roy, B. Bagchi, S. Das, and P. P. Ray, “Biowaste crab shell-extracted chitin nanofiber-based superior piezoelectric nanogenerator,” *Journal of Materials Chemistry A*, vol. 6, no. 28, pp. 13848–13858, 2018.
- [337] P. Saini, M. Arora, and M. N. Kumar, “Poly(lactic acid) blends in biomedical applications,” *Advanced Drug Delivery Reviews*, vol. 107, pp. 47–59, dec 2016.
- [338] H. Zhou, J. G. Lawrence, and S. B. Bhaduri, “Fabrication aspects of PLA-CaP/PLGA-CaP composites for orthopedic applications: A review,” 2012.

Appendices

This section contextualizes the experimental approaches and the instrumentation taking place during the characterization of both ceramics and nanocomposites films.

A. Structure and phase analysis

A. 1. X-ray diffraction

X-ray diffraction (XRD) is a powerful and nondestructive technique used largely for crystallographic characterization of solid materials, based on the basic principles that the angle of reflection of X-rays from a sample is related to the crystal structure and composition of the material. XRD can provide structural information of bulk materials and thin film, and also the composition of crystallographic phases presenting in a sample, the extent of defects, size and orientation of grains, and so on. Crystalline structure of BCZT powders was performed by X-ray diffractometer Panalytical X-Pert Pro and Rigaku SmartLab at room temperature employing a step angle of 0.02° in the 2θ range from 5 to 80° and using a Cu-K α radiation ($\lambda \sim 1.540598 \text{ \AA}$). Phases present in the samples has been identified with the search match facility available with Philips X'pert high score plus and the structure refinement has been performed by FullProf Suite software.

A. 2. Fourier-transform infrared spectroscopy

Infrared spectroscopy is a chemical analytical technique based on the absorption phenomenon that occurs when infrared radiation crosses the material. It detects the vibration characteristics (stretch, contract and bend etc.) of chemical functional groups in a sample as an infrared light interacts with the matter (mostly organic). Fourier transform infrared spectroscopy (FT-IR) was used to monitor the functionalization of BCZT nanoparticles starting with the BCZT powder, hydroxylation, through polydopamine coating and to follow the incorporation of BCZT and BCZT@PDA nanoparticles into the PLA matrix. KBr pellet was prepared by using a manual press for the background spectrum. In the case of BCZT and BCZT@PDA nanoparticles, 1 wt% of previously dried sample under vacuum at 80 °C for 6 h was homogeneously mixed with KBr for spectroscopic measurement. In contrast, PLA and PLA-based nanocomposite films were dried in vacuum at 50 °C for 6 h. The spectrum was recorded by using a Bruker Optics Vertex 70 spectrometer in the range of 4000-450 cm^{-1} with a resolution of 4 cm^{-1} (at 32 scans).

B. Ceramic bulk density measurement

The bulk density of the samples was measured by Archimedes principle using Hildebrand Densimeter H-300 S with a density resolution of 0.001 g/cm^3 . Automatic calculation of density was collected from the apparatus. The formula for the calculation of bulk density is presented in Eq. B.1.

$$\rho = \frac{M_a}{(M_b - M_w)\rho_w} \quad (\text{B.1})$$

where M_a is the mass of the sample in air; M_b is the mass of the sample in air after submerged from water; M_w is the mass of the sample in water and ρ_w is the density of water.

C. Thermogravimetric analysis

Thermogravimetric analysis (TGA) allows the follow of the evolution of the mass of a substance subjected to heating or cooling. To determine the optimal calcination temperature of raw BCZT material in order to produce crystalline BCZT powders, TGA (Sytram LABSYS evo) was performed at heating rate of 10 °C/min from room temperature to 1100 °C in air. Besides, the Discovery TGA 55 device was used to characterize the weight loss of BCZT powders during the process of core-shell structuration of BCZT with PDA layer(BCZT@PDA). In the experimental apparatus, about 8 mg of the sample was placed in a platinum crucible and then heated from room temperature to 900 °C at a rate of 10 °C/min under a nitrogen flow of 40 ml/min.

D. Morphology and composition

D. 1. Scanning electron microscopy

Scanning electron microscope (SEM) analysis involves the detection of secondary and backscattered electrons from a sample subjected to a focused primary electron beam and leads to a surface image with a great depth of field. Moreover, SEM can be useful to reveal the surface morphology of the sample. The coupling with an energy dispersive X-ray spectrometer (EDS) attachment can detect the X-rays emitted from the sample which is irradiated with the primary electron beam and provide information about the chemical composition of a specimen. For SEM experiments, the sample was gold sputtered then fixed to sample holder by conductive carbon tape. For BCZT sintered ceramic, the surface morphology was analyzed using a scanning electron microscope Tescan VEGA-3 under voltage of 10 kV. However, for BCZT nanopowders and PLA-based nanocomposite films, JEOL JSM-7600F electron microscope equipped with an electron gun was used under voltage of 5 kV for high resolution images.

D. 2. Transmission electron microscopy

Transmission electron microscopy (TEM) is a microscopy technique whereby a beam of electrons is transmitted through an ultra-thin specimen, interacting with the specimen as it passes through it, magnified and focused by an objective lens and produces an image. In this work, JEOL-ARM 200F Cold FEG TEM/STEM operating at 200 kV and equipped with a spherical aberration (Cs) probe and image correctors (point resolution 0.12 nm in TEM mode and 0.078 nm in STEM mode), was used to observe the morphogenesis in BCZT powders with complex morphologies. Energy-dispersive X-ray spectroscopy–color mapping (EDS) were used to have an insight on the composition of the nanowires, cubes and multipods in BCZT morphogenesis. Meanwhile, Selected Area Electron Diffraction (SAED) allowed the phase identification of these morphologies. While, the coupling of High-Angle Annular Dark-Field (HAADF) detector and Scanning Transmission Electron Microscope (STEM), was used to observe the core-shell structuration of B_NP and the thickness of the PDA-shell layer in B_NP@PDA nanoparticles.

E. Thickness measurement of the nanocomposite films

The average thicknesses of PLA-based nanocomposite films were measured by a precise coating thickness gauge (Surfix Pro S, Phynix). The gauge was first calibrated using the provided calibration coating-standards. Ten thickness-measurements were carried out at different regions of each nanocomposite film, and the corresponding average thickness, with a resolution of 0.1 μm , was collected from the probe Phynix program.

F. Dielectric measurements

The variations of the capacitance (C) and dissipation factor ($\tan\delta$) with temperature in the frequency range of 20 Hz to 1 MHz were performed using an HP 4284A RLC-meter using a voltage of 0.25 V for BCZT sintered ceramics electroded by silver paste. The

dielectric measurement was carried out in a tubular furnace at a heating rate of 2 °C/min. Though, Hioki IM 3570 impedance analyzer was used for the dielectric properties at room temperature and at the frequency range 100 Hz to 1 MHz of gold sputtered PLA-based nanocomposite films.

G. P-E hysteresis loops

The Polarization *vs* Electric field hysteresis measurements ($P - E$ loops) were carried out by a ferroelectric test system AiXACCT, TF Analyzer 3000 equipped with high voltage amplifier Trek 2220. For BCZT ceramics, the thickness of the pellets was reduced to ~ 0.35 mm and were electroded with silver paste. However, for BCZT/PLA nanocomposite films, the samples were electroded by a gold layer on both sides. All samples were connected to the apparatus electrodes by platinum wires.

H. Piezoelectric force microscopy

The local piezoelectric responses of B_NP@PDA nanoparticles before and after embedding in the PLA matrix were investigated with an atomic force microscope (AFM, Asylum Research, MFP-3D) equipped with a piezo-response force module (PFM). To avoid the sticking of the B_NP@PDA nanoparticles to the PFM tip, the particles were fixed using epoxy resin. A Ti/Ir-coated Si tip with a radius of curvature ~ 20 nm (Asytec, Atomic Force F&E GmbH) was utilized, and the electric field was applied to the sample in the virtual ground regime. The out-of-plane piezo-response amplitude images of B_NP@PDA nanoparticles before and after embedding in the PLA matrix were recorded in dual AC-resonance tracking mode at an ac amplitude signal of 60 V and ~ 350 kHz. The PFM amplitude and phase hysteresis loops were measured in the switching spectroscopy off-electric field mode with the pulse DC step signal and overlapped drive ac signal. The waveform parameters were as follows: the sequence of increasing dc electric field steps was driven at 20 Hz with a maximum amplitude of 150–200 V; the frequency of the triangle

envelope was 200 mHz; an overlapping ac sinusoidal signal with an amplitude of 5 or 10 V and a frequency of ~ 350 kHz was used. Three cycles were measured in an off-electric field mode.

I. Energy harvesting in the BF-PNG

To study the output performances of the 20 vol% B_NP@PDA/PLA piezoelectric nanogenerator (BF-PNG), the open-circuit voltage (V_{oc}) and the short-circuit current (I_{sc}) were measured by using a multi-channel, research grade battery cycler (MPG-2, Bio-Logic). The approximate contact forces of finger tapping and hand slapping were evaluated experimentally by using a dual column mechanical testing system (Instron, 3369) Fig. I.1. All measurements were carried out at room temperature. The different tests carried out during the energy harvesting using the BF-PNG are presented as follow:

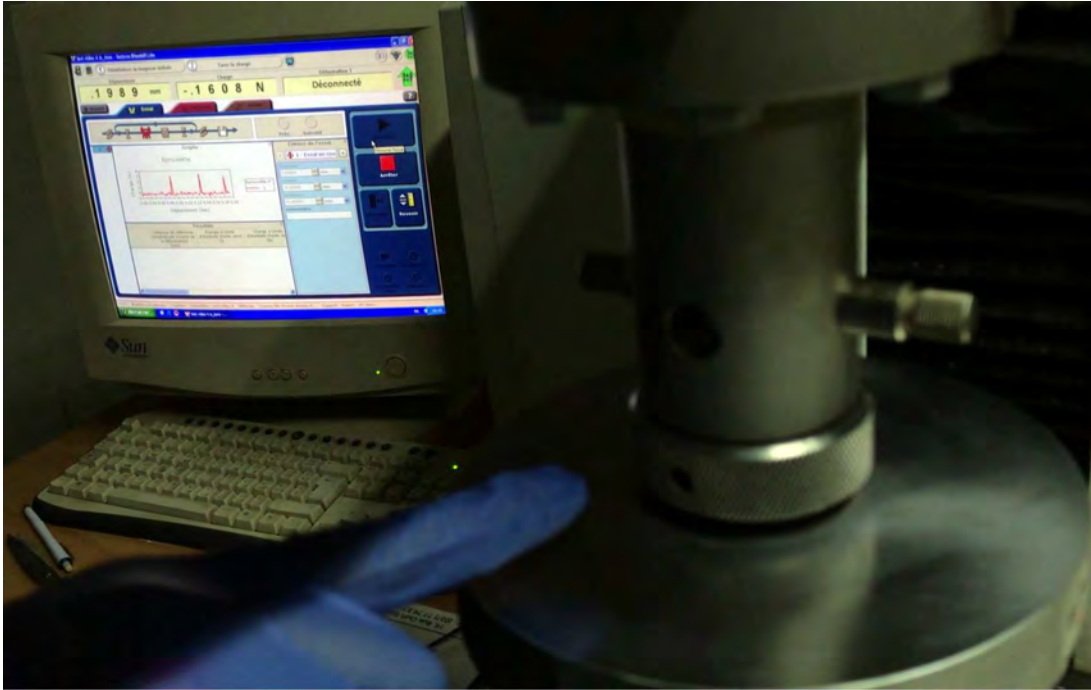


Figure I.1: Contact force measurement under finger tapping.

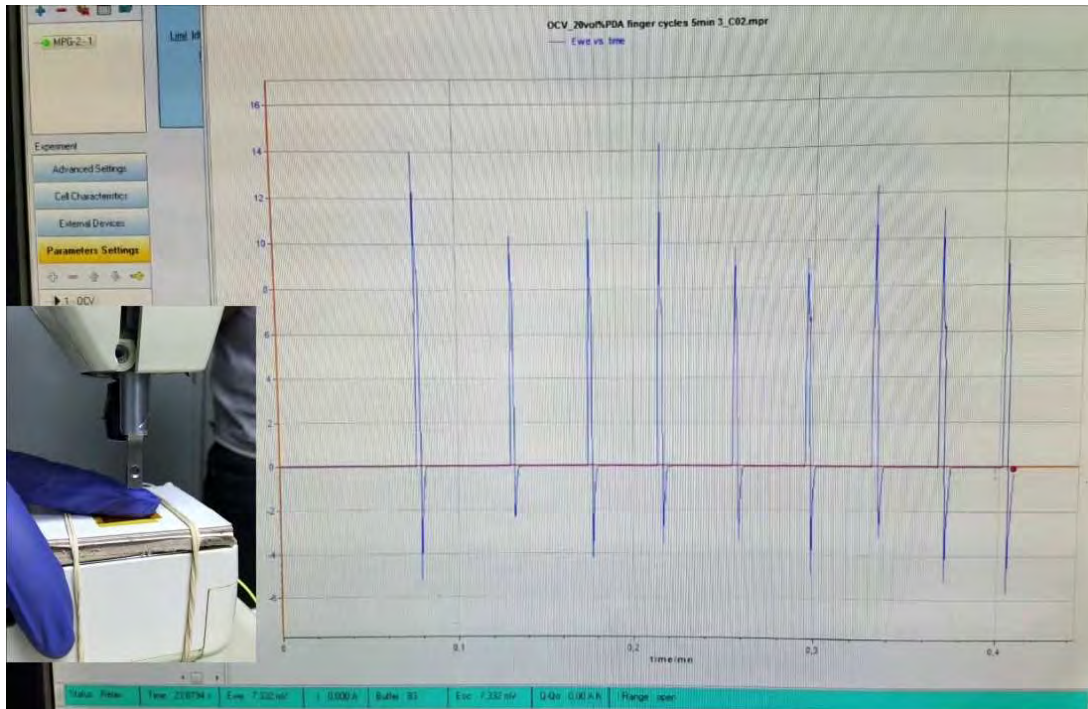


Figure I.2: Open-circuit voltage (V_{oc}) generation under gentle finger tapping.

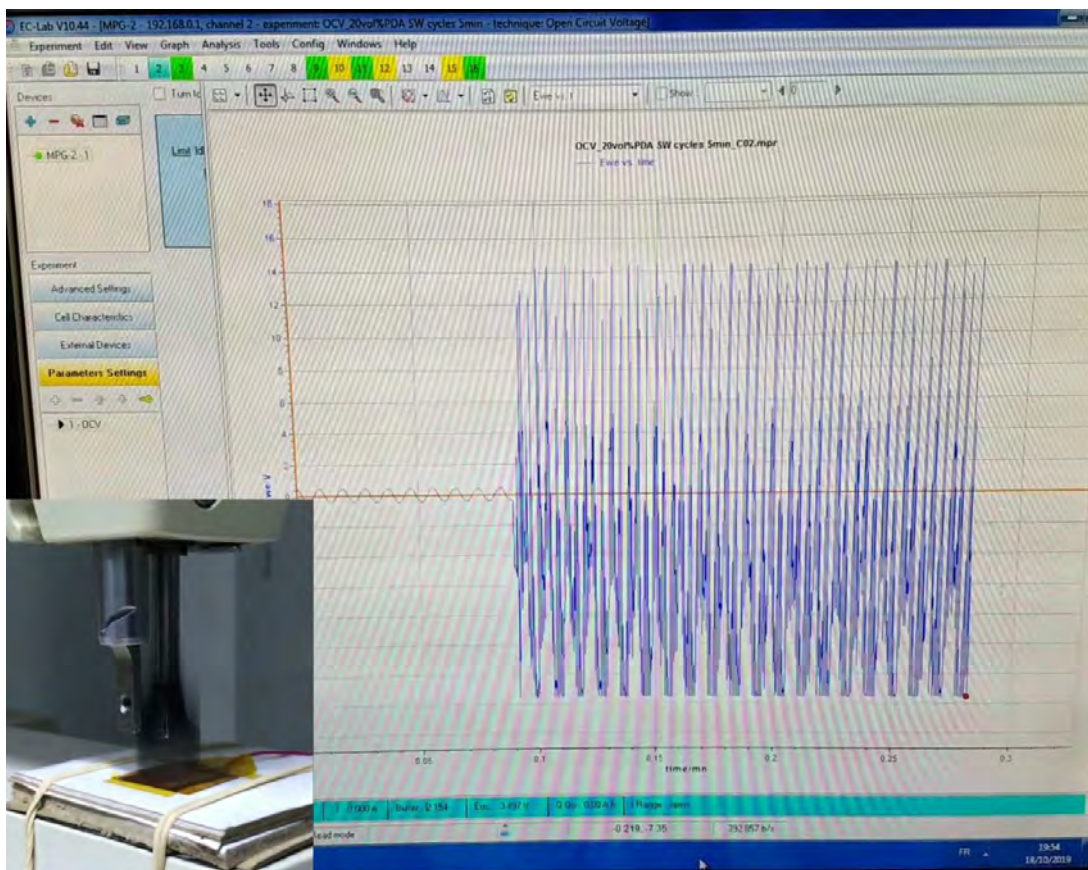


Figure I.3: Stability of the open-circuit voltage (V_{oc}) using a sewing machine.

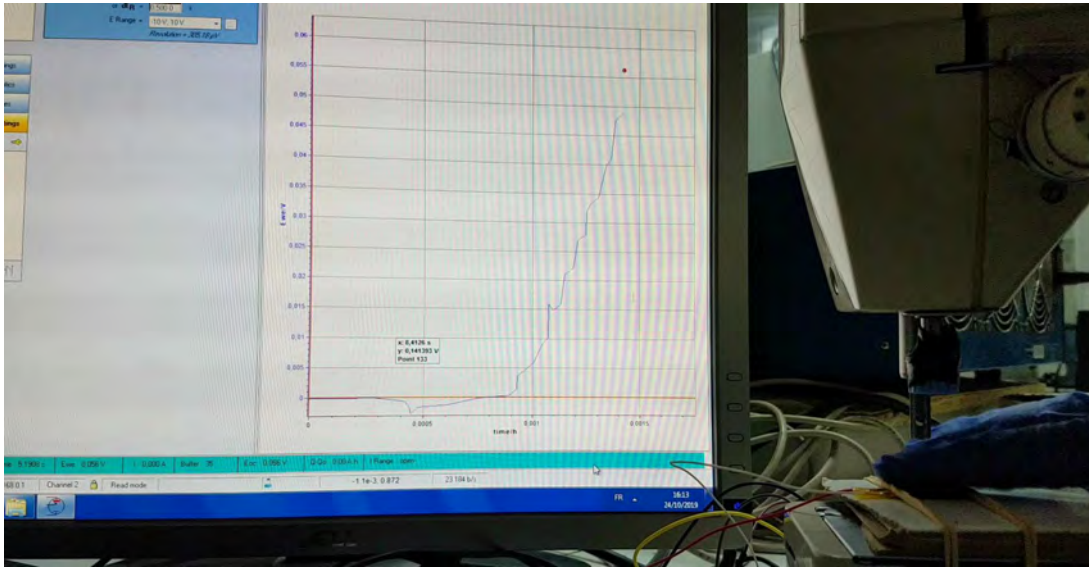


Figure I.4: Capacitor charging by finger tapping.

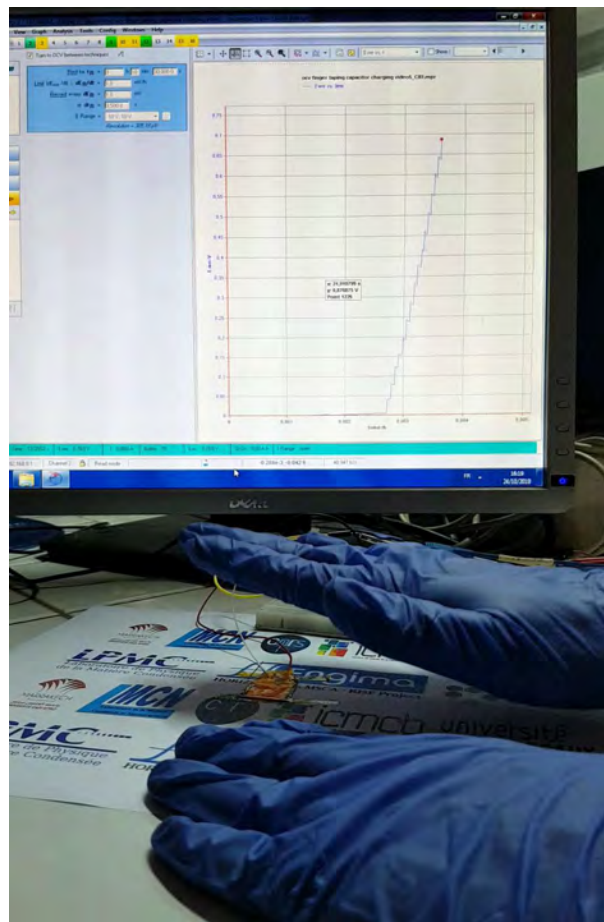


Figure I.5: Capacitor charging by hand slapping.

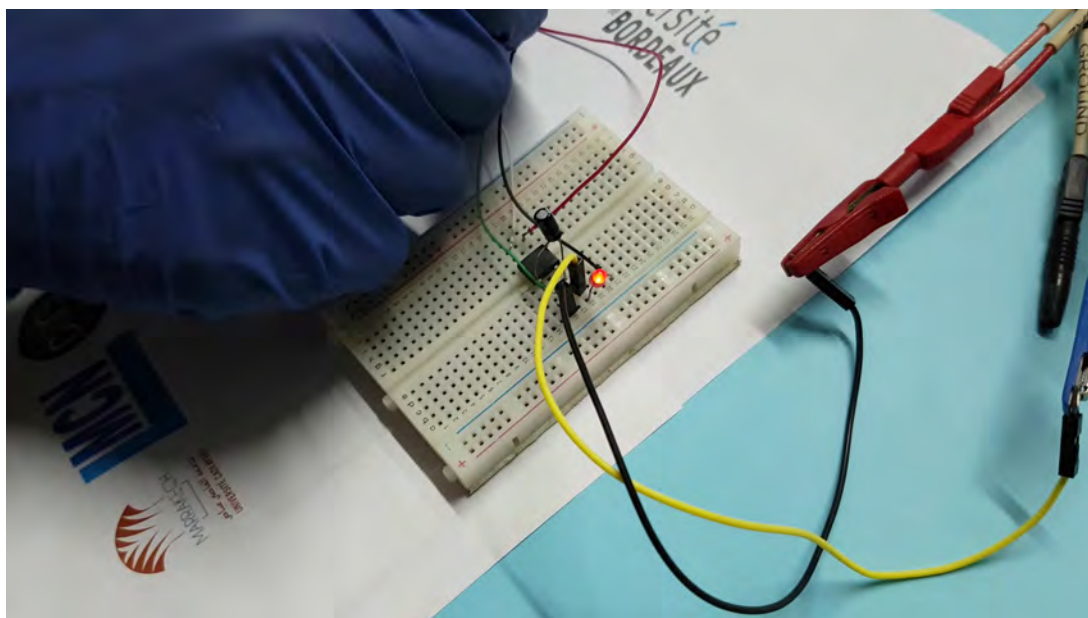


Figure I.6: LED powering by successive finger impartation.